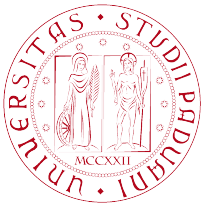

UNIVERSITÀ DEGLI STUDI DI PADOVA

UNIVERSITÀ DEGLI STUDI DI PADOVA
CENTRO INTERDIPARTIMENTALE *"Centro Ricerche Fusione"*

UNIVERSIDADE TÉCNICA DE LISBOA
INSTITUTO SUPERIOR TÉCNICO

JOINT RESEARCH DOCTORATE IN FUSION SCIENCE AND ENGINEERING

CYCLE XXV

Thermal profiles and improved confinement accessibility in RFX-mod and TCV

Coordinator: Ch.mo Prof. Piero Martin

Supervisor: Dott.ssa Lorella Carraro

Doctoral student: Alessandro Scaggion

«Buon giorno», disse il piccolo principe.
«Buon giorno», disse il mercante.
Era un mercante di pillole perfezionate che calmavano la sete. Se ne inghiottiva una alla settimana e non si sentiva piú il bisogno di bere.
«Perchè vendi questa roba?»disse il piccolo principe.
«È una grossa economia di tempo», disse il mercante. «Gli esperti hanno fatto dei calcoli. Si risparmiano cinquantatré minuti la settimana.»
«E che cosa se ne fa di questi cinquantatré minuti?»
«Se ne fa quel che si vuole...»
«Io», disse il piccolo principe, «se avessi cinquantatré minuti da spendere, camminerei adagio adagio verso una fontana...»

Il piccolo principe
Antoine de Saint-Exupéry

L'unico tempo ben speso è quello dedicato all'altro.

Acknowledgments

The research activity which led to this thesis work, has been carried out at Consorzio RFX in the CNR scientific area in Padova and partially at the Centre de Recherche en Physique des Plasmas sited at the Ecole Polytechnique Fédérale de Lausanne.
I would like to express my gratitude to the entire RFX team which gave me the possibility to accomplish my research activity exploiting all the existent facilities. I would like to thank dott.sa Lorella Carraro, dott. Matteo Agostini, and dott. Paolo Scarin for their proficient supervision and encouragement. I gratefully acknowledge support, contributions from and valuable discussions with dott. Fulvio Auriemma, dott.sa Barbara Momo, dott. Gianluca De Masi, dott.sa Rita Lorenzini, dott. Stefano Munaretto dott.sa Maria Ester Puiatti, dott. Gianluca Spizzo, dott. Marco Valisa, dott. Nicola Vianello and dott.sa Barbara Zaniol and the entire FA group of RFX-mod experiment.
I would like to express my gratitude to dott. Stefano Coda and the entire TCV team to actively involved me in TCV experimental session. I would like to thank dott. Holger Reimerdes and dott. Yves Martin for their proficient supervision and support during my stay at CRPP.

MOTIVATION AND THESIS OUTLINE

Humans do not live by bread alone. Physically we are puny creatures with limited prowess, but with unlimited dreams. In the last few decades humankind reached the Moon (1969) and built airports over the sea (1994), but 925 million people are still under- or malnourished (2010). To follow his dream to ensure every human being the same adequate quality of life, humankind needs energy. The long-term world energy scenarios (50-80 years) foresee the need for reliable, sustainable and environmental friendly sources of energy. Thermonuclear fusion is one of the main actors in the energetic basket, it offers the possibility to produce large supplies of energy at relatively low costs reducing the impact on the environment. In fact, thermonuclear fusion represents a promising chance to generate energy without the emission of carbon dioxide and the production of long living radioactive wastes. Moreover, the raw materials used as fuel in the fusion reactions, deuterium and tritium, are easily available on Earth. This chance motivates the efforts on the controlled thermonuclear fusion research. Anyway, the development of nuclear fusion as an energy source is one of the most complex scientific and technical tasks ever undertaken for non-military purposes. The nuclear fusion obtained by magnetic confinement of plasma emerged in the latest years as the most promising concept to menage the power produced by fusion reactions. The studies developed in that direction, since the fifties, yielded more and more encouraging results and important breakthroughs both in physics and technology and inspired the ITER project. This experimental reactor could give, in the next few decades, the definitive answers to many questions on the scientific and technological feasibility of a fusion reactor.

One of the major concerns in magnetic confinement fusion research is the quest for the best plasma performance, which is intimately linked to two main issues: plasma confinement and boundary conditions. Both, incidentally, are connected to plasma stability. The link between confinement and boundary conditions is very strong and found many evidences. For example in the tokamak (the magnetic confinement configuration main line) the quest for a mild plasma-wall interaction a controlled recycling led to the discovery of an ameliorated operating mode with high performance. As a matter of fact, H-mode was discovered in ASDEX the first diverted device. In RFPs (an alternative magnetic confinement configuration) a spontaneous transition to an ameliorated plasma state, the QSH state, is due to a reduced chaos obtained with an accurate control of the magnetic boundary conditions. In turn, the access to the QSH state led to a favorable edge topology characterized by better boundary

conditions. The onset of the QSH state induces an edge helical ripple which reduce the plasma wall interaction. My research activity, reported in this thesis work, focused on the accessibility conditions and characterization of improved confinement regimes in TCV tokamak and RFX-mod RFP devices.
In RFX-mod my research activity focused on the study and the characterization of electron temperature profiles. Temperature is one of the key parameters that qualifies fusion plasma performance and, in RFX-mod plasmas, it is mainly determined by three quantities: plasma current, electron density and plasma magnetic state. Through a large statistical analysis the temperature profile variations were investigated and related to the main macroscopic and operational plasma parameters. This analysis resulted in scaling laws for central temperature, external temperature and temperature gradient. Some further analysis was dedicated to a distinctive feature: the appearance of transport and thermal barriers which result in better plasma performance. The formation of an Internal Transport Barrier (eITB) is triggered by the growth of a dominant MHD tearing mode which, in turn, leads to a reduced magnetic chaos in the plasma core. Starting from previous analysis, these eITBs were investigated and their influence of the whole temperature profile addressed. Besides the established phenomena related to eITBs, the occasional appearance of extremely high gradients in the external region of the plasma column was observed. Some general observations and a first speculation on the physical mechanism leading to their formation will be presented. The work ends up in a wide and general picture which tries to clear up the physics governing the temperature profile modifications and proposes possible operations to trigger them.
Present day tokamaks high performance scenarios rely on the possibility to access the high confinement mode (H-mode). Transition from the standard confinement mode (L-mode) to the H-mode is typically achieved when the external input power exceeds a threshold. This power threshold is found to strongly depend on plasma density, toroidal magnetic field and plasma size, but many experiments have shown this power threshold to also depend on plasma shape and configuration geometry. My activity at TCV aimed at the study of such dependence, in particular the influence of X-point location on H-mode power threshold was investigated. During a two months stay in 2011, a series of experiments was dedicated to such a study. Significant variations in the power threshold due to a reduction of the X-point height has been documented, in agreement with the scaling observed in other machines. Moreover, the well-established non-monotonic density dependence of the H-mode power threshold has been measured and recorded. In this thesis work the analysis procedure followed to the TCV experimental campaign is reported.
The dissertation proceeds as follows:

CHAPTER 1 The worldwide problem of energy production for civil purposes is introduced and thermonuclear fusion is presented as a future low cost and environmental friendly response. The main features of toroidal magnetic confinement are discussed and the tokamak and RFP magnetic configurations are presented as respectively the main line

and an alternative configuration for a future fusion reactor. RFX-mod and TCV, the two toroidal machines on which the thesis work is focused are described.

CHAPTER 2 The issue of plasma boundary in fusion devices is briefly introduced together with its strong link with plasma confinement properties. This topic is then focused on the specific machines. On the one side, the enhanced confinement properties related to the diverted configurations and to the H-mode in Tokamaks are presented and the TCV H-mode properties are briefly reviewed. On the other side, the RFP paradigm amelioration leading to the reduced chaos state (SHAx state) is discussed along with the related favorable edge topology as occurring at RFX-mod.

CHAPTER 3 The wide-range RFX-mod electron temperature profile characterization is discussed. In particular: the influence of the main macroscopic plasma parameters is statistically investigated and empirical scaling laws for core temperature, external temperature and external temperature gradient are presented. Consequently a global physical picture explaining the temperature dependencies and the profile shape changes is proposed.

CHAPTER 4 In RFX-mod, two distinctive phenomena leading to a sharp change of the electron temperature profile shape are observed. On the one hand, the chaos healing effect related to the growth of a dominant MHD tearing mode triggers the formation of electron Internal Transport Barriers (eITBs). On the other hand, the occasional appearance of extremely high gradients developing at $r/a \sim 0.8$ have been related to the formation of an effective SOL at the plasma edge. This chapter is devoted to analyze the eITBs characteristics, to illustrate eETBs phenomenon and to evaluate and compare their impact on the plasma performance and confinement properties.

CHAPTER 5 The TCV unique shaping capabilities are exploited to investigate the H-mode power threshold dependence. Investigations and plasma shaping studies on operations performed during 2011 TCV are presented: the well known non monotonic density dependence has been measured and first confirmations about the beneficial reduction of the X-point height are documented.

CHAPTER 6 The thesis work is summarized, conclusions are drawn and future perspectives for both RFP and tokamak activity are proposed.

KEYWORDS plasma, RFP, RFX-mod, electron temperature, temperature profile, plasma performance, scaling laws, transport barriers, Tokmak, TCV, H-mode, power threshold, X-point, X-point height

L' uomo non vive di solo pane. Fisicamente siamo creature minute con possibilitá ridotte, ma i nostri sogni non conoscono confini. Negli ultimi decenni l'umanitá è sbarcata sulla Luna (1969) e ha costruito aeroporti sul mare (1994), ma 925 milioni di persone sono soffrono ancora la fame (2010). Per inseguire il sogno di assicurare ad ogni essere umano una qualitá di vita decorosa, l'umanitá ha bisogno di energia. Le prospettive energetiche a lungo termine (50-80 anni) prevedono la necessitá di sorgenti di energia affidabili, sostenibili ed eco-compatibili. La fusione termonucleare è una delle possibilitá piú promettenti all'interno del paniere energetico, infatti offre la possibilitá di produrre energia in grandi quantitá a costi relativamente bassi e con un ridotto impatto ambientale. La fusione termonucleare potrebbe diventare una fonte energetica senza emissioni di anidride carbonica e con una minima produzione di scorie radioattive a lunga vita media. Inoltre, le materie prime utilizzate come combustibile nelle reazioni di fusione, deuterio e trizio, sono ampiamente disponibili sulla Terra. Ecco i validi motivi per gli sforzi dedicati allo studio della fusione termonucleare controllata. Ma, lo sviluppo della fusione nucleare come fonte di energia è una delle sfide piú complesse dal punto di vista tecnico-scientifico mai intraprese per scopi non militari. La fusione nucleare a confinamento magnetico del plasma é emersa negli ultimi anni come l'idea piú promettente per gestire l'energia prodotta da questa fonte di energia. Gli studi sviluppati in questa direzione, dagli anni Cinquanta, hanno dato risultati sempre piú incoraggianti, hanno portato ad importanti innovazioni sia nel campo della fisica che della tecnologia e hanno ispirato il progetto ITER. Questo reattore sperimentale potrebbe dare, nei prossimi decenni, le risposte definitive a molte domande sulla fattibilitá scientifica e tecnologica di un reattore a fusione.

Uno dei principali interessi nel campo della ricerca sulla fusione a confinamento magnetico è la ricerca delle migliori prestazioni di plasma. Queste sono intimamente legate a due aspetti: confinamento del plasma e le condizioni alla parete. Entrambi, per inciso, sono collegati alla stabilitá del plasma. Il legame tra il confinamento e le condizioni alla parete è stretto e ben documentato. Ad esempio nel tokamak (la principale configurazione a confinamento magnetico) la ricerca di una ridotta interazione plasma-parete e di un riciclaggio controllato ha portato alla scoperta di una modalitá di funzionamento migliorata caratterizzata da alte prestazioni. Infatti, il modo H è stato scoperto ad ASDEX la prima macchina con divertore. Nei RFP (una configurazione alternativa) una transizione spontanea verso uno stato di plasma

migliorat, lo stato QSH, legata ad un ridotto caos è stata ottenuta ottenuta con un accurato controllo delle condizioni magnetiche a bordo plasma. A sua volta, l'accesso alla QSH ha portato ad una topologia magnetica favorevole caratterizzata da una migliore condizione a bordo plasma. L'insorgere della QSH induce un ripple elicoidale al bordo che riduce l'interazione plasma-parete. La mia attivitá di ricerca, riportata in questo lavoro di tesi, si è concentrata sulle condizioni di accessibilitá e la caratterizzazione dei regimi di confinamento migliorato nei due sperimenti TCV (di tipo tokamak) ed RFX-mod (di tipo RFP).
In RFX-mod la mia attivitá si è concentrata sullo studio e la caratterizzazione del profilo di temperatura elettronica. La temperatura è uno dei parametri fondamentali per qualificare le prestazioni dei plasmi da fusione e, in RFX-mod, è determinata principalmente da tre parametri: corrente di plasma, densitá elettronica e stato magnetico. Attraverso un'analisi statistica ad ampio spettro, le variazioni del profilo di temperatura sono state analizzate e poste in relazione con le principali grandezze macroscopiche ed i parametri operativi della macchina. L'andamento gnerale di temperatura centrale, temperatura esterna e gradiente di temperatura è stato rappresentato attraverso delle leggi di scala. Alcune ulteriori analisi sono state dedicate ad un fenomeno particolare: la comparsa di barriere di trasporto termico che determinano migliori prestazioni di plasma. La formazione di una barriera di trasporto interna (eITB) è innescata dalla crescita di un modo tearing dominante che, a sua volta, porta ad una riduzione del caos magnetico nel centro del plasma. Basandosi su lavori precedenti, le eITB sono state analizzate e la loro influenza sull'intero profilo di temperatura è stata valutata. Oltre ai consolidati fenomeni legati alle eITB, è stata osservata l'occasionale comparsa di gradienti molto elevati nella regione esterna della colonna di plasma. Alcune osservazioni di carattere generale e una prima speculazione sul meccanismo fisico che porta alla loro formazione saranno presentati. Il lavoro termina con un quadro ampio e generale che cerca di valutare la fisica che disciplina le variazioni del profilo di temperatura e propone alcune tecniche operative per il loro controllo.
Negli odierni tokamak gli scenari ad alte prestazioni si basano sulla possibilitá di accedere ad uno stato ad alto confinamento (modo H). La transizione dallo stato di confinamento standard (modo L) al modo H si ottiene tipicamente quando la potenza esterna iniettata nel plasma supera una soglia. Questa soglia di potenza dipende fortemente dalla densitá del plasma, dal campo magnetico toroidale e dalle dimensioni del plasma, ma in molte macchine si è dimostrato come questa soglia dipenda anche dalla forma del plasma e dalla geometria della configurazione. La mia attivitá a TCV è stata dedicata allo studio di queste dipendenze, in particolare nell'analisi dell'influenza della posizione del punto a X. In due mesi di permanenza a Losanna nel 2011, ho partecipato ad una serie di esperimenti dedicati a tale argomento. Si sono documentate variazioni significative della soglia di potenza riducendo l'altezza del punto a X, in accordo con quanto giá osservato in altre macchine. Inoltre, la dipendenza non monotona di tale soglia dalla densità stata misurata e verificata. In questo lavoro di tesi si sono discussi le procedure di analisi seguite alla campagna spetimentale di TCV ed i conseguenti risultati.

La tesi è articolata come segue:

CAPITOLO 1 Si introduce il problema della produzione di energia a scopo civile su scala mondiale e la fusione termonucleare viene presentata come una futura sorgente di energia eco-compatibile ed a basso costo. Si discutono le caratteristiche principali del confinamento magnetico toroidale e le configurazioni magnetiche tokamak e RFP sono presentate rispettivamente come la linea principale e un configurazione alternativa per un futuro reattore a fusione. Infine vengono descritte le due macchine toroidali, RFX-mod e TCV, su cui è focalizzato il lavoro di tesi.

CAPITOLO 2 La fisica del plasma di bordo in macchine da fusione viene brevemente introdotta insieme al suo stretto legame con le proprietá di confinamento. Questo tema è poi declinato rispetto ad ognunga delle due macchine. Da una parte, le proprietá di confinamento avanzate relative alle configurazioni con divertore e al modo H nei Tokamak sono presentate e le proprietá del modo H a TCV sono brevemente passate in rassegna. Dall'altro lato, il paradigma di un RFP migliorato conseguente alla riduzione del caos (stato SHAx) è discusso assime al relativo miglioramento della topologia magnetica a bordo plasma cosí come avviene a RFX-mod.

CAPITOLO 3 Si discute la caratterizzazione ad ampio spettro dei profili di temperatura elettronica in RFX-mod. In particolare: l'influenza dei principali parametri di plasma è analizzata statisticamente e sono proposte leggi di scala empiriche per le temperature centrale ed esterna e per il gradiente di temperatura. Successivamente, viene esposto un quadro fisico globale per spiegare le variazioni di temperatura e del suo profilo.

CAPITOLO 4 In RFX-mod, due diversi fenomeni portano ad un brusco cambiamento della forma del profilo di temperatura elettronica. Da un lato, la diminuzione del caos magnetico legata alla crescita di un modo tearing dominante innesca la formazione delle barriere interne di trasporto elettronico (eITBs). D'altra parte, l'occasionale comparsa di gradienti molto elevati approssimativamente ad $r/a \sim 0.8$ è correlata alla formazione di un SOL efficace a bordo plasma. Questo capitolo è dedicato ad analizzare le caratteristiche delle eITB e ad illustrare il fenomeno delle eETB, nonchè a valutarne e confrontarne l'impatto sulle prestazioni e sulle proprietá di confinamento del plasma.

CAPITOLO 5 Le ampie possibilitá di cambiare la forma del plasma di TCV sono sfruttate per studiare le variaiozni della soglia di potenza del modo H. Le indagini operative e i conseguenti studi realizzati a TCV nel corso del 2011 sono presentati: è stata misurata la nota dipendenza non monotona dalla densitá e si sono documentate le prime conferme dei benefici legati alla riduzione dell'altezza del punto a X.

PAROLE CHIAVE plasma, RFP, RFX-mod, temperatura elettronica, profilo di temperatura, prestazioni di plasma, leggi di scala, barriere di trasporto, Tokmak, TCV, modo H, soglia di potenza, punto a X, altezza del punto a X

CONTENTS

Motivation and thesis outline **i**

Motivazioni e linee generali **v**

Contents **ix**

1 Thermonuclear magnetic controlled fusion **1**
1.1 Introduction: energy need and world perspectives . . . 2
1.2 The thermonuclear fusion . . . 3
1.2.1 Energy from thermonuclear fusion reactions . . . 4
1.2.2 The burning criteria . . . 5
1.2.3 Plasma confinement . . . 7
1.3 Magnetic confinement . . . 8
1.3.1 MHD theory . . . 10
1.3.2 MHD equilibrium . . . 12
Perturbation to the equilibrium . . . 12
1.4 Toroidal magnetic configurations . . . 14
1.4.1 Stellarator . . . 14
1.4.2 Tokamak . . . 15
1.4.3 Reversed Field Pinch (RFP) . . . 16
1.5 RFX-mod: Reversed Field eXperiment . . . 18
1.5.1 Selected diagnostics . . . 19
1.6 TCV: Tokamak à Configuration Variable . . . 22
1.6.1 Electron Cyclotron Resonance Heating . . . 23
1.6.2 Selected diagnostics . . . 24
1.7 ITER: International Thermonuclear Experimental Reactor . . . 27

2 Plasma boundary and confinement paradigm **29**
2.1 Plasma boundary . . . 30
2.1.1 Limiter and divertor concepts . . . 31
2.2 Tokamaks: from the divertor to the H-mode . . . 33
2.2.1 H-mode at TCV . . . 37

2.3 RFPs: From SHAx states to helical divertor concept . . . 39
2.3.1 The RFX-mod edge . . . 43
2.3.2 RFX-mod density issues . . . 47
2.3.3 Dynamo Relaxation Events . . . 48

3 RFX-mod: characterization of temperature profiles 51
3.1 External region characterization method . . . 53
3.1.1 Fitting function choice . . . 53
3.1.2 Limiting the parameters space . . . 56
3.1.3 Full profile matching . . . 59
3.2 Experimental procedure and preliminary analysis . . . 62
3.2.1 Database . . . 62
3.2.2 Temperature profile distinction . . . 64
3.2.3 Peculiar cases discrimination . . . 67
3.2.4 Testing the database: central temperature scaling . . . 69
3.3 Empirical scalings for the external region . . . 73
3.3.1 Spatial extent: $\boldsymbol{\Delta}$ . . . 76
3.3.2 External temperature: $\boldsymbol{T_e^{knee}}$ and $\boldsymbol{T_e^{foot}}$ . . . 79
3.3.3 Maximum gradient: $\boldsymbol{\nabla T_e^{max}}$ . . . 83
3.4 Other influent quantities . . . 84
3.5 Profile changes . . . 87
3.5.1 Effective scrape-off layer . . . 89
3.6 Conclusion and physics overview . . . 93

4 RFX-mod: improved regimes thermal characterization 97
4.1 eITB: Internal Transport Barriers . . . 98
4.1.1 eITB characterization method . . . 99
4.1.2 eITB empirical scalings . . . 104
4.2 eETB: External Thermal Barriers . . . 107
4.2.1 Characteristics and scaling . . . 109
4.2.2 Effective SOL formation: the drive for ETBs . . . 112
4.2.3 Overall physics of ETBs . . . 115
4.2.4 Final remarks . . . 116
4.3 eITBs vs eETBs: plasma performance and confinement properties . . . 118

5 TCV: H-mode accessibility 121
5.1 X-point geometry influence on H-mode power threshold . . . 122
5.2 TCV experiments: experimental setup . . . 130
5.2.1 X-point configuration . . . 130
5.2.2 Target plasma . . . 132
5.2.3 Experimental procedure . . . 132

5.2.4 Power threshold estimate 134
5.3 Threshold power versus density 137
5.4 Threshold power versus X-point height 138
5.5 GAP influence on H-mode power threshold 146
5.6 Summary and remarks 148

6 Conclusion and perspectives **149**
6.1 RFX-mod: temperature profile characterization 150
6.1.1 Main results 151
6.1.2 Future perspectives and developments 155
6.2 TCV: H-mode accessibility 157
6.2.1 Main results 157
6.2.2 Future perspectives and possible developments 157

References **159**

Contributed works **171**

1

THERMONUCLEAR MAGNETIC CONTROLLED FUSION

Anyone who believes exponential growth can go on forever
in a finite world is either a madman or an economist.
Kenneth E .Boulding

In this chapter the worldwide problem of energy production for civil purposes is introduced, some considerations about the important characteristics of a future energy source are proposed. The thermonuclear fusion is presented as a leading actor in the energetic basket because of its possibility to produce large supplies of energy at relatively low costs reducing the impact on the environment. Nevertheless, the development of nuclear fusion as a reliable energy source is one of the most complex scientific and technical tasks ever undertaken for non-military purposes. The main features of toroidal magnetic confinement is discussed and the tokamak and RFP magnetic configurations are presented as respectively the main line and an alternative configuration for a future fusion reactor. The two machines on which the thesis work focused, RFX-mod and TCV, are presented and the ITER project is briefly mentioned as the next step in fusion research.

1.1 Introduction: energy need and world perspectives

Nowadays humankind needs energy, and lots of it, to live a life of comfort. In fact, the quality of life in different regions of the world can be directly correlated with the per capita use of energy[1]. The United Nations Development Programme (UNDP) provided a quantitative way to measure the quality of life in a given part of the world: the *human development index* (HDI). In this regard, HDI of various countries is directly determined by the amount of per capita electricity consumption[1], see Figure 1.1. UN defines as 'developed countries' those with HDI ~ 0.9. In order to provide to every human being the same comfortable quality of life, every country should get to this values. In fact, most of the developing world (~ 5 billion people) is crawling up the UN curve of HDI versus per capita electricity consumption, from abysmally low values of today towards the average of the whole world and eventually towards the average of the developed world. This translates into a massive energy hunger for the globe as a whole. It has been estimated that by the year 2050, the global electricity demand can grow up to factor of 3 the actual consumption.
This need for energy, and thus the increase in energy consumption, is limited by availability of non-renewable energy source and environmental constraint. Today, most of the worldwide electricity demand is satisfied by oil (41%), natural gas (22%), coal (16%), nuclear (15%), and renewables (6%) [1]. If this pattern does not change, the conventional oil and gas resources will last for few tens of years at present levels of consumption, with only coal, the largest emitter of CO_2, having the potential to last a few hundred years. Furthermore, for international political stability, nations will seek electricity supply solutions which allow them to become as independent as possible from the possessors of crucial fuel resources[2]. The large increase in CO_2 emissions over the last century, due to the intense use of traditional fossil fuels, led to considerable climate changes resulting in a destabilization of the worldwide climate system. To stabilize CO_2 concentrations in the atmosphere at non dangerous level, the present energy supply system needs to change towards CO_2-free energy sources. Alternative clean energy resources, such as solar and wind, will probably contribute much more to the world's energy needs than they do at present and have the potential to become a major source of energy. Conversely they yet have to address issues of energy density (which makes them unsuitable for large urban industrial complexes), efficiency and cost of production before they can become a viable alternative. In the past, nuclear energy based on fission has been adopted by many developed and most advanced countries. Technically, the ability to use fission as a longterm energy source has been demonstrated, and the fuel cycle economics and environmental impact are known. The long term wider deployment of fission depends on a full public appreciation of the options and alternatives. A number of countries consider fission a vital element in their current and future electricity supply combination. Nevertheless, many disadvantages are related to fission: the shortage of Uranium that will last approximately for 200 years, the long half life of the radioactive waste that imply a lot of problems about their disposal and, not less important, the fact that fission could develop in a

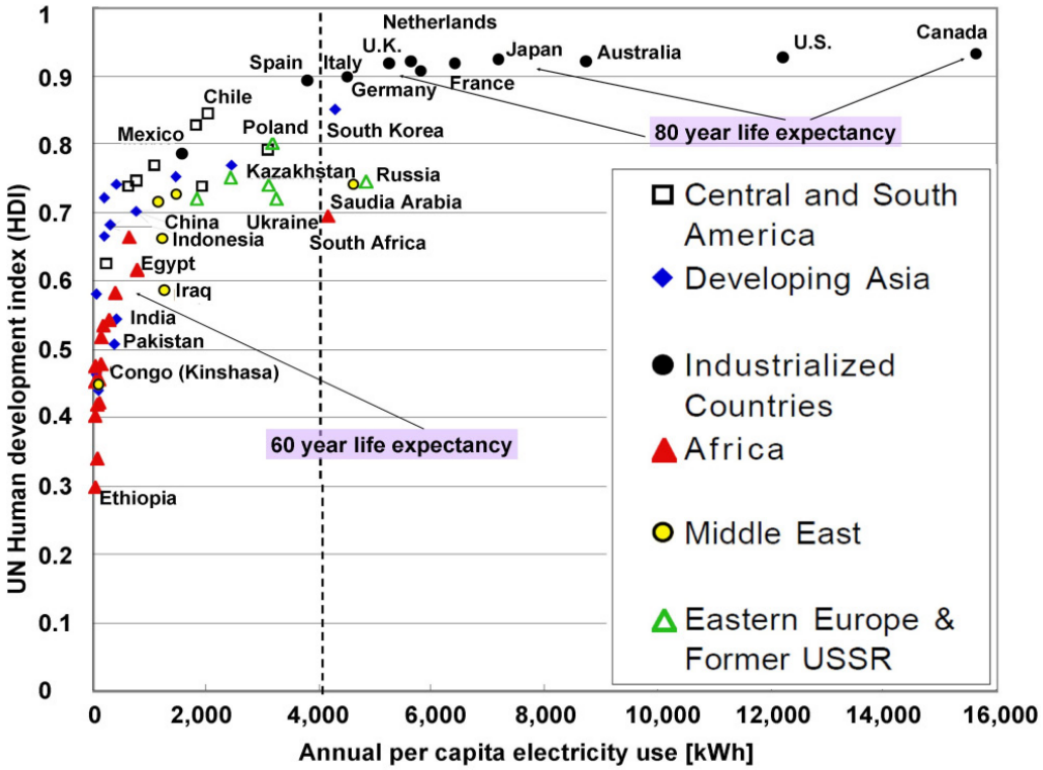

Figure 1.1: United Nations human development index as a function of per capita energy use in kWh (60 countries, 1997). Electricity consumption increases with human development. Taken from [1].

uncontrolled runaway reaction. Thus the human race is at a critical juncture today, when we need to quickly develop a viable alternative source of clean energy with easy global accessibility which can lead to sustainable development. Controlled thermonuclear fusion can be a serious candidate to answer this need[1, 3].

1.2 THE THERMONUCLEAR FUSION

Thermonuclear fusion is referred to as the nuclear reaction among two light nuclei that fuse into a heavier one, releasing other reaction products such as neutrons. This is a widespread phenomenon in nature. It is well known, for example, that fusion reactions provide a huge source of energy to stars. In order for fusion to occur between different nuclei, they must be brought sufficiently close so to allow the short-range attractive nuclear force to overcome the Coulomb repulsion due to the positive charge of the particles. This condition implies that the nuclei must approach each other at high relative speed. For nuclear fusion, temperatures from 10^7 K to 10^8 K are required. At these temperatures the positive charged particles can penetrate the Coulomb barrier by quantum mechanical tunneling and fuse together to form heavier nuclei. In these conditions the fusion fuel is found to be fully ionized, as a quasi-neutral

ensamble of ions and electrons known as *plasma*.

1.2.1 Energy from thermonuclear fusion reactions

The thermal rearrangement in fusion reactions results in a reduction of the total mass and a consequent release of energy in the form of kinetic energy of the reaction products. Because the Coulomb barrier increases as the square of the atomic number, the most feasible reactions involve hydrogen, deuterium, tritium and helium. The main fusion reactions between these light nuclei are:

$$ {}^{2}_{1}\mathrm{D} + {}^{2}_{1}\mathrm{D} \rightarrow {}^{3}_{1}\mathrm{T}\,(1.01\,\mathrm{MeV}) + {}^{1}_{1}\mathrm{H}\,(3.02\,\mathrm{MeV}) \quad (50\,\%) \tag{1.1} $$

$$ {}^{2}_{1}\mathrm{D} + {}^{2}_{1}\mathrm{D} \rightarrow {}^{3}_{2}\mathrm{He}\,(0.82\,\mathrm{MeV}) + {}^{1}_{0}\mathrm{n}\,(2.45\,\mathrm{MeV}) \quad (50\,\%) \tag{1.2} $$

$$ {}^{2}_{1}\mathrm{D} + {}^{3}_{1}\mathrm{T} \rightarrow {}^{4}_{2}\mathrm{He}\,(3.52\,\mathrm{MeV}) + {}^{1}_{0}\mathrm{n}\,(14.06\,\mathrm{MeV}) \tag{1.3} $$

$$ {}^{2}_{1}\mathrm{D} + {}^{3}_{2}\mathrm{He} \rightarrow {}^{4}_{2}\mathrm{He}\,(3.71\,\mathrm{MeV}) + {}^{1}_{1}\mathrm{H}\,(14.64\,\mathrm{MeV}) \tag{1.4} $$

The most favorable one is (1.3) because of its reaction cross section which peaks at the lowest plasma energy of ~ 100 keV, as shown in Figure 1.2. At that energy the D-T cross section is 100 times larger than the D-D and $D - {}^{3}_{2}\mathrm{He}$ cross sections. The supplies of deuterium fuel are limitless, since 0.015% of all the water hydrogen atoms are deuterium. On the other hand

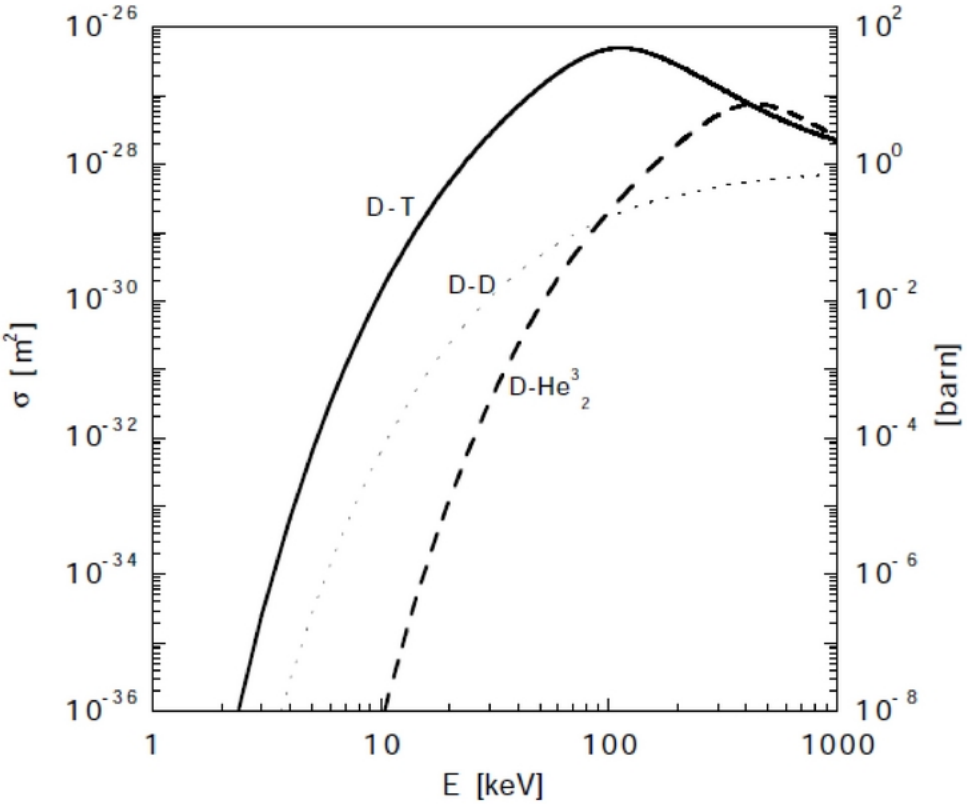

Figure 1.2: Cross section as a function of energy for some fusion reactions.

tritium can not be found in nature given its short lifetime, only 12.3 years. Anyhow tritium can be obtained from lithium, using the neutron released by the D-T reaction:

$$ {}^{6}_{3}\mathrm{Li} + {}^{1}_{0}\mathrm{D} \rightarrow {}^{4}_{2}\mathrm{He} + {}^{3}_{1}\mathrm{T} + 4.8\,\mathrm{MeV} \tag{1.5} $$

$$ {}^{7}_{3}\mathrm{Li} + {}^{1}_{0}\mathrm{D} \rightarrow {}^{4}_{2}\mathrm{He} + {}^{3}_{1}\mathrm{T} + {}^{1}_{0}\mathrm{n} - 2.5\,\mathrm{Mev} \quad . \tag{1.6} $$

The implementation of a lithium blanket surrounding the vacuum vessel of a fusion reactor can therefore provide the necessary tritium fuel supplies.
Compared to fossil fuel power plant, a fusion power plant does not produce greenhouse gases; the main natural product of the fusion reaction is helium, which is completely harmless to life and does not contribute to global warming. In addition in a fusion reactor, unlike in a fission one, there is no risk of uncontrolled runaway of the reaction.

1.2.2 The burning criteria

The aim of nuclear fusion research is to achieve a plasma that generates more energy through fusion reactions than that required to create and sustain it. In order to fullfill this target there is a condition that a thermalized D-T plasma has to satisfy to serve as an energy producing system. beside the energy production through fusion reactions, a plasma can lose energy in several ways. Transport processes such as diffusion, convection, charge exchange and others, are all together empirically described by an energy confinement time τ_E leading to the power loss term $P_t = 3nkT/\tau_E$ where $3nkT$ is the internal thermal plasma energy (n is the electron density). Note that this energy is twice the ideal gas value, since every hydrogen atom is split into two particles (electron and nucleus) the degrees of freedom are doubled. Another loss mechanism is the *bremsstrahlung* radiation, which becomes particularly important at high temperatures and high impurity concentrations. The power loss due to *bremsstrahlung* can be written as

$$ P_b = C_b Z_{eff} n^2 \sqrt{kT} \tag{1.7} $$

with Z_{eff} the effective charge of the plasma[a] and C_b a constant. The fusion reactions power generation can be written as

$$ P_n = W_{DT} \frac{n^2}{4} \langle \sigma v \rangle_T \tag{1.8} $$

where W_{DT} is the energy released by the single D-T fusion reaction, namely 17.59 MeV, and $\langle \sigma v \rangle_T$ is the average, over a Maxwellian distribution, of the cross section times the nuclei relative velocity given as a function of the temperature. Assuming the reaction power P_n to be used to supply the losses with an efficiency η, the self-sustainement condition reads

$$ P_b + P_t \leq \eta (P_b + P_t + P_n) \tag{1.9} $$

[a] *The effective charge of the plasma can be calculated, including all (impurity) species, as* $Z_{eff} = \sum_z n_z Z^2 / n$.

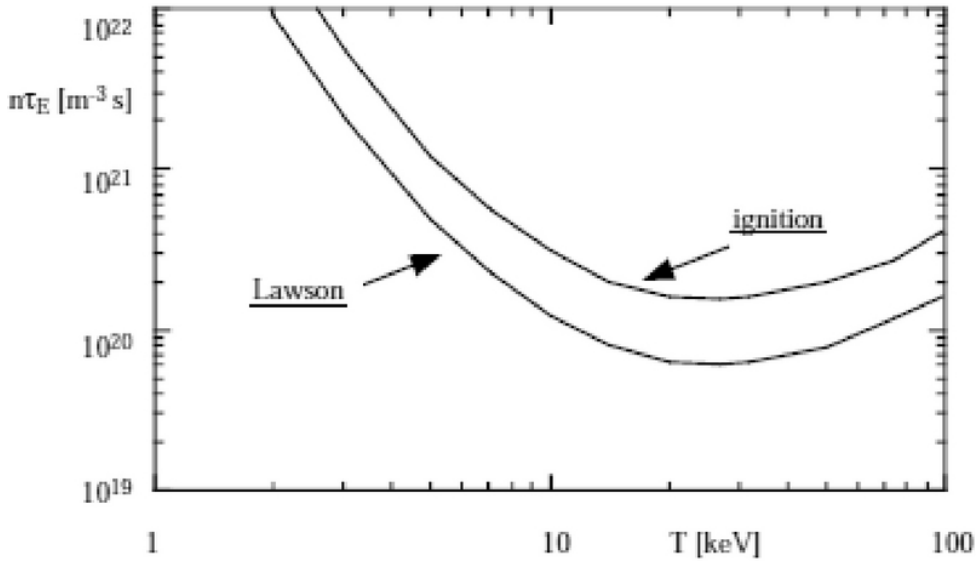

Figure 1.3: The minimum $n\tau_E$ curves for which Lawson's and ignition criteria are satisfied. The Lawson's curve refers to an efficiency $\eta = 30\%$.

and this can be rewritten into the famous *Lawson's criterion*:

$$n\tau_E \geq 3T \left(\frac{\eta}{\eta - 1} \frac{W_{DT}}{4} \langle \sigma v \rangle_T - bT^2 \right)^{-1} \quad . \tag{1.10}$$

Since the right hand side depends only on the temperature, the product $n\tau_E$ satisfying the equality can be plotted as a function of T as can be seen in Figure 1.3 where this curve is shown for an efficiency of $\eta = 30\%$. Notice that it has a minimum value close to 20 keV and the requirements for ignition at this temperature are

$$T \sim 20\,\text{keV} \qquad \Rightarrow \qquad n\tau_E \gtrsim 0.6 \cdot 10^{20}\,\text{m}^{-3}\text{s} \quad . \tag{1.11}$$

In a magnetic confinement reactor α-particles should be confined in the plasma to transfer their energy of 3.5 MeV to the plasma while slowing down, on the other hand neutrons cannot be confined and leave the plasma without interaction. In other words, α-particles are required to sustain the fusion reactor keeping the plasma hot by means of their power P_α, whereas for the electric energy production the neutral particles will be exploited. Given that, the Lawsons's criterion should be modified into the so called *ignition criterion*

$$P_b + P_t \leq P_\alpha \tag{1.12}$$

which can be expressed as

$$n\tau_E \geq 3T \left(\frac{\eta}{\eta - 1} \frac{W_\alpha}{4} \langle \sigma v \rangle_T - bT^2 \right)^{-1} \tag{1.13}$$

with W_α the energy of the single α-particle after the fusion reaction. Noting that $W_\alpha = W_{DT}/5$ it can be understood that this criterion is more strict then the former. In Figure 1.3 it is shown the minimun ignition curve where the new requirements to fullfill the ignition condition is

$$T \sim 20\,\text{keV} \qquad \Rightarrow \qquad n\tau_E \gtrsim 1.5 \cdot 10^{20}\,\text{m}^{-3}\text{s} \qquad . \tag{1.14}$$

An evocative way to summarize the last result is to use the so called *triple product*:

$$n\tau_E\, T \geq 3 \cdot 10^{21}\,\text{m}^{-3}\text{s}\,\text{keV} \qquad . \tag{1.15}$$

1.2.3 Plasma confinement

The fusion triple product (1.15) dictates the strategy for developing fusion power as an energy producing system. One has to reach temperatures of about 10 keV and obtain the required density and energy confinement time simultaneously. There are two distinct approaches to achieve these results:

1. ***Magnetic confinement: maximizing the confinement time***. The hot plasma is confined by strong magnetic fields leading to maximum densities of $\sim 1.5 \cdot 10^{20}$ m^{-3}, approximately 10^5 times smaller than the atom density of a gas under standard conditions. With these densities, the energy confinement time required ranges from 2 to 4 seconds. This approach, which is the main line in fusion research, is the subject of this thesis work. Figure 1.4 shows the values of the triple product reached in magnetic fusion devices, since the beginning of experiment in plasma physics. The clear trend shows the improvement in confinement achieved up to now and the goal that the scientific community must reach to provide a fusion power plant to the world. It has to be noted that, nowadays, only three experiments JET, TFTR and JT-60, have achieved conditions near these requirements.

2. ***Inertial confinement: maximizing the density***. This can be done by strong, symmetric heating of a small D-T pellet. The heating can be done with lasers or particle beams and leads to ablation of some material causing implosion due to momentum conservation. It is clear that the energy confinement time is extremely short in this concept: it is the time required for the particles to leave the hot implosion center. Since it is the mass inertia which causes the finiteness of this time, this approach to fusion is often called 'inertial fusion'. The required density is about 1000 times the density of liquid D-T; the pressure in the implosion center equals (at temperatures of 10 keV) that reached in the center of the sun.

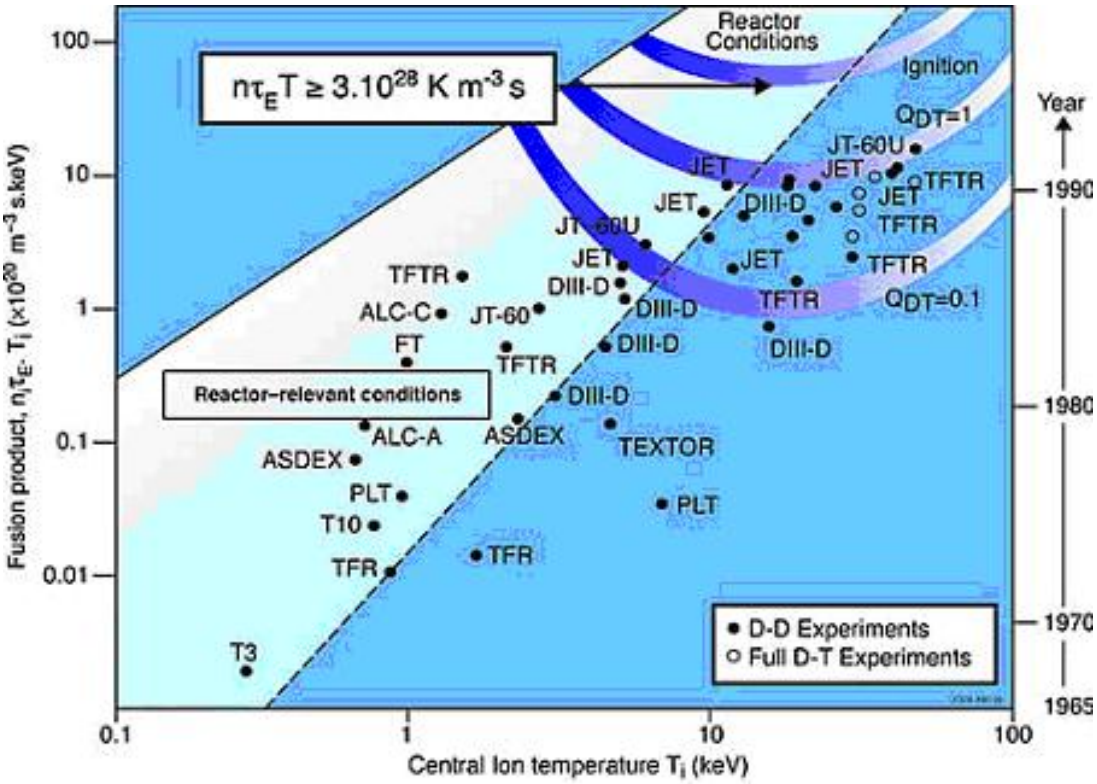

Figure 1.4: Values of the fusion triple product obtained in magnetic fusion experiments as a function of the central ion temperature T_i.

1.3 Magnetic confinement

As previously mentioned, plasma can be confined by magnetic fields. As a matter of fact, in presence of a uniform magnetic field charged particles move on a spiral path along the magnetic field lines, the radius of such a gyration motion being the *Larmor radius* $r_L = \frac{mv_\perp}{qB}$, where m is the particle mass, q the particle electric charge, B the background magnetic field and $v_\perp$ is the particle velocity in the direction perpendicular to the magnetic field. Historically the first experimental configurations were linear, but in these configurations the end losses were large to reach the necessary energy confinement time τ_E. These end losses can be completely avoided in a toroidal system, i.e. making the field lines ending on theirself. But in such a configuration, namely a system with purely toroidal magnetic field, important perpendicular motions arise due to the geometry of the field lines. In fact the magnetic field, generated with properly magnetic coils placed around the torus, is not uniform. Its curvature and gradient result in a vertical drift

$$\boldsymbol{v}_d \propto \frac{1}{q}\frac{\boldsymbol{B}\times\nabla\boldsymbol{B}}{B^3} \tag{1.16}$$

which is in opposite directions for ions and electrons. This charge separation results in an electric field that causes an outward $\boldsymbol{E}\times\boldsymbol{B}$ drift of the whole plasma, being charge independent:

$$\boldsymbol{v}_{E\times B} = \frac{\boldsymbol{E}\times\boldsymbol{B}}{B^2} \quad . \tag{1.17}$$

A configuration with a purely toroidal magnetic field will therefore be unstable. A sketch of such a magnetic field configuration and of these drifts is shown in Figure 1.5a. To avoid this charge separation, it is necessary to twist the magnetic field lines by an additional magnetic field component perpendicular to the former, i.e. a poloidal component. In this way $\boldsymbol{B}$ changes periodically its sign resulting in an average null $\boldsymbol{E}\times\boldsymbol{B}$ drift. A sketch of this configuration is shown in Figure 1.5b. The configurations described in the following paragraphs are characterized by a rotation symmetry around the axis of a torus, so the most useful frame of reference is a toroidal one, which is shown in Figure 1.6.

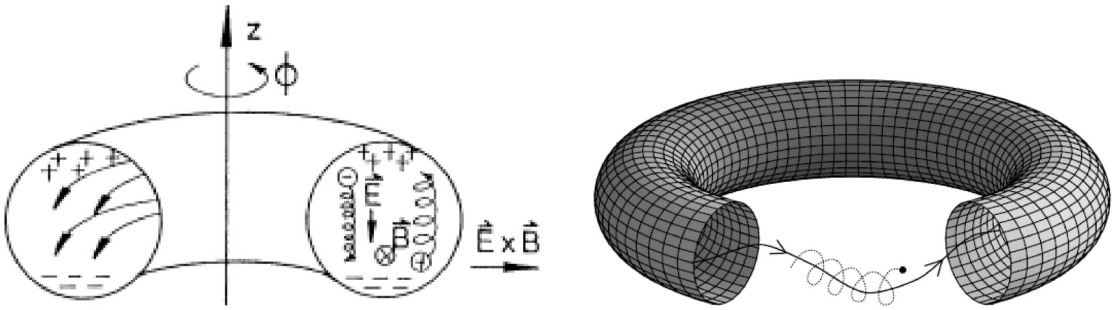

(a) (b)

Figure 1.5: (a) Vertical drifts and associated $\boldsymbol{E}\times\boldsymbol{B}$ in a purely toroidal field. (b) Principle of toroidal confinement. A charged particle gyrates around a magnetic field line and is confined inside the vacuum vessel.

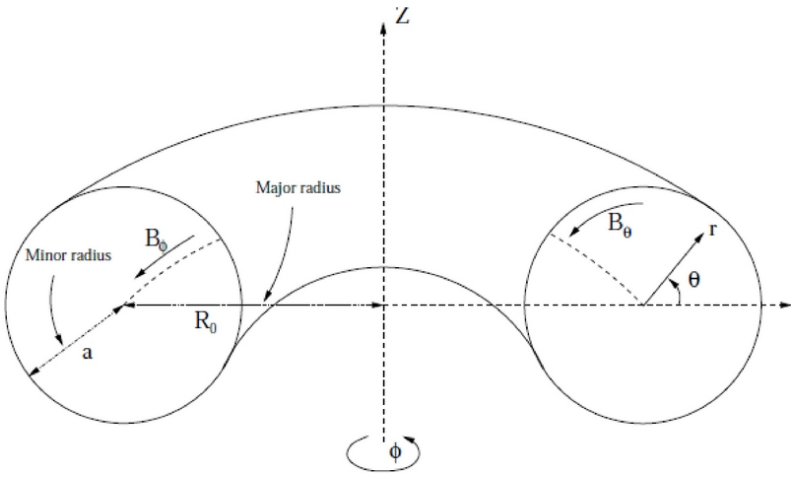

Figure 1.6: The toroidal coordinate system applied to a torus.

1.3.1 MHD theory

A large variety of plasma properties, such as the magnetic equilibria or several instabilities associated with them, can be described using a fluid model called resistive *MagnetoHydroDynamics* (MHD) [4]. A brief introduction to this theory is given in the following. In the two-fluids MHD, where the plasma is described as composed by ions and electrons, the mass and momentum continuity equations can be written as follows:

$$\frac{\partial \rho_\alpha}{\partial t} + \nabla \cdot (\rho_\alpha \boldsymbol{u_\alpha}) = 0 \tag{1.18}$$

$$\rho_\alpha \left(\frac{\partial \boldsymbol{u_\alpha}}{\partial t} + \boldsymbol{u_\alpha} \cdot \nabla \boldsymbol{u_\alpha} \right) = \sigma_\alpha \boldsymbol{E} + \boldsymbol{j} \times \boldsymbol{B} - \nabla p_\alpha + R_{\alpha\beta} \tag{1.19}$$

where $\alpha, \beta = i, e$ (i.e. ions or electrons), $\rho_\alpha = m_\alpha n_\alpha$ is the mass density, and $\sigma_\alpha = \pm e n_\alpha$ is the charge density of the single species. No particle or momentum sources are considered here for simplicity. The electromagnetic quantities $\boldsymbol{E}$, $\boldsymbol{B}$ and $\boldsymbol{j}$ have the usual meaning. The first two terms in the right hand side of equation (1.19) represent the electromagnetic forces, $-\nabla p_\alpha$ is the kinetic pressure force and $R_{\alpha\beta}$ is the rate at which momentum is gained or lost by species α due to collisions with species β.
A plasma can also be described as a single fluid by introducing the following variables: the mass density $\rho = \rho_i + \rho_e$, the kinetic pressure $p = p_i + p_e$, the mass fluid velocity $\boldsymbol{u} = (\rho_i \boldsymbol{u_i} + \rho_e \boldsymbol{u_e})/\rho$, and the charge density $\sigma = e(n_i - n_e)$. By combining the two-fluids equations (1.18) and (1.19) and using the above relations, it is simple to derive the following fluid equations:

$$\frac{\partial \rho}{\partial t} + \nabla \cdot (\rho \boldsymbol{u}) = 0 \tag{1.20}$$

$$\rho_\alpha \left(\frac{\partial \boldsymbol{u}}{\partial t} + \boldsymbol{u} \cdot \nabla \boldsymbol{u} \right) = \sigma \boldsymbol{E} + \boldsymbol{j} \times \boldsymbol{B} - \nabla p \tag{1.21}$$

$$\boldsymbol{E} + \boldsymbol{j} \times \boldsymbol{B} = \eta \boldsymbol{j} - \frac{\boldsymbol{j} \times \boldsymbol{B} - \nabla p_e}{n_e} \tag{1.22}$$

Equation (1.20) is the mass continuity equation, equation (1.21) is the momentum continuity equation, also called single-fluid equation of motion, and equation (1.22) is the generalized Ohm's law, which is not strictly a single-fluid equation, because of the ∇p_e term. What is usually referred to as *resistive MHD model* can be derived by the fluid equations (1.20), (1.21) and (1.22) under the following two approximations:

a) charge quasi-neutrality, $n_i \sim n_e$, which permits to drop the term $\sigma \boldsymbol{E}$ in (1.21);

b) small ion Larmor radius compared with the scale-length of the fluid motion, which causes the Hall ($\boldsymbol{j} \times \boldsymbol{B}/n_e$) and diamagnetic ($-\nabla p_e/n_e$) terms in Ohm's law to be negligible with respect to the other terms.

The latter set of single fluid equations, combined with the Maxwell's equations and a closure term for the heat flux, describes the behavior of plasma in a magnetic field. The heat flux is

usually modeled by an equation of state for pressure of the form $p \propto n^{\gamma}$. The exponent γ can be chosen depending on the phenomena to be modeled. For example, $\gamma = 1$ represents isothermal compression and $\gamma = 5/3$ adiabatic compression. By combining Faraday's law ($\nabla \times \boldsymbol{E} = -\partial \boldsymbol{B}/\partial t$) with Ohm's law, it is simple to derive the following equation, which describes the coupled dynamics of the magnetic and fluid velocity fields in the resistive MHD framework:

$$\frac{\partial \boldsymbol{B}}{\partial t} = \nabla \times (\boldsymbol{u} \times \boldsymbol{B}) + \frac{\eta}{\mu_0} \nabla^2 \boldsymbol{B} \tag{1.23}$$

The first term on the right-hand side in equation (1.23) represents the *dynamo* term and describes the convection of the magnetic field with the plasma and its amplification or reduction due to compressive motion perpendicular to the magnetic field. Starting from this equation, it is possible to show that in the ideal MHD limit, i.e. in the case where the resistivity η is negligible, the magnetic field lines move like if they were frozen into the plasma. The second term describes the *resistive diffusion* of the field across the plasma. Dynamo and resistive diffusion, well known phenomena in magnetic confined fusion, act on different time scales dominating different kind of mechanisms. More in details, given a magnetic structure with a characteristic scale length l, the resistive diffusion time:

$$\tau_R = \frac{\mu_0 l^2}{\eta} \tag{1.24}$$

is the longest time scale involved in resistive MHD equations; in contrast, to the dynamo term corresponds the propagation velocity of the so called *Alfvén waves* [5]:

$$v_A = \frac{B}{\sqrt{\rho \mu_0}} \tag{1.25}$$

which travel the aforementioned spatial scale l in a time

$$\tau_A = \frac{l}{B} \sqrt{\rho \mu_0} \tag{1.26}$$

the so called *Alfvén time*. The Alfvén time is the shortest time scale involved in MHD dynamics. This two time scales can be also used in (1.23) to describe the dynamics of the magnetic field in terms of τ_A, τ_R and l. Combining them the *Lundquist number* is obtained:

$$S = \frac{\tau_R}{\tau_A} \quad . \tag{1.27}$$

Such quantity characterizes the thermodynamic and turbulence properties of a magnetized fluid. Usually, being $\eta \ll 1$, S reaches very high values. In typical laboratory thermonuclear plasmas $S \sim 10^6$ while in astrophysical plasmas S can reach 10^{12}.

1.3.2 MHD equilibrium

The equilibrium of a toroidal configuration is regulated by the ideal MHD equilibrium equation, the so-called *force-balance equation*

$$\nabla p = \boldsymbol{j} \times \boldsymbol{B} \tag{1.28}$$

which comes from (1.21) by applying plasma quasi-neutrality, neglecting inertial terms and considering $\partial \boldsymbol{u}/\partial t = 0$. Taking $\boldsymbol{j}$ from Ampére's law

$$\boldsymbol{j} = \frac{1}{\mu_0} \nabla \times \boldsymbol{B} \tag{1.29}$$

where the displacement current is neglected, and inserting it into the force-balance equation (1.28), the *pressure balance condition*

$$\nabla \left(p + \frac{B^2}{2\mu_0} \right) = \frac{1}{\mu_0} (\boldsymbol{B} \cdot \nabla) \boldsymbol{B} \tag{1.30}$$

can be obtained. The term on the right-hand side of equation (1.30) comes from the bending and parallel compression of the field lines, whereas the terms on the left-hand side indicate that the magnetic field can be considered to have a magnetic pressure given by $B^2/2\mu_0$. The ratio of the plasma pressure to the magnetic pressure is called *beta parameter*

$$\beta = \frac{2\mu_0 p}{B^2} \qquad . \tag{1.31}$$

β measures the efficiency of the magnetic field in establishing the plasma equilibrium. Laboratory plasmas tends to have $\beta \lesssim 10\%$, so that the magnetic field plays a major role in the dynamics of the plasma.
Equation (1.28) tells us that $\boldsymbol{j}$ and $\boldsymbol{B}$ are each perpendicular to ∇p. As a result, they must lie on surfaces of constant p, called *magnetic surfaces*. To a first approximation, one can assume $\beta = 0$, so to neglect toroidal effects. In this case, the magnetic field admits a component B_ϕ in the toroidal direction and a component B_θ in the poloidal one, but no radial component; the same consideration holds for every other field. Moreover, there is a smooth radial pressure gradient ∇p so that the surfaces of constant p are nested, concentric tori. The magnetic axis (defined as the zero radius magnetic surface) corresponds to the geometric axis of the torus. This configuration is sketched in Figure 1.7.

Perturbation to the equilibrium

The MHD equations introduced in Section 1.3.1 predict that under certain conditions a small perturbation in a fluid quantity, e.g density, fluid velocity or magnetic field, can grow and become unstable in time. These phenomena are called *MHD instabilities*. They are present in all fusion devices, where they influence in many ways the global plasma properties and

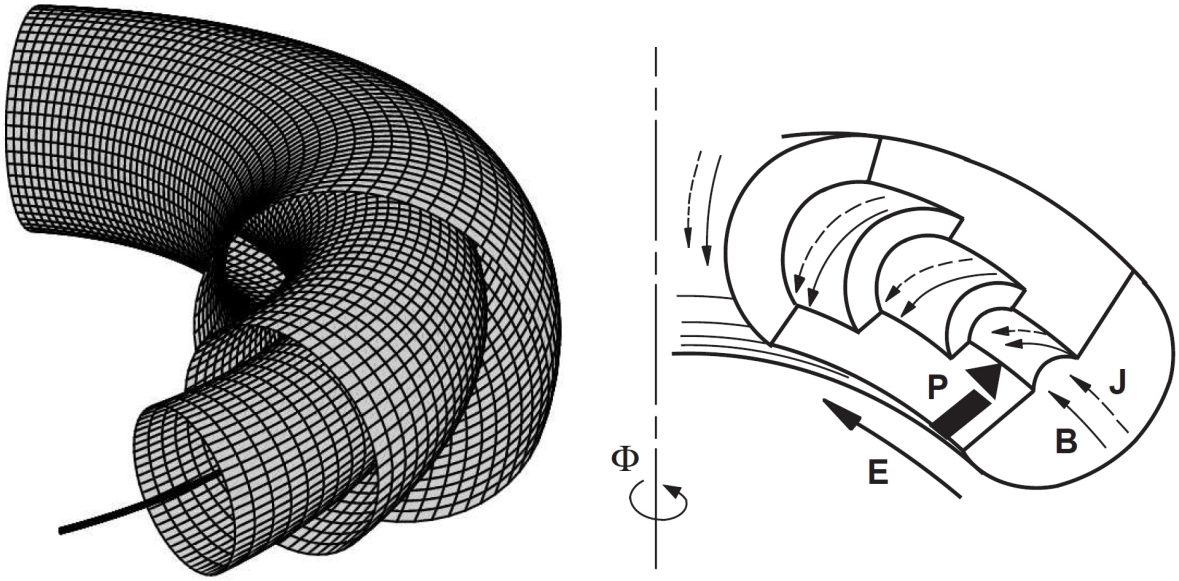

(a) (b)

Figure 1.7: (a) Magnetic surfaces and magnetic axis in toroidal geometry owing to the equilibrium fields. (b) Schematic view of magnetic and current density field lines, pressure gradient and magnetic surfaces for a typical magnetic confinement configuration.

can deteriorate the plasma confinement performance. A perturbation $\widetilde{\boldsymbol{A}}$ of a quantity $\boldsymbol{A}$ in a toroidal plasma can be Fourier analyzed as follows:

$$\widetilde{\boldsymbol{A}}(r,t) \;=\; \sum_k \widetilde{A}_k(r) e^{i(\boldsymbol{k}\cdot\boldsymbol{r}-\omega t)} \;=\; \sum_k \widetilde{k}(r) e^{i(m\theta+n\phi-\omega t)} \tag{1.32}$$

where $\boldsymbol{k} \;=\; (k_r, k_\theta, k_\phi) \;=\; (k_r; m/r; n/R_0)$ is the wavevector in toroidal coordinates, m and n are the poloidal and toroidal mode number, respectively. Each couple (m,n) represents a helical perturbation, or *mode*. The angular frequency ω is, in general, a complex quantity, $\omega = \omega_R + i\omega_I$, the real part of which describes the propagation velocity, while the imaginary part represents an exponential growth ($\omega_I > 0$) or damping ($\omega_I < 0$) of the perturbation amplitude. A helical magnetic perturbation with wavevector $\boldsymbol{k}$ can become unstable if it fulfills the resonance condition $\boldsymbol{k}\cdot\boldsymbol{B} = 0$, where $B = (0, B_\theta, B_\phi)$ is the equilibrium magnetic field. In fact, a perturbation with $\boldsymbol{k}\cdot\boldsymbol{B} \neq 0$ would bend the mean magnetic field, and it would be thus energetically unfavored. The above resonance condition can be rewritten as follows:

$$\boldsymbol{k}\cdot\boldsymbol{B} \;=\; \frac{m}{r}B_\theta + \frac{n}{R_0}B_\phi \;=\; 0 \qquad . \tag{1.33}$$

Defining the *safety factor* q

$$q(r) \;=\; -\frac{r}{R_0}\frac{B_\phi(r)}{B_\theta(r)} \tag{1.34}$$

the instability condition (1.33) reads $q(r) = -m/n$. This shows that helical instabilities can grow only at radial positions where the safety factor assumes rational values. For this reason, these positions are called rational or resonant radii. Like in neutral fluids, a plasma instability can be driven, for example, by a thermal gradient. Under certain conditions, this can provide the necessary free-energy for a whatever small perturbation to grow unstable. But also many other driving terms can be present in plasmas. An important example is given by the so called *tearing mode*[6], which is driven unstable by a gradient in the current density parallel to the magnetic field. The name of this instability comes from the fact that the magnetic field lines tear and reconnect during its evolution. It is possible to show that, when this current gradient is sufficiently high, a tearing instability is triggered causing the magnetic field lines to bend and reconnect. The resulting magnetic configuration is characterized by the formation of a so called *magnetic island*. We do not add here more details on this instability. In the following Chapters, the role of tearing modes in toroidal plasma dynamics, and particularly in the RFP, will be addressed and their effect on toroidal plasma global confinement properties will be discussed.

1.4 Toroidal magnetic configurations

Several magnetic field geometries have been investigated in fusion research looking for the best conditions for plasma confinement. Presently, the toroidal configurations gave the best confinement performances. Three different configurations of the magnetic field have been conceived in the '50s and are under investigation worldwide. A brief overview of these three configurations (the Stellarator[7], the Tokamak[8] and the Reversed Field Pinch [9]) in order of invention is presented in the following. The Tokamak and the RFP both belong to the class of toroidal pinch devices, in which a toroidal current is inductively driven by an external circuit, and generates a poloidal magnetic field that confines and compresses the plasma [10].

1.4.1 Stellarator

The stellarator was designed in 1951 by Lyman Spitzer Jr. at Princeton. In a stellarator the twist of the field lines and the field itself are entirely created by external coils wound around the plasma torus. Because of these external currents, the plasma has a screw-like shape and it does not need a direct-axis flow current component in the plasma. The stellarator can therefore operate in steady state without any particular problem of equilibrium and plasma current control. The main concern on the road to a future stellarator power plant is its technical feasibility. The complex shape of the magnetic winding poses critical demands in terms of mechanical loads and manufacturing precision. A picture of a stellarator configuration is shown in Figure 1.8 which shows the Wendelstein 7-X experiment[11, 12] of the Max Planck Institute for Plasma Physics.

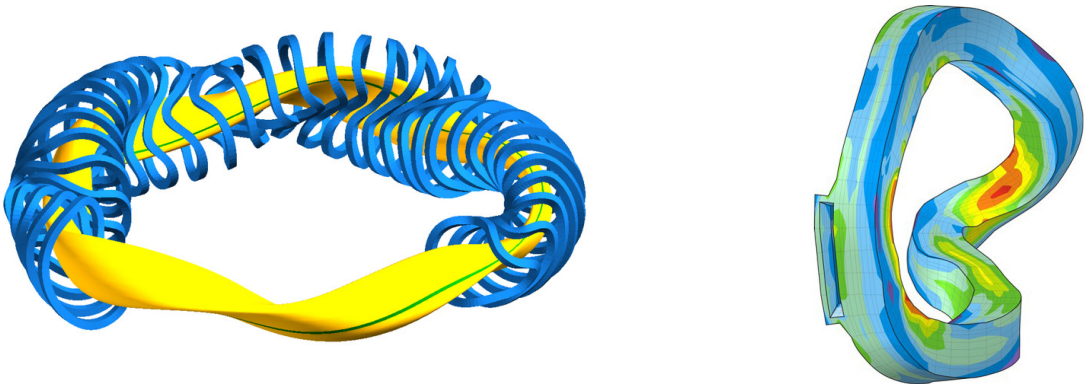

(a) (b)

Figure 1.8: (a) A sketch of W7-X. Coils and a flux surface are reported. (b) One of the modular coils of W7-X. The color code marks the mechanical stress[a].

1.4.2 Tokamak

The Tokamak approach, Russian acronym for 'toroidal magnetic chamber', was proposed by two Russian physicists, Tamm and Sakharov, in 1952 and then realized by another Russian scientist, Artsimovich[13]. In a Tokamak the plasma is compressed by a combination of magnetic fields generated by both external coils and plasma current. The main magnetic field component is the toroidal one, i.e. B_ϕ, while to obtain a stable equilibrium a poloidal $B_\theta \sim B_\phi/10$ and a vertical $B_z \lesssim B_\phi$ field components are needed. While B_ϕ and B_z are generated by external coils, B_θ comes from the toroidal plasma current, I_p. This current is induced by a transformer action with plasma acting as a secondary single turn conductor. A sketch of the typical tokamak radial profile of poloidal and toroidal field components are depicted in Figure 1.9a. Plasma confinement is limited by MHD instabilities that grow mostly on the flux surfaces where the safety factor $q(r)$ becomes a rational number. In tokamaks, this parameter usually increases monotonically with the radial coordinate r, typical values are greater or close to unity in the core, see Figure 1.9b. The safety factor describes the number of toroidal turns a magnetic field line has to perform before completing a single poloidal turn. It is easy to understand that a rational value means that a field line ends on itself and this, in turn, means that an instability can grow sustaining itself. To avoid such a possibility, a stability constraint must be imposed, namely $q(r)$ must be greater than 1. This constraint is known as the Kruskal-Shafranov limit and comes from the application of the Suydam criterion in toroidal geometry[8]. The Kruskal-Shafranov limit is translated in terms of field components as $B_\theta \ll B_\phi$ and, in turn, imposes a limit on the maximum toroidal current for a given toroidal field. This constraint opens one of the most limiting aspects for a future

[b] *Picture (a) taken from* `http://www.mpg.de/4699067/_plasmaphys3_?c=5732343` *and picture (b) taken from* `http://www.power.bilfinger.com/en/services/references/alternative-energy-generation/alternative-energy-generation.html`

tokamak power plant: indeed the limited toroidal current means a limited ohmic heating capability. This, in turn, does not allow to reach thermonuclear conditions exploiting only ohmic heating. Complex additional heating methods, such as neutral beam or radiofrequency heating, must thus be provided.

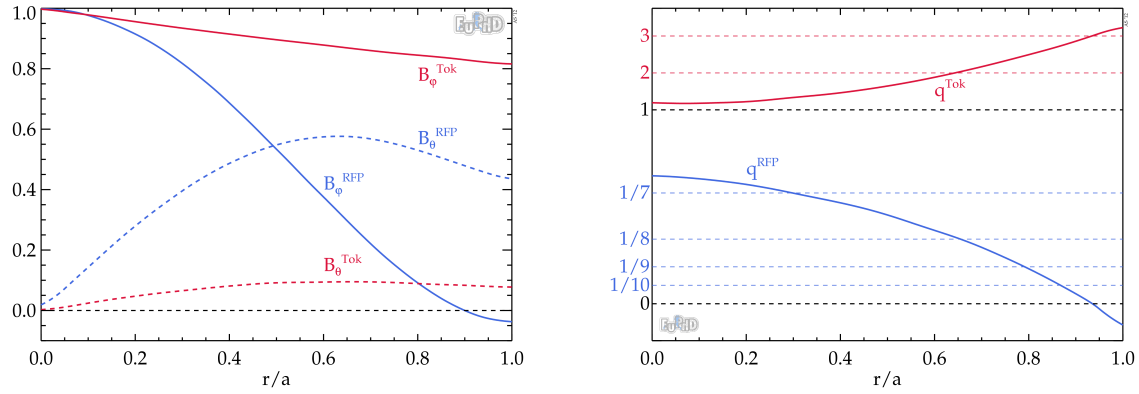

(a) (b)

Figure 1.9: (a) Example of magnetic field profiles for tokamak and RFP configuration. Poloidal components are normalized to the relative toroidal ones. (b) Example of safety factor profiles for tokamak and RFP configurations. The y axis is not in scale.

1.4.3 Reversed Field Pinch (RFP)

The first RFP device was ZETA, in operation from 1954 to 1968 in UK. The RFP magnetic configuration is a near minimum energy state to which the plasma spontaneously relaxes[14]. In the RFP concept the plasma confinement is pursued exploiting the same pinch effect used in tokamaks but, differently from tokamaks, the toroidal and poloidal components of the RFP magnetic field are relatively weak and comparable, $B_\theta \sim B_\phi$, as shown in Figure 1.9a. The name RFP comes from the fact that the toroidal component of the magnetic field reverses its sign near the plasma edge. As a consequence, the safety factor profile also changes its sign at the same radius, as shown in Figure 1.9b. The RFP is thus an intrinsically low safety factor device. For this reason, a broad spectrum of $(m = 1, n \lesssim 2R_0/a)$ magnetic modes resonates throughout the plasma radius, and several $(m = 0, n \geq 1)$ modes resonates at the reversal radius, the radius where the safety factor vanishes. The presence of all these resonating magnetic modes, has many consequences on the RFP dynamics and on its transport properties, as will be seen in Section 2.3. Low safety factor operations in the RFP do not bring to dangerous disruptive behavior. This is due to the combined action of a strong magnetic shear and of a conducting shell (which passively reacts against growing magnetic perturbations). For these reasons, the plasma current in the RFP is not limited by the Kruskal-Shafranov limit and thus the RFP can operate at plasma current values approximately

ten times larger than in tokamaks with the same toroidal field. RFP can therefore theoretically reach β ∼10% through Ohmic heating only. To describe pinch equilibria the so called *pinch parameter* Θ and the *reversal parameter* F

$$\Theta = \frac{B_\theta(a)}{\langle B_\phi \rangle} \qquad F = \frac{B_\phi(a)}{\langle B_\phi \rangle} \quad .$$

are often used. In the previous $\langle \cdots \rangle$ indicate an average over a poloidal cross-section. In terms of such quantities, the tokamak is typically a low-Θ device with $F > 0$, while the RFP is a relatively high-Θ configuration with $F < 0$.

1.5 RFX-mod: Reversed Field eXperiment

The large part of this thesis work has been carried out on the RFX-mod device. RFX-mod (Reversed Field eXperiment modified) [15, 16] is a RFP device derived by a modification of RFX[17, 18], operating at Consorzio RFX in Padova. The first plasma of RFX-mod was obtained in 2004. The main features of RFX-mod (in Figure 1.10a) are listed below

Major radius	2 m
Minor radius	0.459 m
Plasma current	$\leq$2 MA
Toroidal magnetic field	$<$ 0.7 T
Plasma discharge duration	$\leq$ 0.5 s
Plasma density	$1 \div 10 \cdot 10^{19}$ m^{-3}
Plasma volume	$\sim$ 10 m^3

Built to investigate the confinement properties of RFP equilibria up to plasma current of 2 MA, RFX-mod is the world largest operating RFP experiment. The 2 MA target has been reached during 2010 experimental campaign[157], mainly thanks to one of the most advanced feedback control system in the fusion comunity: a set of 192 independently driven saddle coils aimed at the active control of the local radial perturbations at the plasma edge, see Figure 1.10b. The RFX-mod first wall is composed by 2016 graphite tiles, accurately shaped to improve plasma-wall interaction by reducing the heat flux peaking on leading edges. Graphite was chosen for its low atomic number Z and for its capability to withstand high power loads.

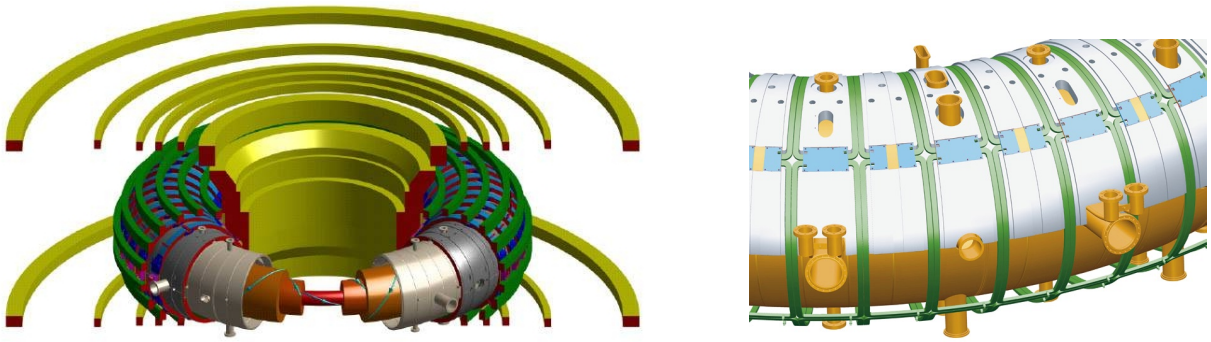

(a) (b)

Figure 1.10: (a) Magnetic coils system of RFX-mod: the magnetizing winding(yellow), the field shaping coils (green), the toroidal circuit (blue). The mechanical supporting structure (dark gray), the vacuum vessel (light gray) and plasma flux surfaces (orange) are also shown. (b) Segment of the vacuum vessel of RFX-mod. The vacuum vessel is shown in orange, the mechanical supporting structure in gray. The green parts represent the saddle coils of the feedback system.

1.5.1 Selected diagnostics

The diagnostic system of RFX provides measurement of the spatial and temporal distribution of all the major plasma quantities. In the following a brief overview of the diagnostics interesting for this thesis work is given.

Thomson Scattering systems

In RFX-mod, the electron temperature T_e is measured by the main Thomson scattering (main TS) diagnostic [19], which covers almost the entire plasma diameter ($-0.96 \leq r/a \leq 0.84$): 84 lines of sight leading to a spatial resolution of $\sim$10 mm. The custom built Nd:YLF (yttrium lithium fluoride) laser ($\lambda = 1053$ nm) produces a fast ($\leq$50 Hz) burst of 10 high energy pulses suitable for measuring the profile evolution during a plasma discharge of 300 ms duration. The main TS signal is collected at $\approx 90^\circ$ scattering angle from the incident beam through three objective lenses which image the laser beam onto a row of 84 pairs of optical fibres. Fibres are then arranged into bundles, fed to 28 spectrometers. Each bundle is made of three different length pairs of fibres. Such a bundle serves as a multiplexing system which allocates 3 scattering volumes per polychromator by means of optical delay lines: the different lengths of the fibres (14 m difference) produce three pulses separated by the time required to run the extra length (70 ns). In each spectrometer, the TS signal is cascaded through four spectral channels in a zigzag path, using a series of relay lenses, with four APD detectors optimized for the IR (3 mm diameter active area). The collection efficiency of the system allows measurements of T_e profiles at an electron density as low as $1{\cdot}10^{19}$ m^{-3}. Signal waveforms are finally recorded by waveform digitizers, so that the three time separated TS pulses are distinguished. As a further advantage, the known pulse shape can be fitted to the measured waveform at a fixed time, well recovering even the weak signals from high noise.
Besides the main TS, an edge Thomson Scattering system[20] (edge TS) has been operating for some experimental campaigns. A Q-switched ruby laser ($\lambda = 694$ nm), produces a single laser pulse per plasma discharge. It enables the measurement of electron temperature and density in the region $0.7 < r/a < 0.95$ once in a discharge. The electron density is obtained by absolutely calibrating the system with anti-Stokes rotational Raman scattering (RRS) in nitrogen.

Multichannel interferometer

Electron density is measured in RFX-mod by a vibration compensated interferometer[21, 22]. The main wavelength is that of a CO_2 laser, $\lambda = 10.64\mu$m. The interferometer consists of two modules. Module A has eight vertical or nearly vertical chords with a maximum impact parameter, i.e. the minimum distance between the chord and the magnetic axis, of 0.33 m. In the present set-up, module B includes one chord similar to those of module A, plus a fan shaped array of four chords which, using in-vessel mirrors, achieve impact parameters up to

0.425 m, corresponding to 3 cm from the plasma edge. For the vibration compensation an He-Ne laser ($\lambda = 3.4\mu$m) and a CO laser ($\lambda = 5.4\mu$m) are used, respectively, for modules A and B. The diagnostic has a bandwidth larger than 1 MHz, but, for most measurements, it was limited to 125 kHz, allowing a time resolution of 8 μs. A sketch of the interferometer chords is shown in Figure 1.11a.

Thermal Helium Beam and Gas Puffing Imaging diagnostics

The radial profile of the electron temperature, density and thus pressure in the equatorial outboard midplane in the region $0.94 < r/a < 1$ and its time evolution is measured with the thermal helium beam (THB) diagnostic[23], with a spatial resolution of 5 mm and a temporal one of 3 ms. It is a spectroscopic diagnostic which locally measures the ratio of three spectral lines emitted by a neutral He cloud puffed into the plasma edge. Exploiting the same He cloud a gas puff imaging (GPI) diagnostic measures the fluctuations of the He I line[24] in the radial-toroidal (r, ϕ) plane, which is the plane perpendicular to the magnetic field in RFP edge; these fluctuations are mainly proportional to the local n_e fluctuations. The GPI is equipped with one fan of 16 chords viewing the plasma edge at 16 different toroidal positions, and with a second fan which measures at 8 different radial positions. The spatial resolution of both fans is 5 mm, with a sampling frequency of 10 MHz. The scheme of both diagnostics is given in Figure 1.11b.

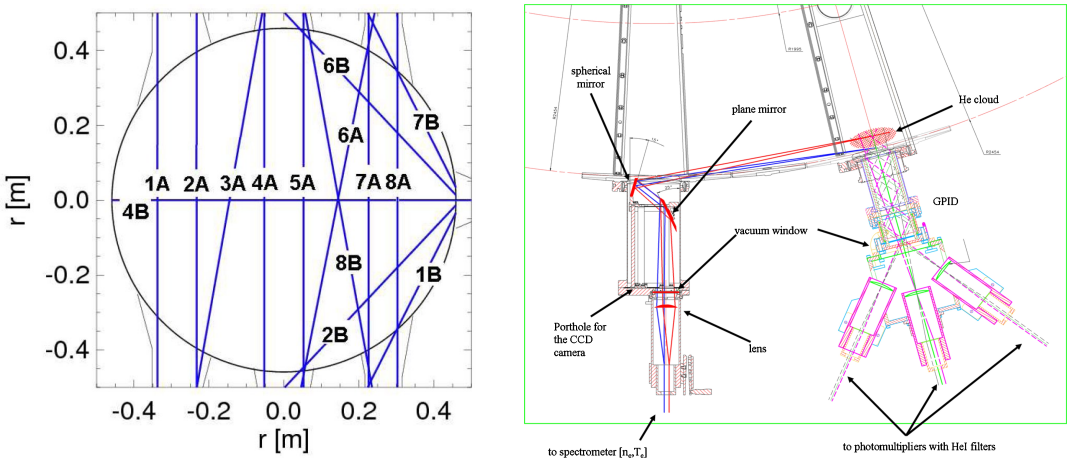

(a) (b)

Figure 1.11: (a) Scheme of the multichannel interferometer, the channels of the two modules are distinguished. (b) Scheme of THB and GPI diagnostics.

ISIS system

ISIS in an invessel edge measurement system which spans almost all toroidal and poloidal angles of the torus[25]. This system consists in 97 electrostatic probes and 139 magnetic coils

with a bandwidth up to hundreds of kHz. All these probes are inserted in the graphite tiles which cover the entire first wall of RFX and are aimed to measure edge fluctuations of magnetic fields, floating potential and saturation current. Probes are arranged in various poloidal and toroidal arrays in order to study not only the local perturbative phenomena but also their correlations and their evolution along both the principal components of the magnetic field at the edge. Some electrostatic pins have been arranged so to obtain simultaneous information about plasma density, electron temperature and floating potential. This can be achieved arranging the probe tips in a configuration known as triple probe[26]. Both electrostatic and magnetic probes are digitally sampled at 5 MSample/s with a minimum bandwidth of 700 kHz [27].

1.6 TCV: Tokamak à Configuration Variable

Part of the studies presented in this thesis was carried on the TCV (Tokamak à Configuration Variable) tokamak experiment of the CRPP (Centre de Recherche en Physique des Plasmas) at the EPFL (Ecole Polytechnique Fédérale de Lausanne). TCV is a medium size tokamak that has been built with a special attention to flexibility in terms of plasma shape[28] and plasma heating. In TCV, plasma shaping is achieved by 16 independently controlled poloidal field coils which are mounted in two vertical stacks on both sides of the plasma outside the vacuum chamber. It started operation in 1992 with the main aim of investigating the effect of plasma shape on confinement and stability. As a confirmation of the large shaping capability of such a device some of the explored plasma shapes are shown in Figure 1.12. The TCV first wall is

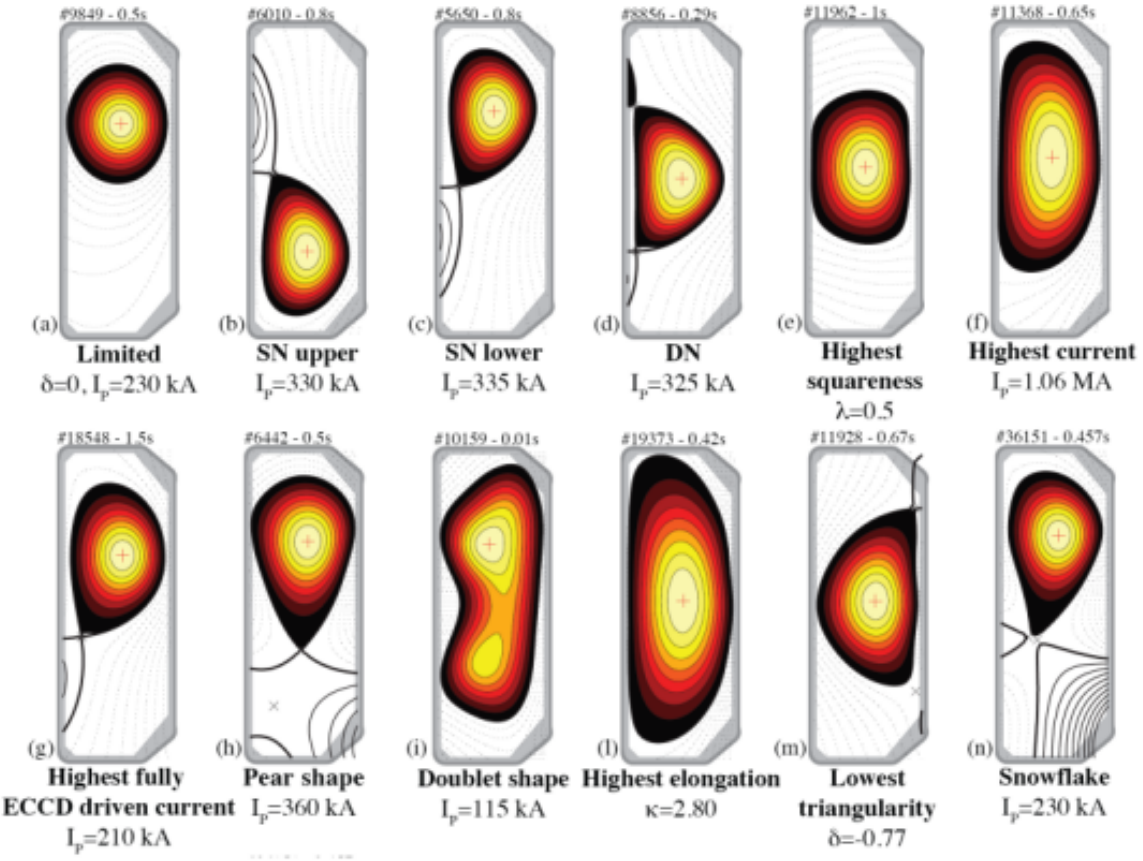

Figure 1.12: Some of plasma configuration achieved on TCV. Figure taken from `http://crpp.epfl.ch/cms/site/crpp/lang/en/research_TCV_Tokamak`

covered with 24mm thick graphite tiles designed to withstand the large power fluxes occurring during ECRH heating. The main machine and plasma parameters are given in Table 1.1.

Major radius	0.88 m
Minor radius	0.25 m
Aspect ratio	$\sim$3.5
Vacuum vessel elongation	2.9
Toroidal field on axis	$\leq$ 1.54 T
Plasma current	$\leq$ 1 MA
X2-ECRH power	$\leq$ 2.7 MW
X3-ECRH power	$\leq$ 1.5 MW
Discharge duration	$<$ 4 s

Table 1.1: Main TCV parameters.

1.6.1 Electron Cyclotron Resonance Heating

TCV is equipped with a very flexible electron cyclotron heating (ECH) and current drive (ECCD) system. It consists of six 82.7 GHz gyrotrons for heating at the second harmonic of the electron cyclotron frequency, and three 118 GHz gyrotrons for heating at the third harmonic, Figure 1.13 [29]. The polarization of each beam can be modified and is usually set for propagation as an extraordinary wave (X2-, X3-mode). The X2-system allows to heat and drive current in plasmas with a density up to the cut-off density for the X2-mode propagation, $n_e = 4.25 \cdot 10^{19}$ m^{-3}. There are two launcher (L1, L4) mounted in equatorial ports and four launcher (L2, L3, L5 and L6) in upper lateral ports. Each launcher has two steering axes, whose combination allows a huge variety of poloidal and toroidal injection angles. The nominal power of each gyrotron is 465 kW. The gyrotrons for L1, L2 and L3 and the gyrotrons for L4, L5 and L6 are powered by two individual power supplies which feature the possibility of power ramps. The gyrotrons of the X3-system are combined in one launcher at the top of the vessel and heat plasmas with a density up to the cut-off density for the X3-mode propagation, $n_e = 11.5 \cdot 10^{19}$ m^{-3}. The microwave beam is injected nearly tangentially to the resonant surface to maximize the beam absorption. The launcher mirror can be moved radially and steered poloidally to optimize the injection angle and the relative position of the beam path with respect to the resonant layer. The nominal power of each gyrotron is 480 kW. Such a system led to achieve fully non-inductive steady-state operation. The plasma has been sustained for 2 s with zero flux variation by co-ECCD with a highest current of more than 200 kA at full power[30].

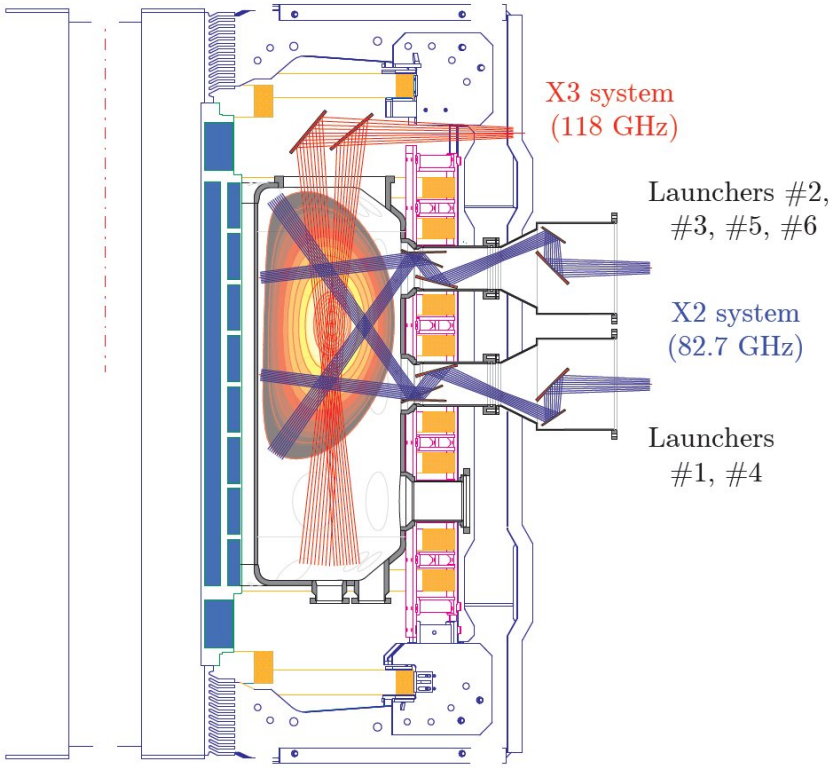

Figure 1.13: TCV plasma heating system: The X2 launchers are placed on the two equatorial (L1, L4) and four upper lateral ports (L2, L3, L5, L6). Two degrees of freedom in the launcher mirror angles allow a wide range of poloidal (ECH) and toroidal angles (ECCD). The X3-launcher is mounted on the top of the machine and has two degrees of freedom to optimize the injection angle radially and poloidally.

1.6.2 Selected diagnostics

This section shortly presents the diagnostics essential to this thesis work.

Magnetic probes

TCV is equipped with a large number of magnetic probes and flux loops[31]. The magnetic probes are located inside the vacuum vessel and measure the time derivative of the poloidal magnetic field tangent to the vacuum vessel. Their signals are used for real-time plasma shape, position control and plasma equilibrium reconstruction. Magnetic probes are spatially distributed poloidally (4 arrays of 38 probes) and toroidally inside the vacuum vessel (3 arrays of 8 probes on the high field side and 3 arrays of 17 probes on the low field side). The flux loops are located outside the vacuum vessel and measure the time derivative of the poloidal magnetic flux. They are used for the plasma equilibrium reconstruction.

Multi-chord Far Infra-Red interferometer (FIR)

A 14-channel Mach-Zehnder type interferometer is used to measure the line-integrated plasma electron density along parallel vertical chords[32]. The system comprises a FIR (Far InfraRed) laser emitting a continuous wave at 214 μm, and a multi-element detector unit (InSb hot-electron bolometer). The laser beam is divided into a reference beam, which is frequency shifted by a rotating grating, and 14 probe beams crossing the plasma at different radial positions. When the probe beams pass through the plasma, the difference in refractive index causes a phase delay with respect to the reference beam. Since the reference beam is frequency shifted, the phase delay can be directly obtained comparing the detector signals at the difference frequency (beat frequency). At given wavelength and polarization, the refractive index of the plasma is directly related to the electron density. Therefore, the system provides continuous measurements of the line integrated density along 14 chords. The measurement along the central chord is used for real time control of the plasma density, as well as to measure the line averaged plasma electron density. Data are acquired at 20 kHz. FIR system is reported in the right panel of Figure 1.14a.

Thomson scattering system

The Thomson scattering (TS) diagnostic measures the local profiles of electron temperature $T_e(\rho)$ and density $n_e(\rho)$ by spectral analysis of the fraction of a laser beam scattered by the plasma electrons. The scattered light is Doppler-shifted due to the electron motion. The width of the Doppler line broadening and the integral over the spectral peak determine the electron temperature and density, respectively. TCV Thomson scattering diagnostic [34, 35, 36] is equipped with three powerful (1.5 J/pulse) Nd-Yag lasers in the near infrared spectrum offering a 20 Hz repetition rate. The light of the three lasers is injected along the same vertical path through the plasma at $R = 0.9$ m, as indicated in left panel of Figure 1.14a. The scattered light is collected by 26 optic fibers installed in three lateral ports of the TCV vacuum vessel. The lines of sight are evenly spaced and cover the whole plasma cross section with a spatial resolution of ~ 4 cm on the lasers path: this is the main TS system. Nine additional lines of sight installed in the upper lateral port aim at increasing the density of data points and thus the radial resolution at the plasma edge, especially for the measurement of H-modes pedestal profiles: this is the edge TS system. The lasers are usually pulsed sequentially, either with evenly spaced trigger times in order to increase the repetition rate to 60 Hz for a higher time resolution, or with 1 ms spaced triple pulses at a 20 Hz rate in order to increase the density of radial data points for a high-quality profile fitting.

Photodiodes

Visible light spectroscopy of TCV plasmas is carried out by a set of 18 photodiodes distributed poloidally on the portholes of a toroidal sector of TCV, and acquired at 50 kHz. A set of filters is installed in front of the diodes to selectively measure the radiation amplitude in spectral bands

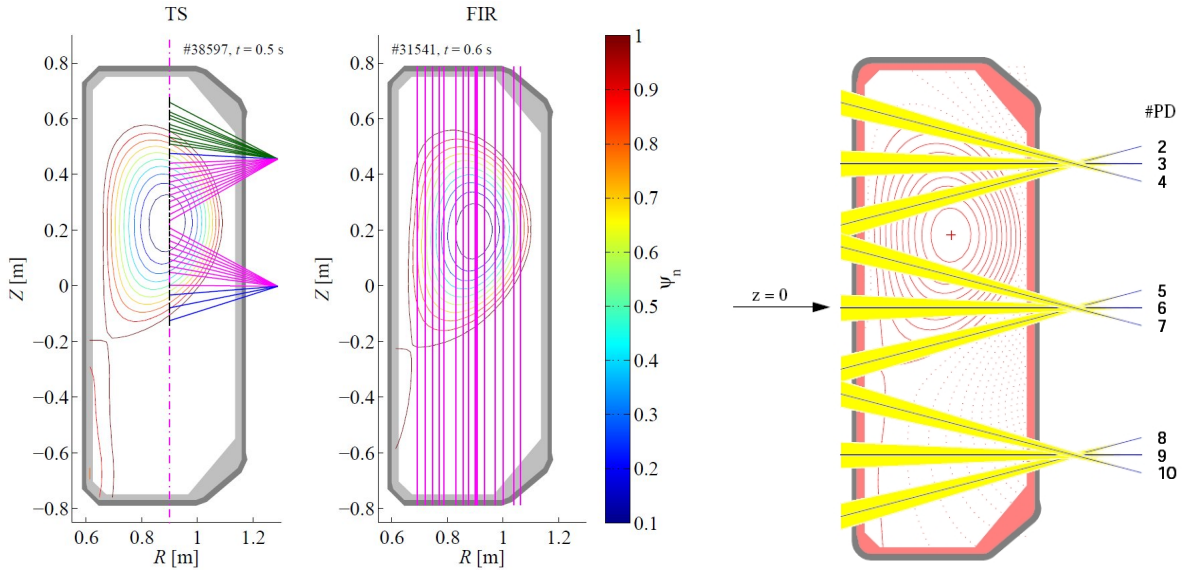

Figure 1.14: (a) Thomson scattering (TS) system and Far Infra-Red (FIR) interferometer lines of sight. Left: TS setup. The 23 main chords are divided in two groups, with low spatial resolution (blue) and high spatial resolution magenta. The TS-edge system chords cover the plasma edge with high spatial resolution (green). Right: FIR interferometer. 14 vertical chords. The central chord (#9,thick line, R ∼0.9 m) is used for the line averaged density measurement. The lines of sight are superposed to a poloidal cross-section of the flux surfaces of a typical diverted plasma (the values of the normalized poloidal flux are indicated by the color code), enclosed by the vacuum vessel (gray). Picture taken from [33]. (b) TCV lateral D_α photodiodes chords. In addition to those sketched, a vertical one sited on top of the machine collects D_α radiation from the floor tiles.

corresponding to transitions between well identified electronic energy levels of bound electrons of partly ionized or neutral atoms. Amongst the variety of atomic spectral lines radiated by the plasma, the emissivity in the so-called D_α line is particularly interesting. Its amplitude is related to the excitation rate of deuterium atoms and is therefore sensitive to transport events in the edge, like ELMs. The 9 lateral photodiodes, with their chords, are shown in Figure 1.14b

1.7 ITER: INTERNATIONAL THERMONUCLEAR EXPERIMENTAL REACTOR

Magnetic fusion energy research has reached the point where a tokamak burning plasma facility in which the thermonuclear heating balances transport and radiation losses for periods of 1000 s or longer has been planned and is nowadays under construction. The achievement of this goal is one of the main tasks that will be faced by the International Thermonuclear Experimental Reactor (ITER). ITER will be the largest tokamak ever built and will have a size, a magnetic field strength, physics phenomenology, and technological basis very close to that of an eventual thermonuclear power reactor, be it a tokamak or some other toroidal configuration[37]. The principal physics goals of ITER are:

a) to achieve extended burn in inductively-driven plasmas with $Q = P_{fus}/P_{aux}$ of at least 10 for a range of operating scenarios and with duration sufficient to achieve stationary conditions;
b) to aim at demonstrating steady state operation using non-inductive current drive with a ratio of fusion power to input power for current drive of at least 5. In addition, the possibility of higher Q operation will be explored if favorable confinement conditions can be achieved.

The ITER nominal fusion power output will be about 500 MW. To achieve this goal, the ITER device will have:

$$\begin{array}{ll} \text{major radius} & R_0 = 6.2\text{m} \\ \text{minor radius} & a = 2\text{m} \\ \text{toroidal magnetic field} & B \leq 5.3\text{T} \\ \text{plasma current} & I_p \leq 15\text{MA} \end{array} \tag{1.35}$$

The discharge duration is designed to be about 400 s, which can be regarded as a stationary condition on the characteristic time scales of the plasma processes. These parameters have been predicted for plasmas with density $n_e \sim 10^{20}$ m^{-3} and core electron and ion temperatures $T_e \sim 8.8$ keV and $T_i \sim 8$ keV respectively. ITER would explore many reactor relevant scientific and technological issues, which are beyond the present experimental capabilities. In particular, regimes in which the α particles contribute significantly to the plasma pressure are very interesting. A variety of technological issues will also be studied in ITER: advanced materials facing component which have to whitstand very large heat and particle fluxes, the concepts for a tritium breeding module, the superconducting technology under high neutron flux and many others. To achieve the conditions expected in ITER, an auxiliary external heating capability of about 73 MW will be provided. A schematic view of ITER is displayed in Figure 1.15. .

[a] *Picture taken from* `http://f4e.europa.eu/Downloads/Gallery/ITER/ITER_graphical_cut-100620101200-Large.jpg`

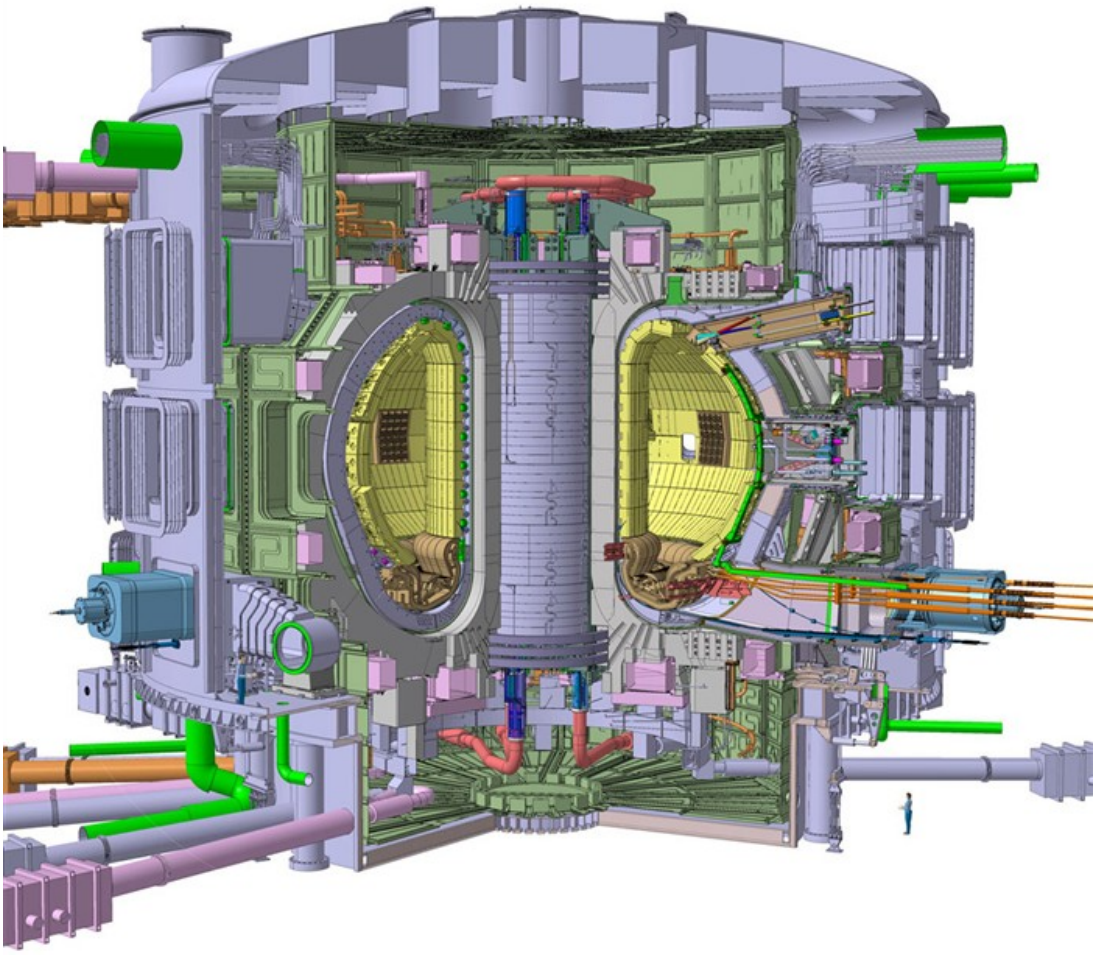

Figure 1.15: Schematic overview of the International Thermonuclear Experiment Reactor[a].

2

PLASMA BOUNDARY AND CONFINEMENT PARADIGM

L'uomo non esiste veramente che nella lotta contro i propri limiti.
Man does exist only within the fight against his limits.

Ignazio Silone

Disregarding the specific configuration, the plasma boundary is the only place in a fusion reactor where the stellar world of hot (keV) plasmas meets the earthly world of cold (sub-eV) solids. This region plays a twofold capital role in the road map of fusion: on the one hand it poses the boundary condition for the well confined plasma, thus for the environment where fusion reactions should occur. On the other hand, it serves as a conduit for plasma exhaust and as a barrier for the material surface. The link between plasma boundary and core confinement is so strong to be two sided: if in tokamaks the quest for a mild plasma-wall interaction led to the discovery of an ameliorated operating mode, in RFPs a spontaneous transition to a reduced chaos state led to a favorable edge topology with a reduced plasma-wall interaction. In this chapter the main features of Tokamak and RFP plasma boundary is presented, together with their link to the confinement characteristics of the main plasma.

In principle, in toroidal fusion devices the magnetic field could be perfectly aligned as to be tangential at every point of the toroidal vessel wall. In practice, such perfect alignment is not possible. The charged particles reach the material wall by both parallel and cross-field motion, so to set a strong entanglement between plasma regions near the wall and far from it. The plasma always strongly interacts with the walls of the containing vessel. This plasma-wall interaction, PWI, has profound effects on both the plasma and the solid. The basic properties of the plasma 'touching' the solid, such as its density and temperature, are strongly dependent on the details of the interaction. At the interface between the wall and the plasma, a thin net-charge layer called the *Debye sheath* develops spontaneously. The most important practical consequence of the formation of a sheath is that it mediates the flow of particles and energy out of the plasma to the solid surface. It therefore plays a central role in establishing the temperature, density and other properties of the plasma near the solid surface. Moreover, strong non-linear connection exists between the processes occurring at the wall, the properties of the plasma edge and those of the main plasma. The ion and electron temperature profiles, the power flow in the plasma edge and its radiated fraction, the concentration and penetration depth of neutrals into the SOL are examples for such strong interlinked quantities[38, 39]. So an appropriate architecture for the plasma edge is essential in order to obtain thermonuclear fusion plasmas with high performance.

2.1 Plasma boundary

Most of the field lines in toroidal devices are *closed*, because they reside on magnetic flux surfaces which do not intersect any of the solid objects bounding the plasma. However, close to the walls, some of the magnetic field lines intersect the solid materials of the vessel at some location and the particles following these field lines are guided into collisions with the first wall depositing their energy onto the plasma-facing material. These are *open* field lines. The volume entirely filled by the closed field lines is called confined volume. Particles escaping this region form the plasma exhaust. The confined region is usually limited by the *last closed flux surface* (LCFS) or separatrix, where a geometric definition of such a surface is possible. The narrow region outside this border, usually only few cm wide, is the area where the plasma is essentially scraped off from the core plasma. In this so-called *scrape-off layer* (SOL), all magnetic field lines are open and particles reaching these field lines will directly intersect material surfaces. The region enclosed between the plasma facing components and the main plasma volume is often referred to as *plasma edge* and is a considerably researched area of fusion plasma physics. The properties of the plasma edge control the power and particle exchange between the main plasma and the vessel.
Disregarding the way the SOL is formed, SOL plasma behavior is frequently dominated by the interaction of ions and electrons with neutrals and solid surfaces. In fact, only a small fraction of ions and electrons impinging the material surface are reflected back into the plasma. The great majority of them recombine into atoms and/or molecules and return in the

plasma as neutrals[40]. The solid surface thus acts as a local sink for the plasma density, while the returning neutrals provide a corresponding volumetric source of equal magnitude. In steady-state, the approximate balance between plasma outflow and neutral inflow is known as *plasma recycling*. The edge plasma thus always contains a certain concentration of neutrals with which it interacts. These interactions provide sources (and sinks) not only of mass but also of momentum and energy for the plasma. If a SOL is formed, a fairly strict separation is posed between the core plasma and its boundary: the source of the energy flowing across the SOL, thus reaching the walls, is indeed firmly located inside the LCFS. The sources (core) and sinks (wall) of energy are thus well separated, with the SOL acting as the medium/conduit for power flow and exhaust. In contrast, the sources and sinks of particles in the SOL cannot be easily decoupled due to the recombination of ions and electrons at the target tiles.
The behavior of plasma edge and SOL is strongly coupled with the plasma-wall interaction. The plasma-facing components (PFC) are subject to particle and heat fluxes that strike them continuously or transiently in bursts. This interaction leads to erosion, releasing surface material into the plasma where it acts as an impurity, which can migrate into the core plasma, causing radiation loss and plasma fuel dilution. Eroded impurities can also be confined in the SOL plasma, often migrating to locations remote from the point of release. The main mechanism for plasma erosion is sputtering[41], which can be distinguished in two main channels. Physical sputtering is the process by which atoms from material surfaces are ejected due to the bombardment by energetic plasma ions and neutrals (with energy above the sputtering threshold energy). Chemical sputtering occurs through the chemical reactions of the wall material and plasma. This is a particular problem when carbon is used as first wall material (as it is in both of the devices studied in this thesis RFX-mod and TCV), in fact hydrogen and deuterium ions and neutrals readily react with carbon to form hydrocarbons with sputtering yields generally much higher than those common to physical sputtering.

2.1.1 Limiter and divertor concepts

To guarantee sufficiently high plasma purity, low fuel dilution and the highest performance, the plasma-wall interaction can be localized and controlled. In most fusion devices, this is achieved by forcing the interaction to occur at specific material surfaces which then define the last closed flux surface and separate open from closed magnetic surfaces. Historically the first and simplest option were the so called *limiters*, objects made of load resistant materials, placed on the walls to limit the confined region by defining the LCFS, left panel of Figure 2.1. As a result, the plasma particle and power loads are restricted to a small fraction of the vessel wall, thus shielding the remainder from undesirable plasma-surface interaction[40]. This concept has two main disadvantages. Firstly, material released by limiter due to the PWI can penetrate straight into the core, thus degrading its properties. Secondly, most of the ionization processes occurs inside the LCFS avoiding the edge cooling effect of local ionization. The hot plasma edge therefore causes power fluxes at limiters which can be unacceptable for a fusion reactor.

Most tokamaks opt for a more sophisticated solution, developed in 1984 at the ASDEX

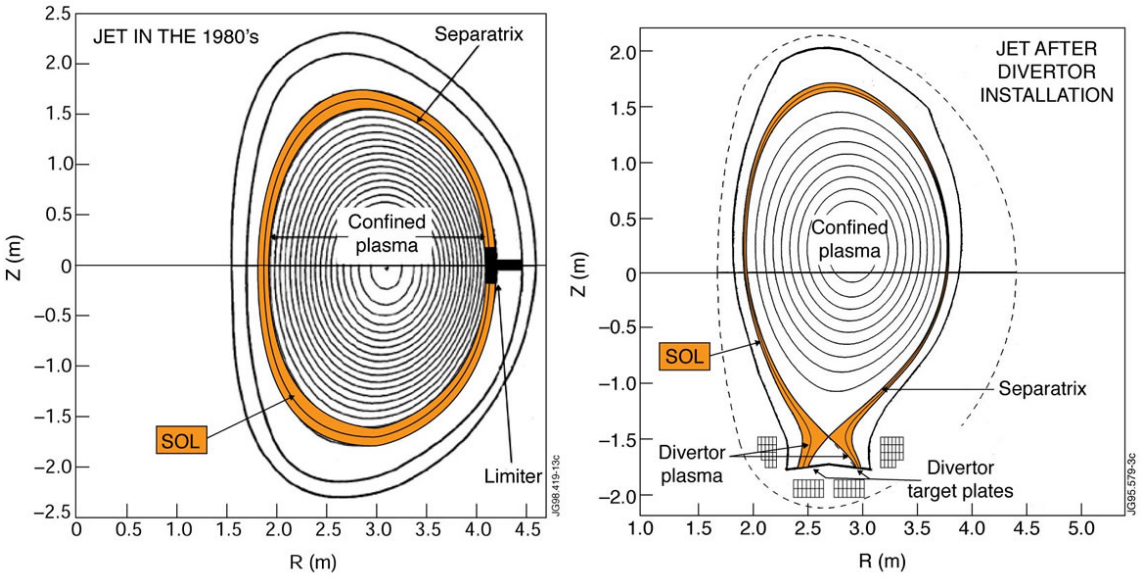

Figure 2.1: Examples of configuration to localize the plasma-wall interaction from JET tokamak: limiter (left) and divertor (right). Picture taken from [42].

experiment[43]. This concept is based on the modification of the magnetic field lines at the plasma edge, so that the field lines of the SOL are diverted into a region separated from the confined plasma, where the plasma-surface interaction and particle exhaust are localized. This configuration is achieved by using the poloidal magnetic field coils or even dedicated internal coils to generate an 'X-point', right panel of Figure 2.1 , where the poloidal magnetic field vanishes. The resulting magnetic field topology is also referred to as a *divertor* configuration. The intersections of the separatrix with divertor plates are called *strike points*. An important advantage of diverted configurations is that the materials facing the plasma are not generally in direct contact with the main plasma, reducing the probability that impurities released by the plasma-wall interaction can penetrate to the core. In addition, the use of a divertor generates regions of amplified particle recycling, in which cold neutral gas cushions can naturally develop reducing charged particle fluxes to the divertor plates. Moreover, this high recycling region improves impurity screening, making it harder for eroded material to reach the confined plasma. The weak poloidal field near the X-point forces magnetic field lines to make many transits around the torus before terminating on the divertor targets. This long particle residence time promotes energy loss (due to collisions with ions, neutrals and electrons), assisting in divertor action. The path of the exhaust particles along a field line from their entry point in the SOL to their intersection with a solid surface is known as *connection length*, L_c. In the symmetric divertor configuration, with equal distances from X-point to both the targets, L_c can be approximated as:

$$L_c \approx \pi R q \approx \pi a B_\theta / B_\phi$$

where R is the major radius, q the safety factor, a the minor radius, B_θ and B_ϕ the poloidal and toroidal magnetic field components. The distance along magnetic field in the SOL between 2 points of contact with the solid surfaces is $\sim 2L_c$. In divertor configurations, this path is longest for the particles residing in the immediate proximity of the separatrix (since in this region the field lines pass closest to the magnetic field null). In fact, the X-point represents the perpendicular projection of a field line with zero pitch. The connection length can be very long (from target to target at the separatrix ~ 30 m in TCV, ~ 200 m in ITER). This results in the cooling down of the plasma at the targets allowing electrons and ions to recombine and form neutrals locally extinguishing the plasma.
Although tokamak and RFP confinement mechanisms are based on the same pinch-effect, the confinement properties of such configurations are completely different. In the following a brief summary of the confinement properties of tokamaks and RFPs relevant for this thesis work are presented. Particular attention will be devoted to the ameliorated confinement properties related to the *H-mode* in TCV and to *SHAx state* in RFX-mod.

2.2 TOKAMAKS: FROM THE DIVERTOR TO THE H-MODE

Present day tokamaks high performance scenarios rely on the possibility to access the high confinement mode *H-mode*[44]. It is an enhanced operation scenario discovered at ASDEX tokamak in 1984 with the installation of the divertor, and it is the projected baseline operational scenario for ITER[45]. Access to the H-mode is typically observed when the auxiliary heating power crosses a critical value, leading to the formation of a narrow, insulating region, or *transport barrier*, at the plasma edge. The pressure rises steeply from the plasma edge through the transport barrier to create a *pedestal* on which the core pressure sits. The barrier formation leads to a broadening of density and temperature profiles, which in turn results in a reduced plasma pressure peaking factor[46]. It is this pedestal that provides the H-mode with such good confinement and it is due to a substantial reduction in the measured plasma turbulence. In addition, the extra pressure gradient at the edge drives a substantial bootstrap current, reducing the need for current drive. Some of the major outstanding plasma physics questions for fusion are associated with the properties of this narrow, but very important, region. One particularly important issue is a class of instabilities called Edge Localized Modes, or *ELMs*. These are violent events, which repetitively eject particles and energy from the plasma surface towards the edge, see [47] for an extensive review. These events are predicted to lead to unacceptable erosion of plasma facing components in future devices, such as ITER, unless the magnitude of the transient wall loadings can be maintained at a very low level. Experiments comparing L- and H-mode local transport rates have shown reductions in the electron thermal diffusivity, ion thermal diffusivity and angular momentum diffusivity, with the reduction in the electron thermal diffusivity being especially prominent, as reviewed in [48]. This improvement of energy, particle, impurity and momentum transport occurs simultaneously at the onset of the H-mode. The enhancement of energy confinement

between L- and H-mode is generally performed comparing the energy confinement time

$$\tau_e \;=\; \frac{W_e}{P_{tot}}$$

where W_e is the internal plasma energy and P_{tot} is the total heating power, which usually doubles passing from L-mode to H-mode. The H-mode energy confinement time is generally compared to the multi-machine *ITER-IPB98(y,2)* scaling[49]:

$$\tau_{IPB98(y,2)} \;=\; 0.0562\, I_p^{0.93}\, B_t^{0.15}\, \langle n_e \rangle_l^{0.41}\, P_{tot}^{-0.69}\, R_0^{1.97}\, \kappa^{0.78}\, (a/R_0)^{0.58}\, M^{0.19} \tag{2.1}$$

and the confinement improvement factor $H_{IPB98(y,2)}$ can be obtained from the ratio

$$H_{IPB98(y,2)} \;=\; \frac{\tau_e}{\tau_{IPB98(y,2)}} \qquad .$$

In equation (2.1) I_p is the plasma current (MA), B_t the vacuum toroidal field at the magnetic-axis (T), $\langle n_e \rangle_l$ the plasma line-average density (10^{19} m^{-3}), P_{tot} the total input power (MW), R_0 the major radius (m), κ the elongation of the plasma cross-section, a the minor radius (m) and M the average ion mass (amu). This multi-machine scaling is shown in Figure 2.2. In present day tokamaks, operations are restricted by hard operational boundaries as the high-density limit and radiation limits. Within this operational domain, different conditions must be fulfilled and a sufficient amount of heating power must be provided to trigger a transition from L- to H-mode. The scaling of these conditions and, indeed, the key parameters which control them, are uncertain and make an extrapolation to a next-step machine difficult. Further investigations can reduce the uncertainty of the prediction to ITER and possibly reveal means to facilitate H-mode access in ITER. In the following, a brief overview of the present understanding about the H-mode power threshold is presented.

H-mode power threshold

Transition from the standard confinement mode (L-mode) to the H-mode is typically achieved when the power flowing across the last closed flux surface,

$$P_L \;=\; P_{ohm} + P_{aux} - dW/dt - P_{rad,bulk} \tag{2.2}$$

exceeds a threshold $P_{L,LH}$. In equation (2.2) P_{ohm} is the Ohmic input power, P_{aux} the auxiliary heating power, dW/dt the plasma internal energy variation and $P_{rad,bulk}$ is power radiated, inside the LCFS, by the bulk plasma. The last term, $P_{rad,bulk}$, is dropped when comparing results from different machines, because measuring the radiation of the bulk plasma requires the capability of distinguishing it from the radiation coming from the edge region and the separatrix surrounding. The tomographic reconstruction of the plasma radiation is readily available only in some machines. The trigger for the L-H transition is one of the mainly

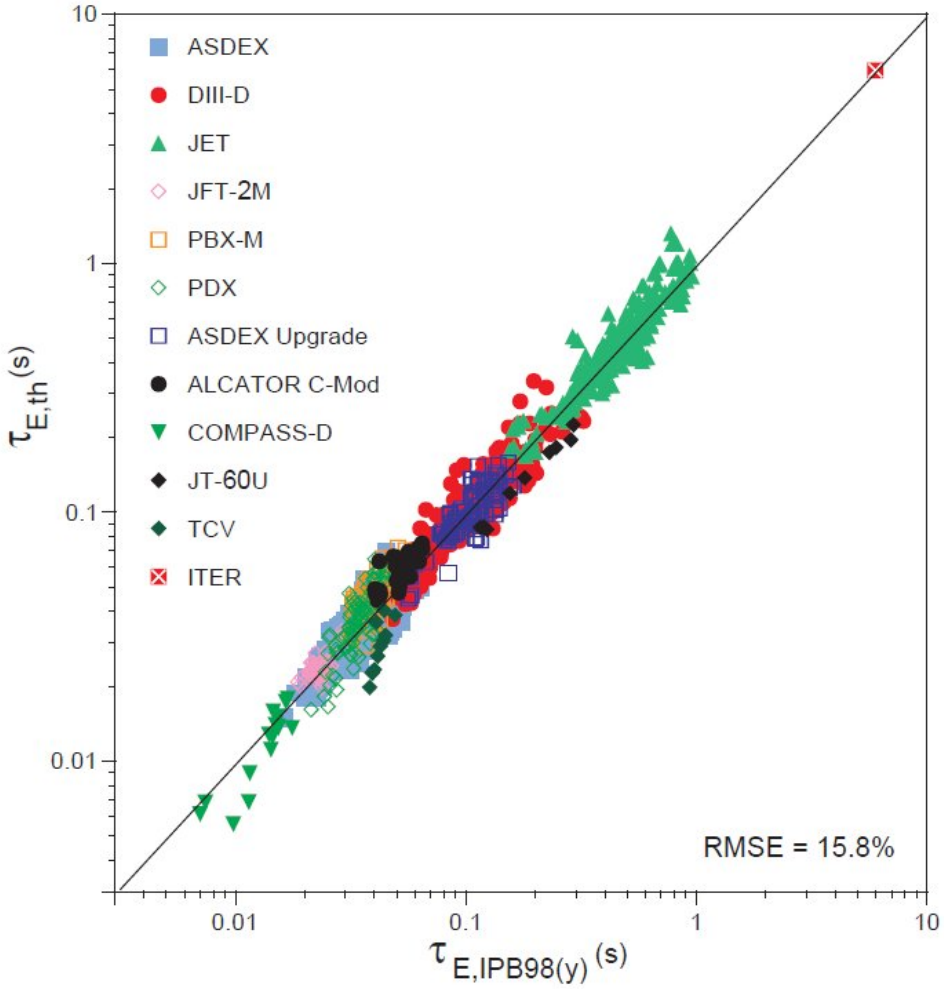

Figure 2.2: H-mode thermal energy confinement time compared to the scaling expression in equation (2.1) for ITER H-mode database. Figure 9 from [49].

discussed topic in tokamaks community but a conclusive and adequate model is yet to be developed[a]. Disregarding the physical mechanism leading to the L-H transition, the H-mode power threshold is found to strongly depend on plasma density, toroidal magnetic field and plasma size. The input power requirements for accessing H-mode in future devices, such as ITER, can be obtained through a general power-law scaling derived from a multi-machine database:

$$P_{thresh} = 0.0488 \langle n_e \rangle_l^{0.72} B_t^{0.80} S^{0.940} \tag{2.3}$$

where $\langle n_e \rangle_l$ is the plasma line-average density (10^{20} m^{-3}), B_t is the vacuum toroidal field at the magnetic-axis (T) and S is the plasma boundary surface area (m^2) [54]. Figure 2.3 depicts the comparison between equation (2.3) and the experimental data set from which it was extracted.

[a]*The discussion of such a topic is out the scope of this thesis work so we refer to literature for an extensive discussion[50, 51, 52, 53].*

Following (2.3), extrapolation to ITER gives a threshold power of ~ 52 MW in a deuterium

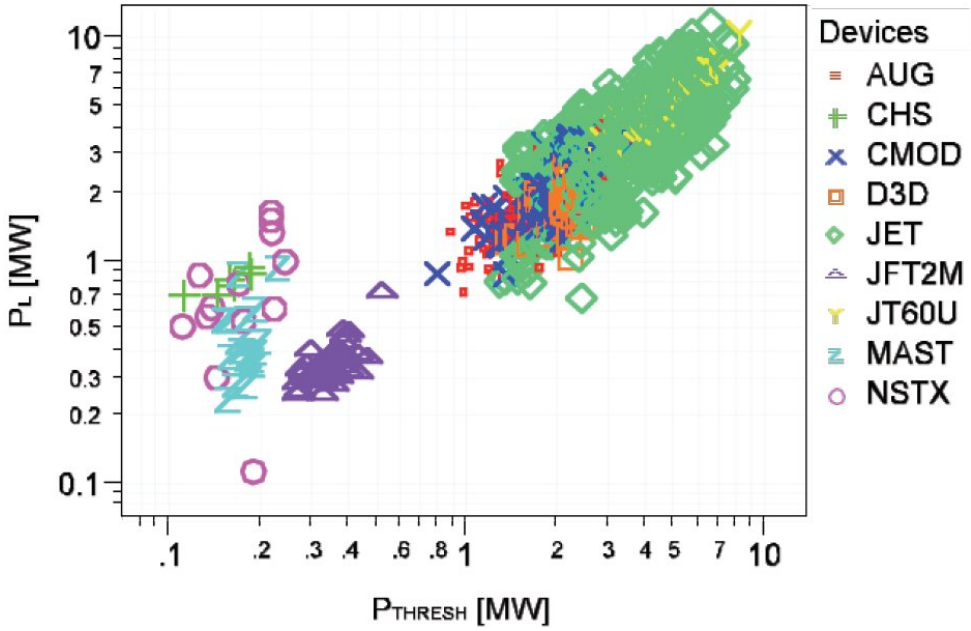

Figure 2.3: Actual versus fitted threshold power for tokamak time slices used in the fit (Alcator C-Mod, ASDEX Upgrade, DIII-D, JET, JFT-2M, JT-60U). In addition, spherical tokamaks and helical system threshold power are superimposed to show their distance to the fit (MAST, NSTX, CHS). Figure 1 from [54].

plasma at a line average density $\langle n_e \rangle_l = 5 \cdot 10^{19}$ m^{-3}. At the nominal ITER H-mode density, $\langle n_e \rangle_l = 1 \cdot 10^{20}$ m^{-3}, the foreseen threshold power is ~ 86 MW, more than the total available input power at the beginning of ITER operations. However, it is known that equation (2.3) is only valid for a sufficiently high density and $P_{L,LH}$ dependencies can vary from one device to another. A list of the main dependencies of $P_{L,LH}$ is provided below:

a) *density* The $P_{L,LH}$ dependence on density differs from one device to another, so equation (2.3) is valid for density above the 'device-dependent low density limit' for H-mode access. As a matter of fact, many devices observed the presence of a minimum in the threshold power as a function of the plasma density (JT-60U[55], JET[56], ASDEX-Upgrade[57], Alcator C-Mod[58]). The density of the minimum threshold power has not a unique value for the different devices and seems to slightly depend on magnetic field value and on machine size. Moreover, experiments in JET indicate that a change in the divertor geometry may have lowered the $\langle n_e \rangle_l$ at which $P_{L,LH}$ has its minimum[56].

b) *magnetic configuration* The power threshold is considerably lower for diverted configurations rather than limited ones. Limited operation does not exclude the possibility to access H-mode but require a considerably lager amount of input power, see for example[59]. The influence of magnetic configuration on $P_{L,LH}$ is highly machine dependent, as this dependence is the main topic for this thesis work a deeper insight on

the available experimental evidences will be given in Section 5.1

c) *ion ∇B-drift* It is well established that the power threshold is lower for *single null* (SN) configurations with the ion ∇B-drift towards the X point (favorable configuration), than for SN with the opposite ion ∇B-drift direction[60, and references therein].

d) *ion mass number* $P_{L,LH}$ has been shown to decrease with the ion mass number approximately as $1/M$ in Hydrogen, Deuterium or Tritium discharges. Scaling this result to ITER, makes it possible to foresee a 20% decrease of the power threshold for operation with a 50:50 DT mixture[61]. It is worth noting that helium plasma discharges are not in agreement with this simple ion mass scaling. For example, in DIII-D Helium plasmas was reported to have a 30%-50% higher threshold power than Deuterium plasmas[62].

e) *safety factor* During TCV experiments power threshold was found to increase gradually when the q_{95} decreases below 2.5 [63].

f) *effective Z* $P_{L,LH}$ has been shown to strongly depend on Z_{eff}: $P_{L,LH} \propto Z_{eff}^{0.7}$ [63].

g) *divertor neutral density* H-mode has been triggered on JFT-2M with the injection of neutrals through gas puffing near the X-point[64].

Many other dependencies have been documented and involve quantities not necessarily with a physical meaning. These other dependencies are collectively lumped into the nomenclature of *hidden variables*[65]. Some examples of these *hidden variables* are listed below:

a) *elongation and wall distance* In DIII-D a dependence of $P_{L,LH}$ on elongation κ and on plasma-wall distance was shown. A distance between plasma and machine components lower than 3 cm has been found to trigger anomalously high threshold values in different devices[66, and references therein].

b) *X-point geometry* $P_{L,LH}$ is affected by the geometry of the X-point with respect to the vacuum vessel. Particular attention will be devoted to this topic in Section 5.1.

The list above is far from being complete, $P_{L,LH}$ has been shown to be also affected by torque injection as well as applied 3D non-axisymmetric fields and other quantities even more difficult to quantify, e.g. wall conditioning techniques or the effect of neutrals. We reported the main ones and those which are more relevant to the performed experimental analysis.

2.2.1 H-mode at TCV

In TCV, the access to H-mode is easily obtained with a number of different configuration and operational scenarios, with or without additional heating. Ohmic H-modes are routinely obtained even with the ion ∇B-drift away from the X- point, but in most conditions these are ELM-free and terminate in a high density disruption. Stationary and robust ELMy H-modes can be obtained only for SN configurations in a narrow range of discharge parameters which does not limit the investigation capability because the H-mode is robust enough to allow wide variation of current, density and elongation[67]. Ohmic L-H transitions were only rarely observed in low density plasmas ($\langle n_e \rangle_l < 4 \cdot 10^{19}$ m^{-3}). In these ohmic discharges, the L-H transition is usually produced when the plasma becomes diverted[68]. The power threshold

for such discharges has been measured and its density dependence investigated: an exponent similar to the ITER scaling proposed in [66] has been found, suggesting that the density dependence is similar in discharges with and without additional heating[68].
Exploiting the strong and flexible electron heating capability, the lower density limit of the aforementioned H-mode access has been overcome: in ECRH-assisted discharges H-mode have been obtained at density values as low as $\langle n_e \rangle_l \sim 2.5 \cdot 10^{19}$ m^{-3}[69]. While the H-mode power threshold was found to increase with density in Ohmic H-mode above $\langle n_e \rangle_l \sim 4 \cdot 10^{19}$ m^{-3}; in ECRH assisted discharges below $\langle n_e \rangle_l \sim 3.5 \cdot 10^{19}$ m^{-3} the H-mode threshold has been found to decrease with density[69], see Figure 2.4b. H-mode threshold power studies were replied comparing ohmic, X2-heated and X3-heated discharges, results are reported in Figure 2.4b. First indications of the presence of a density turning point in the H-mode power threshold was obtained: the L-H transitions produced by ECH-X2 with unfavorable ion ∇B-drift (stars in Figure 2.4b) exhibit a higher threshold power than the corresponding Ohmic cases (triangles). Moreover, Ohmic and X3-ECH heated discharges show similar power threshold at similar density. This similarity suggests that the underlying transition physics does not depend on the heating scheme[68].

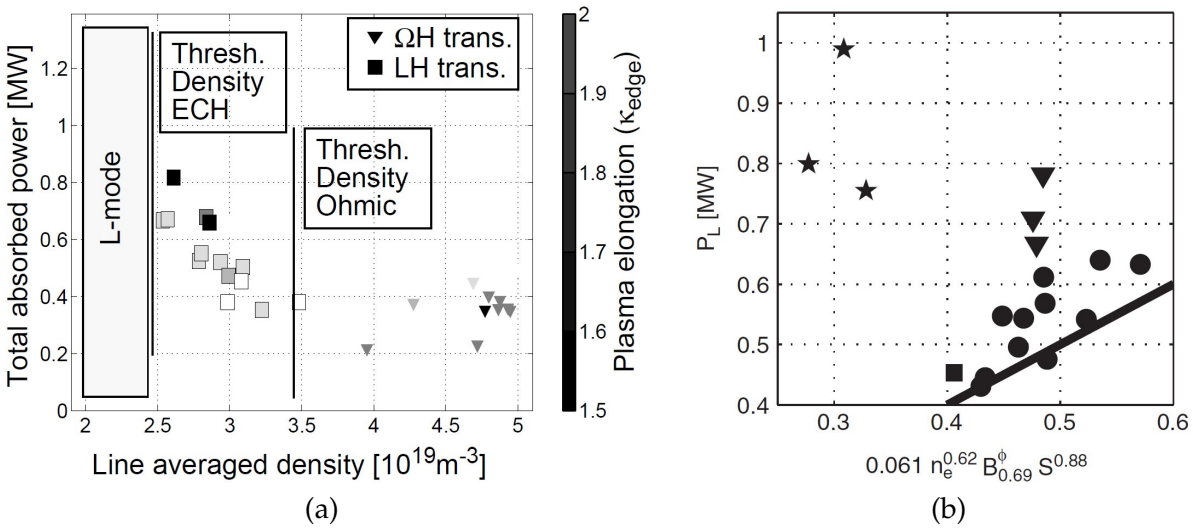

Figure 2.4: (a) L-H transition threshold power in ohmic (triangles) and ECRH (squares) heated discharges. Figure 5 from [69]. (b) Loss power ($P_L = P_{OHM} + P_{AUX} - dW/dt$) as a function of the threshold power estimated from the ITER scaling[66] at the LH transition for different cases: (circles) Ohmic with favorable ion ∇B-drift; (triangles), Ohmic with unfavorable ion ∇B-drift; (squares), ECH (X3) with favorable ion ∇B-drift; (stars), ECH (X2) with unfavorable ion ∇B-drift. Figure 1 from [68].

2.3 RFPs: From SHAx states to helical divertor concept

The RFP is considered an alternative way to tokamaks for providing the basis for a future fusion reactor. The weaker requirements on toroidal field coils current and the possibility of reaching ignition with ohmic heating only are the attractive features pointing to a relatively simple, compact and inexpensive reactor based on the RFP concept. However, until recently these positive features were overcome by the poorer stability properties, which led to the growth and saturation of several MHD instabilities giving rise to an ergodization of the magnetic field over most of the plasma volume and eventually downgrading the confinement performance. These instabilities, represented by Fourier modes in the poloidal and toroidal angles θ and ϕ as

$$B = \sum_{m,n} b_{m,n} exp\left[i(m\theta - n\phi)\right] \qquad \text{with} \quad m = 1 \quad \text{and} \quad n > 3R/2a \qquad ,$$

were considered to be intrinsic to the configuration as responsible for the dynamo self-organization process, which allows to sustain the poloidal currents flowing in the plasma against resistive decay and is thus necessary to sustain the configuration[9, 70, 71]. In fact, according to linear MHD, the RFP configuration needs a mechanism generating the poloidal current to sustain the toroidal component of the magnetic field, which conversely is expected to decay exponentially within some resistive times. Such mechanism is called *dynamo effect* and can be formally explained writing the Ohm's law for the electric field component along the main magnetic field:

$$E_{\|} = \frac{(\boldsymbol{E} + \boldsymbol{u} \times \boldsymbol{B}) \cdot \boldsymbol{B}}{B} = \eta j_{\|} \qquad . \tag{2.4}$$

From the former one expects $E_{\|}$ to follow the $j_{\|}$ profile, experimentally found to flow in the same direction throughout the entire plasma. Conversely $E_{\|}$ is experimentally found to mimic the profile of B_{ϕ}, changing sign at the plasma edge, see Figure 2.5. This discrepancy is usually related to the so called *dynamo term*, E_d: separating magnetic and velocity fields in equation (2.4) and distinguishing their average from the fluctuating contribution, this new term arises

$$E_{\|} + E_d = E_{\|} + \langle \tilde{\boldsymbol{v}} \times \tilde{\boldsymbol{b}} \rangle = \eta j_{\|} \qquad .$$

This dynamo term comes from the coherent interaction between the velocity and magnetic field fluctuations, respectively $\tilde{\boldsymbol{v}}$ and $\tilde{\boldsymbol{b}}$. Thus the RFP sustainment is strongly related to the presence of a self-organized velocity field in the plasma. In more details, the dynamo process implies the existence of a finite plasma resistivity leading to the growth of a sea of MHD tearing instabilities responsible for the dynamo term. This sea of MHD modes, resonating at different radii, gives rise to overlapping magnetic islands which results in a chaotic region, extending over most of the plasma volume[72], where the magnetic surfaces are destroyed and the confinement level is modest. This condition is generally dubbed as the *multiple-helicity state* (MH).

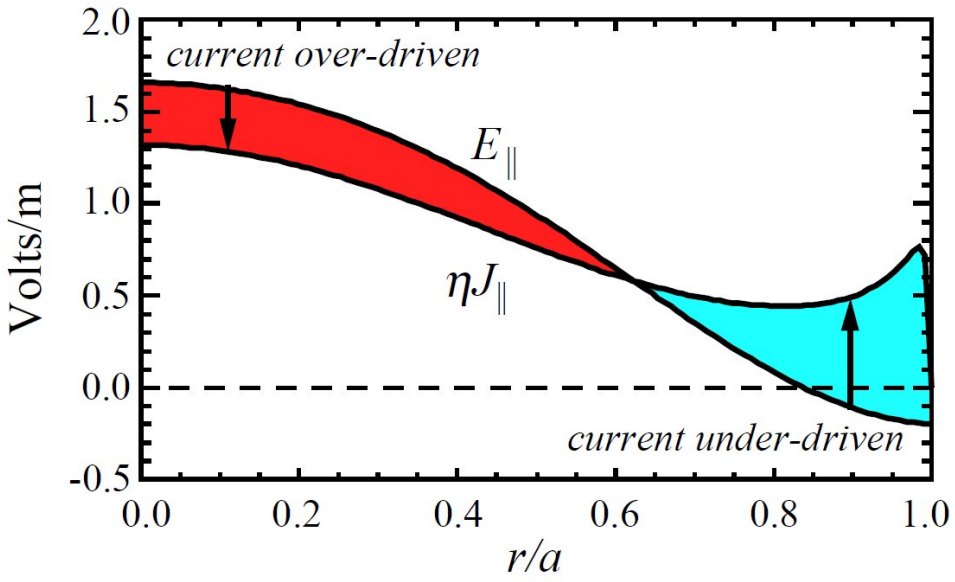

Figure 2.5: Typical radial profile of $E_\parallel$ and $\eta j_\parallel$ in a RFP configuration. The discrepancy is accounted by the dynamo term E_d.

This picture is changed, thanks to the theoretical prediction of a dynamo processes achieved with only one MHD mode [73, 74]. This condition is named *single-helicity state* (SH). To now, the best experimental approximation of single helicity are the *quasi-single-helicity states* (QSH): here, the innermost resonant $m = 1$ mode dominates over the others, the so-called secondary modes, which maintain a finite amplitude. QSH states have been observed in several RFP devices[75, 76, 77] and predicted in numerical simulations[78]. They are an intermediate state between the MH and the theoretical SH ones, because the secondary modes are still present. The onset of the QSH state gives rise to a magnetic island in the stochastic core, which appears as a thin, hotter structure within the temperature background, centered off-axis, on the resonant surface of the dominant mode. In RFX-mod, within the medium current regime (0.7÷1.2 MA) the spontaneous QSH phases are short and rare, since the plasma preferentially stays in a MH state and the transitions to QSH occur only occasionally. The situation drastically changes whether the plasma current reaches values larger than 1.2 MA, in this current regime the plasma preferentially stays in QSH, although intermittent transitions (crashes) to MH still occur. After each of such crashes the dominant mode rapidly increases, then saturates and the QSH lasts up to tens of milliseconds. The difference between the two plasma states can be seen in Figure 2.6 where the time evolution of the dithering between MH and QSH state is shown for two discharges with low and high current value. In these phases the plasma is in a helical equilibrium. In general, QSH states have been observed to occur more and more frequently and for longer durations as the plasma current is raised[80]. Moreover, at high plasma current a spontaneous transition to a new magnetic topology, dubbed *single helical axis state* (SHAx) was discovered[80, 81, 82]. In this state, which is a

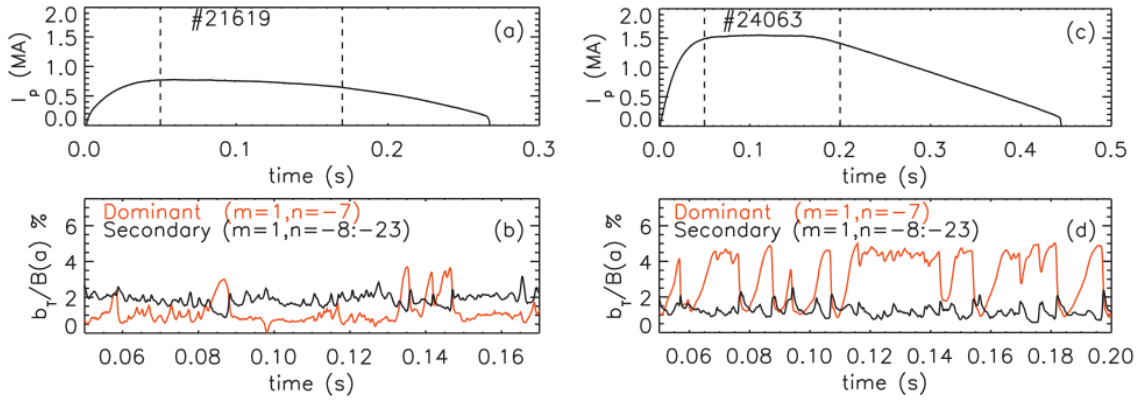

Figure 2.6: Time trace of the plasma toroidal current I_p for the medium current discharge 21619 (a) and for the high current discharge 24063 (c). The vertical dashed lines delimit the flattop. Time trace of the amplitude of dominant mode (in red) and of the total amplitude of secondary modes (in black) during the flattop of the discharge 21619 (b) and of the discharge 24063 (d). Figure 3 from [79].

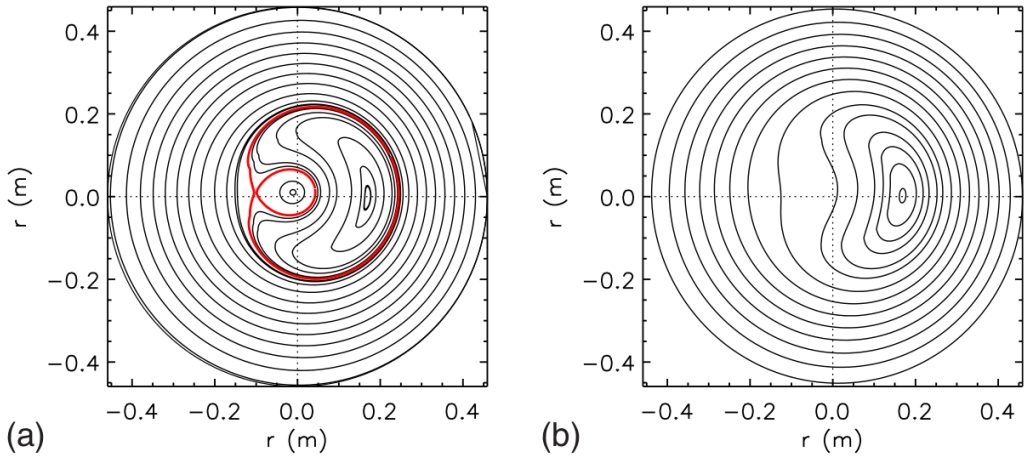

Figure 2.7: Magnetic topology reconstructed using only the axisymmetric fields and the eigenfunction of the dominant mode: (a) QSH with a magnetic island or DAx, the separatrix is highlighted in red. (b) SHAx state. Figure 7 from [79].

special instance of the more general QSH condition, the separatrix of the dominant mode magnetic island is expelled, while its X-point collapses onto the main magnetic axis of the discharge. The resulting configuration is characterized by a helical magnetic axis, which is the former island O-point. Figure 2.7 plots the difference between a QSH state with a magnetic island, also dubbed *double-axis state* (DAx), characterized by the presence of the separatrix and a SHAx state where the separatrix disappeared. In SHAx condition order emerges from magnetic chaos in the core plasma and a transport barrier develops, so that the confinement properties of the configuration are enhanced[80]. Such barrier is marked by the presence of the steep temperature gradients in the core region, see Figure 2.8. The transport barrier

bounds a hot region which is larger than the typical one associated to DAx states, and extends in both sides of the geometrical axis of the machine. The thermal structure occupies a significant fraction of the plasma core, up to 40% of the total plasma volume. These changes in the magnetic configuration and confinement properties are mainly related to the behavior of the $m = 1$ modes.

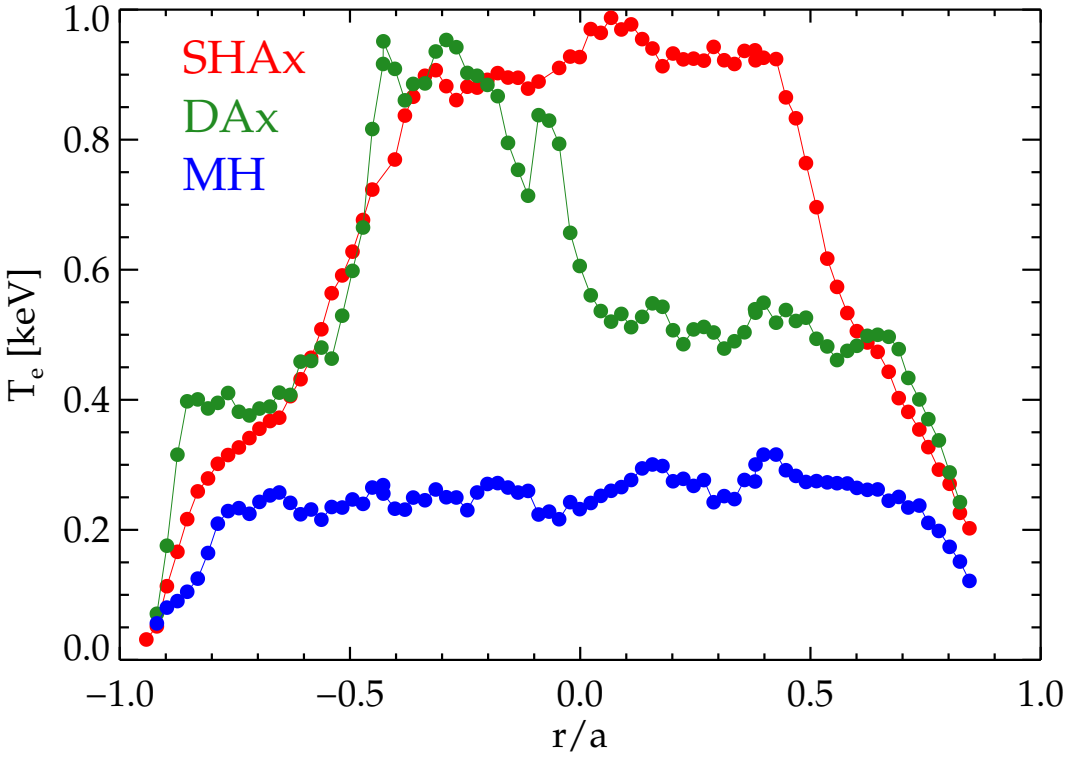

Figure 2.8: Comparison between three typical thermal profiles mapped on machine coordinate: MH state (blue), DAx state (green) and SHAx state (red).

It is important to note that also $m = 0$ modes are resonant in the RFP. Their resonance radius is located on the toroidal field reversal surface, namely where $q = 0$. This can be positioned more or less distant from the first wall, depending on the current imposed in the toroidal field coils. The distance from the wall is indirectly quantified by the reversal parameter F. The $m = 0$ and $m = 1$ modes strongly interacts with each other, the former being strongly affected by the onset of QSH states. In fact the $m = 0$ mode spectrum features many low n modes in low current operation, while increasing the current tends to peak on the $n = 7$ one as the $m = 1$ spectrum does. The prevailing of the $m = 0/n = 7$ mode as current is increased is a direct consequence of the same behavior observed for the $m = 1/n = -7$ one[80], due to the toroidal coupling of the two modes. The $m = 0$ spectrum displays the same behavior with increasing plasma current of the $m = 1$ one, i.e. the dominant $n = -7$ mode increases its relative amplitude while the secondary modes amplitude is reduced. Thus, it is possible to

conclude that the RFP evolves, as plasma current is increased, towards a SHAx state characterized by the presence of a dominant $m = 1$ mode and a dominant $m = 0$ mode, both having the same n periodicity[83].

2.3.1 The RFX-mod edge

The RFX-mod edge is a quite complex region characterized by a very fast dynamics and a number of different interacting phenomena. Definitely, most of them are linked to the reversal of the toroidal component B_ϕ and to the location of the reversal surface. The magnetic topology of the outermost plasma region is indeed strongly affected by the chain of poloidally symmetric $m = 0$ islands forming around the $q = 0$ surface. The role of the edge magnetic topology is further intensified by the geometry and the characteristics of the RFX-mod material boundary: the plasma-wall interaction is spread all over the material surface so the interaction pattern is completely defined by the edge magnetic topology. As additional outcome of this influence, the edge magnetic topology indirectly controls the plasma refueling. In fact, in RFX-mod, the main source of density is the neutrals extracted by the carbon wall: the higher is the power impinging on the wall the larger is the amount of hydrogen taken out from the wall inventory[84]. Before entering the details about all these complicated mechanisms, it should be reminded that none of the carbon tiles is pumped, so the neutrals extracted from the wall accumulate at the plasma edge.
The reversal surface, thus the $m = 0$ islands chain, can be positioned more or less distant from the first wall, depending on the current imposed in the toroidal field coils. Moreover, it has already been mentioned that increasing the plasma current the $m = 0$ modes spectrum tends to peak as the $m = 1$ one does. Thus, the interplay between $m = 0$ and $m = 1$ modes changes when the magnetic state of the plasma is changed. The edge topology is thus complicated and interpretation of data coming from this plasma region consequently requires a detailed comparison with the local magnetic topology. Making use of the Poincaré plots the edge topology for the various conditions is shown in the following.

Edge topology in MH conditions

At low current, thus in MH conditions, the $m = 0$ islands actually act as a transport barrier due to the very low degree of order of the surrounding plasma[85]. In this conditions the $m = 0$ modes tend to phase lock to each other as the $m = 1$ does, with the $m = 0$ locking close to the position where the $m = 1$ modes lock to the wall[86, 87]. The topological characteristics of the external region in this regime is quite complicated: a large helical deformation due to phase and wall locking of the $m = 1$ modes superposes to the funnel-like shape of the plasma column due to the aforementioned phase locking of the $m = 0$ modes. An example of such a magnetic topology characterizing MH state is given in Figure 2.9 where an accurate reconstruction of the outer region of the RFX-mod experiment obtained with a Field Line Tracing (FLiT) code[88] is depicted. The chain of $m = 0$ islands deformed by the $m = 1$ and

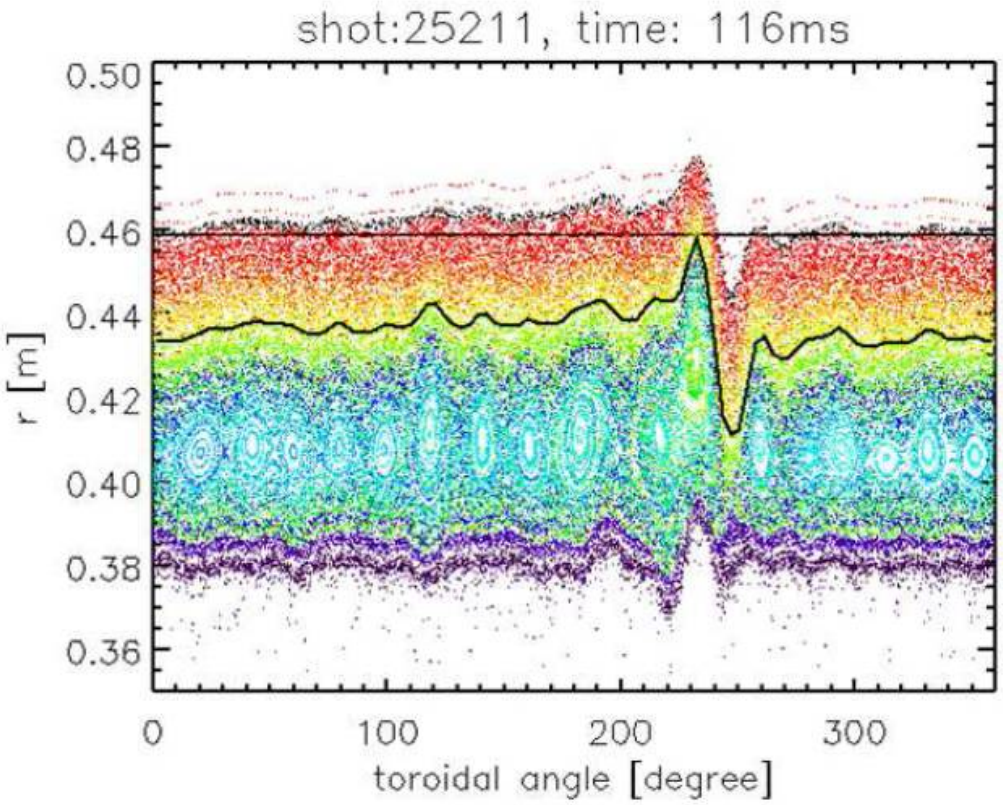

Figure 2.9: (r, ϕ) plane in the outer region of the RFX-mod device. Poincaré plot of a deep F discharge in MH conditions. The $m = 0$ islands chain is evident around $r \sim 0.4$ m. In black the Last Closed Flux Surface is reported.

$m = 0$ phase locking is clearly seen around $r \sim 0.4$ m and $\phi \sim 230°$. As a consequence, the LCFS is also deformed and touches the wall at the locking position. Depending on the value of the reversal parameter F, the interaction of the plasma with the first wall drastically changes. In the case of deep reversal condition, as the one depicted in Figure 2.9, the distortion corresponding to the wall locking induces a toroidally localized plasma-wall interaction, only partially alleviated by the amelioration of the plasma boundary induced by the feedback system. At shallow F, the $m = 0$ islands can deeply intercept the first wall, ruling out any effect of the outermost magnetic surfaces. This situation has changed since the introduction of the active saddle coil system for the control of the radial magnetic field at the plasma boundary (*Clean Mode Control*)[89]. This control scheme has lowered the tearing mode amplitude and created a more ordered situation, so that good conserved magnetic surfaces exist in the outer plasma region. Indeed, the $m = 0$ islands have been found to be a source of flattening of the local temperature profile, due to their effect of short-circuiting different plasma radii[86].

It is important here to spend some time stressing how the LCFS can be defined in a RFP

experiment. In fact, even if looking at Figure 2.9 a sort of order can be seen[a], no real conserved flux surfaces exist because of the magnetic chaos produced by the mode overlapping. So, a proper Last Closed Flux Surface does not exist in MH states in an RFP. Nevertheless, something similar can be defined considering the connection length of the field lines, namely the distance covered from each field line from the rational surface where it begins up to the wall. A closed flux surface would have an infinite connection length, so a LCFS-like surface can be defined looking for those field lines with infinite connection length. In the RFP case the LCFS is defined considering for each surface element $(d\theta, d\phi)$ the outermost field line which does not touch the wall. See [83] for deeper analysis and discussions.

Edge topology in QSH conditions

The situation described up to now changes drastically when a QSH state develops. In fact, the inner $m = 1/n = -7$ helical structure, toroidally rotating during the QSH states, imposes a similar toroidal $n = 7$ periodicity to the aforementioned $m = 0$ islands pattern. The phase relation between the $m = 0$ islands and the main helical $m = 1$ deformation is defined by the tridimensional geometry. In the outer equatorial region ($\theta = 0$, where the main diagnostic systems are located) a reconstruction made by another field line tracing code (ORBIT [90, 91]) reveals a phase $\Phi = \pi$ between the two maximum $m = 0$ and $m = 1$ deformations. Namely, the O-points of the $m = 0$ and the X-points of the $m = 1$ islands are located at the same toroidal angle. Conversely, at the HFS the the maximum deformations due to $m = 0$ and $m = 1$ modes are found in phase[158]. The coupling becomes stronger if SHAx state is achieved. Differently from the MH case, in SHAx conditions no strong localized distortion of the plasma column due to mode locking[87] is found. Thus, provided that the absolute value of the reversal parameter is small enough, the $m = 0$ islands intercept the first wall and the LCFS does not touch the first wall anymore. The X-points formed between the $m = 0$ islands are able to produce a divertor-like configuration[83] if an efficient pumping capability is provided[b]. Such situation is reminiscent of the island divertor concept which is being explored as a mean to control plasma-wall interaction in stellarators. The overall result is an edge plasma helical displacement with a 7-folded toroidal periodicity, due to the convolution of the $m = 1$ helical ripple with the $m = 0$ islands chain[92, 93]. The PWI indeed assumes the same topology, as a proof the H_α emission is found to follow the same helical pattern with the maximum particle influx located at the maximum outward plasma displacement. The LCFS is also correspondingly modulated, showing an $m = 1/n = -7$ ripple where the outermost edges correspond to the $m = 1$ islands O-points. These edges correspond also to $m = 0$ islands X-point on the LFS and to $m = 0$ islands O-point on the HFS[93]. The situation is depicted in Figure 2.10b and compared to

[a] *In Figure 2.9 the colors mark point from which a field line is followed to track the Poincaré plot. The purple points mark field lines 'starting' around $r = 0.38$ m while red ones mark field lines starting just inside the wall radius. So the footprint of order is the existence of regions near to each other with a marked color difference.*

[b] *Such condition can be obtained with wall conditioning techniques as prolonged Glow Discharge Cleaning[92].*

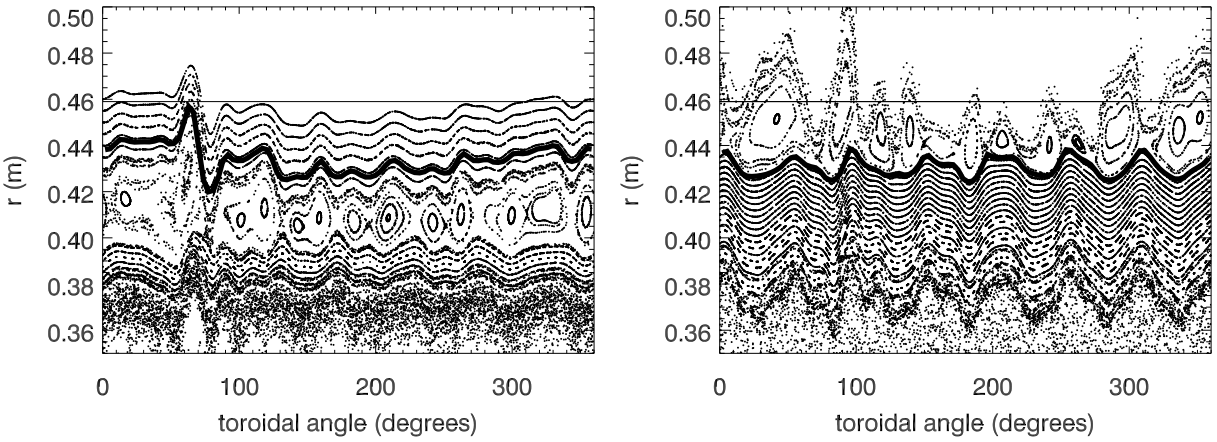

Figure 2.10: Poincaré plot of the magnetic field lines on the outer equator for a SHAx state at 1.5 MA and deep reversal (a) and for a similar condition at shallow reversal (b). The thick line marks the position of the LCFS. The horizontal line at $r = 0.459$ m indicates the first wall position. Courtesy of B. Momo.

Figure 2.10a, where two discharges performed at shallow and deep F are shown. At deep F, i.e. Figure 2.10a, the situation is similar to the MH case of Figure 2.9. Conversely at shallow F, namely Figure 2.10b, the LCFS is separated from the wall by the $m = 0$ islands chain that acts as an effective scrape-off layer. Following these findings, one is led to infer that the special features of the plasma boundary in high current SHAx RFP plasmas could be exploited for building a divertor, similar in concept to the island divertor used in some stellarators[83]. The dichotomy shallow F-deep F has been investigated during SHAx states, so to become quantitative. The transition from a limiter-like geometry, i.e. Figure 2.10a, to a diveror-like geometry, namely Figure 2.10b, has been tracked and is represented in Figure 2.11 where the distance between the LCFS and the material surface, δ_{min}, is shown as a function of F. At deep F ($F \lesssim -0.1$) the LCFS touches the wall ($\delta_{min} = 0$) forming the limiter-like configuration. This causes a strong local PWI which triggers the release of hydrogen from the graphite wall. Conversely, at shallow F ($F \gtrsim -0.1$) the LCFS is not touching the wall anymore ($\delta_{min} > 0$) resulting in a mitigated PWI. During QSH states, the $m = 1, n = -7$ helical ripple, which modulates the edge topology, forces the PWI to assume a helical pattern[92, 93]. The portion of wall wetted by the helix is subject to a power load as large as 5 MW/m^2. However, when a back-transition from the QSH to the chaotic state occurs leading to mode wall locking, the region of plasma-wall interaction gets smaller and the localized power load can increase up to tens of MW/m^2 [94]. Such picture led to conclude that *shallow F* operation constitutes the optimal condition for high current operation [83], as long as an efficient wall pumping is provided.

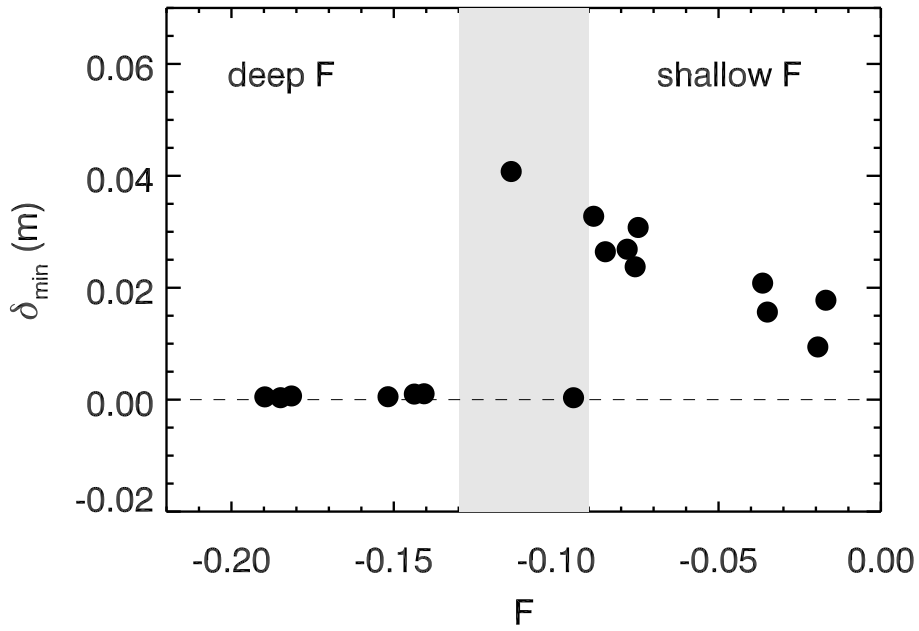

Figure 2.11: Minimum distance of the LCFS from the first wall plotted as a function of the reversal parameter. The shaded region marks the F range where transition from a limiter-like geometry to a divertor-like one occurs. Courtesy of B. Momo.

2.3.2 RFX-mod density issues

In RFX-mod, due to the high Hydrogen retention capability of carbon, plasma density is generally established by the wall desorption rather than by the fuelling rate, as a matter of fact the recycling coefficient, R, can generally exceed unity. During operations, the wall can get so saturated that feeding the machine by the minimum amount of particles necessary to the breakdown is sufficient for the plasma discharge to be completely sustained by atoms released by the wall. This amount of particles depends both on wall power load and on the number of particles stored into the graphite tiles. The discharge density is therefore established by the combination of different factors: the previous discharges history, the ohmic input power and the local magnetic topology[94]. As a consequence, density control results generally difficult, and gets even more tricky at high plasma current[95]. On the other hand, the particle confinement time is of the order of some milliseconds[96], bounding RFX-mod to the need of operating with $R \sim 1$ given the present low capability of the fuelling system. Each density increase results in an edge density peaking which is accompanied by a decrease of the local temperature. The plasma edge gets therefore highly resistive and a large ohmic power is required to sustain the discharge.
To tackle the puzzling density control and to reduce the graphite H retention, wall conditioning techniques have been optimized: Glow Discharge Cleaning and wall boronization are routinely performed[97, 98]. More recently, Lithium conditioning has been tested in order to obtain a hot and low-density plasma edge: substantial effects have been

obtained on edge temperature and density profile but no macroscopic amelioration of the plasma performance has already been observed[99, 100, 94].
Summarizing, the operational space for helical states in RFX-mod is found to be limited in attainable normalized density fraction. This limit depends on different competing mechanisms which act to modify the plasma edge conditions: $m = 0$ island width, wall proximity of the reversal surface and wall conditioning. An increase of the plasma current corresponds to a large amplitude of both the dominant mode and its $m = 0$ counterpart. This can explain the difficulties encountered to achieve high plasma density in high current regimes. After a few shots from wall conditioning, the PWI due to the MHD dynamics produces a wall out-gassing and a consequent loss of QSH cycles[92].
In RFX-mod MH-state a density limit similar to the MARFE phenomenon in tokamaks has been documented, it resulted non-disruptive like in stellarators and was parametrized in terms of the Greenwald density. At $n/n_G \gtrsim 0.35$ a sharp increase in $m = 0$ modes amplitude takes place leading to a strong $m = 0/n = 1$ deformation of the plasma column due to the coherent, wavelike superposition of $m = 1$ and $m = 0$ modes, known in the RFP community as the *locked mode*. In the vicinity of the X-point of this deformation the electrons accumulate leading to a reversal of the radial electric field next to the wall. Consequently the toroidal plasma flow also reverses its sign forming a stagnation point which leads to a localized accumulation of density with a consequent decrease of temperature through radiative cooling which finally results in a soft landing of the plasma current. The flow reversal takes place at $n/n_G \sim 0.35$ can be seen as precursor of the density limit and, in a strict sense, states the impossibility of sustaining a discharge at $n/n_G \sim 1$ [101, 91]. The overall picture of the density limit in the RFP is therefore that a transition from a high-confinement to a low-confinement state takes place at $n/n_G \sim 0.35$, with associated toroidal inhomogeneity and unbalanced flows in the edge.

2.3.3 Dynamo Relaxation Events

A further complication to the edge picture of an RFP is posed by the occurrence of a significant sawtooth activity related to *Dinamo Relaxation Events* (DRE)[102]. Such events periodically determine a temporary 'back transition' from the QSH towards a more chaotic MH state and usually destroy the previous magnetic order throughout the whole plasma. These events are the discrete responsible for the poloidal current (and hence for the toroidal flux) generation through MHD dynamo. DRE events have been widely studied in the RFP community[103, 104, 70]; the common picture emerging from these studies is that of a toroidal flux generation occurring through the non linear interaction of the tearing modes with a strong local and toroidally asymmetric character. Furthermore, if the modes are phase locked, the development of the flux perturbation and the phase locking[105] of MHD modes are found to occur at the same toroidal position. The occurrence of DREs results in cyclic loss of particles and energy confinement, a significant fraction of which occurs at the wall locking

position of the $m = 1$ modes. These events strongly modifies the geometry of the LCFS usually leading to an enhanced plasma-wall interaction. DREs are strongly related to modes dynamics and are responsible for the typical sawtooth activity affecting the time evolution of the reversal parameter F. The $m = 1$ modes are destabilized following a cascade process that starts from the innermost resonating harmonic and propagates to the outer ones. The amplitudes of the secondary $m = 1$ modes peak for a transient time of the order of 1 ms, while the $m = 0$ display a similar dynamics. This leads to a crash of the F parameter ($\Delta F \approx 0.1$) which then recovers the initial value on the same timescale of approximately 1 ms. During a DRE the electron density generally increases, with a behavior that mirrors the evolution of F. The density increase is not toroidally symmetric, while it is strongly concentrated around the locking position. No outstanding changes was highlighted in the temperature profile during a DRE[106].

3

RFX-MOD: CHARACTERIZATION OF TEMPERATURE PROFILES

In questioni di scienza, l'autoritá di mille non vale l'umile ragionare di un singolo.
In questions of science, the authority of a thousand is not worth the humble reasoning of a single individual.

Galileo Galilei

In RFP plasmas, temperature is almost completely determined by three parameters: plasma current, density and amplitude of secondary modes[107]. Plasma current is the main knob to control RFX-mod plasma, its magnetic topology can be influenced by external means, conversely density is barely controllable. Investigations on the influence of such parameters on temperature profiles were performed. Some efforts have been devoted to investigate whether or not other quantities can be used as a knob to change the temperature profile. In this chapter these two purposes are faced together through a statistical analysis on a large database containing all the three different plasma states (MH, DAx and SHAx). Investigations are performed on different quantities: central temperature, external temperature and temperature gradient to asses both magnitude and shape changes. Statistical studies and experimental evidences will be presented and summarized in a global physical picture at the end of the chapter.

Temperature is one of the key parameters that qualifies fusion plasma performance. In RFX-mod, temperature is mainly determined by three parameters: plasma current, density and amplitude of secondary modes[107]. In particular, plasma current is extremely effective on controlling electron temperature via two different mechanisms. On the one hand plasma is totally heated by ohmic means, so an increase in current directly increases the temperature. On the other hand, the value of the plasma current is closely related to the different magnetic topologies. Recalling Section 2.3, increasing plasma current above 1 MA a spontaneous transition from Multiple Helicity state to Quasi Single Helicity state occurs in RFX-mod. The two different plasma states are characterized by different magnetic topologies. Moreover, the change from MH to QSH induces a decrease in the amplitude of the secondary modes decreasing the plasma stochasticity level. These evidences, in RFX-mod device, were summarized in an multi-parameter scaling proposed in [107]:

$$T_e^0 \propto I_p^{1.09\pm0.01} \langle n_e \rangle_l^{-0.30\pm0.01} \left(b_\varphi^{sec}\right)^{-0.28\pm0.01} \quad . \tag{3.1}$$

In the previous expression T_e^0 is the central electron temperature, I_p the plasma current, $\langle n_e \rangle_l$ the line average density and b_φ^{sec} is the amplitude of the internally resonating secondary modes:

$$b_\varphi^{sec} = \left[\frac{1}{2} \sum_{n=-15}^{-8} b_\varphi^{1,n}(a)^2 \right]^{1/2} \quad . \tag{3.2}$$

Expression (3.1) was obtained using discharges performed with the *Clean Mode Control* scheme[89], and does not contain any information about temperature profile. In [107], in fact, any *a priori* distinction on magnetic configuration (MH, DAx or SHAx) was made, even if this information is implicitly expressed by the b_φ^{sec} term. Nevertheless, QSH states are characterized by the spontaneous appearance of an ordered magnetic structure in the plasma core with much higher temperature than the background temperature[80]. This region can extend towards $r/a \sim 0.5$ and involves at most the 40% of the plasma volume. The plasma edge is also strongly affected by the presence of the dominant mode: modulation of the plasma kinetic properties, which follow a helical $m = 1/n = -7$ pattern, has been documented[92]. Conversely, the remaining region extending from $r/a \sim 0.5$ towards the last closed magnetic surface, seems to be not that sensitive to the different magnetic topologies[106]. Given the large plasma volume enclosed in this domain, improvements of global plasma performance are closely linked to the identification of the physical mechanisms occurring in this region. Moreover, extremely high temperature gradients were observed from time to time in the external region of the plasma column. These strong edge gradients can extend the high temperature central region up $r/a \sim 0.9$ [159, 157]. Aiming at the comprehension of these topics, a wide-ranging characterization of electron temperature profiles has been performed posing particular attention to the region extending across $0.6 \lesssim |r/a| \lesssim 0.9$. This thesis work, grounded on previous studies[107, 106], was

mainly intended to provide scaling laws for temperature and temperature gradient occurring in the external region, investigation in this sense will be entirely presented in this chapter. To this extent, a characterization method was specifically conceived and adopted. Before entering the proper discussion about RFX-mod thermal properties such a method is presented.
The chapter proceed as follows: Section 3.1 and Section 3.2 are entirely dedicated to explaining and testing the *Fermi fit* method used to characterize the temperature profile. In Section 3.3 such Fermi fit is exploited to conceive a model based on macroscopic quantities to represent the temperature profile changes. Through a further statistical analysis, the model is applied to different temperature profile characteristics and the relative scalings are reported and commented (Section 3.3 and Section 3.4). In Section 3.5, reducing the database the variations of the temperature profile are visualized, presented and discussed. To conclude, Section 3.6 merges all the previous evidences with the present physics knowledge into a unique comprehensive picture.

3.1 External region characterization method

The method to characterize the temperature profile across the external region, $0.6 \lesssim |r/a| \lesssim 0.9$, was forced by the main Thomson Scattering (main TS) capability. Being the radial resolution ≈ 1 cm, roughly 10 measurement points are available in that region. High field and low field sides are not equally covered by the main TS, the region $0.85 < |r/a| < 0.95$ is diagnosed only on the high field side. This lack is healed by the edge TS system, when operating. Unfortunately this system has been operating only for a short period. So, on the low field side (LFS), a stand-alone analysis is generally difficult. To overcome this limit two strategies were adopted. A fixed fitting function was imposed and boundary conditions were used to limit the parameter space of the fitting function.

3.1.1 Fitting function choice

Starting from a selected database of complete T_e profiles (main and edge TS) the profile shape of the external region has been analyzed. This limited set was selected considering the neatness of the entire profile and trying to collect at least a case for every plasma magnetic state and for different values of plasma current and density. As a first suitable solution to match the temperature profile, in the region under analysis, the *modified hyperbolic tangent function*[108] was considered. This function is widely used in the tokamak community to characterize the H-mode pedestal region because of its excellent matching of H-mode profiles and for the strong intuitive appeal of its parameters, which provide a quantitative way to measure important characteristics of the pedestal. The expansion of the hyperbolic function and the multiplying factor were considered so to allow for a linearly rising profile in the core. Moreover, in tokamaks, the *tanh* function can be exploited to match density, temperature and pressure pedestal profiles with a unique function[108]. Nevertheless, in the case of RFX-mod, some differences triggered the choice of a different function. On the one side, matching

density, pressure and temperature with a unique function would have been difficult because density and temperature profiles are sensibly different. On the other side, the linear rise towards the core is not a characteristic feature of the RFX-mod temperature profiles, which usually shows a large flat core region. Furthermore, the limited number of available measurement points suggested to look for a fitting function with the smallest possible number of parameters. So, trying to maintain the intuitive appeal of the parameters and aiming at the best match of the typical temperature decrease in the region under analysis, the *Fermi function* has been adapted to the temperature profile

$$sT_e(r) = \Delta T_e \left[e^{4\frac{r-r_{max}}{\Delta}} + 1 \right]^{-1} + D \quad . \tag{3.3}$$

An example of a complete RFX-mod electron temperature profile is given in Figure 3.1, both main and edge TS data are shown together with the Fermi fit of the external region on both sides. In Figure 3.2a a widen view of the region under investigation is depicted. From equation

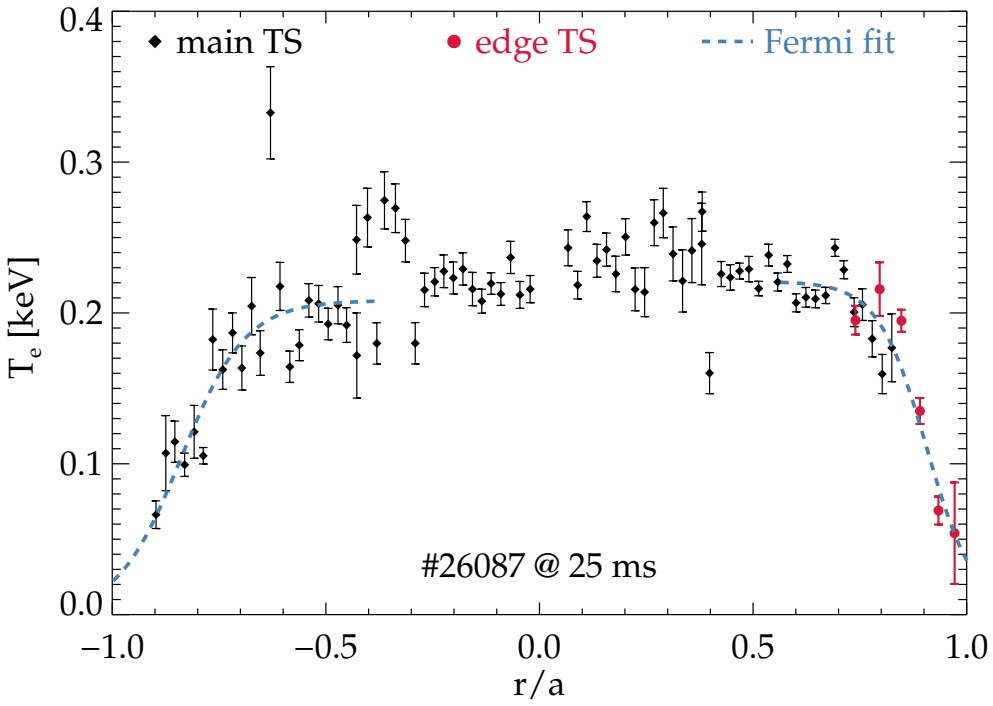

Figure 3.1: Electron temperature profile: ✦ main TS measurements, ● edge TS measurements while the dashed blue lines are the two fits performed to characterize the external region.

(3.3) it is easy to understand the meaning the Fermi function parameters assume:

$$\text{spatial extent} : \Delta \tag{3.4a}$$

$$\text{temperature drop} : \Delta T_e \tag{3.4b}$$

$$\text{average temperature} : \langle T_e \rangle = D + \Delta T_e/2 \tag{3.4c}$$

$$\text{max. gradient} : |max(\nabla T_e)| = \nabla T_e^{max} = \Delta T_e/\Delta \tag{3.4d}$$

$$\text{max. gradient position} : r_{max} = B \tag{3.4e}$$

$$\text{min. characteristic length} : min(L_{T_e}) = \frac{\langle T_e \rangle}{\nabla T_e^{max}} = \big[\Delta(D + \Delta T_e/2)\big]/\Delta T_e \tag{3.4f}$$

These quantities become immediately obvious looking at Figure 3.2b, where an example of the performed fit is given. While Δ, r_{max} and ΔT_e significance is straightforward, D does not represent any physical interesting quantity, thus it was not marked with any distinctive name. In fact, D is an offset for the Fermi function which is fundamental to a proper matching of the profile but it has no physical meaning. Furthermore, it is important to not confuse D with the electron temperature at the wall, namely $T_e(r = a)$. Considering the two profiles in Figure 3.2, the difference is clear: on the right $T_e(r = a) \sim D$ because of the steepness of the temperature decrease, while on the left $T_e(r = a) > D$. Expression (3.4f) can be further simplified

$$min(L_{T_e}) = \frac{\Delta}{2} + \frac{D}{\Delta T_e}\Delta \approx \frac{\Delta}{2}$$

being usually $D/\Delta T_e \ll 1$. As final remark, the similarity of the Fermi function to the modified tanh function would permit a direct comparison of the results obtained with the two fitting methods, thus comparing RFX-mod results with that coming from the tokamak community.

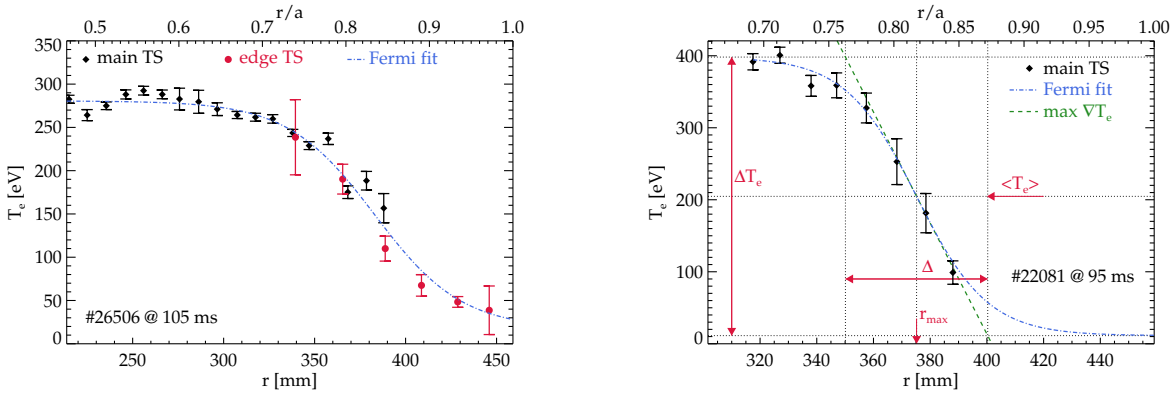

(a) (b)

Figure 3.2: Example of temperature profile characterization via the *Fermi function*. (a) Low field side: Main TS and edge TS. (b) Low field side: only main TS. Some of the fit parameters are described.

3.1.2 Limiting the parameters space

The lack of measurement points on the LFS, in absence of the edge TS, can be a source of arbitrariness in the outcomes of the procedure. In order to limit it, some assumptions were introduced. The fitting function was forced to assume a limited range of value near the wall, i.e. for $r/a > 0.95$. This was possible exploiting two different diagnostics: the Thermal Helium Beam and Langmuir probes, which measure the electron temperature respectively across $0.9 < r/a < 1$ and at $r/a = 1$. Electron temperature at the plasma edge, as measured by these diagnostics, is depicted in Figure 3.3 as a function of the normalized density

$$n/n_G \equiv \langle n_e \rangle_l / n_G \qquad \text{where} \qquad n_G[10^{20}\text{m}^{-3}] = \frac{I_p[\text{MA}]}{\pi a^2}$$

being n_G the *Greenwald density*[109]. Such a general trend was used to set a boundary condition for the temperature profile fitting function. A regression for the temperature at $T_e^{0.95}$ and T_e^1 was performed respectively on THB and Langmuir probes data. So, fitting the temperature profile, the temperature near the wall, namely at $r/a = 0.95$ and $r = a$, were forced to lie inside a standard deviation from the regressions values. In Figure 3.3 the Greenwald density fraction regressions are plotted together with the THB and Langmuir probes data. In the same graph the space available for the $T_e^{0.95}$ and T_e^1 values achieved by the Fermi fitting function is shaded. Being $T_e^{0.95}$ and T_e^1 usually non that different the slope of the fitting curve is generally quite flat in that region and the THB data was used as an upper limit and the probes data as a lower limit for both $T_e^{0.95}$ and T_e^1. An example of the accuracy of the profile matching is given in Figure 3.4. The goal of the proposed fitting method was the overall match of the temperature profile in the external region of the plasma, even if data of the edge TS were missing. Figure 3.4 gives a proof of the viability related to this method. The discrepancy between the fit and the THB for $r/a > 0.9$ is hardly perceived looking at the complete profile, the THB data are mapped with an accuracy as low as 20 eV, which is remarkable if compared with the temperature drop of the main TS data. It is important to recall that the boundary condition for the fit comes from a general scaling, being the THB measurement available only for a restrict set of discharges. A further improvement of the fitting procedure can point towards an additional term allowing the function to have a small slope outside $r_{foot} + \Delta/2$[a].

A second hypothesis was made on the spatial extent Δ of the temperature drop. A reliable matching of this drop requires at least 6 points, 4 of which should be on the gradient region. This requirement turns in a lower limit for Δ: it has to be larger than the minimum spatial interval containing 4 measurement points. The main TS measurements are approximately 10 mm apart from each other, so $\Delta \gtrsim 30$ mm. This assumption has no physical meaning so the lower limit was not strictly set. The decision to accept or reject cases which exceeded the limit was based on a probabilistic approach. Suppose that a first regression procedure led to a value

[a] *Such a discussion is left to Chapter 3.6*

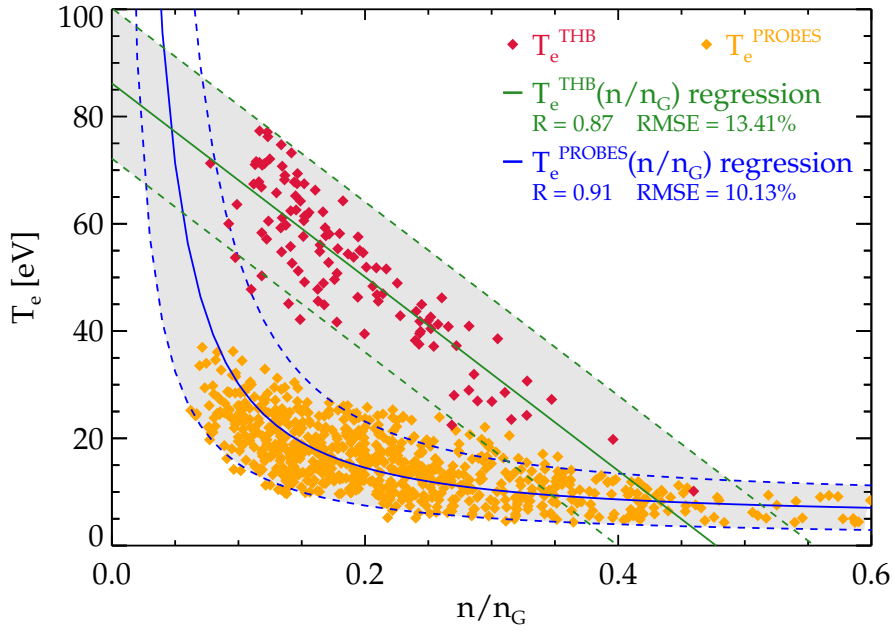

Figure 3.3: Limits to the fitting function parameters space: edge temperature. Data from THB and Langmuir probes are depicted limiting respectively $T_e^{0.95}$ and T_e^1. Green solid line represents the regression on THB, blue solid line represents the regression on probes data. The dashed lines set the limits to the achievable fit values: the regressions are shifted upward and downward by a standard deviation of the population from which they come. The gray shaded area represents the space where the achievable temperature values at $r/a = 0.95$ and $r/a = 1$ were bounded to lie.

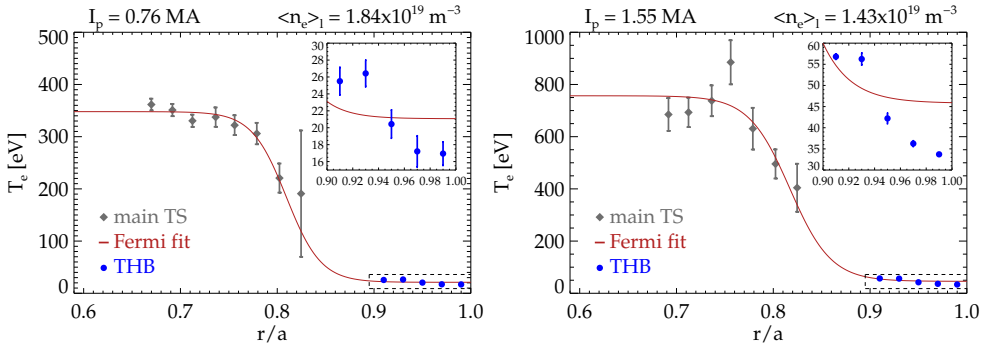

Figure 3.4: Edge mapping accuracy comparison. In each graph data from the main TS and from the THB are reported together with the Fermi fit. The small plane depicts a zoom of the edge region bounded by dashed lines in the main figure. The values of plasma current and electron density relative to the profiles are given on top of each graph. The relative Greenwald density fractions are: (a) $n/n_G = 0.135$, (b) $n/n_G = 0.123$.

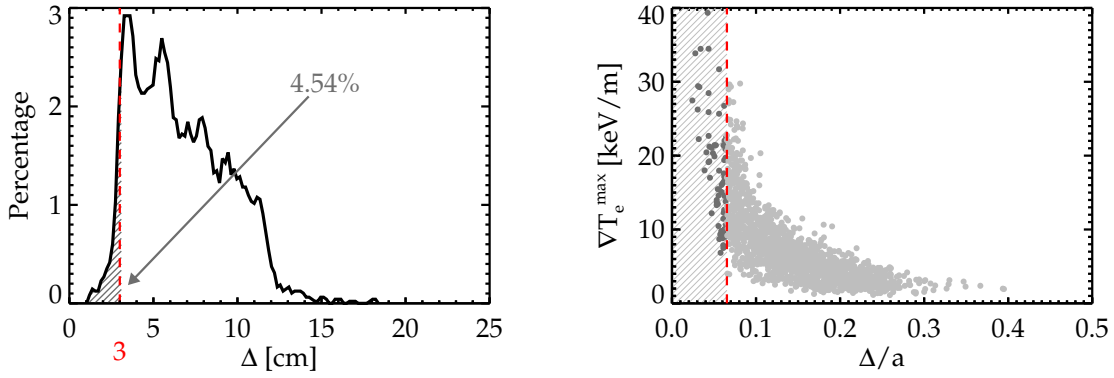

Figure 3.5: Spatial extent of temperature drop. (left panel) The probability distribution function of Δ is depicted. The 30 mm limit is highlighted. The cases exceeding the limit are colored. (right panel) The influence of Δ on the maximum gradient value as calculated in (3.4d)

of Δ lower than 30 mm, lets mark with χ^* the outcome of such regression procedure. When this happened the procedure was repeated forcing the regression to lead a new parameters set which had complies with the limit on Δ, let call χ such a new outcome. To decide which of the two outcomes one should keep, a statistical comparison based on the *F-test* technique[110] was carried out. In other words: the quality of each fit was measured, let say $Q = Q(\chi)$ and $Q^* = Q(\chi^*)$, and they was compared modifying the Q^* with a penalty coefficient, k, inversely proportional to the difference between the evaluated Δ and the limit set. The parameter set with the higher quality was kept. So, *in formulae*:

$$\left.\begin{array}{lll} \chi^* & \text{with} \quad \Delta \leq 30\,\text{mm} & \rightarrow \\ \chi & \text{with} \quad \Delta > 30\,\text{mm} & \rightarrow \end{array} \begin{array}{c} \left\{ \begin{array}{c} Q^* \\ k = k(\Delta) < 1 \end{array} \right. \\ Q \end{array} \right\} \Longrightarrow \left\{ \begin{array}{lll} \text{if} & Q > kQ^* & \text{then} \quad \chi \\ \text{if} & Q < kQ^* & \text{then} \quad \chi^* \end{array} \right.$$

Once decided which parameters set to keep, the regression, as any other did, was subject to a quality test to decide whether it had to be included in the database or not[a]. This method led to the Δ distribution function shown on the left panel of Figure 3.5. Only the 4% of the whole dataset has a Δ lower than 30 mm.

A lower limit to the spatial extent of the temperature drop turns in an upper limit to the temperature gradient. For example, if $\Delta T_e \sim 600$eV the cut-off value for ∇T_e^{max} would have been 20 keV/m. This constraint should not exclude any physics since typical gradient values reported in earlier studies[112, 86] did not exceed 15 keV/m. Focusing on the right panel of

[a] *The regression would have been included in the database only if the value of the* reduced chi-square, χ^2_ν, *was less then 0.5. This condition corresponds, for approximately 10 degrees of freedom, to a 90% probability of obtaining fits that are not better then the one under analysis[110, 111].*

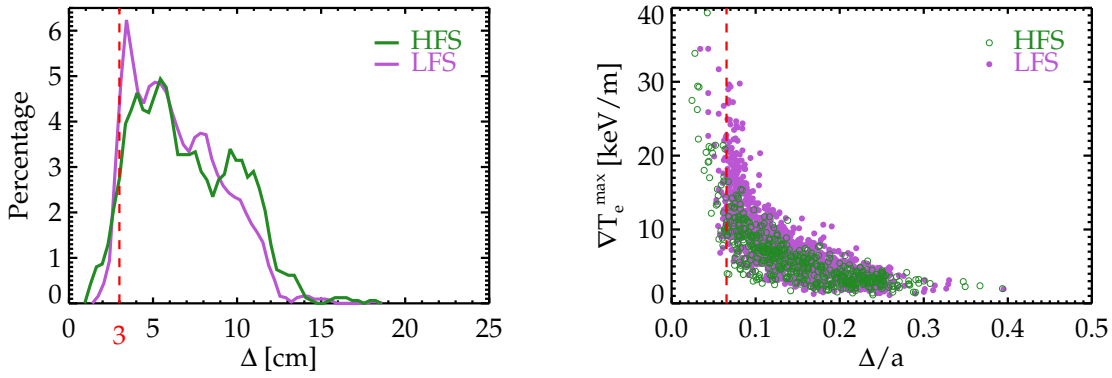

Figure 3.6: Spatial extent of temperature drop distinguished between HFS and LFS. (left panel) The probability distribution function of Δ is depicted. The 30 mm limit is highlighted. (right panel) The influence of Δ on the maximum gradient value as calculated in (3.4d)

Figure 3.5, one can notice that the cases exceeding the limit are characterized by the highest gradient values. The inverse proportionality between Δ and ∇T_e^{max} is obvious from (3.4d), but doubts can arise about its physical basis. One can speculate that the pronounced anticorrelation between the two quantities originates from an high degree of arbitrariness introduced by the applied regression method, due to the poor coverage of the main TS system on the LFS when the edge TS measurements are not available. In fact, the HFS is covered by the main TS up to $r/a \approx 0.95$. This doubt can be removed comparing the values obtained for HFS and LFS. Considering Figure 3.6, large differences can not be noticed between the HFS and LFS probability distribution function of Δ nor on ∇T_e^{max} values. The larger scatter of LFS ∇T_e^{max} values can be ascribed to the larger number of cases collected.

3.1.3 Full profile matching

Only some of the main TS profiles were fitted on both LFS and HFS, in the large amount of cases the quality test was passed by one of the sides only. For these TS profiles a complete profile match was performed. Using expressly defined functions, all kind of temperature profiles was matched. In order to get the best match, the fitting functions were built splitting the whole profile in several radial sections and then joining together the different functions. In this way an analytical description of the whole profile cannot be obtained, this is the price to be paid for a good match. As for the edge plasma region, every profile undergoes a quality test before being included in the database. The full profile match was performed in order to leave the possibility of further investigation like heat transport evaluation, pressure profile investigation and many others. Some examples of full profile matching are reported in Figure 3.7. No analytical function has still been proposed to represent DAx or SHAx states, in [106] the SHAx-like profiles were fitted using two polynomials functions, while in [113] the

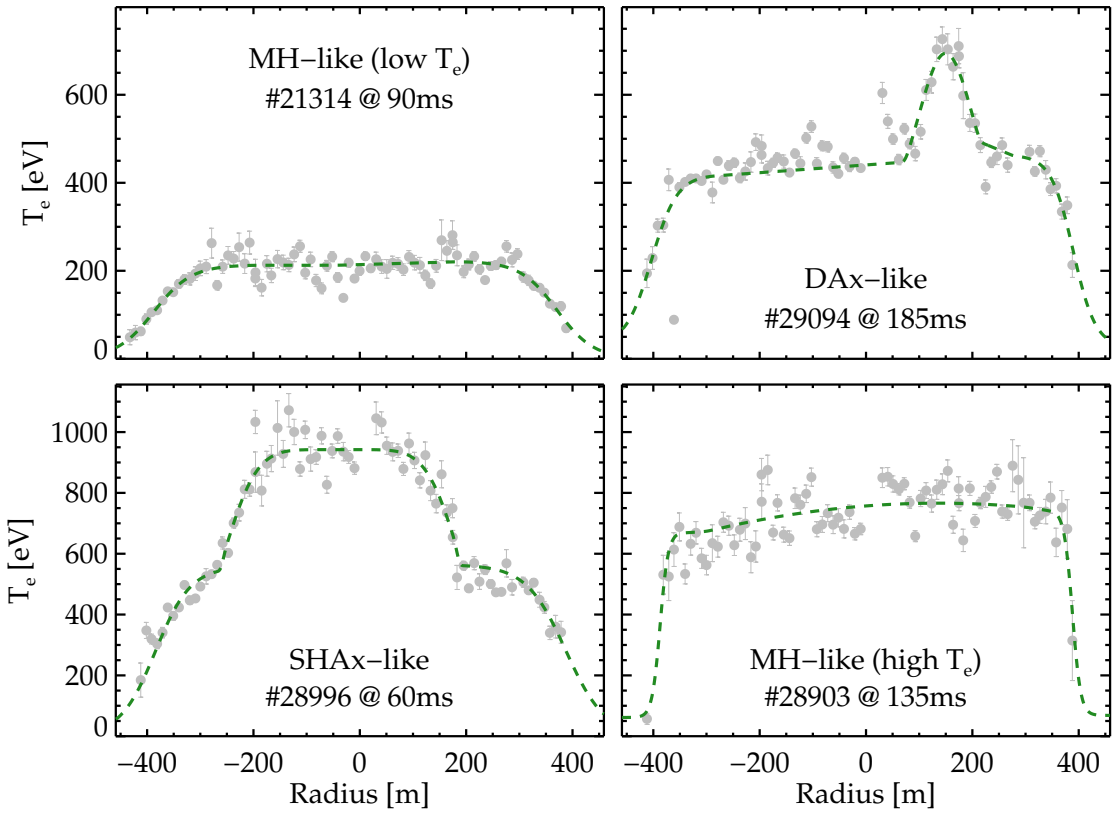

Figure 3.7: Examples of full temperature profile matching for different kind of profiles: MH, DAx and SHAx cases.

SHAx-like profiles were matched using the interpolation routine provided by the ASTRA transport code[114]. Conversely, previous study on MH states was based on analytical functions to fit the temperature profile. The choice for a non-unique analytical description was made on the basis of quality. Two analytical fitting functions was used in the past to reproduce MH-like profiles. Since most T_e profiles are typically flat in the core, a two-parameters *power law* function was firstly used:

$$\text{power law}: \qquad T_e(r) = T_e^0 \left(1 - r^\alpha\right) \tag{3.5}$$

where T_e^0 represents the core temperature and α is the global curvature parameter. After the upgrade of the main TS diagnostic, a more accurate four-parameter fit was provided. This is capable to resolve the plasma column width $(a - \delta)$ and position ϵ:

$$\text{modified power law}: \qquad T_e(r) = T_e^0 \left[1 - \left|\frac{r - \epsilon}{a - \delta}\right|^\alpha\right] \tag{3.6}$$

where a is the chamber minor radius[19]. Even if these analytical functions are straightforward they were not suitable for the purpose of investigating the external region of

the plasma. Figure 3.8 depicts the comparison between these functions and the match performed starting from Fermi functions. The quality of the external region match is hardly comparable.

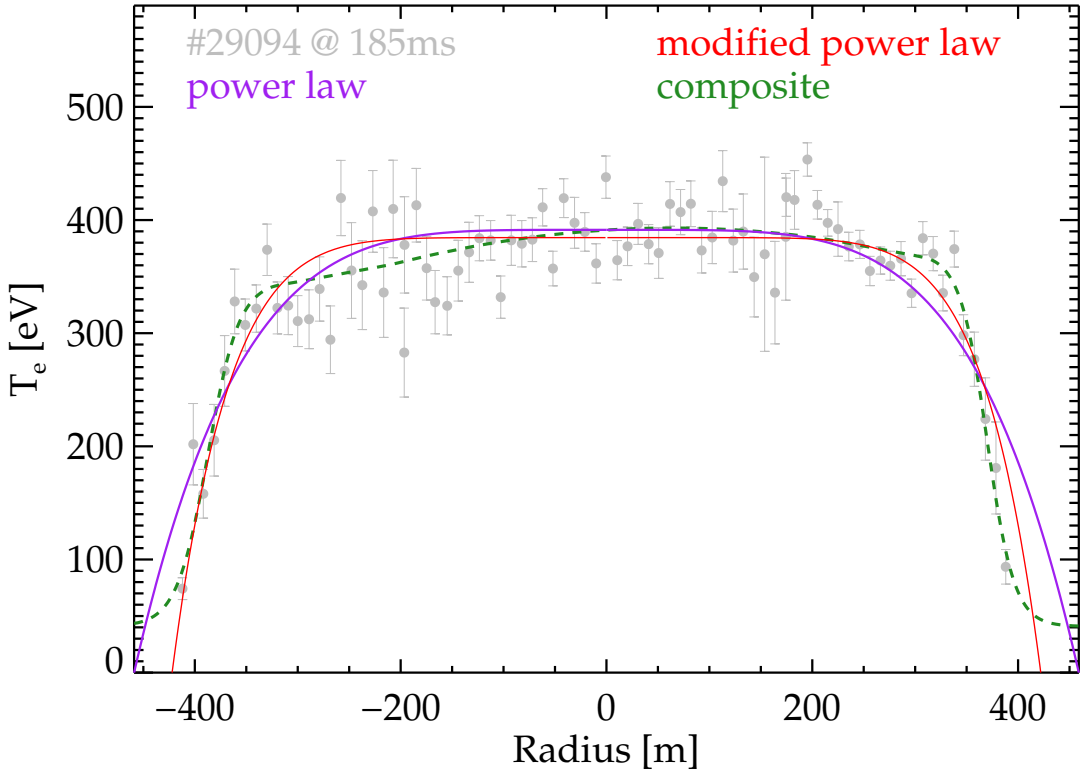

Figure 3.8: Comparison between different full T_e profile matching methods.

3.2 Experimental procedure and preliminary analysis

A series of test and confirmation of the characterization method was performed before the actual analysis. In this Section such verifications are presented together with the database selection.

3.2.1 Database

To evaluate scaling laws in the widest possible way, the largest available database of validated measurements was chosen. The database contains nearly 1000 temperature profiles taken from 626 hydrogen discharges, performed between September 2006 and October 2010. In [107] the beneficial effect of the improved feedback control system was reported, so only discharges performed with the *Clean Mode Control* scheme[89] have been taken into account. All the considered temperature profiles were obtained using the main TS diagnostic, where possible the edge TS was also included. Every TS profile is treated as an independent measurement and all the associated time resolved plasma measurements were averaged over 4 ms around the TS firing time, approximately twice the RFX-mod energy confinement time[107]. To select only almost stationary conditions, a constraint was set on the amplitude of the time derivative of plasma current I_p, reversal parameter F and line average density $\langle n_e \rangle_l$. Plasma current and reversal parameter are two of the main knobs to control the MHD equilibrium, so an abrupt change in one of the two is a clear mark of non stationary conditions. In particular, the constraint on the plasma current limits the range of acceptable TS measurements to those occurring in the current flat top phase. The constraint on the F derivative, instead, avoid the so called Dynamo Relaxation Events (DRE)[102] to be included in the database. The density fluctuations constraint was set in order to minimize the possibility of polluting the database with measurements performed during transient density increase, like pellet injection or strong and localized Plasma-Wall Interaction. In Figure 3.9a the whole database is shown on the $\left(I_p\,,\,\langle n_e \rangle_l\right)$ plane. The wide plasma current range explored, 400 kA $< I_p <$ 2 MA, is a unique feature of RFX-mod experiment. Despite the wide scan in density, no discharges above one half of the *Greenwald density* are present in the database. This is due to the high hydrogen adsorbing capabilities of the graphite first wall which prevents the easy control of plasma density. In fact, the density value is mainly due to hydrogen wall inventory and to the amount of power impinging on the wall [84, 94]. For this reason performing density scans is not an easy task in RFX-mod and they are usually done by progressively loading the wall after a He glow discharge cleaning[84]. Moreover discharges with $n/n_G \gtrsim 0.35$ have to be treated carefully, at those Greenwald density fractions a transition from a high-confinement to a low-confinement state can be triggered[91], recall Section 2.3.2. This transition is associated to the onset of toroidal inhomogeneities and unbalanced flows in the plasma edge due to a sharp increase in $m = 0$ modes amplitude. This results in a strong modification of the topology of the ambipolar radial electric field, due by the dynamical trap effect caused by the $m = 0$

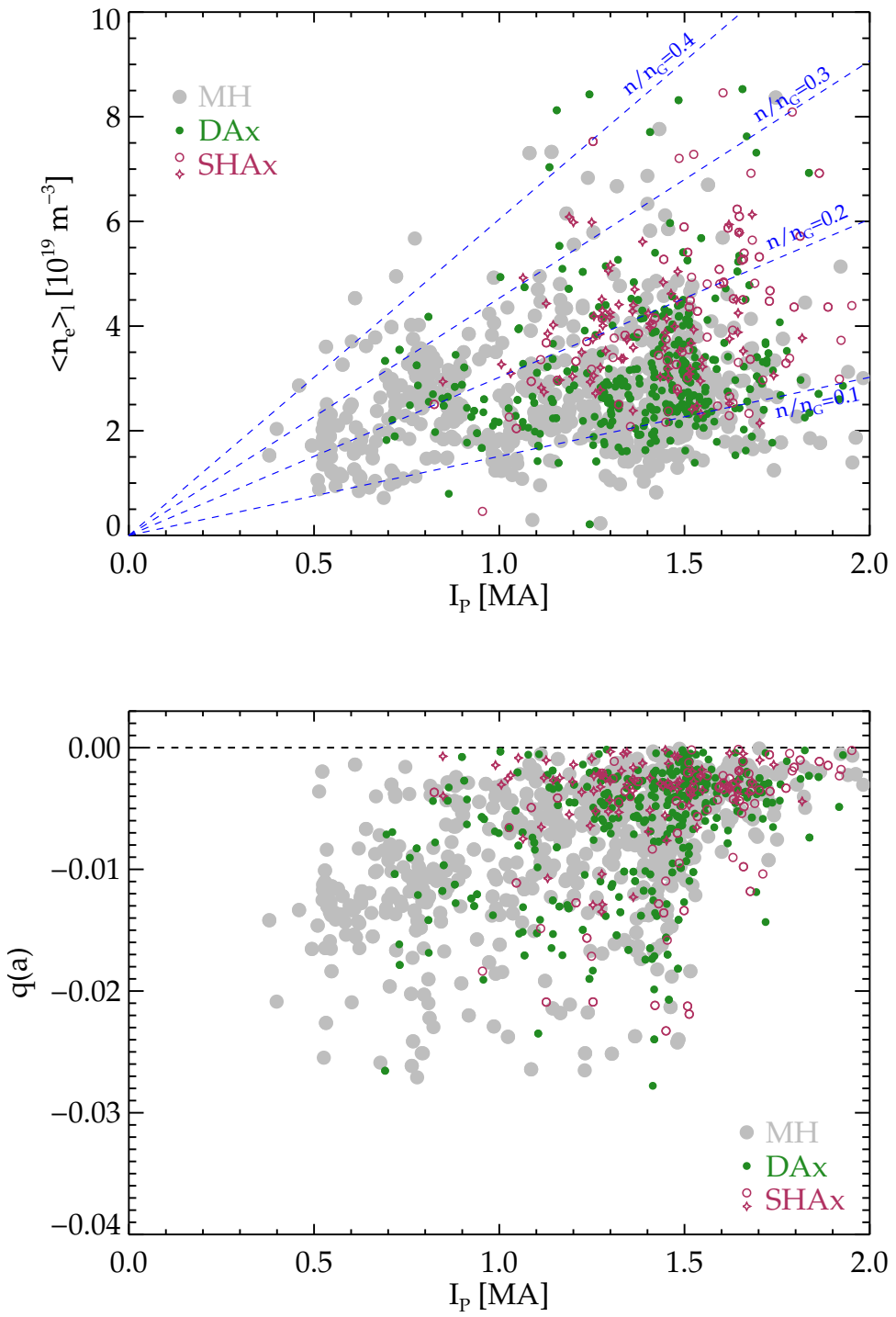

Figure 3.9: Operational range. The whole dataset reported in the $(I_p, \langle n_e \rangle_l)$ plane (upper panel) and in the $(I_p, q(a))$ plane (lower panel). Different discharges are distinguished according to the shape of the temperature profile: MH-like, DAx-like and SHAx-like.

X-point on the electrons motion, with a consequent modification of the transport at the edge of the plasma[91]. These physical mechanisms cause a localized accumulation of density at the plasma edge with a consequent decrease of temperature through radiative cooling which finally results in a soft landing of the plasma current. For this reason, in RFX-mod, it is hard to obtain long lasting flat top phases with $n/n_G \gtrsim 0.35$. None of this discharges are included in the database because of their implicit non stationary nature.
In Figure 3.9b the explored range in edge safety factor $q(a)$ is reported versus plasma current. As can be seen, the operational space is not fully covered: high current operations are performed only at the lower values of $|q(a)|$, usually known as *shallow F* operations. The narrow $q(a)$ range is related to operational choice due to the better control of the plasma-wall interaction (PWI) obtained at low $|q(a)|$. The better control of the PWI can be related to different reasons. Firstly $m = 0$ modes are the major responsible for PWI and they are naturally mitigated driving the reversal surface to the edge. Moreover, SHAx states are favored at shallow F[100]. Going towards smaller values of $|q(a)|$, the *reversal surface*, where all the $m = 0$ modes resonates, gets closer to the wall. Provided that the $|q(a)|$ is small enough, the $m = 0$ magnetic islands formed on the reversal surface directly intercept the first wall. In this case the Last Closed Flux Surface is not touching the first wall any more inducing a milder PWI[83], as described in Chapter 2.

3.2.2 Temperature profile distinction

In Figure 3.9 different symbols and colors represent the three different characteristic temperature profiles of MH and QSH states reported in Figure 2.8. Throughout the entire analysis the following convention will be used:

MH-like profile (blue profile in Figure 2.8) will be marked by full gray dots (●);

DAx-like profile (green profile in Figure 2.8) will be marked by full green dots (●);

SHAx-like profile (red profile in Figure 2.8) will be marked by magenta empty dots and stars (○✧);

SHAx-like profiles has been further distinguished in two different cases. This is due to the different analysis method used to treat the measurements: circles mark measurements analyzed using the fitting method explained in 3.1, while stars represent profiles fully fitted according to the method that will be explained in Section 4.1. Thus, there are TS profiles considered in both of the analysis scheme, but generally this is not the case. The two methods are different because they focus on different issues. In particular, TS measurements marked with circles are particularly well diagnosed in the plasma external region so to allow a univocal output to the characterization method explained in 3.1. Conversely, TS measurements marked by stars are characterized by a net profile shape, this request will become more clear in Section 4.1. The discrimination between the three cases has been done visually, in order to emphasize the qualitative differences between MH, DAx and SHAx. In

this way the three plasma states are distinguished discriminating between their thermal characteristics, i.e. the T_e profile. The complementary way to distinguish MH from QSH states is based on the evaluation of the magnetic characteristics of the discharge. Formally, this is done evaluating the *spectral width*[75] N_S:

$$N_S = \left[\sum \left(W_{n,\varphi} / \sum W_{n,\varphi}\right)^2\right]^{-1} \quad . \tag{3.7}$$

In the previous $W_{n,\varphi}$ is the magnetic energy pertaining to the toroidal component of the $(1,n)$ MHD mode and so N_S represents the number of significant modes in the MHD spectrum[a]. $N_S = 3$ has been chosen as a threshold for the transition from MH to DAx state[115]. The further transition from DAx to SHAx, due to the separatrix expulsion, occurs when the amplitude of the dominant mode exceeds the threshold of $\sim 4\%$ of the total magnetic field at the edge[79]. Even if the different magnetic states are associated to the different characteristic temperature profiles, the link between the magnetic states and their thermal footprint is not strictly verified. In fact, at very high current and in QSH magnetic state with $N_S < 3$, MH-like temperature profiles can still be found. The reason for this behavior is still not clear, recent

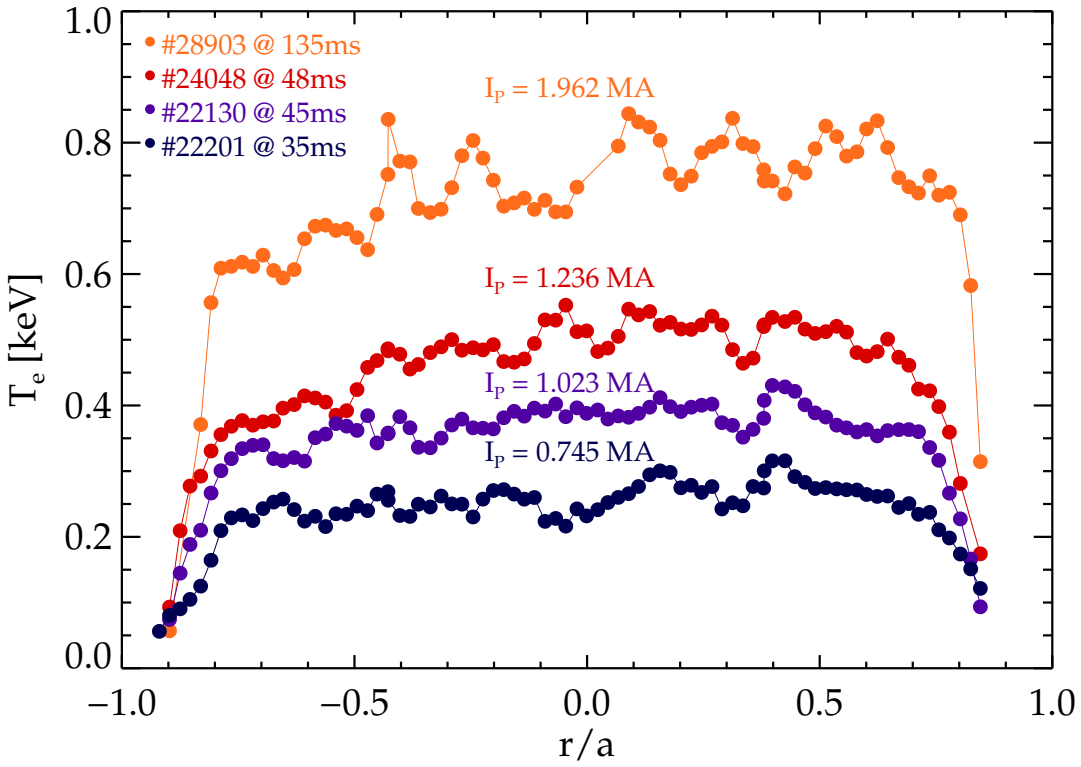

Figure 3.10: MH-like temperature profiles at four different plasma current values. Increasing the current the whole profile swells up.

[a] *For a pure single mode perturbation N_S would be equal to 1.*

works relate this behavior to the strong dithering between the Single Helical Axes phases or to their occasional short duration[116].As a consequence, plasma shots with similar N_S can display different temperature profile shapes. An increase in the plasma current can thus lead to two different situations: a change in the magnetic state followed by a consequent change in the shape of the electron temperature profile or to a swelling up of an MH-like profile, as shown in Figure 3.10. In order to emphasize the characteristics of the different temperature profile shapes, rather than the magnetic properties of the plasma, a visual distinction was applied. Every single TS measurement was visually inspected and assigned to one of three categories: MH-like, DAx-like or SHAx-like. The profiles were labeled with MH-like, etc. instead of simply MH, etc. in order to highlight the distinction method based on visual similarity rather than on magnetic measurements. Such a distinction between profiles did not heal the discrepancy between the magnetic states and their thermal footprint. This ambiguity is immediately clear considering the left panel of Figure 3.11. In [79], to show that SHAx-like temperature profiles appeared when the amplitude of the dominant mode exceeded the 4% threshold was used a plot similar to the left panel of Figure 3.11. It is clear that for the database under analysis this picture does not hold, SHAx-like profiles are found at values of $b_{\phi}^{1,-7}/B_{\theta}(a)$ sensibly lower than 4%. This was explained in [116], where exploiting the high time resolution of Soft X-Rays diagnostic[117] it was possible to show that high internal gradients start to develop already in the growing phase of the dominant mode. Moreover, in Figure 3.11, MH-like and DAx-like profiles are found near the threshold. Again, this was elucidated in [116]: during the stationary phase of the dominant mode, back transitions to flat or low gradient profiles are usually found to occur. To conclude, it is worth to point out that

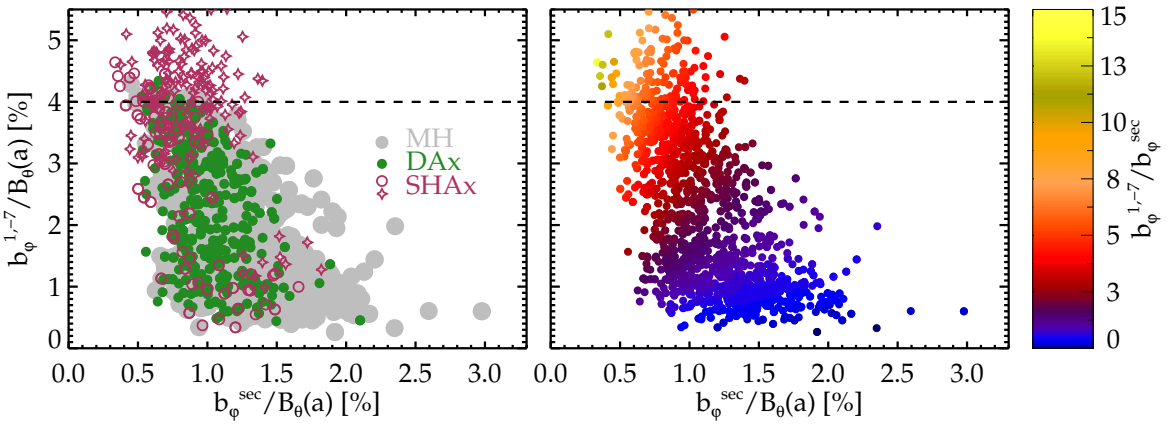

Figure 3.11: The amplitude of the dominant mode $b_{\varphi}^{1,-7}$, versus the total amplitude of secondary modes b_{φ}^{sec} both normalized to the magnetic field at the edge, for the complete dataset. The horizontal dashed line highlights the threshold, mentioned in [79], the dominant mode amplitude have to exceed it in order to obtain a SHAx. (left panel) The complete dataset is reported and divided according to the three different temperature profile shapes. (right panel) In the color scale the ratio between the amplitude of the dominant and secondary modes is reported.

Figure 3.10 represents one of the main reasons that triggered this thesis work: the occasional appearance of extremely high gradients developing in the external plasma region linked to MH-like temperature profiles[159]. Central temperature values, close to 1 keV, extending all the way to $r/a \sim 0.8$, with a consequent steep decrease towards the edge, directly reminds the pedestals of temperature associated to important improvements in Tokamak and Stellarators confinement performances (H-mode)[44, 118]. These particular MH plasma states, without the thermal footprint distinctive of the good magnetic configuration typical of the QSH states, represent a better confined plasma. The next chapter will be dedicated to these distinctive cases.

3.2.3 Peculiar cases discrimination

As mentioned before, the entire database contains peculiar cases with extremely high external gradients ($r/a \sim 0.8$) which will be treated separately. The selection was made considering as working hypothesis the almost linear increase of the edge temperature gradient with plasma current reported in [86]. In Figure 3.12 the *maximum external temperature gradient* ∇T_e^{max} is plotted versus the plasma current for the selected set of data[a]. The data are fitted with a power law regression:

$$\begin{gathered} \boldsymbol{\nabla T_e^{max}(I_p) = \alpha\, {I_p}^{\gamma_{I_p}}} \\ \begin{cases} \boldsymbol{\alpha} &= (2.23 \cdot \pm 1.32) \cdot 10^{-7} \quad (59.4\%) \\ \boldsymbol{\gamma_{I_p}} &= \quad 1.22 \pm 0.04 \quad\quad (3.46\%) \end{cases} \\ RMSE = 59.67\% \quad R = 0.39 \end{gathered} \tag{3.8}$$

and the fit is shown in the same figure. Each parameter of the fit is reported with its absolute and percentage uncertainties as given by the fitting routine. To evaluate the quality of the fitting function two parameters were chosen: the *percent root mean square error* $RMSE$, i.e. the square root of the quadratic sum of the residuals normalized by the average of the population[b], and the *correlation coefficient* R which measures the degree of linear correlation between the population and the fitting function. This symbology will be used throughout the entire discussion. Despite the poor quality of the modeling function, as proved by the high $RMSE$ value and the relatively low correlation coefficient, we consider this model as a good representation of the population. It is clear that the poor quality of the model is partially due to the points exceeding 20 keV/m, which correspond to the peculiar cases that have to be excluded. To choose which points to expunge from the database, treating them as particular cases with extremely high edge temperature gradient, a method similar to the *outliers detection*[119] was applied. Given a modeling function $y(x) = \alpha x^{\gamma}$, we can define as *distance*,

[a] *Remember that ∇T_e^{max} is the maximum value achieved by the electron temperature gradient in the region $0.7 < r/a < 0.9$, evaluated as explained in 3.1.*

[b] *In formulae: given a population (x_i, y_i) and a fitting function f then $RMSE = \sqrt{\sum_i \left(f(x_i) - y_i\right)^2} / \sum_i y_i$*

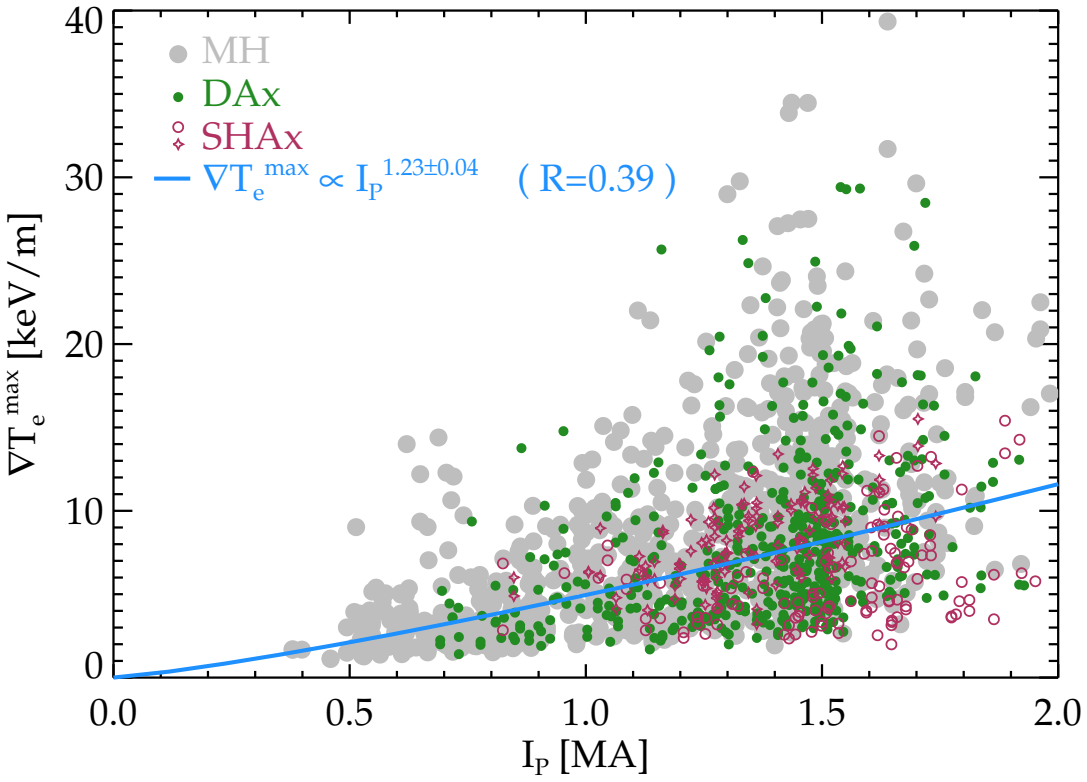

Figure 3.12: Maximum external gradient versus plasma current. The database is divided according to the three different temperature profile shapes. The scaling law (3.8) is depicted.

between two different experimental realizations (x_1, y_1) and (x_2, y_2), the difference

$$\Delta_\gamma^{1,2} = \gamma_1 - \gamma_2$$

where γ_1 and γ_2 are the values of γ obtained maintaining fixed the value of α and matching γ so to let the modeling function pass exactly through the points y_1 and y_2, *in formulae*:

$$\text{imposing} \quad \begin{cases} y_1 = \alpha x_1^{\gamma_1} \\ y_2 = \alpha x_2^{\gamma_2} \end{cases} \quad \Longrightarrow \quad \begin{cases} \gamma_1 = \dfrac{\log(y_1/\alpha)}{\log x_1} \\ \gamma_2 = \dfrac{\log(y_2/\alpha)}{\log x_2} \end{cases} .$$

In this way we can define a *distance* Δ_γ^i between each experimental realization (x_i, y_i) and the modeling function $\tilde{y}(x) = \tilde{\alpha} x^{\tilde{\gamma}}$ obtained from a regression on the entire database, namely the function (3.8). The expression for Δ_γ^i follows directly from the previous:

$$\Delta_\gamma = \Delta_\gamma^i = \tilde{\gamma} - \gamma_i = \tilde{\gamma} - \frac{\log(y_i/\tilde{\alpha})}{\log x_i} .$$

Dropping for simplicity the index i, Δ_γ can now be used to discriminate between cases. The definition of *peculiar case* is completely arbitrary, here a threshold was fixed on the Δ_γ distribution function. Those profiles laying outside the 95% of this distribution were identified as peculiar ones. These were dismissed from the entire database and will be treated separately in a dedicated section in the next chapter.
The regression (3.8) was repeated on the restricted database as a first check on this selection method:

$$\begin{gathered} \boldsymbol{\nabla T_e^{max}\left(I_p\right) = \alpha\, {I_p}^{\gamma_{I_p}}} \\ \begin{cases} \boldsymbol{\alpha} &= (1.58 \pm 0.85) \cdot 10^{-7} \quad (53.9\%) \\ \boldsymbol{\gamma_{I_p}} &= \quad 1.24 \pm 0.04 \qquad (3.08\%) \end{cases} \\ RMSE = 48.12\% \quad R = 0.50 \end{gathered} \tag{3.9}$$

The maximum external gradient scales almost linearly with plasma current, moreover this single scaling is suitable to describe all the three classes of temperature profiles: MH-like, DAx-like and SHAx-like. Far from being a conclusive model to represent the population of data, the overall quality of the regression is increased after the selection. In fact, excluding the highest gradients, $RMSE$ decreased by approximately 20% and the correlation of the data with the proposed model is now quite significant. In contrast, the power of the scaling law results almost unchanged giving a first clue on the strong influence of plasma current on the determination of external temperature gradients. It is worth mentioning that the selection method excluded only MH-like and DAx-like profiles from the complete dataset. This lack of high edge gradient values for SHAx-like profiles leads to the idea of a mutual exclusion between the two phenomena, as already proposed. Increasing the plasma current one of the two: either the temperature profiles undergoes a shape change, from an MH-like to a SHAx-like profile, or it swells up with an increase of the edge gradient.
Concluding, in the definition of Δ_γ, $\tilde{\alpha}$ was implicitly assumed to be constant. This assumption does not change the physics of the problem being $\tilde{\alpha}$ only a normalization coefficient.

3.2.4 Testing the database: central temperature scaling

In order to test whether the collected database was accurately representing RFX-mod performance, a direct comparison with expression (3.1) was performed. So the central temperature dependence on plasma current, density and secondary modes was investigated. It is worth mentioning that T_e^0 was evaluated differently from [107]: for MH-like and DAx-like profiles the central temperature was evaluated as an average on the 10 central main TS lines of sight, covering approximately 10 cm. A check was performed for DAx profiles, in order to avoid points on the developing thermal structure. For SHAx profiles T_e^0 represents the maximum temperature at the top of the central structure, which accurately match the flat

plateau inside the internal transport barrier. The regression results

$$\boldsymbol{T_e^0\left(I_p,\langle n_e\rangle_l,b_\varphi^{sec}\right)=\alpha\, I_p{}^{\gamma_{I_p}}\langle n_e\rangle_l^{\gamma_{n_e}}\left(b_\varphi^{sec}\right)^{\gamma_{sec}}}$$

$$\begin{cases} \boldsymbol{\alpha} &= (4.57\pm1.97)\cdot10^{-6} \quad (43.03\%) \\ \boldsymbol{\gamma_{I_p}} &= 1.199\pm0.021 \quad (1.74\%) \\ \boldsymbol{\gamma_{n_e}} &= -0.178\pm0.010 \quad (5.52\%) \\ \boldsymbol{\gamma_{sec}} &= -0.400\pm0.013 \quad (3.34\%) \end{cases} \tag{3.10}$$

$$RMSE = 16.19\% \quad R = 0.86$$

The multi-parameter scaling (3.1) and (3.10) are comparable: secondary modes influence results stronger while density dependence is weaker in this case. The discrepancy on γ_{n_e} can be ascribed to the different density range characterizing the two databases. In the case under analysis, as already pointed out, density is limited to values lower than $n/n_G \sim 0.35$ while in [107] discharges with n/n_G up to 0.8 were included. The larger values of density can strongly affect the scaling, in particular in the low current region. Thus, we should remind that the influence of density on temperature can be underestimated in the present work. The stronger power of secondary modes can be attributed to the larger current range: to higher current corresponds a higher possibility to get into QSH states, thus to lower levels of secondary modes. The expected negative sign of γ_{sec} states the favorable effect of a reduced magnetic chaos.

A further improvement of the regression was proposed in [107] where the ratio between the amplitude of the dominant and the secondary modes was shown to affect T_e^0. The good quality of the regression discouraged the author from including any other parameter into the $T_e^0\left(I_p,\langle n_e\rangle,b_\varphi^{sec}\right)$ model. In that work, where no *a priori* assumption was made on temperature profiles, this ratio was the only way to convey the information about the appearance of the core temperature structure typical of the SHAx states. In this case, the different profiles was detected as different from the beginning. The highest values of T_e^0 pertain to the SHAx-like cases and are generally found in the range of low normalized amplitude of secondary modes being favored by large amplitudes of the dominant mode (Figure 3.11). Thus the normalized amplitude of the dominant mode, $\tilde{b}_\varphi^{1,-7}$, was also included in the regression. In order to equally weight secondary modes and dominant mode contribution both of them were normalized to the total edge magnetic field

$$B_\theta(a) = \frac{\mu_0 I_p}{2\pi a} \quad .$$

Thus in the new model

$$\tilde{b}_\varphi^{sec} = b_\varphi^{sec}/B_\theta(a) \qquad \text{and} \qquad \tilde{b}_\varphi^{1,-7} = b_\varphi^{1,-7}/B_\theta(a)$$

has been considered. With the new parameters the scaling results:

$$\boldsymbol{T_e^0}\left(\boldsymbol{I_p},\langle \boldsymbol{n_e}\rangle,\tilde{\boldsymbol{b}}_{\boldsymbol{\varphi}}^{\boldsymbol{sec}},\tilde{\boldsymbol{b}}_{\boldsymbol{\varphi}}^{\boldsymbol{1,-7}}\right) = \boldsymbol{\alpha}\,\boldsymbol{I_p}^{\gamma_{I_p}}\,\langle \boldsymbol{n_e}\rangle^{\gamma_{n_e}}\left(\tilde{\boldsymbol{b}}_{\boldsymbol{\varphi}}^{\boldsymbol{sec}}\right)^{\gamma_{sec}}\left(\tilde{\boldsymbol{b}}_{\boldsymbol{\varphi}}^{\boldsymbol{1,-7}}\right)^{\gamma_{1,-7}}$$

$$\begin{cases} \boldsymbol{\alpha} &= (5.53\pm 1.61)\cdot 10^{-3} \quad (29.14\%) \\ \boldsymbol{\gamma_{I_p}} &= 0.772\pm 0.020 \quad (2.64\%) \\ \boldsymbol{\gamma_{n_e}} &= -0.171\pm 0.010 \quad (5.74\%) \\ \boldsymbol{\gamma_{sec}} &= -0.279\pm 0.016 \quad (5.77\%) \\ \boldsymbol{\gamma_{1,-7}} &= 0.112\pm 0.008 \quad (7.11\%) \end{cases} \tag{3.11}$$

$$RMSE = 15.2\% \quad R = 0.88$$

Both $RMSE$ and R do not show significant improvement of the fit quality, but the addition of the new parameter permits to clarify the physical situation. As one could expect $\gamma_{1,-7}$ is positive, e.g. a higher amplitude of the dominant mode corresponds to a higher central temperature. This link is not strictly verified for all of the considered cases, but it certainly marks out the highest central temperature of the SHAx-like profiles. Adding $\tilde{b}_\varphi^{1,-7}$ both the powers of current and secondary modes decrease in absolute value. This can be seen as a sort of camouflage with I_p and $\tilde{b}_\varphi^{sec}$ taking some part of the role played by the missing parameter $\tilde{b}_\varphi^{1,-7}$: generally a higher $\tilde{b}_\varphi^{1,-7}$ is obtained increasing the plasma current and is linked to a lower amplitude of the secondary modes. Moreover, the reduction of γ_{I_p} can be also due to the fact that to a higher value of the current corresponds a higher total magnetic field, thus generally higher secondary and dominant mode amplitudes. On the contrary, the normalized amplitudes $\tilde{b}_\varphi^{sec}$, $\tilde{b}_\varphi^{1,-7}$ behave differently: while the former is found to decrease the latter increases, the situation is depicted in Figure 3.13.

The model (3.11) states that the more incisive method to increase the central temperature is to increase the plasma current. Being RFX-mod heated by ohmic means only, an increase of the current implies a lager plasma heating with a consequent increase of the temperature. Nevertheless the importance of an improvement of the magnetic state is evident: considering only the dependence on current, (3.11) foresees the need of ~ 4 MA to increase the central temperature by 1 keV. In fact, the low correlation of the central temperature with the amplitude of the dominant mode does not exclude the advantage of the QSH states over the MH states. In general, both in MH and in QSH states secondary modes, resonating through a large part of the plasma section directly affect the core temperature. The innermost mode, although acting directly in a small portion of the plasma section, can be effective in contributing to the dynamo action, lowering the requirement on the amplitude of secondary modes. In other words, γ_{sec} and $\gamma_{1,-7}$ confirm that QSH magnetic states can be seen as a way to sustain an RFP configuration with a low amplitude of the secondary modes (other ways to reduce the amplitude of secondary modes are, for example, replacing the dynamo action by inductive or RF current drive, using a closer fitting shell or realizing a better feedback correction of the edge radial field)[107]. Moreover, under many operational conditions in a

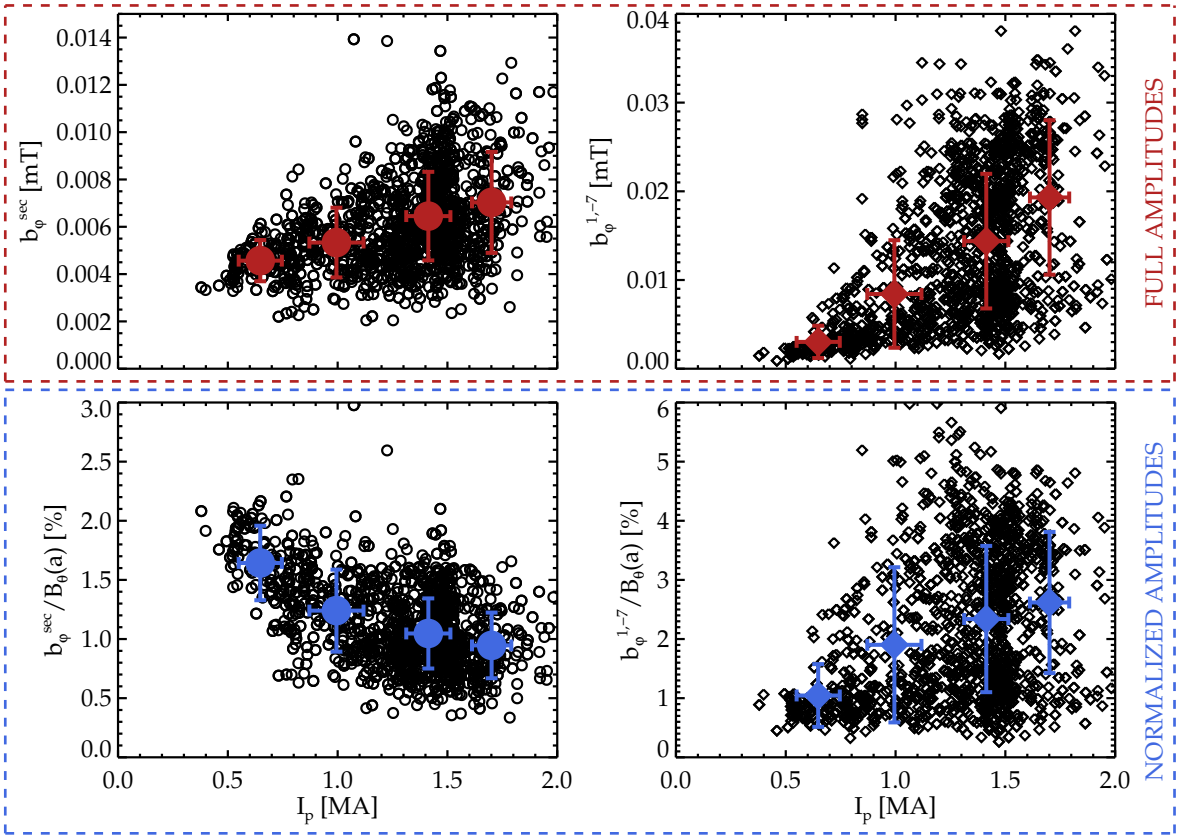

Figure 3.13: Secondary and dominant MHD modes amplitude as a function of the plasma current. In first row the full amplitudes b_φ^{sec}, $b_\varphi^{1,-7}$ are shown. In the second row the same amplitudes normalized to the total edge magnetic field $B_\theta(a)$ are depicted.

large part of the plasma cross section the particles and energy transport are dominated by parallel transport in a stochastic magnetic field[88]. Thus, the negative correlation between the central temperature and the normalized amplitude of the secondary modes states the favorable effect of a reduced chaotic transport related to the secondary modes reduction.
A dedicated consideration deserves the effect of density. As a matter of fact, the density influence on the core temperature seems to be marginal. The low negative power, γ_{n_e}, states that a larger density leads to a lower central temperature. This low correlation can be explained with the limited density range explored during RFX-mod operation. As can be seen in the upper panel of Figure 3.9, $\langle n_e \rangle_l$ values lager than $5 \cdot 10^{19}$ m^{-3} are rarely obtained. The limited and scarcely controlled density source, i.e. the material wall, hinders the possibility of easily reach higher values. Moreover the density profiles are usually flat or eventually hollow at RFX-mod, so an increase in $\langle n_e \rangle_l$ can not be directly linked to a similar increase in the core density.

3.3 EMPIRICAL SCALINGS FOR THE EXTERNAL REGION

The work presented in [107] and the former scalings outline the behavior of the central core region disregarding what happens to the whole temperature profile. While the plasma core region and the plasma edge, $r/a > 0.95$, are well diagnosed and extensively investigated there is a lack of information about the remaining region, namely $0.6 \lesssim |r/a| \lesssim 0.9$. Using the *Fermi fit*, introduced in Section 3.1, a map of the temperature profile in that region can be drawn.
In tokamaks the pedestal region is usually described using a simplified picture:

$$T_e^{ped} \sim T_e^{sep} + \nabla T_e \cdot \Delta$$

where T_e^{ped} is the temperature at the top of the pedestal, T_e^{sep} is the temperature at the saparatrix, i.e. at the bottom of the pedestal, Δ is the spatial extent of the pedestal region and ∇T_e is the average gradient forming across this region. This description is useful because of the different physics phenomena governing each parameter. T_e^{sep} deals with the scrape-off layer physics, and in particular with the heat conduction along the field lines to the divertor plates. ∇T_e is governed by the instabilities growing approximately at the separatrix (Edge Localized Modes) and their stability limits. Conversely, the width of the pedestal region, Δ, is still an open issue and no outstanding comprehension of the physical phenomena affecting it is nowadays available. Such a paradigm can not be literally applied to the RFX-mod situation. Recalling the description of RFX-mod edge made in Section 2.3.1, nothing similar to a separatrix usually exist. The well confined plasma is not neatly separated from the open field line region. As a consequence the fixed physical limit imposed by the LCFS is usually not defined, and a parameter similar to T_e^{sep} can not be defined in most of the cases under analysis. Nevertheless, an effective scrape-off layer can form when the LCFS is well separated from the wall by the $m = 0$ islands chain[83]. Such a situation occurs only when a helical equilibrium is well established at low values of the reversal parameter. In this specific case a grounded parallel can be drawn between the two systems. Exploiting the similarity between the *Fermi fit* and the *modified tanh fit* the external temperature decrease in RFX-mod can be characterized using three quantities:

- $\boldsymbol{\Delta}$: the spatial extent of the temperature decrease, as obtained in (3.4a)
- $\boldsymbol{T_e^{rev}}$: representing the temperature at the reversal surface
- $\boldsymbol{\nabla T_e^{max}}$: the maximum of the temperature gradient occurring in the temperature decrease region, as obtained in (3.4d)

Δ and ∇T_e^{max} intuitively maintain similar significance of the tokamak case while T_e^{rev} somehow replaces T_e^{sep}. This link can be understood considering the change in the edge transport induced by the presence of $m = 0$ islands. Inside each island no heat source term exist and the short-circuited radial transport induces a flattening of the temperature profile[86]. Thus T_e^{rev} represents not only the temperature at the reversal surface but also the

flat temperature inside the $m = 0$ islands. Considering that the LCFS is located just inside the convolution of the islands chain, the temperature at the LCFS can be identified with T_e^{rev}. Such cases are interesting and deserve a particular attention, they will be discussed later on in Section 3.5.1.

The picture just drawn clearly does not hold if the LCFS is not separated from the wall by the $m = 0$ islands chain, namely the situation occurring for the large part of the discharges contained in the database, and in particular for low current discharges operated at $F \lesssim -0.1$ and for discharges where the Greenwald fraction exceeds 0.35. In order to analyze the largest possible number of discharges still maintaining the intuitive character of the analysis, T_e^{rev} has been replaced with a more statistical parameter: $\boldsymbol{T_e^{foot}}$ which represents the temperature at the bottom of the temperature decrease, namely $T_e(r = r_{max} + \Delta/2)$. Such parameter is not linked to the specific geometry of the equilibrium and does not have any particular physical meaning. Nevertheless T_e^{foot} somehow tracks what occurs outside the main temperature decrease, thus is useful to highlight the possible relationship between the physics governing the plasma edge, $r/a \geq 0.95$, and what happens in the region $0.6 < r/a < 0.9$, investigated via Δ and ∇T_e^{max}. These three quantities are shown in Figure 3.14. In the next sections the influence of machine parameters on these three quantities will be addressed and the physics governing them will be investigated.

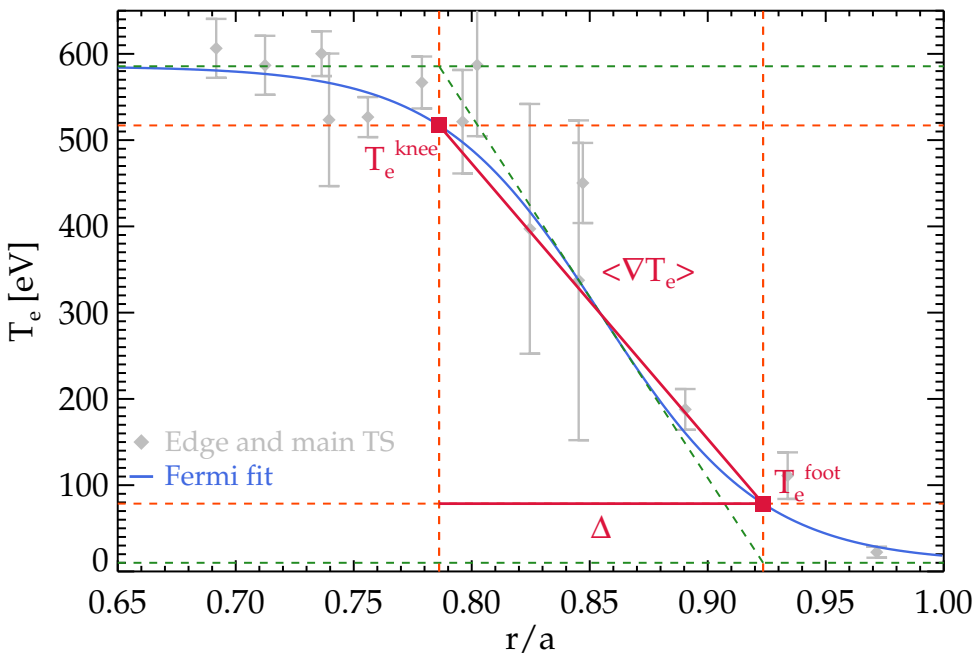

Figure 3.14: External region characterization : quantities in (3.12) are depicted in red. In green the parameters of the Fermi fit are reported: horizontal lines represents D, $D + \Delta T_e$ and the slope depicts ∇T_e^{max}

Before entering the discussion about the three parameters just explained, some attention must be paid to what they represent in the three different profiles shape. Further extending the comparison with tokamaks, a quantity resembling T_e^{ped} can be defined:

$$T_e^{knee} \equiv T_e(r = r_{max} - \Delta/2) \sim T_e^{foot} + \langle \nabla T_e \rangle \cdot \Delta \quad . \tag{3.12}$$

In the former $\langle \nabla T_e \rangle \sim 0.75 \nabla T_e^{max}$ while T_e^{knee} represents the temperature at the top of the temperature decrease. In the left panel of Figure 3.15 T_e^{knee} is plotted versus the ratio $b_\varphi^{1,-7}/b_\varphi^{sec}$ for the different profile shapes. The SHAx-like profile shows remarkably lower values of T_e^{knee} if compared to MH-like and DAx-like profiles. This is easily explained looking at the right panel of the same figure, where T_e^{knee} is normalized to the core temperature. While the temperature decrease in MH-like and DAX-like profiles occurs almost entirely in the Δ region, in SHAx-like profile the temperature decrease occurs only partially in the external region, i.e. across Δ, a significant fraction of the further temperature decrease occurs in the central region and is due to the presence of the temperature structure in the plasma core. Values of T_e^{knee}/T_e^0 greater than one do not mark hollow temperature profiles, but they represent the lowest core temperature profiles, i.e. $T_e^0 \lesssim 300$ eV, in which small errors in the fitting function or fluctuations in the flat central part of the temperature profile can lead to either underestimated values of T_e^0 or to overestimated ΔT_e. T_e^{knee} can give information about eventual change of the transport characterizing the external region, and has been thus included in the analysis. One can notice that the distinction of the SHAx-like profiles with two different symbols is not used as before. This is because the second method (full matching of the temperature radial profile) was not conceived to accurately match the external region, and its output is neglected throughout all this section. The electron temperature at the knee, T_e^{knee}, seems to slightly

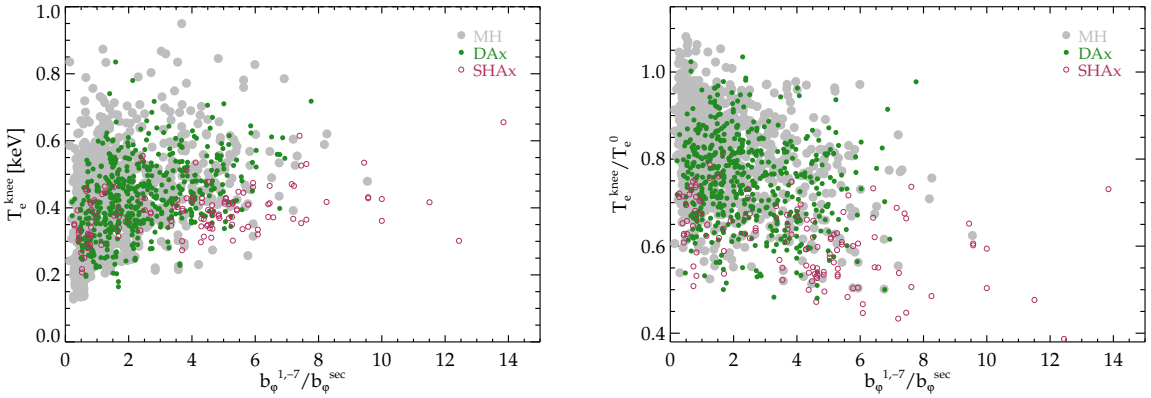

Figure 3.15: (a) T_e^{knee} and (b) T_e^{knee} normalized to core temperature versus the ratio between dominant and secondary modes amplitude. The database is divided according to the three different temperature profile shapes.

increase when the ratio $b_\varphi^{1,-7}/b_\varphi^{sec}$ increases, without distinction between the three plasma states (MH, DAx and SHAx). Such a trend states that the positive influence of a chaotic transport reduction seen on central temperature (Page 71), can be extended from the plasma center to the knee, $r/a \sim 0.75$

Hereafter the dependence of the parameters chosen for the characterization method will be investigated and discussed. After all the experimental evidences will have been exposed an overall picture of the physics governing the region under analysis will be presented.

3.3.1 Spatial extent: Δ

Something about the spatial extent of the temperature decrease has been already mentioned in Section 3.1.2. Although Δ varies approximately by an order of magnitude within the selected dataset, no outstanding dependence on machine parameters has been highlighted. First of all, Δ seems to be not correlated to variations of the amplitude of the MHD modes, neither the dominant nor the secondary. Δ is also insensitive to the temperature profile shape, as can be seen in Figure 3.16a. No clear trend is visible and the three different profile shapes show similar values of Δ. The only macroscopic parameter found to affect the spatial extent of the temperature decrease is the Greenwald density fraction n/n_G. The whole database has been divided in three classes and the probability distribution function for Δ has been computed over each class, the result can be seen in Figure 3.16b. To a higher Greenwald density fraction corresponds an average higher Δ. In RFX-mod, generally, the Greenwald density fraction gives a flavor about the wall conditions and the density profiles. In fact, increasing n/n_G the density profile tends to peak at the plasma edge[120] and the layer $n_e \sim 1 \cdot 10^{19}$ m^{-3} gets closer to the wall[121]. Thus, a higher n/n_G means higher density gradient and a lower neutrals penetration which, in turn, result in a more localized density source towards the wall. As the density profile becomes more peaked at the plasma edge, and the neutrals are more and more gathered in the external region, the profile of the temperature tends to flatten. Therefore, the slight increase of Δ with increasing Greenwald density fraction points towards a direct influence of the plasma edge conditions on the external region and on the temperature profile across it.

This insensitivity of Δ to plasma parameter differet from n/n_G can be attributed to the poor spatial coverage of the region $r/a > 0.85$, a certain degree of arbitrariness can indeed hide eventual dependencies. The point has already been discussed and there is no way to improve the analysis at the moment. It is also possible for Δ to be influenced by local parameters instead of global ones, as the formation of localized $m = 0$ islands at the measurement location or to the plasma shift due to modes interaction. Unfortunately both these tasks can hardly be addressed in a large database statistical analysis: the first one because it would require a fine topological analysis which is highly time demanding; the second one would deserve a probing spatial resolution that is presently not available. Δ would deserve a much detailed analysis to highlight other eventual dependencies and to possibly verify these

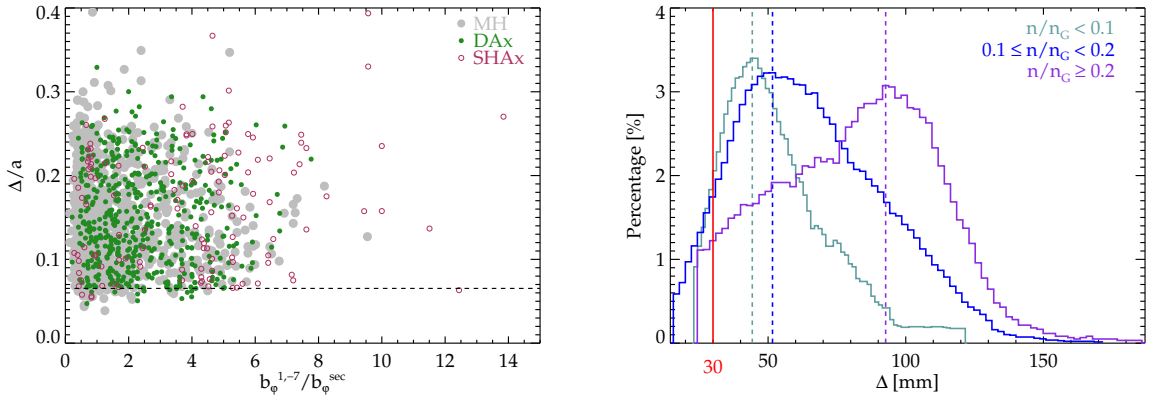

(a) (b)

Figure 3.16: (a) Spatial extent as a function of the ratio between dominant and secondary modes amplitude. The database is divided according to the three different temperature profile shapes. (b) Influence of normalized density on temperature decrease spatial extent. Vertical dashed lines mark the most probable values of each PDF. The black dashed horizontal line in (a) and the continuous red vertical line in (b) mark the 30 mm imposed as limit to the fitting parameters space, as explained in section 3.1.2.

conjectures. Such a deeper analysis necessarily require a better probing capability, is thus postponed to the time when the edge TS would be available again. Its finer spatial resolution together with the continuous mapping from $r/a = 0.8$ all the way to the wall, will allow a more precise determination of Δ. Moreover the possibility of a simultaneous temperature and density profile measurement, as given by the edge TS, would improve the investigation capability giving the possibility to track the change of pressure as an interplay between temperature and density.

The parameters characterizing the temperature decrease, as obtained by the Fermi fit, do not show any significant correlation between them. Obviously this is not true for the quantities derived by the four initial parameters, in particular the strong link between Δ and ∇T_e^{max} has already been highlighted in section 3.1.2. Because of this strong dependence and the impossibility to relate Δ to any machine parameter, it has been decided to consider Δ as a machine parameter and to use it to draw scaling laws for T_e^{foot} and ∇T_e^{max}. In this way any hidden dependence of Δ would be included in the scaling of the other quantities.

As said before, in RFX-mod there is no strong geometric limit fixing the location of temperature decrease, this is confirmed by the investigation method. Considering that r_{max} (i.e. the radial location of the temperature drop middle point) is located at the middle of the temperature decrease[a], changes in r_{max} reflect the spatial movement of the temperature drop region. As seen for Δ, the spatial location is not affected by the magnetic state of the plasma

[a] *The* Fermi function *is indeed symmetrical about* r_{max}.

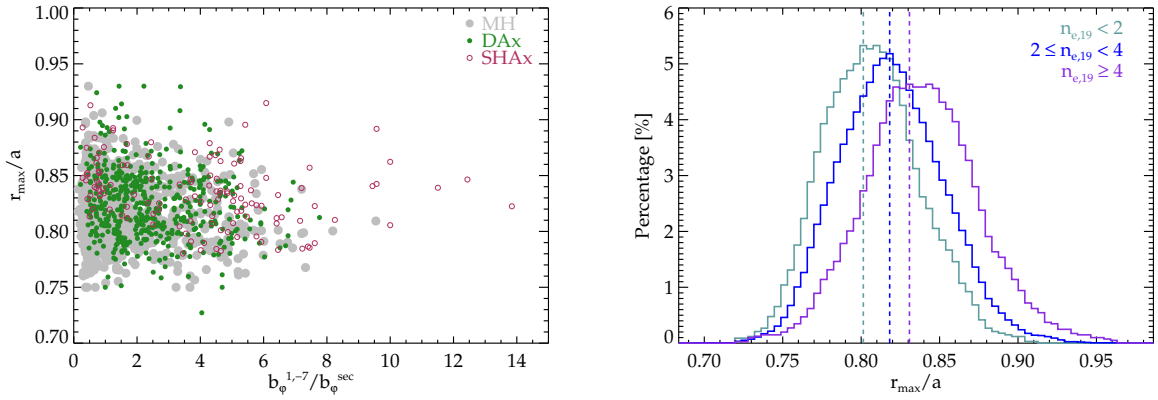

(a) (b)

Figure 3.17: (a) Average temperature drop location as a function of the ratio between dominant and secondary modes amplitude. The database is divided according to the three different temperature profile shapes. (b) Influence of density on r_{max}, in the graph $n_{e,19}$ marks the line average density $\langle n_e \rangle_l$ in units of 10^{19} m^{-3}. Vertical dashed lines mark the most probable values of each PDF.

and does not vary changing the temperature profile shapes, see Figure 3.17a. The only macroscopic parameter found to affect the spatial location of the temperature drop is the density: increasing $\langle n_e \rangle_l$ r_{max} gets closer to the wall, Figure 3.17b.

As a direct consequence of the similar density dependence of Δ and r_{max}, the *knee*, $r_{knee} = r_{max} - \Delta/2$, and the *foot*, $r_{foot} = r_{max} + \Delta/2$, of the temperature decrease show an opposite behavior: while the *foot* gets closer to the wall with increasing density, the *knee* remains approximately fix, or eventually moves a bit inward. This evidence, depicted in Figure 3.18, allows us to speculate the existence of two different regions separated by r_{knee}: the core region, enclosed by r_{knee}, with an almost flat temperature or eventually, with the presence of the typical SHAx-like core structure, which is weakly sensitive to n/n_G variations and the region outside r_{knee} where the larger fraction of the temperature decrease occurs, which tends to enlarge as n/n_G increases. These different behaviors allow to conclude that the first wall conditions strongly influences the region near the foot and becomes less effective moving towards the plasma core, in fact r_{knee} does not move if n/n_G changes. It is worth noting that r_{foot} comes from two parameters of the fitting function and does not necessarily assume always a physical meaning, this is the case for the lower current discharges where the core temperature is below 300 eV. In these cases Δ can be as large as half of the minor radius and r_{foot} can largely overcome a. Evaluating a temperature at such position can thus be meaningless. To avoid such problem whenever r_{foot} was greater than a its value was bounded to $a = 459$ mm.

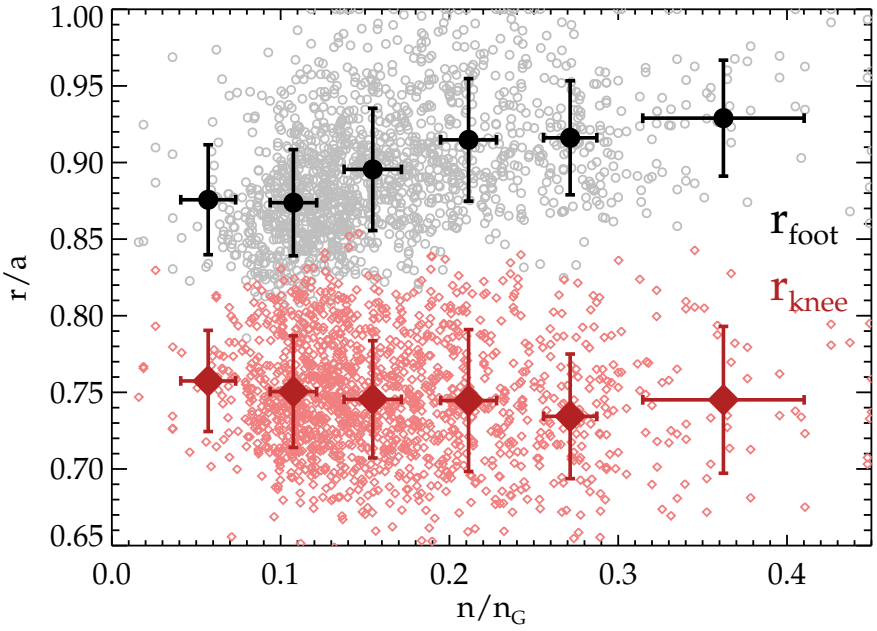

Figure 3.18: Normalized radial location of *foot* and *knee* of the temperature decrease versus Greenwald density fraction. A moving average is superposed to the database. Error bars represent the standard deviation of each averaged sample.

3.3.2 External temperature: T_e^{knee} and T_e^{foot}

The analysis of temperature values in the external region is fairly complicated. In fact, the lack of a fix geometric constraint, as the separatrix in the tokamak case, does not allow to decrease the degrees of freedom of the problem. One has thus to decide whether to consider the value of the temperature at a fixed spatial location, which has no particular physical meaning, or at a meaningful location which can change with respect to the machine coordinates. In other words one has to choose between T_e^{foot}, being mindful of the fact that r_{foot} varies with n/n_G, and $T_e^{87} = T_e(r = 0.87a)$ which is completely regardless of the plasma conditions. The situation is depicted in Figure 3.19: on the left the dependence of T_e^{foot} on r_{foot} is evident, on the right the comparison between T_e^{foot} and T_e^{87} shows that only the first one of the two conveys information about the plasma density even if $r/a = 0.87$ represents the most probable location for r_{foot}[a]. It should be stressed that the influence of n/n_G on T_e^{foot} is clearly affected by the variation of r_{foot} with n/n_G. T_e^{foot} has to be indeed treated with particular attention to obtain a correct interpretation of its behavior, anyhow Figure 3.19b clearly states that n/n_G strongly affect the external temperature. Conversely, considering T_e^{87} one is led to believe that temperature in the external region of the plasma is only slightly affected by n/n_G which is not consistent with former experimental results, see [92]. In the following, the first strategy is adopted, i.e. considering T_e^{foot} and r_{foot} to compute scalings.

[a] $r/a = 0.87$ *represents the location of the maximum of the probability distribution function for* Δ.

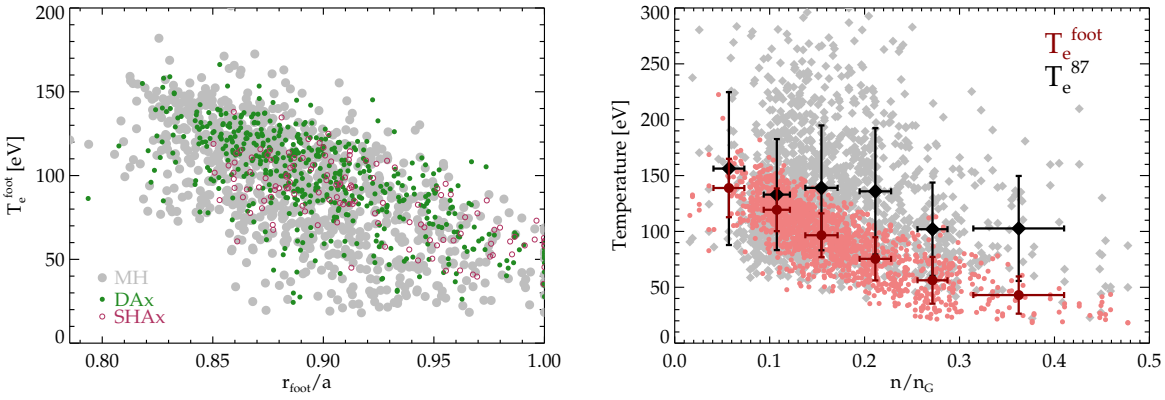

(a) (b)

Figure 3.19: (a) Temperature at the *foot* of the temperature decrease versus the *foot* location. The database is divided according to the three different temperature profile shapes. (b) Comparison between T_e^{foot} and $T_e^{87} = T_e(r = 0.87a)$ as function of the Greenwald density fraction. A moving average is superposed to the database. Error bars represent the standard deviation of each averaged sample.

In order to compare the external region to the plasma core, an expression similar to the model in (3.11) was considered. However it is clear that the model used to interpolate T_e^0 is not well suited to represent the external temperatures. First of all, neither T_e^{knee} nor T_e^{foot} shows a significant dependence on the magnetic state of the plasma, as stated by Figure 3.19a and Figure 3.15a. In addition, we already mentioned that T_e^{foot} can convey information about the position at which is evaluated, thus this possibility must be taken into account. The eventual dependence on Δ should be also included to track eventual hidden dependencies on local parameters. Investigating regions near the reversal surface, the reversal parameter F should reasonably play some role, it was therefore included. The improvement in plasma conditions linked to change in magnetic state (passing from MH to QSH state) is mainly related to the quench of the secondary amplitudes, rather than growth of the dominant mode. As a proof, the temperature in the central region, the region more interested by the presence of the $m = 1, n = -7$ dominant mode, is more influenced by $\tilde{b}_\varphi^{sec}$ rather than $\tilde{b}_\varphi^{1,-7}$, recall Page 71. Moving towards the plasma edge this influence should increase so the eventual dependence on the dominant mode has been dropped. The new model becomes:

$$T_e\left(I_p, \langle n_e\rangle_l, |F|, \tilde{b}_\varphi^{sec}, \Delta\right) = \alpha\, {I_p}^{\gamma_{I_p}}\, \langle n_e\rangle_l^{\gamma_{n_e}}\, |F|^{\gamma_F}\, (\tilde{b}_\varphi^{sec})^{\gamma_{sec}}\, \Delta^{\gamma_\Delta} \quad . \tag{3.13}$$

The regression procedure has been performed for both T_e^{knee} and T_e^{foot}, to simplify the comparison the procedure was replicate for T_e^0. The results of the performed regression are given in Table 3.20a and plotted in Figure 3.20b.

	T_e^0	T_e^{knee}	T_e^{foot}
α	$0.003 \pm$ <0.001	0.008 ± 0.002	0.037 ± 0.011
γ_{I_p}	0.780 ± 0.018	0.774 ± 0.023	0.650 ± 0.024
γ_{n_e}	-0.208 ± 0.009	-0.256 ± 0.010	-0.318 ± 0.011
γ_F	-0.054 ± 0.006	-0.096 ± 0.007	-0.055 ± 0.009
γ_{sec}	-0.333 ± 0.012	-0.103 ± 0.016	-0.046 ± 0.018
γ_Δ	$-0.003 \pm$ <0.001	0.004 ± 0.011	-0.177 ± 0.013
$RMSE$	13.53%	17.12%	18.68%
R	0.90	0.83	0.80

(a)

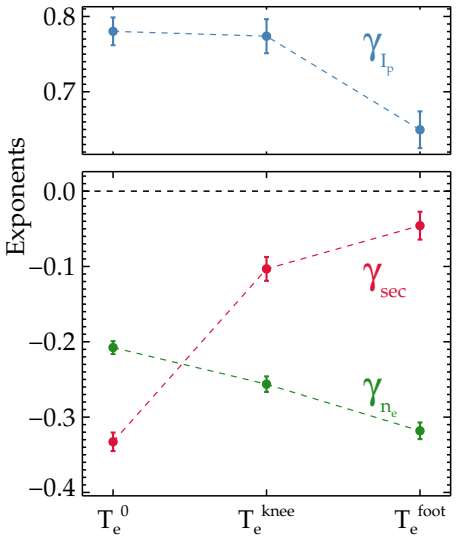

(b)

Figure 3.20: (a) Summary of the regression performed on T_e^0, T_e^{knee} and T_e^{foot} based on the model (3.13). (b) Some of the exponent in (a) plotted for visual comparison, the horizontal axis is not on scale.

The overall picture well fits previous evidences and expectations. Plasma current remains the quantity that really establish the temperature, even if its contribution becomes less important approaching the wall. Conversely, moving towards the wall, the dependence on density become more important. The stronger relationship between temperature and density in the external region is probably due to the density profile variation. In fact, as the Greenwald fraction increases the density profile tends to peak at the plasma edge becoming hollow[120, 122, 88]. Moreover, thanks to the THB diagnostic the inverse proportionality linking local edge temperature and density has been proved, at least up to $r/a \sim 0.9$. With the same diagnostic, the edge temperature at $r/a = 0.95$ was shown to also decrease with increasing Greenwald density fraction, to a higher plasma current corresponds a more accentuate inverse proportionality between T_e and n/n_G[123]. Accordingly with expectations, approaching the wall γ_{sec} decreases becoming negligible for the T_e^{foot}. This further confirms how changes in the amplitudes of secondary modes do not have a direct influence on temperature in the external region, but remains important in the central one. It is worth mentioning that the secondary modes considered for this analysis are those with $m = 1, |n| < 15$, namely the ones that generally resonate across $r/a < 0.7$. Conversely, in the region $0.7 < r/a < 1$ resonate all the $m = 1$ modes with $|n| \gtrsim 16$, but only those with $|n| \leq 24$ are measured. So, an influence of the high $|n|$ modes can not be excluded.
The resulting picture can be summarized as follows: the plasma current is the main knob to

increase electron temperature throughout the entire plasma column, while the reduction of the normalized secondary modes amplitude, related to the the change of the magnetic state, seems to be beneficial for central part of the plasma (T_e^0 and T_e^{knee}) and almost ineffective in the external region (T_e^{foot}). Conversely, the importance of the density as a temperature modifier is reversed: moving from the wall towards the core it becomes less and less relevant. So, the temperature increase due to the current is quenched by different mechanisms whose importance depends on the plasma region, inside or outside T_e^{knee}.
The dependence on F appears to be weak for all the three temperatures but does not show a particular trend. Anyhow the role of F can be different depending on the considered plasma region. As a matter of fact, as F increases towards 0 the normalized amplitude of the $m = 0/n = 1, 2$ harmonics of the radial magnetic field component decreases. These modes are responsible for the non-linear coupling between the dominant and the secondary modes $m = 1$. As a result, as F approaches 0 the dominant mode normalized amplitude tends to decrease while $\tilde{b}_\varphi^{sec}$ increases[100]. Considering the different T_e dependence noticed just few lines above, it is easy to understand that the effect of F on T_e^0 and T_e^{foot}, even if similar, can act through different mechanisms. It should be stressed the meaning of a negative power for F, which is directly linked to the use of the absolute value of F for the regression, needed to avoid computational problems. The negative sign of γ_F implies that higher temperature values are found for the smaller values of $|F|$, as a well established experimental experience confirms. The decrease of F away from zero means to increase the separation between the reversal surface and the wall, which directly affects the edge plasma condition. Deep F equilibria indeed show a larger edge density[121] and a lower edge temperature, thus a more resistive plasma. Considering that a non negligible current flows in the same edge region, operating at deep F means a strong ohmic power deposition in the plasma edge, where the plasma itself is not well confined. As a consequence less ohmic power can heat the plasma core thus degrading the overall plasma performance and leading to a lower average temperature[a]. The positive influence of shallow F operation together with the negative sign of γ_F is thus explained.
As expected, Δ is found to play some role in establishing T_e^{foot}, while is completely ineffective on T_e^0 and T_e^{knee}. The values of γ_Δ prove the validity of the investigation method, being null for T_e^0. Conversely the influence of Δ on T_e^{foot} is probably due to the dependence of T_e^{foot} on r_{foot} showed in Figure 3.19a. It should be stressed that although the regression model is changed, the quality of the match for T_e^0 is unaltered.

[a] *This is valid at least at current values above 1 MA.*

3.3.3 Maximum gradient: ∇T_e^{max}

The model (3.13) has been also used to obtain an empirical scaling law for the external gradient:

$$\boldsymbol{\nabla T_e^{max}}\left(\boldsymbol{I_p}, \langle \boldsymbol{n_e}\rangle_l, |\boldsymbol{F}|, \tilde{\boldsymbol{b}}_{\boldsymbol{\varphi}}^{\boldsymbol{sec}}, \boldsymbol{\Delta}\right) = \boldsymbol{\alpha}\, \boldsymbol{I_p}^{\gamma_{I_p}} \langle \boldsymbol{n_e}\rangle^{\gamma_{n_e}} |\boldsymbol{F}|^{\gamma_F} (\tilde{\boldsymbol{b}}_{\boldsymbol{\varphi}}^{\boldsymbol{sec}})^{\gamma_{sec}} \boldsymbol{\Delta}^{\gamma_\Delta}$$

$$\begin{cases} \boldsymbol{\alpha} &= (3.21 \pm 1.72)\cdot 10^{-3} \quad (53.35\%) \\ \boldsymbol{\gamma_{I_p}} &= 0.825 \pm 0.036 \quad (4.36\%) \\ \boldsymbol{\gamma_{n_e}} &= -0.272 \pm 0.015 \quad (5.66\%) \\ \boldsymbol{\gamma_F} &= -0.134 \pm 0.012 \quad (9.20\%) \\ \boldsymbol{\gamma_{sec}} &= -0.051 \pm 0.025 \quad (48.54\%) \\ \boldsymbol{\gamma_\Delta} &= -0.831 \pm 0.018 \quad (2.13\%) \end{cases} \tag{3.14}$$

$$RMSE = 20.99\% \quad R = 0.92$$

The regression is shown in Figure 3.21. The general picture drawn for the external temperatures in the previous Section seems to hold also for ∇T_e^{max}, with the only significant difference of the strong influence of Δ. As a matter of fact, the scaling of ∇T_e^{max} seems to merge the dependencies of T_e^{knee} and T_e^{foot} adding a further strong dependence on Δ. Such a marked dependence can be expected since the relation linking the two. It is interesting to note that ∇T_e^{max} shows a stronger dependence on both I_p and F if compared with the temperatures. Furthermore, the amplitude of the MHD modes is confirmed to be ineffective

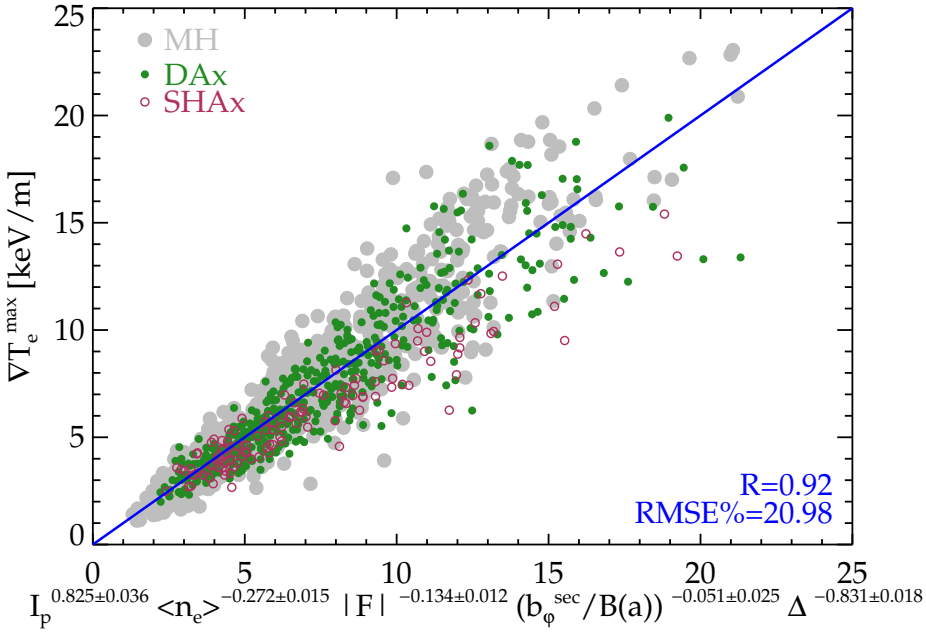

Figure 3.21: Empirical scaling law for temperature gradient, i.e. expression (3.14). The database is divided according to the three different temperature profile shapes.

on the external region ($\gamma_{sec} \sim 0$). This leads to believe that while the core region transport is well represented considering only the amplitudes of the secondary modes with $|n| < 15$, the external region needs some further information about the magnetic state to be well represented.

3.4 Other influent quantities

In the previous section empirical scaling laws has been obtained for the external region characteristic quantities. Such scaling laws took into account only those machine parameters representing physical quantities characterized by a sensible variation within the database. But many other important issues for machine operation and other physical quantities was not considered, their influence will be assessed in the following.
The wall conditions is known to affect both the main plasma confinement properties and the edge plasma characteristics in all kind of magnetic confinement device. A properly conditioned material wall indeed reduces impurities level and can reduce the recycling. The wall performance can not be easily measured nor an accurate characterizing parameter exists able to fill such need. The particle influx, measured by the H_α radiation, gives information about the PWI but is strongly affected by the local modification of the plasma column[92], so it is not a well suited indicator to estimate global wall conditions. The main conditioning technique used at RFX-mod is the Helium Glow Discharge Cleaning. This technique is routinely performed at the beginning of each experimental session and helps to obtain a controllable plasma density. In fact the carbon wall of RFX-mod act as a strong Hydrogen getter and thus as a large, usually satured, reservoir which releases the Hydrogen atoms when heated. Given the large power load interesting the wall during a plasma discharge, the recycling factor is usually larger than unity resulting in a tricky plasma density control. So the proximity of a given plasma discharge to a Helium Glow Discharge Cleaning (GDC) has been used as an estimator of the wall condition impact on the temperature profile. Clearly it has not a quantitative meaning, but it qualitatively marks the wall loading, i.e. to a more recent GDC a less loaded wall should correspond. Figure 3.22 depicts how the probability distribution function of T_e^{foot}, T_e^{knee} and ∇T_e^{max} residuals[a] changes comparing shots performed just after a GDC (blue curve) against shots performed later than that (red curve). T_e^{foot}, T_e^{knee} and ∇T_e^{max} residuals are respectively the three population normalized by the empirical scalings, thus residuals greater than 1 indicate points laying above the empirical scaling laws, the opposite consideration holds for residuals lower than unity. The PDF of the residuals rather than those of the full magnitudes have been considered in order to rule out all the eventual dependencies already examined. In general, when the first wall is well conditioned (just after a GDC) the probability of obtaining values below the empirical laws is lower than compared to non-conditioned wall one. The PDFs are centered at unity for the well conditioned case, while

[a] *The term 'residuals' depicts the ratio between a given quantity, let say T_e^{knee}, and its empirical scaling $T_e^{knee}(I_p, \langle n_e \rangle_l, |F|, \tilde{b}_\varphi^{sec}, \Delta)$.*

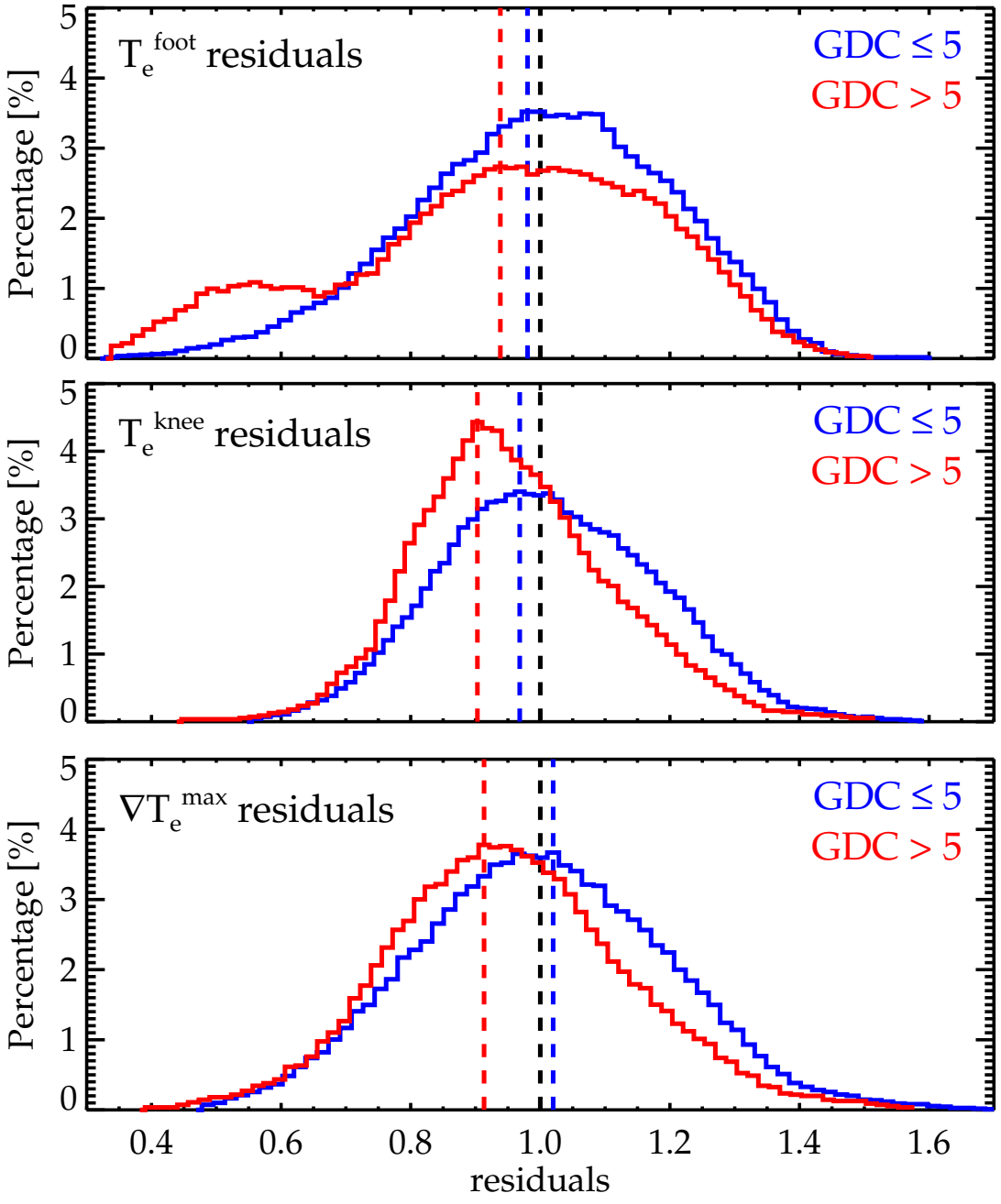

Figure 3.22: Probability distribution function for: (top) T_e^{foot}, (middle) T_e^{knee} and (bottom) maximum gradient residuals with different wall conditions. The blue curves represent discharges near a GDC, i.e. well conditioned, red curves represent discharges far from a GDC.

the most probable value is below unity in the other case. Moreover, for the PDF of T_e^{foot}, the range of residuals lower than unity is more populated for the red curve rather than the blue one. When the first wall is conditioned (just after a GDC) the probability of obtaining higher gradient is larger compared to non-conditioned wall one.
Many others physical quantities have been taken into account without giving any evident correlation with the parameters chosen to characterize the external region, they will be only listed and briefly discussed. This lack of correlation is caused by the dominant role of plasma current in establishing the physics of RX-mod. A lot of the quantities discussed below indeed shows a certain degree of correlation with the modifications of the temperature profile. But, at a deeper investigation such correlation results mediated by the plasma current. In other words, once a narrow plasma current range is chosen the correlation is no more visible. To verify if edge local properties affected the external region, the local shift due to the deformation of the plasma column was taken into account. The local shift has been shown to strongly affect both density and pressure in the region $r/a > 0.95$ [92, 158]. No similar link was found for T_e^{foot} nor for the radial position of the *foot*. In the same way, data from the ultrafast microwave reflectometer[124] were used to check whether the dependence found on the line average density remained valid using local density measurements. The actual setting of such diagnostic allows to measure the radial distance between the layer of density lying in the range $(1 \div 1.1) \cdot 10^{19}$ m^3 and the wall, called d_c. Mapping the reflectometer data to the toroidal location of the main TS, in order to take into account the plasma column deformation as explained in [121], the link between local density and temperature profile was investigated. Increasing d_c (lowering the edge density and the global plasma-wall interaction) Δ was found to slightly decrease while T_e^{foot} tended to increase, conversely T_e^{knee} and ∇T_e^{max} remained almost unvaried. These trends confirm the dependence already found on density and wall loading but do not add any further information. It would had been interesting to investigate further these links considering subset of data with homogeneous plasma current and density in order to rule out the d_c dependence on global parameters[121]. The common database consisted in less than 200 discharges so these further discrimination was not possible. Some attention has been posed to verify if the distance of the main TS from the toroidal position of the mode locking induces changes in the temperature profile. No such changes has been highlighted, this is probably due to the lower impact of the mode locking on plasma performance during discharges performed with the CMC control scheme. Moreover, the influence of the locking gets stronger when operating at Greenwald density fraction above ~ 0.35, but only a few of such discharges were present in the database. To conclude, eventual dependence on toroidal velocity was investigated using three different velocity estimates. Recalling that the magnetic field is mainly in the poloidal direction at the RFX-mod edge, the toroidal velocity should be responsible for an eventual turbulence pacing effect[125]. Toroidal flows were investigated exploiting passive spectroscopy diagnostics measuring different impurities as carbon (CV), the main impurity coming from the graphite first wall, and boron (BIV) being available due to the first-wall conditioning process by boronization[98]. The

average radial position of such impurities are peaked in the region $r/a \sim 0.8 \div 0.9$, slightly depending on plasma temperature. The velocity measurements are line integrated so they are not spatially well localized giving an average estimate of the plasma flow in the toroidal or poloidal plane. Considering subset of data with homogeneous density, in order to rule out the dependence of these measurements[126], no particular dependence of the temperature profiles on toroidal flow was found. The toroidal edge velocity can be obtained using two different methods: from cross correlation analysis of the 16 toroidally spaced lines of sight of the GPI diagnostic[127] and from the estimate of the k-frequency spectral density $S(k_\varphi, f)$ from the toroidal array of internal magnetic pick-up coils (the ISIS system) [128]. This method combines the information from frequency decomposition with the spatial information coming from the toroidally evenly distributed sensors. Although the k-spectrum is rather broad, in particular, at higher frequencies, an almost linear dispersion relation may be estimated at least up to 30 kHz, from which an evaluation of the toroidal propagation can be done. Both these measurements, which are found to be comparable, are higher at lower values of the normalized density and tends to saturate at approximately 20 km/s for Greenwald density fraction $\sim 0.35 \div 0.4$ [86]. Any link found between the edge toroidal flow and the temperature profiles was a consequence of the density dependence, no neat link left once a specific range of density was selected.

3.5 PROFILE CHANGES

The indications obtained performing regressions over the whole database, can be summarized using a different approach: how the temperature profile in the external region changes while varying a single machine parameter? To answer this question the database has been divided in subsets to single out a unique parameter at a time, trying to maintain fixed all the others. A further division in classes allows the visual exam of the profile changes.

The influence of plasma current has been evaluated using a sample of ~ 500 temperature profiles with $2.5{\cdot}10^{19}\ \mathrm{m}^{-3} < \langle n_e \rangle_l < 3.5 \cdot 10^{19}\ \mathrm{m}^{-3}$ and $F > -0.075$. This subset was then divided in four classes of current values and the temperature profile were averaged within each class. The result of such procedure is shown in Figure 3.23. Looking at the left panel, where the average profile for each class is plotted, is easy to see that increasing the current the temperature increases too. The link between current and temperature is not linear, the temperature increase is less evident when the current is increased over 1.5 MA. This can be due to the enhanced solicitation of the wall related to the highest current values. This, turns in a higher desorption and in a higher level of impurity present in the plasma. As a matter of fact, the two largest I_p classes have approximately the same average ohmic input power, ~ 32 MW, but an average 15% higher radiated power is measured for the discharges pertaining to the highest current class. The four profiles are highly self-similar, as confirmed by the right panel of Figure 3.23: the former profiles have been normalized to their average

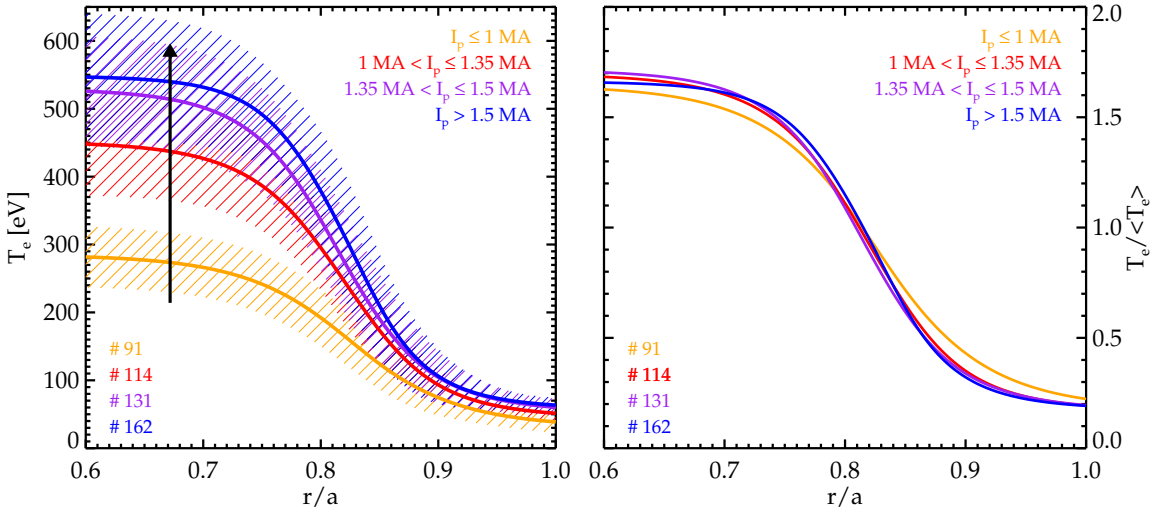

Figure 3.23: Effect of plasma current on temperature profile. An homogeneous subset has been divided and averaged over four I_p classes. (left) The average over the four classes, the shaded area represents the standard deviation of the population within each class. (right) To make the shape comparison easier, each profile has been normalized to its average value. In each graph: in the right top corner the four classes are defined, while in the left lower corner the number of averaged profiles for each class is given.

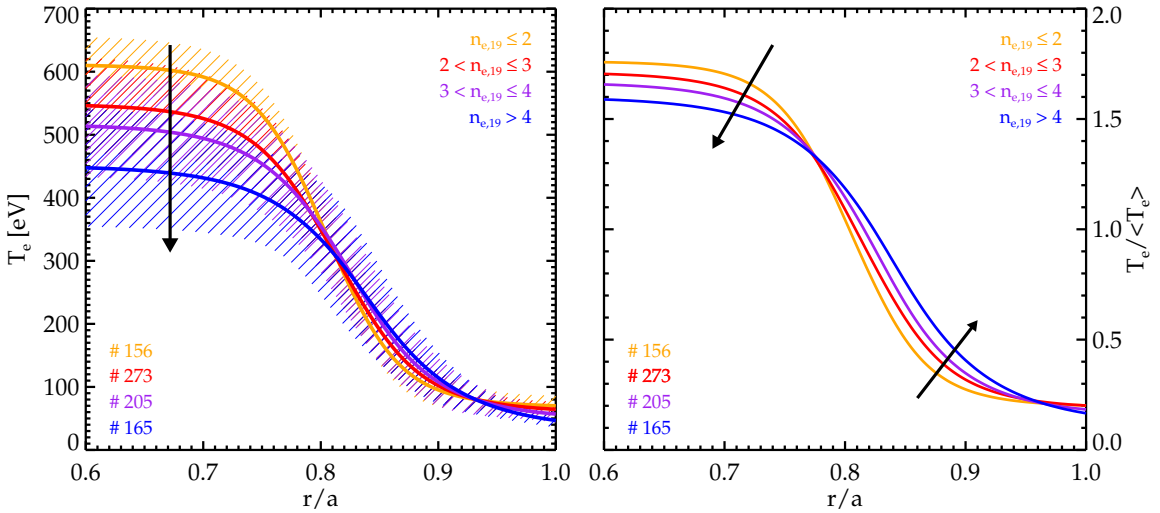

Figure 3.24: Effect of the electron density on temperature profile. An homogeneous subset has been divided and averaged over four $\langle n_e \rangle_l$ classes. (left) The average over the four classes, the shaded area represents the standard deviation of the population within each class. (right) To make the shape comparison easier, each profile has been normalized to its average value. In each graph: in the right top corner the four classes are defined, while in the left lower corner the number of averaged profiles for each class is given. In the graph $n_{e,19}$ stands for $\langle n_e \rangle_l$ in unity of 10^{19} m^{-3}

values. The profile shape remains approximately constant throughout the entire explored current range. Increasing the current the minimum temperature characteristic length, L_{T_e}, decreases from $\sim$ 20 mm down to $\sim$ 13 mm, but the location of such a minimum is approximately fix at $r/a \sim 0.86$.

The self-similar character highlighted while varying current is not maintained while changing density. Considering approximately 800 T_e profiles with 1.3 MA $< I_p <$ 1.6 MA and $F > -0.075$, the density influence has been investigated dividing the subset in four density classes. Given that the current is almost fixed, each density class approximately corresponds to a class of Greenwald density fraction. The left panel of Figure 3.24 plots the external temperature profiles pertaining to the four density classes: increasing the density the temperature decreases. At fixed plasma current a denser plasma is also colder, thus the central temperature drops with the entire profile. But this is not the only consequence of a larger plasma density. In fact, looking at the right panel of Figure 3.23 where the normalized profiles are depicted, one can see how the temperature decrease tends to broaden. A smaller density turns in steeper and less spatially extended temperature decrease, as expected from former observations about Δ and r_{max}, Section 3.3.1. Increasing the density L_{T_e} increases from $\sim$ 13 mm up to $\sim$ 16.5 mm, and its location moves towards the wall from $r/a \sim 0.84$ to $r/a \sim 0.88$.

3.5.1 Effective scrape-off layer

A particular attention deserves the influence of the reversal surface location on the external temperature profiles. As mentioned before, in some special cases a well-defined LCFS exists separated from the material wall by the $m = 0$ islands chain. In these cases an effective SOL forms outside the LCFS, recovering the picture of the pedestal region similar to the tokamak one. The picture assumes not only a descriptive appeal but also important physical meaning. In fact, the appearance of an effective SOL disentangles the regions inside and outside the LCFS ameliorating the transport inside the LCFS and reducing the PWI. This is immediately evident in Figure 3.25 where a subset of approximately 500 temperature profiles with 1.3 MA $< I_p <$ 1.6 MA and $1.5{\cdot}10^{19}$ m$^{-3} < \langle n_e \rangle_l < 3.5 \cdot 10^{19}$ m^{-3} has been divided in three classes distinguished by F values. F approximately quantifies the weight of the $m = 0$ modes and so the eventual presence of a good LCFS. The F values characterizing the three classes was chosen considering the range of F for which the effective SOL can or can not be present, see [83]. Looking at the left panel a first effect of operating at different F can be seen: generally operating at shallow F, namely $F > -0.05$, results in better plasma performance. The topic was already touched linking the shallow F to a hotter plasma edge. Nevertheless the capital difference appears remapping every profile to

$$r \longrightarrow \frac{r - r_{rev}}{a}$$

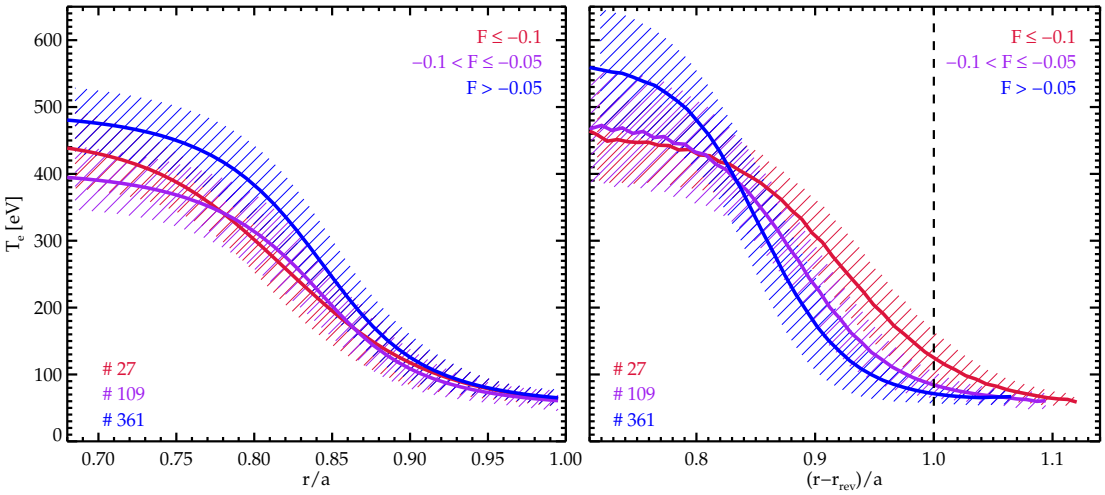

Figure 3.25: Changes of temperature profile as evidence for the formation of an effective SOL. An homogeneous subset has been divided and averaged over three F classes. (left) The average over the three classes. (right) Each profile has been remapped on the new coordinate $(r-r_{rev})/a$. The shaded area represents the standard deviation of the population within each class. In each graph: in the right top corner the four classes are defined, while in the left lower corner the number of averaged profiles for each class is reported.

where r_{rev} represents the average location of the reversal surface[a]. The profiles plotted on the new coordinate are shown in the right panel of Figure 3.25. The remapping brings two differences. On the one hand, the role of F is clearer and the beneficial effect of operating at shallow F is more evident. On the other hand, the appearance of the effective SOL can be recognized looking at the profile in the vicinity of the reversal surface: at shallow F, where the effective SOL does exist, the profile outside $(r - r_{rev})/a = 1$ is flat and the temperature at $(r - r_{rev})/a = 1$ equals the wall temperature. For intermediate F, where the effective SOL may exist, the temperature outside $(r - r_{rev})/a = 1$ is no more flat but still lower than the deep F case where the temperature at $(r - r_{rev})/a = 1$ already doubles the wall one. It is now clear that the similarity between the LCFS in these cases and the tokamak or stellarator separatrix holds also experimentally. Nevertheless while drawing this parallel one need to be mindful of the differences that still holds between the RFP and tokamak. In fact, if the SOL picture holds while considering the magnetic topology of the configuration, the same picture can not be extended to the recycling properties and the neutrals removal characteristic typical of a real SOL in diverted plasmas. If, on the one hand, the well confined plasma is actually separated from the open field lines region, the absence of any kind of localized PWI and dedicated pumping systems avoid the possibility to obtain the neutrals removal effect. So

[a]*The reversal surface is not toroidally nor poloidally symmetric, in fact the presence of $m = 0$ islands and the helical geometry imposed by the dominant mode, if present, can strongly modify it. This estimation of r_{rev} comes from a reconstruction of the axisymmetric equilibrium field, thus can be considered as an average estimate on the whole toroidal angle.*

while the temperature profile is beneficially influenced, the electron and neutrals density are globally unaffected by appearance of the effective SOL[a]. Nevertheless the effect on the temperature profile is evident, both at the reversal surface and inside it.
Considering all the available discharges with $1.3\,\mathrm{MA} < I_p < 1.6\,\mathrm{MA}$, a scaling of the remapped profile properties can be performed and is reported in Figure 3.26. In the top panel the temperature at the reversal surface is reported. A marked difference exists between the three populations being the deep F characterized by a higher temperature at the reversal surface. This difference marks the effect of separating the main plasma from the effective SOL, if it exists. In deep F cases, i.e. no effective SOL, the $m = 0$ islands do not intercept the wall and the LCFS lays between the reversal surface and the wall, so the temperature at r_{rev} deals with the temperature inside the main plasma rather that of the plasma edge. Conversely, pushing the reversal surface towards the wall the $m = 0$ islands chain may intercept the wall, the LCFS moves to more internal radii with respect to the reversal surface location and the effective SOL may appear. In these cases T_e^{rev} is completely affected by the complicated plasma edge topology and PWI. As a consequence of such a separation, there is a strong change in the transport paradigm. In the deep F case the radial heat transport is large because of the flow along the filed lines connecting the edge with the reversal region and to the short-circuit inside $m = 0$ islands which connects region inside the LFCS at different radii. In the shallow F case such contribution vanishes: there is no field lines connecting the edge plasma with more internal region and the $m = 0$ short-circuit flattens the temperature only outside the LCFS. Passing from deep F to shallow F the parallel transport is reduced and only the perpendicular contribution remains. As a matter of fact the plasma inside the LCFS results hotter and steeper gradients forms, as can be seen in the middle and bottom panels of Figure 3.26. It should be stressed that the spread in the scalings is due to the fact that the formation of the effective SOL does not occur systematically when operating at shallow F, other conditions must be fulfilled. In fact the presence of a strong mode locking, thus of a strong and localized modification of the edge topology, can prevent the formation of the effective SOL. In general the formation of such effective SOL are strongly favored at high current, namely larger than 1.5 MA. In fact, increasing the current the mode locking is generally weaker and the regular LCFS topology is preserved. We do not enter the details of the mode locking physics which can be found in [129, 130, 131]. As a counter check, the same analysis was performed on a similar database at lower current, e.g. $I_p < 1$ MA. The beneficial effect of operating at shallow F is still visible, but the mapping on $(r - r_{rev})/a$ does not convey any difference in the region outside the reversal surface, pointing towards the absence of the effective SOL.

[a] *Edge temperature and density was found to strongly fluctuate with the local topology[92], but no evidences is nowadays available of an overall beneficial effect.*

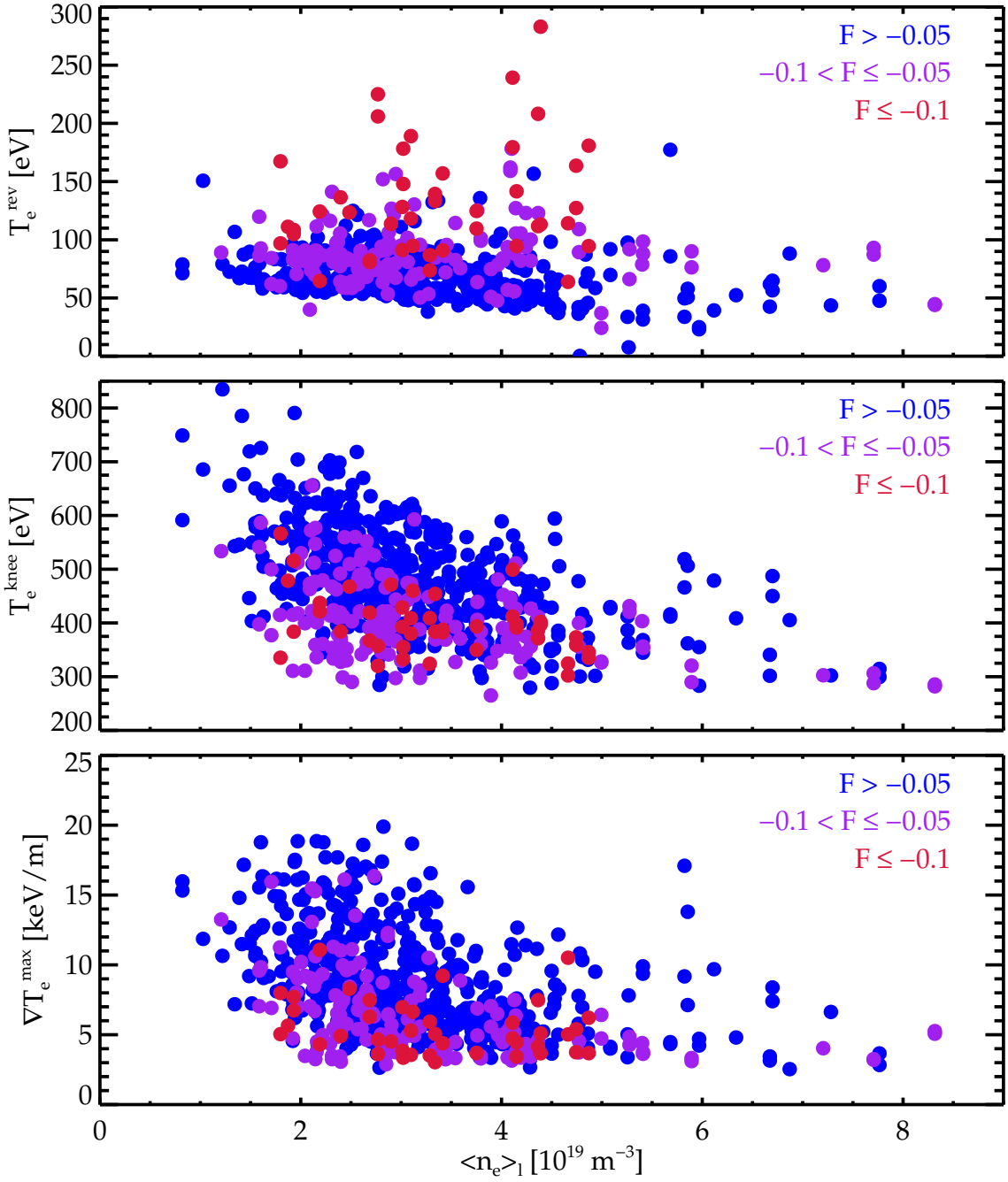

Figure 3.26: Main parameters characterizing the external region temperature profile versus electron density divided into the three F classes.

3.6 Conclusion and physics overview

Within the chapter the wide characterization of the electron temperature profile has been presented. The analysis method based on the *Fermi fit* was introduced and its starting assumptions were discussed. Then scaling laws have been proposed for different parameters chosen to characterize the temperature profile in the external region: T_e^{foot}, T_e^{knee} and ∇T_e^{max}. These scaling laws were discussed and summarized evaluating the changes of the profile shape due to a single machine parameter at a time. To conclude the chapter, an effort to convey all the aforementioned findings on temperature profile in a global picture, together with the present knowledge about the physics ruling the region $0.6 \lesssim |r/a| \lesssim 0.9$, will be attempted.

In general, electron temperature in the region $0.6 \lesssim |r/a| \lesssim 0.9$ mainly depends on plasma current and density, with plasma current being dominant over density in establishing the temperature value. The general picture one has to bear in mind is represented by Figure 3.27. External temperature and density lie approximately on isobars which moves towards higher pressure values as the plasma current increases. The role of current and density are switched considering the plasma shape: while the current does not affect the temperature profile shape, a higher electron density turns in a flattening and a spatial widening of the external temperature profile. Anyhow, the whole physics can not be entirely bounded inside these two

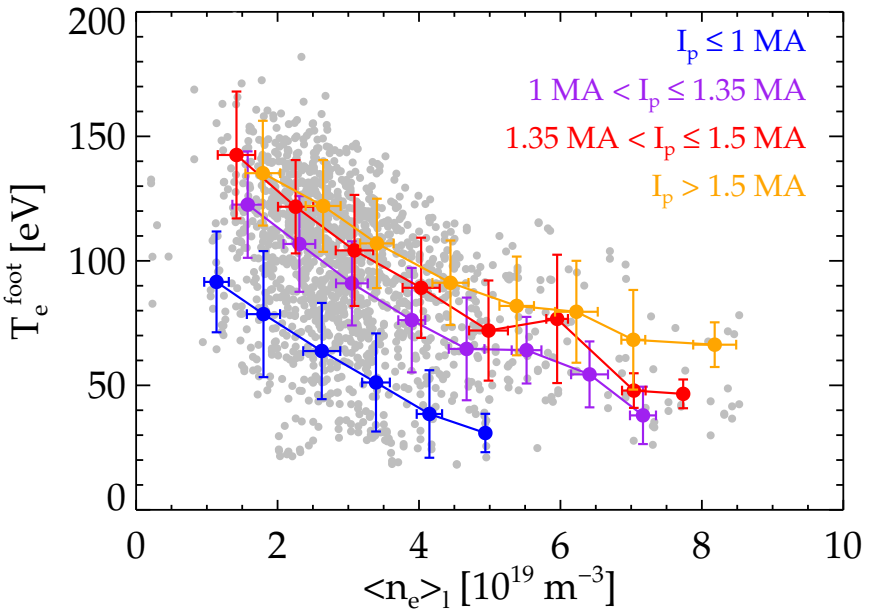

Figure 3.27: general picture of the most significant external temperature dependence. External temperature and density approximately lie on isobars where pressure increases with increasing plasma current.

sentences, in fact the magnetic equilibrium and the magnetic state of the plasma are decisive to determine the plasma behavior. Moreover, this picture changes moving towards the plasma core with the magnetic state becoming more important and density decreasing its importance. Focusing on the external region, the role played by the magnetic state can be noted in the marked increase of the average temperature exceeding 1 MA plasma current. Below 1 MA, in fact, the plasma is affected by a sea of MHD modes having all the same amplitude leading to a chaotic character affecting the entire plasma column. Increasing the current above 1 MA this chaotic situation is partially healed, especially in the core plasma, leading to a more ordered situation with well conserved flux surfaces. In turn, such order leads to an ameliorated plasma confinement and enhanced plasma performances. Nevertheless, in the region under analysis ($0.6 \lesssim |r/a| \lesssim 0.9$), the decreased interaction between the secondary modes and the well conserved volumes are probably not enough to significantly decrease the degree of stochastic transport as happens in the plasma core. Such behavior can be explained as a consequence of a residual magnetic chaos generated by the overlapping of the non-vanishing secondary modes. The region $0.75 < r/a < 0.85$ is populated by a huge amount of resonances, those of the modes with $20 \lesssim |n/m| \lesssim 60$.
The overall plasma performance, i.e. higher average temperature, are enhanced when operating at shallow F. Larger values of $|F|$ corresponds to a colder plasma external region and thus to a lager ohmic power deposition in that region, reducing the heating capability of the plasma core and to a lower average temperature. Moreover, shallow F operation can also lead to a major modification of the edge topology: the formation of an effective SOL layer with a considerable improvement of the plasma-wall interaction. This turns in an amelioration of the edge plasma properties and in a further enhancement of the overall plasma performance. Changes of the magnetic equilibrium are also related to modification of the PWI properties which, in turn, was shown to qualitatively affect the temperature profile.
The entire analysis, being the first of this kind performed at RFX-mod, is far from being complete and to conclude it is important to point out that the neutrals was never taken into account. In RFX-mod, apart from transient situation linked to the presence of the mode locking, a toroidally and poloidally spread PWI can be assumed as characterizing the machine operation. The lack of any limiting surface, limiter or divertor, and consequently of any localized pumping system leads to a complicated density sink/source system in the plasma edge. If in general, the sources and sink of particles in the SOL cannot be easily decoupled, they are even more entangled in RFX-mod where a real SOL does not exist. To the large local plasma density sink provided by the solid surface corresponds a larger volumetric density source provided by the neutrals returning from the wall. So the RFX-mod plasma edge results a region of high density where the atoms are rapidly ionized and their density decreases by orders of magnitude in a few centimeters. So neutral particles desorbed by the wall do not reach the plasma core since their penetration depth is about 5 cm, hence the particle source is localized at the plasma edge $r/a \gtrsim 0.9$ [122]. This causes a self-sustaining process: the density source is completely localized in the external region, this leads to steep density gradient which

in turn hinders the neutrals penetration. Moreover, if on the one side an increase of current, thus of the temperature, should turn in more energetic neutrals with larger penetrating capability, on the other side an increase of the current corresponds to a higher thermal load to the wall which means higher influxes and thus a cooling of the plasma edge. Being the plasma edge and the plasma core not completely separated (the separatrix is missing) the edge boundary conditions strongly reflects in the adjacent region $0.6 \lesssim |r/a| \lesssim 0.9$. The final outcome of such situation is the almost fixed shape of the external temperature profile that, apart from minor changes due to the density increase, is self-similar in all the discharge conditions. The only exception has to be made for those cases in which the effective SOL forms. Such effective SOL does not heal the problem of the edge localized density source but has strongly beneficial aspect: the LCFS, acting as a separatrix, disentangle the plasma boundary from the region inside the LCFS. In this way the plasma boundary remains cold and dense but the PWI is mitigated. Moreover the parallel transport is strongly reduced resulting in a hotter plasma inside the LCFS. To conclude, it is important to draw a last parallel between RFX-mod and the tokamaks. In fact, adopting the tokamak picture for the pedestal width, Δ can be related to SOL neutrals physics, hence giving a possible explanation for the insensitivity of Δ to all of the machine parameters. A further investigation relating temperature, density and neutral density is thus mandatory to achieve a deeper insight on the extreg region of RFX-mod.

4

RFX-MOD: IMPROVED REGIMES THERMAL CHARACTERIZATION

By doubting we come to questioning,
and by questioning we perceive the truth.

Pierre Abélard

In RFX-mod, three distinctive shapes of temperature profile mark the achievement of three different magnetic states. The baseline Multiple Helicity state, characterized by a flat temperature profile, is ameliorated by the growth of a dominant MHD perturbation partially healing the magnetic chaos which governs the plasma volume. The reduced chaos leads to the appearance of a narrow high temperature structure in the plasma core (DAx state) which eventually widens covering approximately the 40% of the plasma volume triggering the formation of an electron Internal Transport Barrier (eITB) called SHAx state. This collection of temperature profile shapes is enlarged by the occasional appearance of extremely high gradients developing at $r/a \sim 0.8$ dubbed electron External Thermal Barriers (eETB). eITBs and eETBs thus mark the possibility to improve the overall RFP plasma performance. Characterize the two phenomena, understand the physics governing them and evaluate the possibility to couple them are important steps towards an advanced confinement paradigm for RFX-mod. eITBs are nowadays extensively studied while eETBs represent a relatively unexplored investigation area. This chapter is devoted to analyze the eITBs characteristics, to illustrate eETBs phenomenon and to evaluate and compare their impact on the plasma performance and confinement properties.

The previous chapter was dedicated to a wide characterization of the RFX-mod temperature profile where particular attention was posed to investigate the region $0.6 \lesssim |r/a| \lesssim 0.9$. Two distinctive phenomena were left out from the discussion: the appearance of *electron Internal Transport Barrier* (eITB) related to QSH states and the occasional advent of extremely high gradient in the external region not linked to a particular shape of the temperature profile. In this chapter the two topics will be faced and compared.
The analysis performed in Chapter 3 did not show any striking difference between the three profile shapes MH-like, DAx-like and SHAx-like for what concern the external plasma region. Thus one may believe the plasma column to be divided into two region behaving almost regardless to each other: the plasma core strongly affected by the magnetic state of the plasma where the eITBs form during SHAx states and the external region, i.e. $0.6 \lesssim |r/a| \lesssim 0.9$, which behaves disregarding the temperature profile shape (MH-like, DAx-like and SHAx-like). Nevertheless, the eITB appearance does trigger minor changes in the temperature profile outside $r/a \sim 0.5$; for example, T_e^{knee} assumes lower values in SHAx-like profiles for a fixed $b_\varphi^{1,-7}/b_\varphi^{sec}$ if compared to MH-like or DAx-like profiles, see Figure 3.15. Such an evidence triggered the interest for a deeper investigation of SHAx-like profiles so to understand if the ameliorated plasma core confinement (eITB) has a direct influence on the external region. To this extent a full profile matching of the SHAx-like profiles was performed adopting the *Fermi fit* function. Such procedure allows the direct comparison between the eITB and the temperature decrease occurring in the external region along with the investigation of possible links between the two regions. Such a topic will be discussed in Section 4.1.
In Section 3.2.3 discharges featuring extremely large external gradient was expunged from the database and a dedicated discussion was postponed. The gradient values measured in such cases was so large to remind the pedestal formation typical of the tokamak H-mode, for this reason these cases has been dubbed as *electron External Thermal Barrier* (eETB). In Section 4.2 the topic will be faced: the experimental evidences of their occurrence, some general scalings and a first speculation on the physical mechanism leading to their formation will be presented. Finally, in 4.3 eITB and eETB will be compared: their plasma performance and confinement characteristics will be opposed and compared to general RFX-mod scalings.

4.1 eITB: Internal Transport Barriers

As mentioned before, the investigation of eITB, related to the thermal structure appearing in the plasma core during SHAx states, is intended to compare the external region temperature drop with the eITB temperature drop. It is worth noting that in the previous chapter this kind of temperature profiles was dubbed SHAx-like profiles. With this respect, the characterization of the full temperature profile is needed, thus well diagnosed SHAx-like profiles are necessary. For a selected subset of such discharges a more accurate analysis was performed. The SHAx-like profiles are not symmetric in the machine frame of reference so a characterization method different from the one used in the previous chapter was necessary. Advantage was taken from

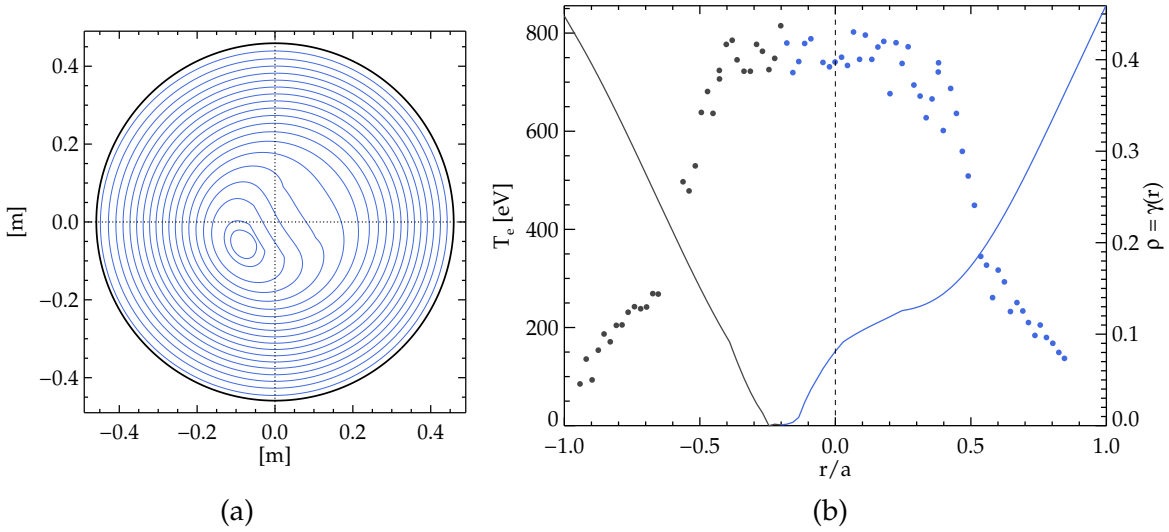

(a) (b)

Figure 4.1: Shot #22181 at 99 ms. (a) Flux surfaces computed as contours of the helical flux at the toroidal position of the main TS diagnostic. Courtesy of B. Momo. (b) Electron temperature profile of a SHAx state and the $\gamma(r)$ map. The two colors represent the new mapping of internal and external side.

the mapping of the temperature profile on a new helical coordinate system. This new set of coordinate is built in order to describe the helical deformation of the plasma column given by the growth of the dominant mode. In this context we are interested only in the new radial coordinate ρ_h which is the square root of the normalized toroidal helical flux[132], namely a label for the flux surfaces[a]. The quantity ρ_h, from now on simply ρ, is a flux function for single helicity states. In Figure 4.1 the flux surfaces for a SHAx state are depicted, together with the map $\gamma = \gamma(r) : r \to \rho$ which tracks the machine coordinate r to the new coordinate ρ.

4.1.1 eITB characterization method

The intrinsically asymmetric temperature profile of SHAx states, as measured in the machine frame of reference, becomes symmetric when represented in helical coordinates. So the characterization method proceeded in this way: initially a fit was preformed on the new coordinate system, then the analytic function was applied to the map γ so to obtain a numerical function describing the temperature profile mapped on the machine coordinate. Dubbing $H(\rho)$ the analytic fitting function used in helical coordinates, the numerical function tracking the temperature profile over r is $P = H \circ \gamma$, or similarly $P(r) = H(\gamma(r))$. In this way, the non symmetric profile displayed in the machine frame of reference is strictly mapped via the map $\gamma(r)$ which takes into account this asymmetry. The fitting function used to

[a] *The complete discussion of the helical frame of reference can be found in [132].*

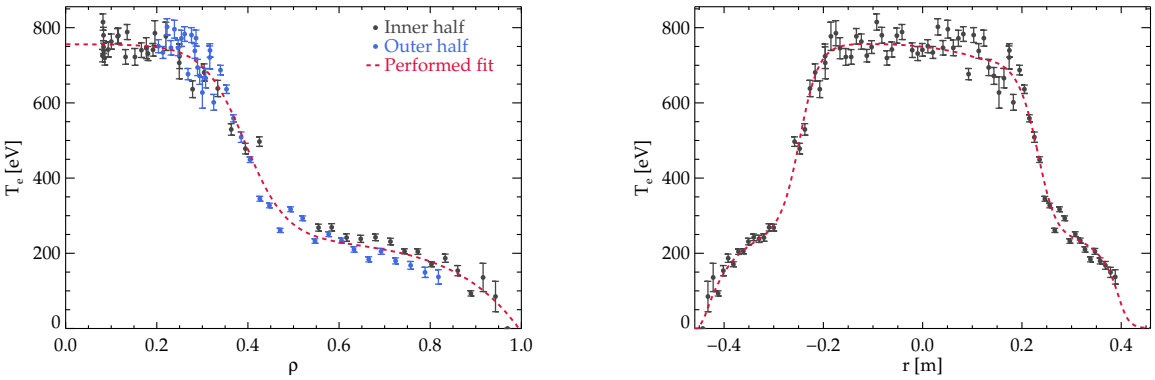

(a) (b)

Figure 4.2: Temperature profile characterization of a SHAx-like profile related to SHAx state. (a) A mapping of T_e on the helical coordinate system and the performed fit are shown. (b) The temperature profile, as it appears in the machine coordinate system, depicted together with the numerical function representing the whole profile.

characterize the temperature profile on the helical coordinate system is:

$$H(\rho) = A\left[e^{\frac{\rho-B}{C}}+1\right]^{-1} + D - e^{G(\rho-F)} \quad . \tag{4.1}$$

The former is similar to (3.3). In this case the Fermi function is used to characterize the internal transport barrier, while the decaying exponential term takes into account what happens in the region outside the barrier. The temperature profile in the machine frame of reference can be tracked applying the $H(\rho)$ function to map $\gamma(r)$, so to obtain a numerical function. This procedure is shown in Figure 4.2, where the two profiles are compared. The reason to choose a decaying exponential instead of the Fermi function to match the external region in this case is evident from Figure 4.2a: in the new frame of reference the external region temperature drop shows a smooth decay rather than a well defined slope bounded by almost flat regions. Such a shape would not have been well represented if the Fermi function was used.
Following the characterization of eITB given in [113], different quantities was estimated: T^{top}, r^{top} and T^{bott}, r^{bott} respectively temperature and position at the beginning and end of the barrier[a]. From this quantities others can be derived:

$$\text{spatial extent} : \Delta = r^{top} - r^{bott} \tag{4.2a}$$

$$\text{temperature drop} : \Delta T_e = T_e^{top} - T_e^{bott} \tag{4.2b}$$

[a] *In [113] the temperature on which the barrier sits was referred to as T_e^{foot}, T^{bott} was used here in order to avoid confusion during the discussion with T_e^{foot} characterizing the external region. Similarly the location will be dubbed as r^{bott} to refer to the* bottom *of the eITB location.*

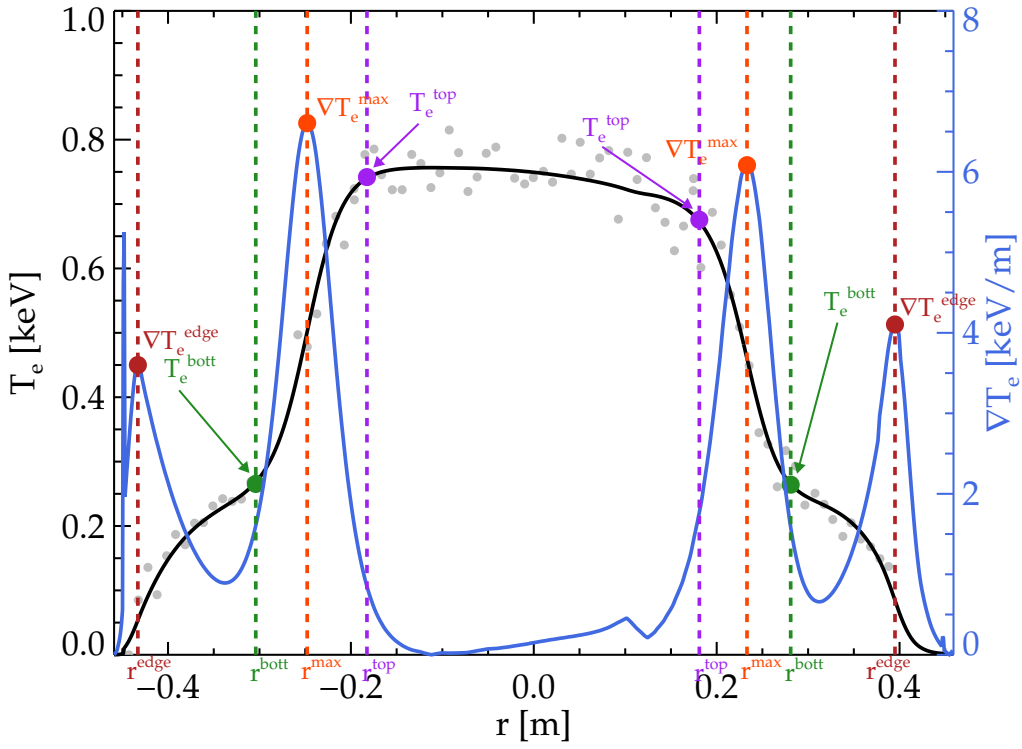

Figure 4.3: Full-matching method to characterize the SHAx state temperature profile.

accompanied from direct calculation of the eITB strength defined as the maximum gradient occurring inside the eITB spatial extent. These quantities are explicitly represented in Figure 4.3. The reason for mapping the SHAx profiles on machine coordinates is the need of a quantitative comparison between the strength of the external gradient and the eITB one. Such a comparison would be much more complex comparing dT_e/dr with $dT_e/d\rho$ because the changing the frame of reference, from r to ρ, has a complex metric whose computation is highly time consuming.

The quantities in expression (4.2) are similar to those used in the previous Chapter to characterize the temperature drop occurring in the external region. They have the same meaning but the method through which they are obtained is different. In fact, an exact parallel could have been drawn only if we had considered directly the fitting function $H(\rho)$ to calculate Δ and ΔT_e. Conversely, the further application of the map $\gamma(r)$ to obtain measurements in the machine frame of reference forced the choice of a different calculation method. The analytic calculation of Δ and ΔT_e was no more possible once H has been applied to γ. A numerical method was thus implemented. The details of the numerical calculation will not be discussed but a flavor of them can be found in Figure 4.3. Once the numerical derivative of $H(\gamma(r))$ was evaluated it has been used to localize the regions where $H(\gamma(r))$ flattens and to obtain a ∇T_e^{max} for both the ITB region and the external one. Then some manipulation was applied so to match as much as possible the analytical calculation to the

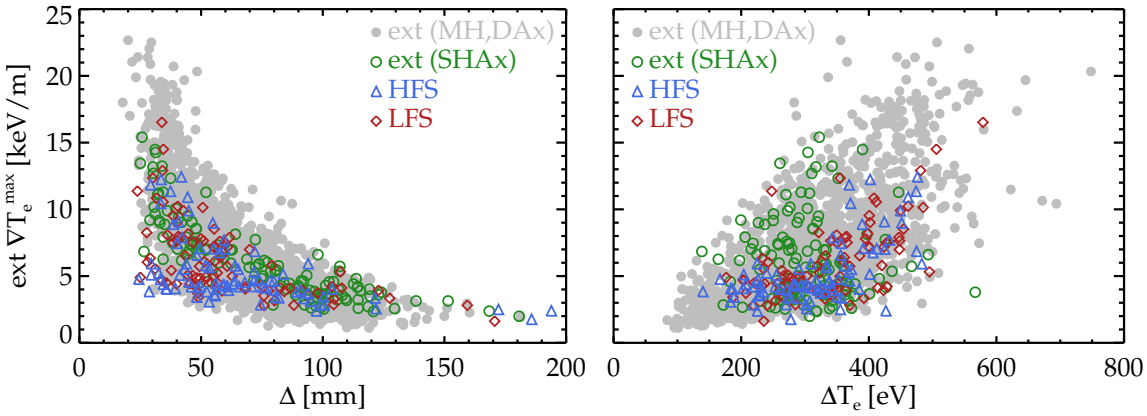

Figure 4.4: The quantities characterizing the external region temperature decrease evaluated via the two different methods are compared. Circles refer to the *Fermi fit* method applied to the external region explained in Chapter 3 while diamonds and triangles mark respectively LFS and HFS quantities estimated via the full profile matching method just explained. (left) Maximum temperature gradient versus temperature drop spatial extent. (right) Maximum temperature gradient versus temperature drop.

Fermi function outcome described in the previous chapter for the external region. Appreciable similarity has been reached but small differences still exist. These differences affect the evaluation of both the quantities characterizing the eITB region and the external one. Exploiting the already existing database of external profile matched with the Fermi fit, i.e. those analyzed in the previous chapter, the two methods was opposed on a restricted database of discharges pertaining to both databases. Such check highlights that the spatial extent of the external temperature decrease, Δ, for the SHAX-like profile, can be slightly underestimated if compared to those obtained for the external region in Chapter 3. Thus the ∇T_e^{max}can result a bit larger than the previous analysis. Nevertheless the two methods lead to comparable estimates, examples are given in Figure 4.4. From now on, the estimates of the quantities characterizing the external region coming from the two fitting methods will be considered equivalent and treated consequently. The characterization procedure of the full SHAx-like profile has been performed on 86 profiles from 67 discharges extracted from the database used in [113] having: $1.0\,\text{MA} \leq I_p \leq 1.8\,\text{MA}$, $2 \cdot 10^{19}\,\text{m}^{-3} \leq \langle n_e \rangle_l \leq 7{\cdot}10^{19}\,\text{m}^{-3}$ thus $0.1 \leq n/n_G \leq 0.3$ and $-0.08 \leq F \leq -0.03$.

Validation of the characterization method

A first test on the reliability of the characterization method was given: the quantities characterizing the external region obtained with the two different methods are comparable. Anyway, there was no possibility to test in a self-consistent way whether the method was reliable also for matching the eITB region. In fact, mapping the SHAx-like profiles in the machine frame of reference can introduce some errors and even some arbitrariness. In order to

further validate the method, its outcomes were opposed to a previous analysis performed with a different method. In [113] the temperature profile was matched using the interpolation routine provided by the ASTRA transport code[114], the quantities characterizing the profile were evaluated consequently. In that paper the eITB temperature drop and strength are reported to increase as the normalized amplitude of the secondary modes decreases, see Figure 4.5a and Figure 4.6a. To test the reliability of the method just proposed the two scalings has been replicated, Figure 4.5b and Figure 4.6b. In each of the two graphs, three different estimates are given: the two obtained from high and low field side in machine coordinates and the one obtained in the helical frame of reference. The temperature gradient assumes the right dimension because ρ_h has been multiplied by the minor radius of the plasma column, as used in [113]. The three estimates are markedly comparable. A qualitative match can be noticed considering both Δ values and the overall scaling in Figure 4.5. Conversely, in Figure 4.6, the match between the eITB strength is not as clear as the former, but still visible. One can note that the present analysis leads to larger gradient values if compared with [113], but this not affect the overall satisfying agreement of the two. It is worth to note that in the two plots b_φ^{sec} has been calculated according to [113] in order to ease the comparison. In fact, in [113] only the modes resonating around the barrier location was considered, namely $m = 1, -12 \leq n \leq -8$. In the rest of the discussion, anyhow, all n down to -15 will be considered, for the sake of coherence with the previous chapter. It should be stressed that the analysis under discussion is applied to a subset of the database considered in [113], some discharges have been dismissed because the characterization method did not provide a satisfying match to the experimental profile[a].

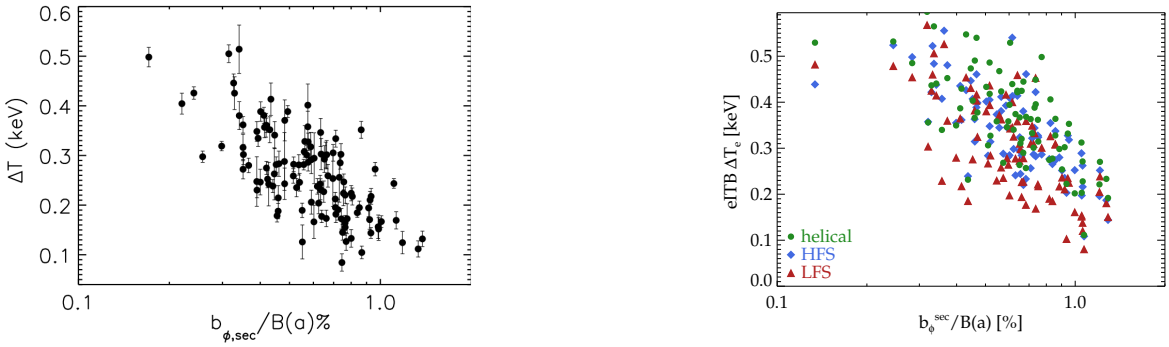

Figure 4.5: Electron temperature drop across the eITB, plotted as a function of the secondary mode amplitude normalized to the total magnetic field at the edge. (a) Figure 2 from [113]. (b) Data coming from the present analysis, distinguished between High and Low Field Side for calculation in machine coordinate. The values obtained from the calculation in ρ are also shown.

[a] *A statistical test has been performed to decide whether to expunge a discharge or not.*

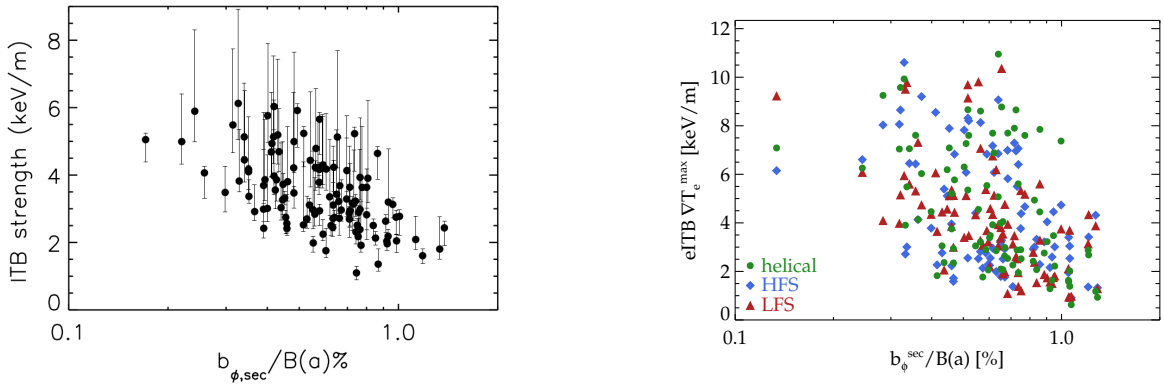

(a) (b)

Figure 4.6: ITB strength plotted as a function of the secondary mode amplitude normalized to the total magnetic field at the edge. (a) Figure 3 from [113]. (b) Data coming from the present analysis, distinguished between High and Low Field Side for calculation in machine coordinate. The values obtained from the calculation in ρ are also shown.

4.1.2 eITB empirical scalings

The eITB region is clearly governed by the physics related to the topological change of the magnetic equilibrium, thus to the chaos healing effect of the separatrix expulsion. Nevertheless, the residual magnetic chaos driven by the non-vanishing secondary modes is still the main source of electron energy transport in this region[113]. At the barrier the thermal confinement improves significantly, the heat diffusivity is reduced to $\chi_e \sim 5 \div 10$ m^2/s[113]. Such values are well below the typical values of the region outside the eITB ($r > r_{bott}$) where $\chi_e \sim 20 \div 100$ m^2/s, typical values of MH states[133]. Also in the outer region ($r > r_{bott}$), the transport is likely to be due to magnetic chaos. In fact, field-line tracing codes show the presence of persistent magnetic chaos in this region[134]. The effect of a reduced magnetic chaos on the eITB region has already been verified in this analysis, figurename 4.5 and Figure 4.6, while in Chapter 3 empirical scaling laws for the temperature profile changes in $0.6 \lesssim |r/a| \lesssim 0.9$ has been obtained. It is interesting to merge these considerations in order to compare the average behavior of the temperature profile in the external region to that of the SHAx states. To this extent, the model (3.13) has been used to fit the central temperature T_e^0, the temperature at the top of the eITB T_e^{top} and the temperature at its bottom T_e^{bott}, the result is shown in Table 4.7a and plotted in Figure 4.7b. At a first glance at Figure 4.7 one can note that T_e^0 and T_e^{top} show similar dependencies on the considered physical parameters, as one would expect. In fact, in SHAx-like profiles the temperature at the top of the barrier is almost equal to the core temperature, only small differences can be found due to asymmetry of the mapping in the machine frame of reference. The distinction here was maintained just to verify once more the characterization method. From now on T_e^0 and T_e^{top} will be considered as the

	T_e^0	T_e^{top}	T_e^{bott}
α	0.018 ± 0.022	0.014 ± 0.018	0.002 ± 0.002
γ_{I_p}	0.652 ± 0.084	0.661 ± 0.088	0.900 ± 0.091
γ_{n_e}	-0.197 ± 0.048	-0.177 ± 0.050	-0.457 ± 0.050
γ_F	0.010 ± 0.023	-0.008 ± 0.025	-0.108 ± 0.027
γ_{sec}	-0.297 ± 0.042	-0.304 ± 0.045	-0.043 ± 0.047
γ_Δ	-0.075 ± 0.048	-0.014 ± 0.018	-0.045 ± 0.051
$RMSE$	11.91%	12.51%	12.80%
R	0.75	0.73	0.83

(a)

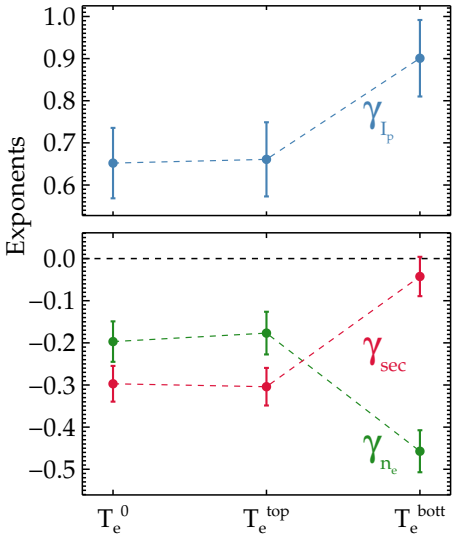

(b)

Figure 4.7: (a) Summary of the regression performed on T_e^0, T_e^{top} and T_e^{bott} based on the model (3.13) for eITB. (b) Some of the exponent in (a) sketched for visual comparison, the horizontal axis is not on scale.

same. Conversely T_e^{bott} behaves differently from the former two, as can be expected. Before entering the details of Figure 4.7, it is interesting to note that the bottom of the ITB is generally located at $r_{bott} = 314 \pm 24$mm, i.e. $r_{bott}/a = 0.685 \pm 0.053$, thus remain generally more internal with respect to the location of the knee of the external temperature drop obtained in Chapter 3 $r_{knee} = 342 \pm 19$mm, i. e. $r_{knee}/a = 0.75 \pm 0.041$.

First of all, I_p has the main role in establishing the temperature, as generally happens for the temperature in the core and in the external region. However a clear difference arises between the eITB region and the region outside the barrier. The plasma current influence is stronger outside the barrier (T_e^{boot}) rather than inside it (T_e^{top}). This is probably due to the marked importance taken by the magnetic state of the plasma. Inside the barrier, in fact, $\gamma_{sec} \sim -0.3$ similar to the value found for T_e^0 in the general analysis. But, in this case, this strong influence is radially extended all the way to $r_{top}/a \sim 0.2$. It is important to note that the secondary modes decrease is more effective than density in influencing the barrier region. This situation is reversed outside the barrier where T_e^{bott} is almost insensitive to the amplitude of the secondary modes and the density contributes significantly to establish the temperature. The region outside the barrier thus behaves similarly to the general case, indicating that the transport improvement is effectively limited to the region enclosed by the barrier. To conclude $|F|$ and Δ are rather ininfluent on the temperature inside the barrier, while T_e^{bott} is weakly dependent on $|F|$ as was observed for T_e^{knee}. To summarize, in the eITB region the secondary modes reduction is so important in establishing the temperature to reduce the effectiveness of

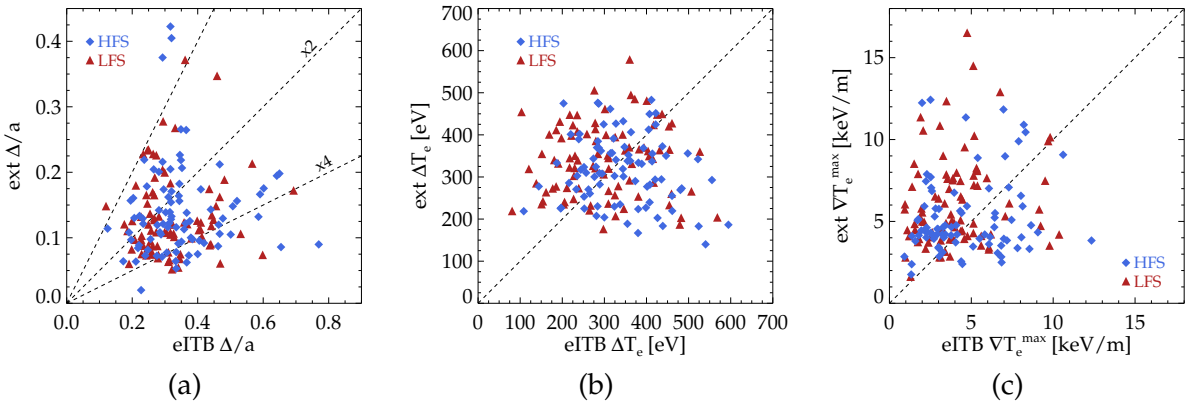

Figure 4.8: Comparison between the eITB and external region in SHAx-like profile. (a) Spatial extent, (b) temperature drop and (c) maximum gradient. The database are distinguished between the two sides of the plasma. The axes are isotropic in (b) and (c), this is not the case for (a). In each graph the bisector is reported, in (a) also the two-fold and four-fold lines are shown.

current and density. Conversely, in the region outside the barrier $r \geq r_{bott}$ the secondary modes are less influent leaving current and density as main temperature modifiers.
We can draw a parallel between the *knee* of the external region and the *bottom* of the eITB: both of them mark the frontier between two regions behaving differently. The *knee*, sitting approximately at $r_{foot}/a = 0.75$, is probably governed by the chaotic transport due to the overlapping of a sea of MHD modes and separates the external temperature increase which deals mainly with wall conditions, edge topology, density profile and neutrals penetration depth from the inner region. Similarly, the *bottom* of the eITB is probably governed by the same physics governing the *knee*, and it separates the barrier region interested by the topological change due to the growth of the dominant mode from the region outside the eITB which is less affected by such a new topology. It is worth noting that a regression was tried also on ∇T_e^{max}, i.e. the eITB strength, even using different models. It was not possible to find a model matching the database with a significant quality. A satisfying explanation for the fact is still missing, so we assume ∇T_e^{max} to increase with decreasing amplitude of the secondary modes, recall Figure 4.6b, and increasing current without any other particular dependence.
The temperature in the region $0.6 \lesssim |r/a| \lesssim 0.9$ was shown to be only scarcely affected by the kind of thermal profile (MH, DAx or SHAx), see Chapter 3, anyhow such an evidence can be further investigated probing the eventual link between the temperature drops occurring in the eITB region and in the external one. In Figure 4.8 the spatial extent, the temperature drop and the maximum gradient of the two regions in SHAx-like profiles are compared. A first clear evidence is that no relation exists between the two regions, this leads to two direct consequences. On the one hand, it reinforces the idea that the two regions are governed by different physics, or at least that the secondary modes reduction is effective only inside the

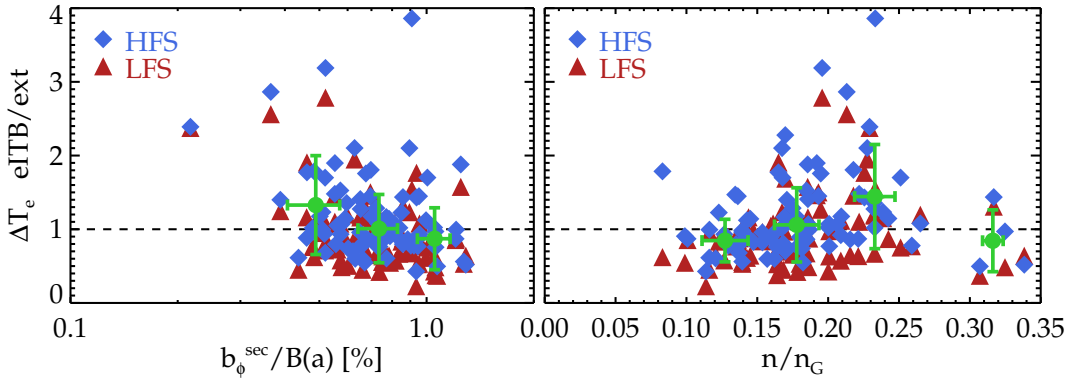

Figure 4.9: Comparison between the eITB and external region in SHAx-like profile, the ratio between eITB region and external region temperature drops is reported. (left) Temperature drops ratio versus amplitude of the secondary modes. (right) Temperature drops ratio versus Greenwald density fraction. A moving average is superposed to the database. Error bars represent the standard deviation of each averaged sample.

eITB region. On the other hand, it states that the two regions are not negatively interacting thus leaving open the possibility to a concurrent amelioration of the transport affecting both the regions. Deepening the examination, one can note that while the magnitudes of the temperature drop are similar, the external spatial extent is generally half of the eITB one leading to an average higher gradient in the external region.
If the two regions were actually ruled by different mechanisms one would expect to find the ratio between corresponding parameters to scale with some macroscopic parameter. As a matter of fact, this is the case as can be seen in Figure 4.9. The ratio between the temperature drop across the eITB region and across the external region is found to slightly vary with both the amplitude of secondary modes and Greenwald density fraction. As the secondary modes are suppressed the ratio between the two ΔT_e is found to increase suggesting that a reduced chaos is more effective in the eITB region rather than in the external one. Conversely, to an increasing Greenwald density fraction corresponds an increase of the ΔT_e ratio confirming the idea that a change in the wall conditions affects the external region but does not alter, or only weakly affects, the remaining fraction of the plasma column. This evidence points towards the short penetration of neutrals as a relevant issue to solve in order to improve the confinement properties of the RFX-mod plasma.

4.2 eETB: External Thermal Barriers

In Chapter 3 an open issue was left: the discussion of extremely high gradients occurring in the external region, which were expunged by the database, was postponed. It is important to remember that the selection was made on statistical basis: values too far from the scaling law representing the ∇T_e^{max} population were dismissed. This subset includes maximum gradient

values raging from ~ 10 keV/m up to ~ 40 keV/m. The occasional appearance of such strong temperature gradients was one of the reason that motivated the entire analysis. In order to simplify the discussion such peculiar cases will be dubbed as *electron External Thermal Barrier* (eETB). Figure 4.10 depicts an example of such a case in comparison with a SHAx-like profile, i.e. a temperature profile characterized by the appearance of the Internal Transport Barrier. One can note how steep is the gradient in the eETB case: the two profiles show a similar temperature drop $\Delta T_e \sim 600$ eV, but while the internal barrier extends for approximately 14 cm the external one spans only ~ 3.5 cm. Thus the average eETB gradient is approximately 20 keV/m, four times larger than the eITB one.

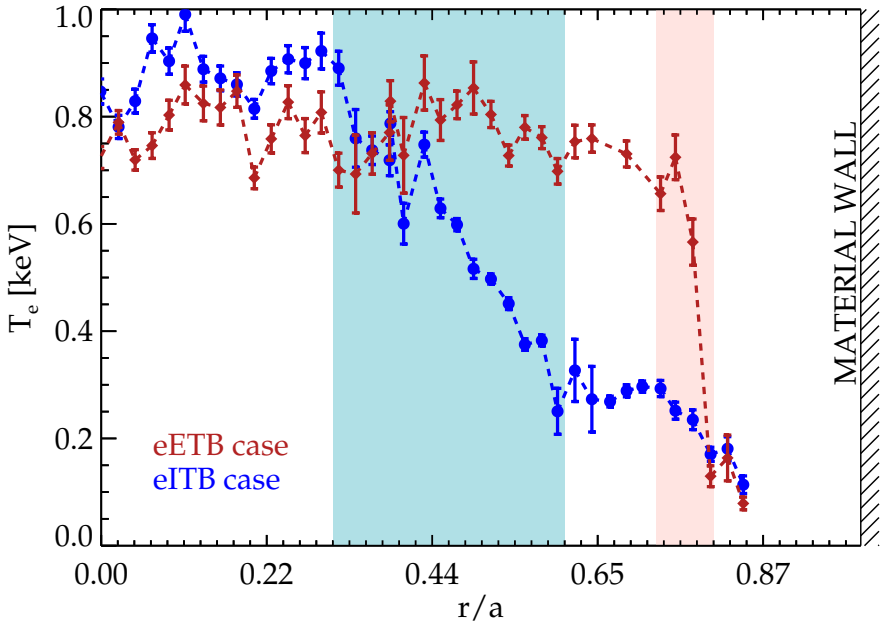

Figure 4.10: Temperature profiles comparison: in blue an eITB case while the eETB is represented in red. Only half of the profile is shown to enhance the comparison. The regions characterized by the barriers are shaded.

86 profiles were dismissed from the general database and thus form the eETB database represented in Figure 4.11. The selection method, based on a statistical procedure, does not allow to find any necessary condition related to macroscopic parameters for the eETB formation. In fact no hard limit can be seen in the $(\tilde{b}_\varphi^{sec}, I_p)$ plane neither in the $(q(a), I_p)$ plane. Anyhow, one can note that none of such high gradients are found simultaneously to the formation of an internal transport barrier. Given the poorer statistics of both the barriers (eITB and eETB), one can not exclude that they could coexist and there is no evident physical reasons to reject such a possibility.

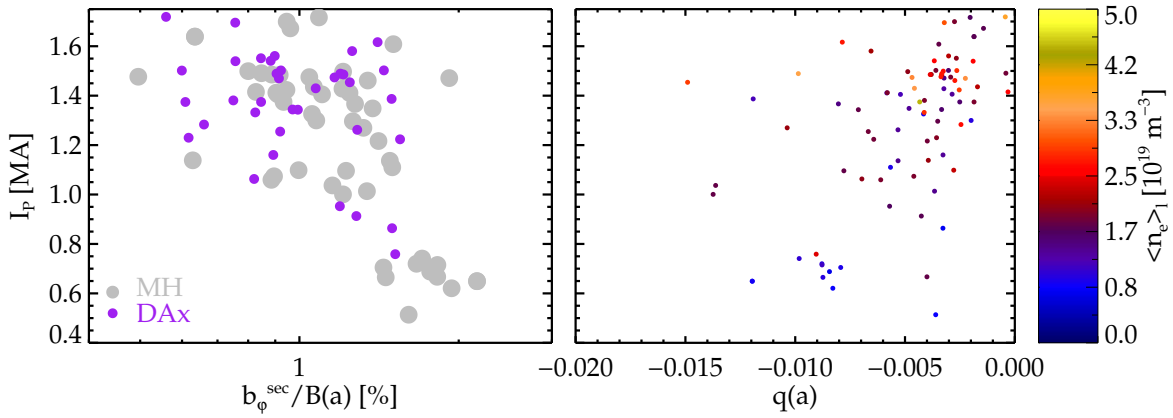

Figure 4.11: Database of the eETB cases. (left) Plasma current versus secondary modes amplitude. The dataset is divided accordingly to the kind of temperature profile(MH-like or SHAx-like). (right) Plasma current versus edge safety factor. The color scale marks the line average density.

4.2.1 Characteristics and scaling

The reduced number of data did not allow to perform a parametric analysis as done before. A multi-parameter regression based on the model (3.13) was tried but the outcome was not trustworthy. All the powers, apart from the current one, were approximately null or compatible with 0 within the error bars. So that method was left and a more direct visual analysis will be proposed.

Even if no necessary nor sufficient conditions can be found to link the eETB occurrence to macroscopic parameters, the formation of eETBs is favored at shallow reversal and low Greenwald density fraction. More than the 70% of eETBs are found for $F > -0.04$ where also the largest gradient values are located. Moreover no eETBs are found for density values exceeding $n/n_G \sim 0.2$. On average, the eETBs are located at $r = 367 \pm 15$ mm, i.e. $r/a = 0.80 \pm 0.03$, but their location gets closer to the wall with increasing plasma current. As a matter of fact both the *knee* and the *foot* of the eETB moves towards the wall increasing the current, see Figure 4.12a. Being $r_{max} \approx (r_{knee} + r_{foot})/2$, the barrier location moves consequently[a]. The outward shift of r_{knee} and r_{foot} is net and evident up to $I_p \sim 1.2$ MA, beyond such value the trend becomes largely scattered and eventually no more visible. Interestingly such movement is related only to plasma current and not to density, as it was found in the general case. The explored range in Greenwald density fraction is limited suggesting density to act as a show-stopper for the eETBs: once exceeded $n/n_G \sim 0.2$ no more eETBs can be found, below this limit the role of density seems to become marginal. The outward shift of the barrier extremes is really similar, thus no net dependence on current was found for the eETB spatial extent. Δ is not influenced neither by density even if two distinct

[a] *r_{max} marks the location where the maximum gradient occurs, namely the center of the temperature decrease. Refer to Page 55 to revise the symbology related to the Fermi fit method.*

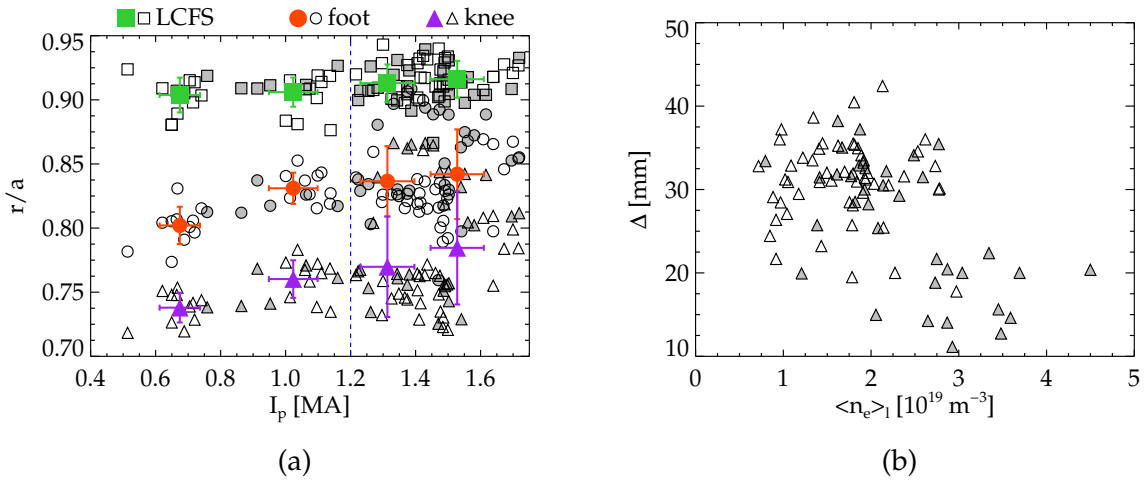

Figure 4.12: Scaling of eETB spatial characteristics. (a) *knee* and *foot* location versus plasma current. The average position of the LCFS is also shown. (b) Spatial extent versus line average density. Void symbols mark MH-like profiles while gray shaded symbols mark DAx-like ones. In (a) a moving average is superposed to the database. Error bars represent the standard deviation of each averaged sample.

groups seem to exist, see Figure 4.12b. A numerous group with $\Delta \sim 30$ mm is located below $\langle n_e \rangle_l \sim 3 \cdot 10^{19}$ m^{-3}, while another group, less numerous, with smaller Δ extends through the entire density range. No difference was found between the two groups apart from this one, but considering that 30 mm was the limit imposed by the fitting method such discrepancy can be related to the fitting procedure[a]. So a first difference arises with the general behavior of the temperature decrease in the external region: while the temperature profile across the external region generally tends to flatten expanding towards the wall when Greenwald density fraction is raised, the eETBs move rigidly outward as current increases up to $I_p \sim 1.2$ MA. For higher current values the barrier is approximately fix while its spatial width is scattered. It is worth noting here that the lowest values of Δ and the highest values of r_{knee} and r_{foot} pertain almost exclusively to DAx-like profiles and are related to the highest density values.
Given the scalings found in Chapter 3, one can expect T_e^{knee} and T_e^{foot} to increase with current. As a matter of fact this does happen, see Figure 4.13a. The trend for both the temperatures is extremely net, the few points deviating a bit from it, for $I_p > 1.2$ MA, are those with the lowest Δ values . As for *knee* and *foot* locations, the two temperatures does not show to be influenced by the normalized density, but their difference does. In fact, in Figure 4.13b the temperature drop is shown to decrease with increasing Greenwald density fraction. It is important to point out that this dependence in mainly due to plasma current while the role of density is only

[a] *It is worth to remember that the possibility for Δ to achieve values below 30 mm was evaluated statistically, see Section 3.1.2. A sort of discontinuity can arise in the discrimination method which was based on a 'yes/no' F-test. More details can be found in [110] where the F-test technique to compare two different regressions is explained.*

marginal. In other words: at the lowest density ΔT_e from 200 eV up to 800 eV are found, increasing the density this range shrinks coming to the point that at the highest density no ΔT_e larger than 400 eV are present. Thus the temperature drop depends clearly on current and weakly on density, this two trends together lead to Figure 4.13b. As a last remark, the linear link between the maximum gradient and the plasma current can be noticed in Figure 4.13c. Such behavior was expected since $\nabla T_e^{max} \propto I_p^{0.825}$ was found to generally hold in the external region, see Section 3.3.3. This trend reflects once more that to a higher input power corresponds a higher edge gradient, even when eETBs are formed.
Recalling the model used to represent the temperature variation in the external region (3.13) and the results found in 3.3.2, one should expect the density to be more effective on T_e^{knee} and T_e^{foot} and F to be marginally important in comparison to what have been just highlighted. This is not the case of eETBs and the reason relies on the magnetic topology related to the occurrence of such strong edge gradients. As a matter of fact, even if not all of them was checked, eETBs occurrence can be related to the formation of an *effective SOL*, recall Section 2.3.1 and Section 3.5.1. Such an evidence allows to explain the different scaling of the eETB characteristics compared to those generally found for the external region. Before entering the details of such a discussion is important to note that there are many experimental findings pointing towards a direct link between the eETB occurrence and the formation of the effective SOL.

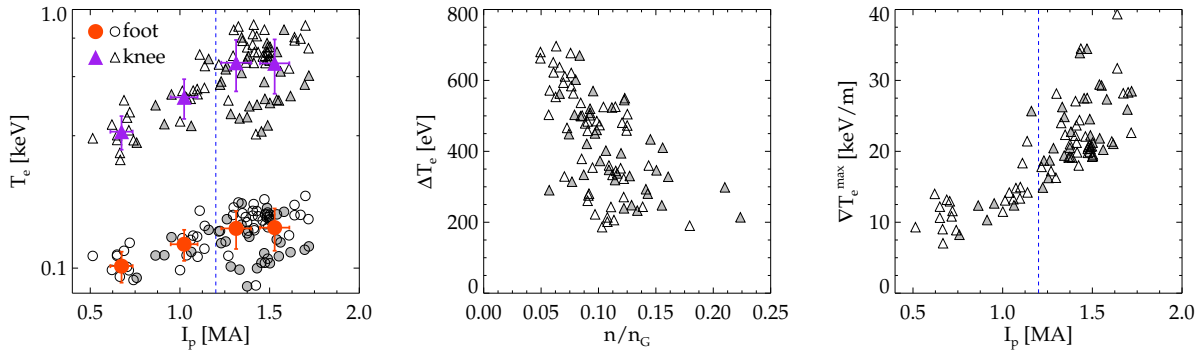

Figure 4.13: Scaling of eETB temperature drop characteristics. (a) *knee* and *foot* temperature versus plasma current. (b) Temperature drop versus Greenwald density fraction. (c) Maximum gradient versus plasma current. Void symbols mark MH-like profiles while gray shaded symbols mark DAx-like ones. In (a) a moving average is superposed to the database. Error bars represent the standard deviation of each averaged sample.

4.2.2 Effective SOL formation: the drive for ETBs

First of all, a visual check of the edge topology via the Poincaré plot was performed for some of the eETB cases, one of them is shown in Figure 4.14. On the left, the Poincaré plot of the plasma edge at the main TS firing time is shown. Such a plot was computed by the Field Line Tracing code FLiT[88]. The black solid line marks the LCFS. On the right the temperature profile and the associated Fermi fit are plotted. It can be seen, as showed by the arrow, that the LCFS is located outside the temperature increase. Such picture is coherent with previous

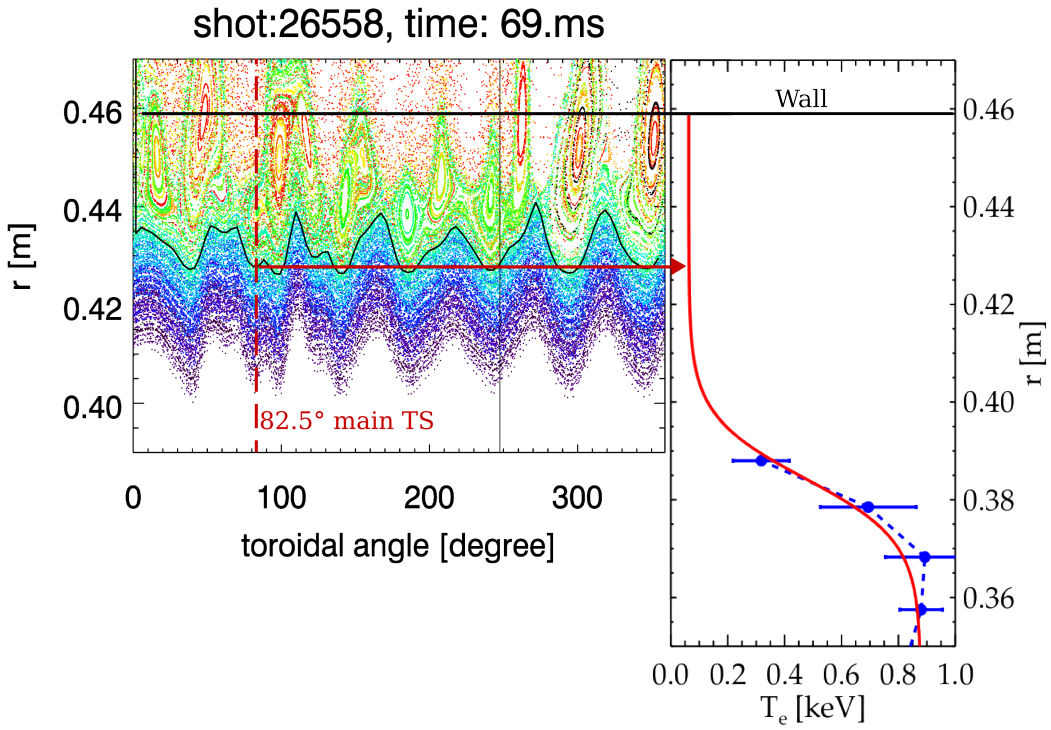

Figure 4.14: Poincaré plot of the RFX-mod plasma edge corresponding to an eETB. The solid black line marks the position of the LCFS. The dashed vertical line represent the toroidal location of the main Thomson Scattering diagnostic. Courtesy of B. Momo. On the right the temperature profile is reported together with the Fermi fit. The horizontal arrow marks the position of the LCFS at the main TS location on the temperature profile.

findings: the $m = 0$ islands create a short-circuit between different plasma regions and, in this case, they directly intercept the first wall. Consistently with the observation of flat temperature profiles inside the $m = 0$ structures[86], a flat temperature region extending from the wall to the LCFS location is expected in this situation. As a matter of fact, the temperature increase is located inboard with respect to the $m = 0$ islands chain. This phenomenology maps exactly the profile change linked to the formation of the effective SOL already explained at Page 89. This is not the whole story, in fact the formation of eETBs is related to a further improvement of this topology. In fact, the strongest barriers arise when the volume of the

plasma characterized by short magnetic connection lengths is small enough, namely when the LCFS is strongly pushed towards the wall without intercepting it. The eETB barrier develops where ordered magnetic surfaces start to appear out of the chaotic region at inner radii[159], namely $r \lesssim 0.39$ m in Figure 4.14. To verify such picture a Poincaré analysis of each case would had required, but the large time demand related to such a procedure drove the need for an alternative way. As a response, an approximated method to evaluate the position of the LCFS was conceived.

Considering an equilibrium magnetic field, the reconnection of magnetic field lines produced by an applied perturbation can be treated analytically. Consequently, the width of the magnetic island produced by the field lines reconnection can be consistently evaluated[8]. Such treatment applied to RFX-mod plasma edge case, thus considering an $m = 0/n$ perturbation, leads:

$$w_n \approx 4\sqrt{\frac{r_{rev}\, b_r^{0,n}}{nq'\big|_{r_{rev}} B_\theta(a)}} \tag{4.3}$$

where w_n is the island width related to the $m = 0/n$ Fourier component, n is the toroidal wave number of the perturbation, r_{rev} is the reversal radius, i.e. the radius of resonance of the $m = 0$ modes. In addition, $b_r^{0,n}$ is the amplitude of the $m = 0/n$ Fourier component of the radial perturbation, $q'\big|_{r_{rev}}$ is the radial derivative of the safety factor profile evaluated at r_{rev} and $B_\theta(a)$ is the total poloidal field at the plasma edge. Such a formula holds only if the perturbation has a monochromatic character, thus it does not take into account the possible interplay between different Fourier components. Clearly this is not the case for the real situation where all $m = 0/n$ components resonate at the reversal surface. Anyhow, a single component generally dominates over all the others: the $m = 0/n = 1$ in MH states, while in QSH states the $m = 0/n = 7$ component dominates over the others. The evaluation in (4.3) has been applied to each of the eETB cases. In order to be as accurate as possible, the island width for all the components $1 \leq n \leq 15$ has been evaluated and the largest of them has been used, thus:

$$w \equiv \max_{1 \leq n \leq 15} w_n \qquad .$$

For the large part of the considered cases the largest contribution was related to $n = 7$, the remaining fraction was related to $n = 1$. In such cases w_1 differs from w_7 by less than 2 mm, so they can be considered as equal. Expression (4.3) does not contain any information about the toroidal asymmetry of the edge region and can not aim at representing the complex topology reported in Figure 4.14. Anyhow the estimate in (4.3) can be assumed as representative for the average $m = 0$ islands width. Exploiting the few cases for which the Poincaré plot was evaluated, a visual verification of the estimate given by (4.3) was made. The island width resulted to be overestimated by a factor two, so to correct this overestimation the outcome of (4.3) has been reduced by a factor two. Such overestimation can be ascribed to the simplification of the model used to obtain (4.3), as already mentioned. The edge topology is so complex that

this simple analytic treatment is generally not suitable to estimate the island width. Anyhow, when the $m = 1/n = -7$ mode dominates, the large localized deformation of the $m = 0/n = 1$ mode is no more visible and the estimate (4.3) becomes qualitatively acceptable. Now, having an average estimate of the $m = 0$ island width, w, and the average radial position of the reversal surface, r_{rev}, an average location of the LCFS can be estimated as:

$$r_{LCFS} = r_{rev} - w/2 \quad .$$

As an example, referring to Figure 4.14, calculation gave $w = 38.6$ mm, being $r_{rev} = 0.440$ m the LCFS average location result $r_{LCFS} = 0.421$ m. Such an estimation is far from being accurate, but for the scope of this analysis and given the radial accuracy of the Fermi fit method in mapping the edge region it is fair enough. r_{LCFS} is found to map the more inward protruding edges of the real LCFS within 1 cm accuracy. Recalling the δ_{min} defined as the distance between the real LCFS and the wall at Page 47, the similarity $(a - r_{LCFS}) \sim \delta_{min}$ holds.

Using such an estimation, the picture relating the eETB occurrence to the effective SOL formation can be strengthen. In fact, in the large majority of eETB cases the estimated LCFS lies outside the foot of the barrier, suggesting that outside the LCFS the temperature is low enough to be comparable to the wall temperature. Furthermore, the mutual distance between the foot and the LCFS location increases with increasing r_{LCFS} and for most of the cases is larger than 2 cm, see Figure 4.15a. As a result, the temperature at the LCFS approximately matches the wall temperature for all the eETBs. It should be noted that this fact is strongly related to the Fermi fit characteristics, in fact for radii outside $r_{foot} + \Delta/2$ the profile is completely flat. Given the extremely narrow spatial extent of the eETBs, this generally

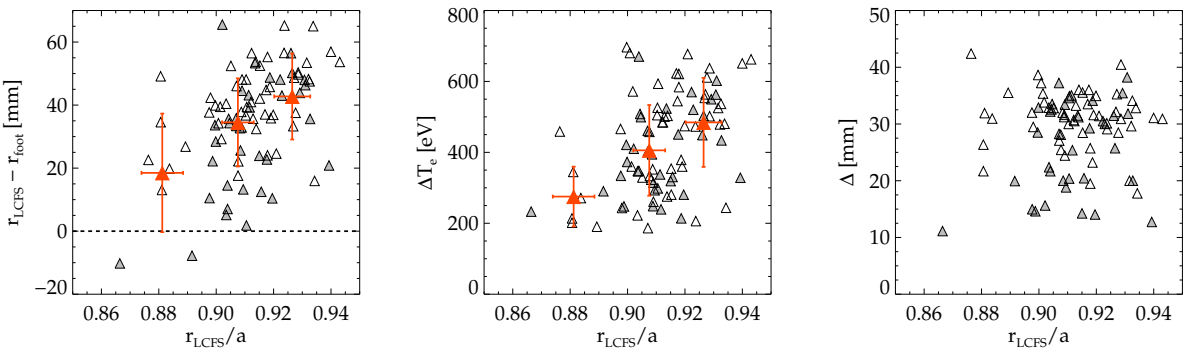

(a) (b) (c)

Figure 4.15: Scaling of eETB characteristics. (a) distance between the *foot* and the LFCS, (b) temperature decrease and (c) spatial extent as functions of the LCFS location. In (a) and (b) a moving average is superposed to the database. Error bars represent the standard deviation of each averaged sample. Void symbols mark MH-like profiles while gray shaded symbols mark DAx-like ones.

happens approximately 2 cm outside the foot position and the ratio $T_e^{rev}/T_e(r=a)$ is exactly 1 in the 80% of the cases. Such a consideration has a purely mathematical flavor and could seem artificial, we left Section 4.2.4 to discuss the reliability of the analysis method. As the LCFS approaches the wall, the temperature drop across the barrier is found to significantly increase, apart from a reduced set of cases, as shown in Figure 4.15b. It is worth to point out that the LCFS does not sensibly move increasing the current, see Figure 4.12a. In fact, if on the one hand, the high current operations are always performed at shallow F, on the other hand pushing the reversal surface towards the wall the amplitude of the $m=0$ modes are generally reduced[100], thus the islands width reduces. As a consequence, in this database, as the current increases the eETBs foot gets closer to both the wall and the LCFS, Figure 4.12a. This has an important consequence: the increase of ΔT_e with increasing r_{LCFS} plotted in Figure 4.15b. Pushing the LCFS towards the wall does not affect the spatial extent of the temperature decrease, Figure 4.15c. So in the eETB case no net relation between Δ and any macroscopic parameter has been found. Despite so, the maximum gradient follows the behavior of ΔT_e, it increases when the LCFS gets closer to the wall.

4.2.3 Overall physics of ETBs

The section has been dedicated to the investigation of electron External Temperature Barriers, extremely high gradients developing approximately at $r/a=0.8$. The occurrence of eETBs has been related to a change in the edge plasma topology, more precisely to the formation of an effective SOL, extending for some centimeters inside the material surface, due to the intersection of $m=0$ islands chain with the material wall. This forces the LCFS to move inboard with respect to the $m=0$ islands chain setting a separation between the edge plasma dominated by the transport short-circuit due to the presence of the magnetic island and the more internal region dominated by parallel transport in a stochastic magnetic field. Therefore, the edge/core separation induced by the formation of the SOL leads to the formation of strong external gradient with an extremely small spatial extent, $\Delta \sim 3$ cm, entirely located inboard with respect to the LCFS, the eETBs. The barrier foot, in fact, is found to lie some centimeters inside the LCFS leaving an almost flat temperature region outside it. Provided the effective SOL is formed, the temperature drop across the barrier is found to increase pushing the LCFS towards the material surface and an increase of the plasma current triggers a shift of the barrier position towards the LCFS. Such eETBs are found only at Greenwald density fraction lower than 0.2. The spatial extent of the temperature decrease occurring in the region $0.6 \lesssim |r/a| \lesssim 0.9$ was found to generally decrease with increasing n/n_G, recall Chapter 3. In fact, increasing n/n_G the density profile tends to peak at the edge becoming hollow[120] with a consequent flattening of the temperature profile due to the higher edge electron density and to the lower penetration of neutrals.
During the entire discussion of the eETB nothing was said about the magnetic state of the plasma. In fact, as generally happens for the region outside r_{knee}, the eETB characteristics are

not sensitive to a reduction of the magnetic chaos as measured by the amplitude of the secondary modes or by the ratio $b_\varphi^{1,-7}/b_\varphi^{sec}$. In other words, the two former quantities convey information about the transport in the core of the plasma, thus the insensitivity of the region $r/a \gtrsim 0.8$ to changes in such parameters should not be surprising. Conversely, one could expect to find a correlation of the eETB characteristics with the amplitude of the low-n $m = 0$ modes, produced by their nonlinear coupling with the $m = 1, n = -7$ mode due to the $m = 1, n = 0$. Such perturbations, in fact, jeopardize the formation of the effective SOL. Nevertheless none of the temperature profile characteristics were found to correlate to the amplitudes of such modes. Probably the analysis technique is not sensitive to such degree of detail.

4.2.4 Final remarks

Doubt can arise about the whole analysis of the eETB, in fact it has been based on considerations made upon a radial region poorly diagnosed and where no TS measurement are available, namely $r/a \gtrsim 0.9$. As a matter of fact the Fermi fit procedure was intended to match the temperature profile in the region $0.6 \lesssim |r/a| \lesssim 0.9$ without any ambition to map simultaneously the plasma edge[a]. Nevertheless the physics outcome of this Section is based on a series of different and independent measurements which can hardly admit to consider the whole picture as a fortuity. *A posteriori*, we can state that the Fermi fit procedure is also capable to qualitatively represent what happens at the plasma edge. A few discharges where eETB occurred were diagnosed with the Thermal Helium Beam diagnostic, so a direct test can be given. Figure 4.16 plots such a comparison for four different profiles at different plasma current and electron density values. It is evident that the temperature is not flat in the region diagnosed by the THB, but the value assumed by the Fermi fit through the entire region is accurate within 20 eV. Such an error is not appreciable if the whole profile is considered. Insertable probes measurements showed that inside an edge $m = 0$ island in RFX-mod, the temperature is almost flat with a fluctuation of ~ 20 eV [86]. Figure 4.16 is consistent with such measurements and the approximated flat profile given by the Fermi fit is thus qualitatively acceptable.

[a] *It is important to remember that average edge conditions was used to bound the fit parameters at the plasma edge, see Page 57*

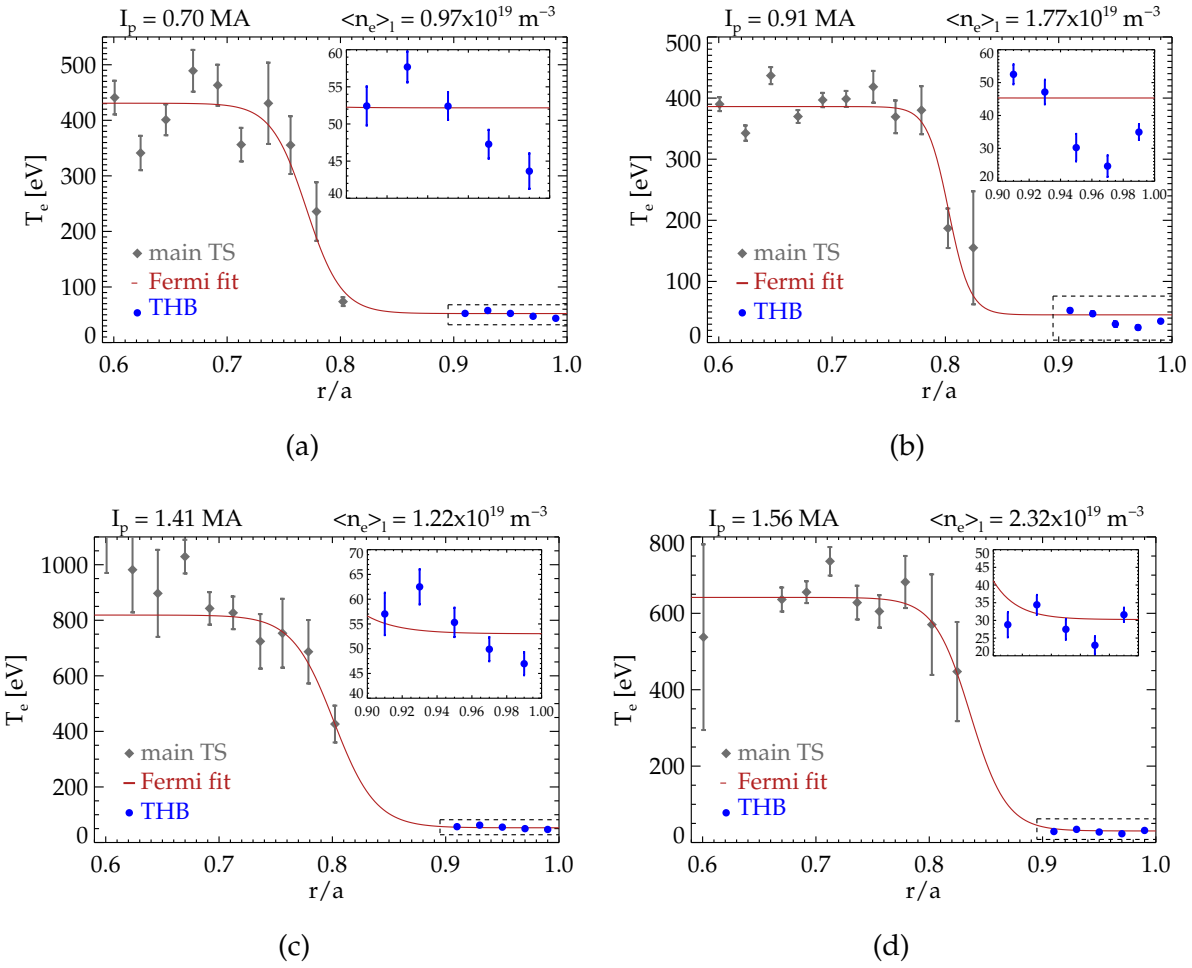

Figure 4.16: Edge mapping accuracy comparison. In every graph, representing an eETB, data from the main TS and from the THB are showed together with the relative Fermi fit. The small plane depicts a zoom of the edge region bounded by dashed lines in the main figure. The values of plasma current and electron density relative to the profiles are given on top of each. The relative Greenwald density fraction are: (a) $n/n_g = 0.092$, (b) $n/n_g = 0.129$, (c) $n/n_g = 0.057$, (d) $n/n_g = 0.097$.

4.3 eITBs vs eETBs: plasma performance and confinement properties

To conclude the chapter a brief discussion about the confinement properties of plasmas characterized by internal and external barriers is proposed. For the eITB case transport analysis was performed and the heat diffusivity, χ, at the barrier was evaluated by a power balance equation with the helical 3D magnetic equilibrium as an input (SHEq code, [135]) in a number of cases. χ ranges from 5 to 10 m^2/s and was reported to decrease with decreasing $b_\varphi^{sec}/B(a)$ [113]. Conversely, for plasmas characterized by the eETBs no detailed transport studies has already been performed. So, to verify if the occurrence of eETBs was actually accompanied by enhanced plasma performance, the β_θ parameter and the electron energy confinement time, $\tau_{E,e}$, have been calculated. A few discharges characterized by the occurrence of eITB or eETB has been chosen considering the quality of the complete temperature profile match. For such discharges the density profile was evaluated through the inversion of interferometric data so the pressure profile can be obtained as the product of density and temperature, an example of two such discharges is shown in Figure 4.17.

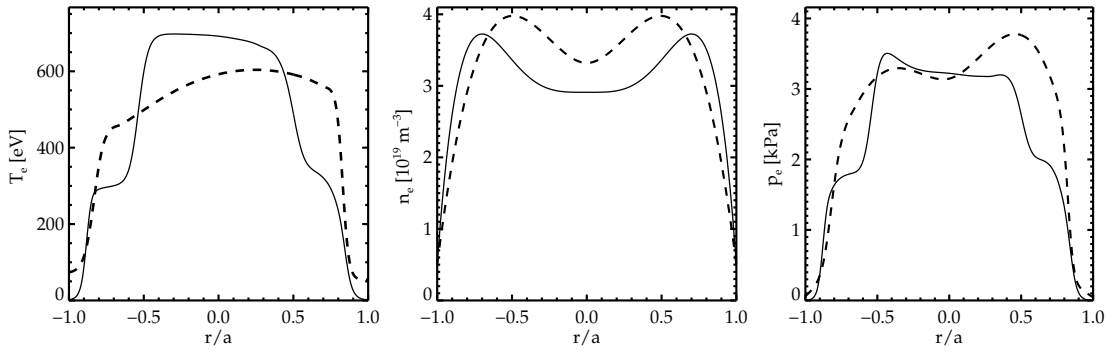

Figure 4.17: eITB (solid line) vs eETB (dotted line): electron temperature, density and pressure radial profiles mapped in the machine frame of reference. Electron temperature profiles are fully fitted according to the different methods while density profiles are obtained inverting data from the interferometer. Electron pressure is evaluated as the product of temperature and density. The Greenwald density fraction are: $n/n_G = 0.2$ in the eITB case and $n/n_G = 0.144$ in the eETB case.

The poloidal beta

$$\beta_\theta = \frac{\langle p_e \rangle}{B_\theta^2(a)/2\mu_0} \qquad \text{where} \qquad \langle p_e \rangle = \frac{\int_S p_e dS}{\int_S dS}$$

is easily obtained from the pressure profile through a numerical integration, remembering that $B_\theta(a)$ is given by the plasma current. The electron energy confinement time was evaluated considering stationary conditions, thus

$$\tau_{E,e} = \frac{E_{k,e}}{P_{ohm}} \qquad \text{where} \qquad E_{k,e} = \frac{3}{2}\int_V n_e k_B T_e dV \qquad .$$

$E_{k,e}$ is the total electron kinetic energy and P_{ohm} is the total ohmic input power. This last contribution can not be evaluated using the Ohm's law for the toroidal current density, the Spitzer resistivity and the loop voltage. Conversely, it must be obtained via a power balance leading to the relation:

$$P_{ohm} = V_{loop} I_p + V_\theta I_\theta - \frac{dU_M}{dt}$$

where V_{loop} is the loop voltage, I_p is the plasma current, V_θ and I_θ are respectively the external poloidal voltage and current, and U_M is the internal magnetic energy[136, 107]. β_θ and $\tau_{E,e}$ obtained for the considered database was compared to the relative general scalings proposed in [107], Figure 4.18a and Figure 4.18b. Looking at Figure 4.18a one can notice that the presence

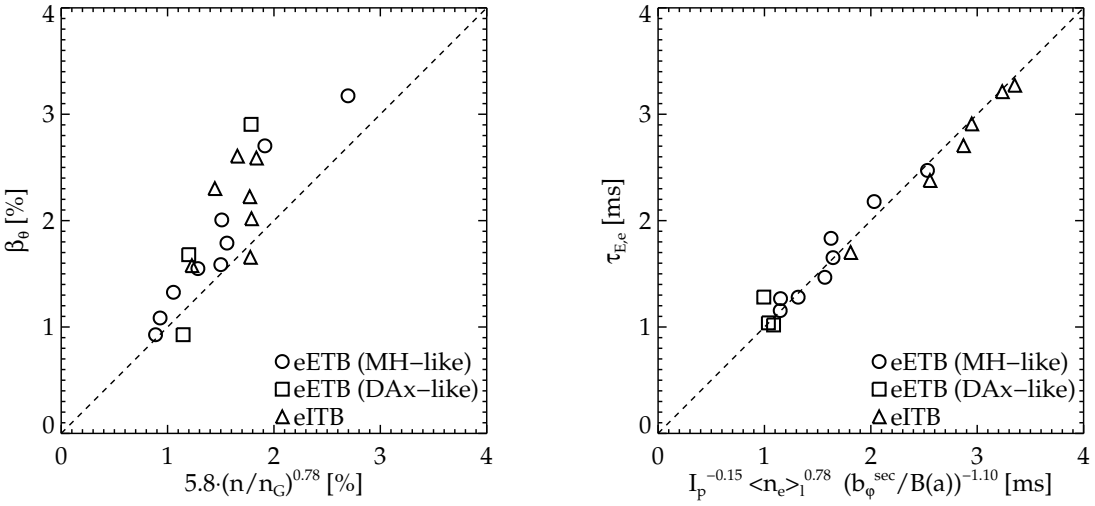

(a) (b)

Figure 4.18: eITB and eETB plasmas confinement properties compared to general RFX-mod scalings. (a) β_θ parameter, (b) electron energy confinement time. The eETB cases have been distinguished considering the profile shape (MH-like or DAx-like). The horizontal axes represents the empirical scaling based on a large RFX-mod discharges database[107].

of a barrier, disregarding the kind, ensures a β_θ larger than the average one. Clearly, for a given Greenwald density fraction the appearance of a barrier leads to a larger average pressure: in the eITB case this happens because of the higher core temperature, in the eETB case because the appearance of the strong external gradients extends the central region with high temperature. For what concern the electron energy confinement time the picture is less promising. Both eITB and eETB plasmas are found to lie on the general scaling. The total thermal energy, $E_{k,e}$, is generally higher for low secondary modes amplitude, so for eITB case, but at the same time for these shots P_{Ohm} is larger. The situation is reversed for eETB cases. Therefore two ways to reach similar conditions are found: on the one hand eITBs are characterized by a lower stochastic

transport but also affected by generally cold external region and plasma edge. Vice versa, the stochastic transport level in eETB cases is not better than in average plasma conditions, nevertheless a colder plasma edge and a larger hot plasma region reduces the overall plasma resistivity leading to a lower P_{Ohm}. At this point, is clear that to significantly improve the RFX-mod overall performance one has to find the way to couple the beneficial effects of eITBs and eETBs. To this extent experiments are ongoing: the divertor-like plasma edge can be triggered by applying non-zero boundary conditions (BCs) to both the dominant $m = 1/n = -7$ and $m = 0/n = 7$ radial field harmonics so to actively control the helical edge ripple[137].

5

TCV: H-MODE ACCESSIBILITY

> It is a capital mistake to theorize before one has data. Insensibly one begins to twist facts to suit theories, instead of theories to suit facts.
>
> *A Study in Scarlet*
> *Sir Arthur Conan Doyle*

Access to the high confinement mode (H-mode) regime is critical for the commercial viability of fusion energy by magnetic confinement. The access to the H-mode is usually achieved through the application of a sufficient quantity of input power. This power threshold, $P_{L,LH}$, is found to strongly depend on plasma density, toroidal magnetic field and plasma size. Many experiments have also shown plasma shape and X-point geometry to affect $P_{L,LH}$. The Tokamak à Configuration Variable *has unique and well established shaping capabilities, is therefore well suited to extensively investigate the influence of the X-point geometry on $P_{L,LH}$. Dedicated experiments were performed during 2011 operations: the beneficial reduction of the X-point height was documented. The influence of density and plasma-wall distance on H-mode power threshold was also investigated. The chapter is devoted to present and discuss the experiments performed on TCV and the following analysis.*

The chapter focuses on the discussion of the experimental investigation of the conditions to access the H-mode in TCV. Before entering the proper discussion about the experiments done in TCV, a brief summary of the present experimental evidences is presented (Section 5.1). The main goal of the work was to investigate the influence of the X-point height on the H-mode power threshold $P_{L,LH}$. The experimental setup conceived for this study is discussed in Section 5.2. During the experimental campaign the H-mode power threshold non-monotonic dependence on electron density was measured (Section 5.3). The beneficial effect of the X-point height reduction on $P_{L,LH}$ is discussed in Section 5.4. Section 5.5 shows that a reduced plasma-wall distance can hinder the possibility to access the H-mode. Finally the results of the experimental work are summarized in Section 5.6.

5.1 X-POINT GEOMETRY INFLUENCE ON H-MODE POWER THRESHOLD

In many devices the relative location of the X-point in the poloidal plane and its geometry are reported to affect the H-mode power threshold. In the following, the present experimental evidences from the principal tokamaks are summarized. Because the X-point geometry influence is found to vary from one device to another, each device is considered individually within its own literature. Only at the end, a schematic view of the state of the art is proposed as a summary. For the sake of clarity some symbology is fixed and will be adopted throughout the entire discussion. The TCV standard Single Null configuration is taken as an example (this is the configuration chosen for the studies devoted to investigate the X-point influence on the H-mode threshold power). The plasma geometric configuration is shown inside the TCV vacuum vessel. See Figure 5.1 to visualize the following quantities.

$\boldsymbol{R_{Xpt}}$ radial position of the X-point in the poloidal plane

$\boldsymbol{Z_{Xpt}}$ *X-point height*, the minimum distance between the X-point and the lower material limit of the vacuum chamber

$\boldsymbol{L_{in}^{Xpt}}$ *inner X-point leg length*, the poloidal distance between the X-point and the inner strike point (likewise $\boldsymbol{L_{out}^{Xpt}}$ for the outer strike point)

$\boldsymbol{L_{in}^{c}}$ *inner connection length* distance, along a field line, from the outboard midplane to the inner strike point (similarly for the outer strike point, $\boldsymbol{L_{out}^{c}}$)

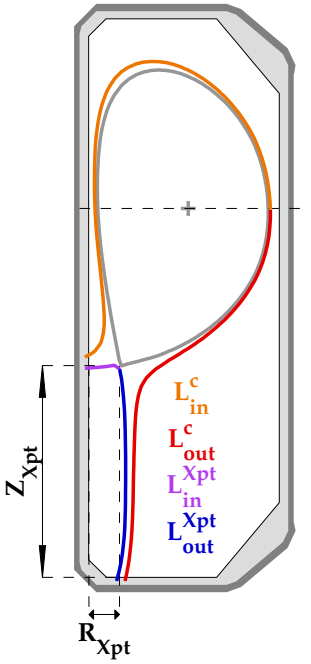

Figure 5.1: X-point geometry definitions referred to the TCV standard single null configuration.

JET

Studies from JET firstly showed that the divertor configuration influences the L-H transition power threshold[138]. The L-H power threshold was measured while the X-point was lowered on to the septum which separated the inner and outer MkII GB divertor legs, see upper panel of Figure 5.2a. The operation was then repeated when the divertor septum was replaced with a septum replacement plate (SRP), such that inner and outer divertor legs are no longer separated, see lower panel of Figure 5.2a. Figure 5.2b shows $P_{L,LH}$, referred to as P_{th} in Andrew paper, normalized to the power threshold scaling of [139] as a function of X-point height from the septum top, or virtual septum in the case of the SRP. The L-H power threshold is reduced by almost a factor of two when the X-point is lowered onto the septum. The comparison shows that creating a more open divertor with the removal of the septum, increases $P_{L,LH}$. Moreover, at X-point height greater than 6 cm, the strike points remained on the vertical targets and $P_{L,LH}$ does not vary with X-point height. So, $P_{L,LH}$ is only sensitive to the X-point height when the inner and outer strike points and SOL are on the horizontal targets. In the same paper an increase of divertor D_α emission with decreased X-point height is reported and interpreted as a divertor neutral density increase in the vicinity of the X-point.

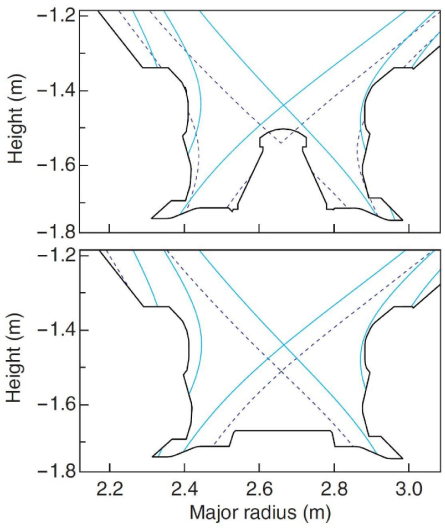

(a)

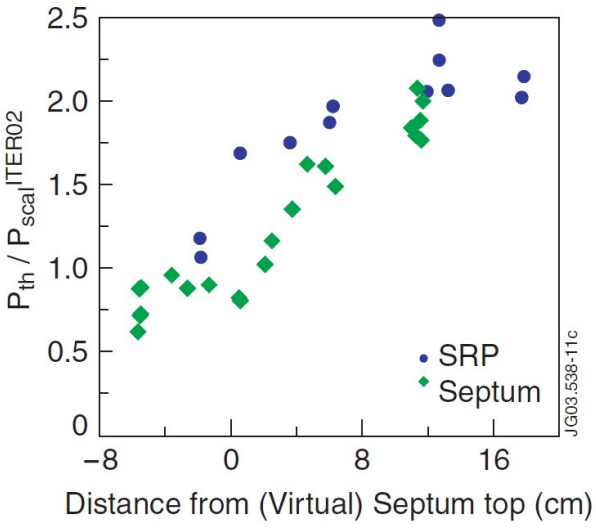

(b)

Figure 5.2: JET: (a) MkII GB divertor showing the range of the X-point height scans: (top panel) with the septum, -6 to 6 cm from the septum top (bottom panel) With the SRP, -2 to 6 cm from the virtual septum top. Both investigation were performed at 3 MA/3.4 T. Figure 1 from [138] (b) Power threshold for L-H transition normalized to the scaled power threshold from [139] plotted against distance from the (virtual) septum top. Figure 2 from [138]

DIII-D

In DIII-D the X-point height influence has been investigated using an unbalanced double null configuration[140]. The magnetic geometry had a null at both vertical ends, but a downward plasma bias made the lower null the only active one. A scan in the X-point height was performed with all other gaps between the plasma LCFS and the vessel surfaces being maintained at nearly constant values. The different plasma configurations maintained the same radial X-point location with the only change being in the lower triangularity. The scan was performed with different main species and heating schemes and is shown in Figure 5.3. The decrease of $P_{L,LH}$, P_{TH} in [140], with decreasing X-point height is observed for all of the main ion species irrespective of the heating method. Such evidence let the authors to suggest a common physics process underlying this effect for all of the ion species[140]. The change in X-point height has been related to a change in the neutral recycling in the vicinity of the divertor. As the X-point height was lowered from 30 to 10 cm the D_α intensity from the outer strike point dropped by a factor of 2 and correlates with a large change in power threshold. This observation induced the authors to point at scrape-off layer (SOL) neutrals as a player in the power threshold change.

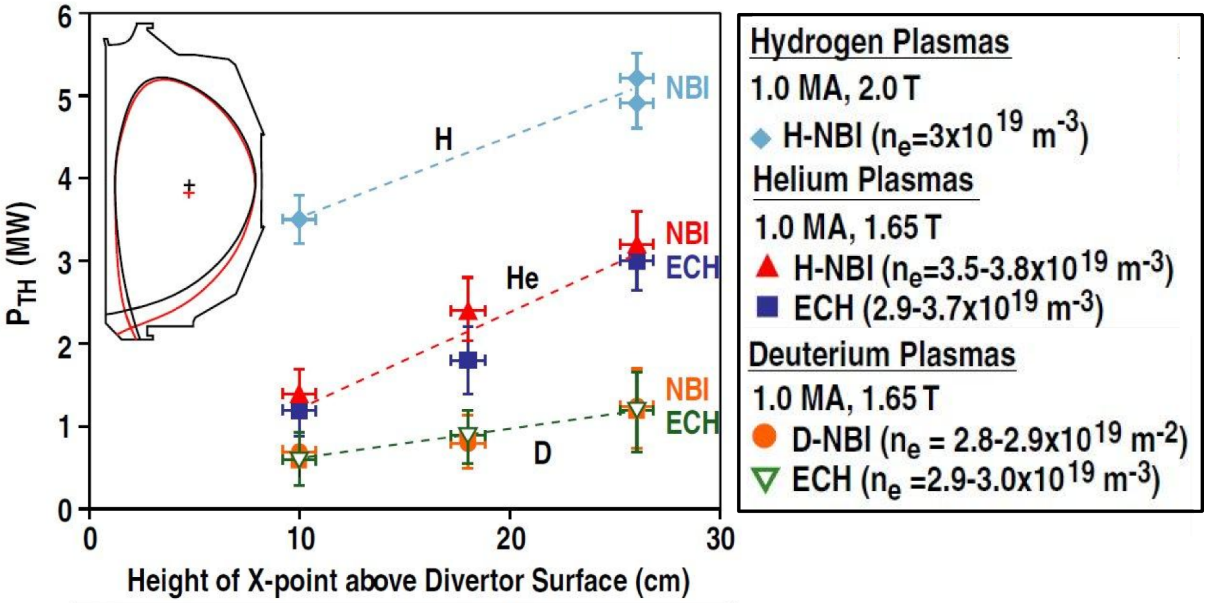

Figure 5.3: DIII-D: H-mode power threshold as a function of the lower X-point height with respect to the lower divertor surface for H, D and He plasmas and different auxiliary heating schemes. The density values in brackets correspond to the range of L-mode densities used in the scan. Figure 4(a) from [140]

MAST

In contrast to the observations on most conventional tokamaks, H-mode access on MAST is greatly improved in a connected double null (CDN) configuration where both X-points are practically on the same flux surface[141, 142, 143]. The ease of H-mode access is lost if the two flux surfaces passing through the X-points are radially separated, δr_{sep}, by more than one ion Larmor radius, ρ_i, at the low-field-side mid-plane. When δr_{sep} is held lower than $\rho_i/2$, $P_{L,LH}$ is reduced by at least a factor of 2 compared with SN discharges with the ion ∇B-drift toward the X-point [141]. The physics of the higher threshold power in SN compared with DN has been related to the changes in the SOL flow pattern and radial electric field values[142]. When MAST is operated in lower SN the length of the outer divertor leg can be used to control the Edge Trasport Barrier, thus controlling the H-mode transition. In Figure 5.4a it is shown how consecutive H-L-H phases were induced by changing the connection length of the outer divertor leg. The different phases are clearly visible in the D_α light. With the shorter connection length, Figure 5.4b, the plasma is in H-mode, and with the longer leg, Figure 5.4c, the plasma is in L-mode. More recently new MAST experiments showed that the X-point height affects the $P_{L,LH}$ both in SN and DN configurations. In SN configurations similar to that in Figure 5.4c, the magnetic axis was decreased by 10 cm while the plasma shape was kept fixed. The H-mode power threshold was found to decrease by a factor 1.7 for the lower X-point height discharge. In DN configuration the X-point height has varied changing the plasma elongation κ. The higher κ, i.e. lower X-point, discharges showed a lower $P_{L,LH}$[143].
Similarity experiments with MAST have been performed on ASDEX Upgrade and NSTX with the aim of confirming the reduction of $P_{L,LH}$ in connected DN discharges. The comparison

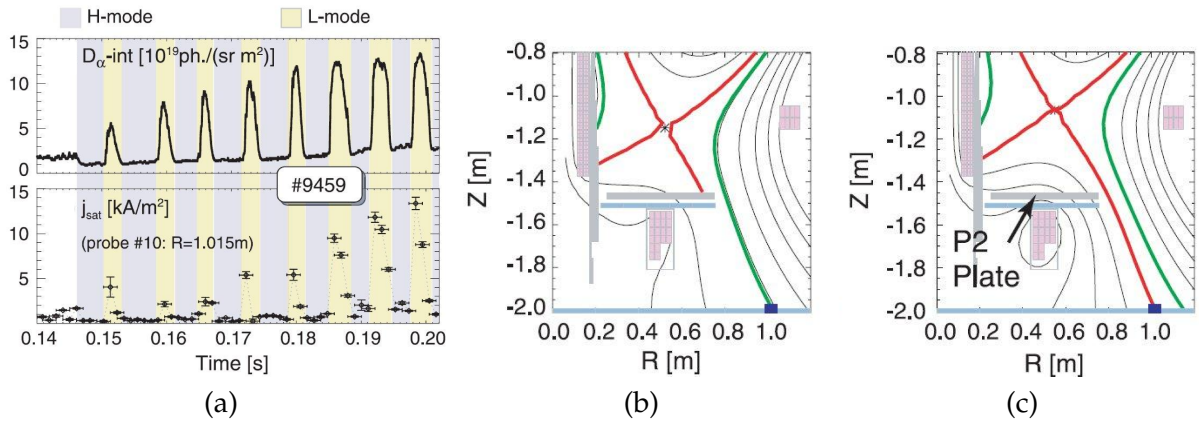

Figure 5.4: MAST: (a) Repetitive H-L-H phases induced by a change in the outer divertor leg length. The darker shaded H-mode phases correspond to the divertor configuration with the short leg (b), the L-mode phases correspond to the long leg (c). Shown are the D_α emission from a top view looking towards the divertor (top) and the ion saturation current from a probe located at R = 1.015 m and Z = -2 m (bottom). The probe position is indicated by the blue dot in both (b) and (c). Figure 5 in [142].

showed that there is at least a local minimum of the L-H threshold in CDND compared with lower SN. The reduction of $P_{L,LH}$ has been related to a more negative radial electric field in L-mode inside the last closed flux surface[144].

Alcator C-mod

In Alcator C-mod the pervasive sensitivity of $P_{L,LH}$ on X-point topology has been investigated using 7 different X-point configurations[59, 145], those defined in Figure 5.5a. The variation of $P_{L,LH}$ has been related to changes in the direction of the transport-driven flows on the inner SOL. In fact, the direction of the flow (co- or counter-current) depends on how filed lines connect between the low- and high-field SOL regions, which depends on X-point topology. Figure 5.5b captures the essence of the observed threshold dependencies in

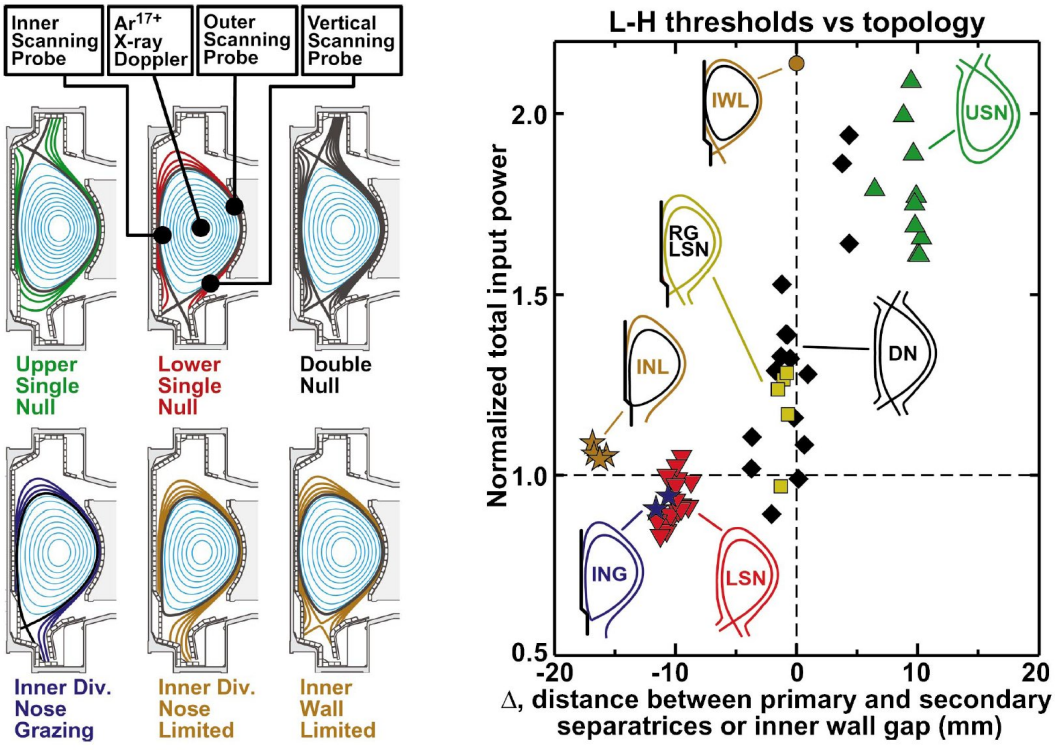

(a) (b)

Figure 5.5: Alcator C-Mod (a) X-point and limiter-defined magnetic configurations in Alcator C-Mod. Flux contours outside the last closed flux surface correspond to a 5 mm spacing, mapped to the outer midplane. Figure 1 from [59]. (b) L-H power thresholds observed for seven different X-point and limiter-defined magnetic configurations, normalized by the scaling law for LSN power thresholds reported in [146]. The parameter Δ corresponds to the smaller of (i) the distance between primary and secondary separatrix surfaces or (ii) the distance from the LCFS to the inner wall midplane both mapped to outer midplane, multiplied by minus one when a lower X-point or a lower limiter surface defines the LCFS. Figure 9 from [59]

Alcator C-Mod and suggest a possible explanation. INL, ING, and LSN discharges, which have favorable direction SOL flows (co-current), have the lowest values of power threshold. In DN discharges and RGLSN discharges the transport-driven SOL flows are weaker, being affected by topology changes, and $P_{L,LH}$ is increased. USN discharges have transport-driven SOL flows in the unfavorable direction (counter-current) and $P_{L,LH}$ reaches its maximum. In IWL discharge no active X-point is involved, thus the significantly higher $P_{L,LH}$ is probably due to other effects[59]. More recently, in Alcator C-mod, has been performed a refined study of the X-point geometry influence on $P_{L,LH}$ with lower single-null configuration. In particular

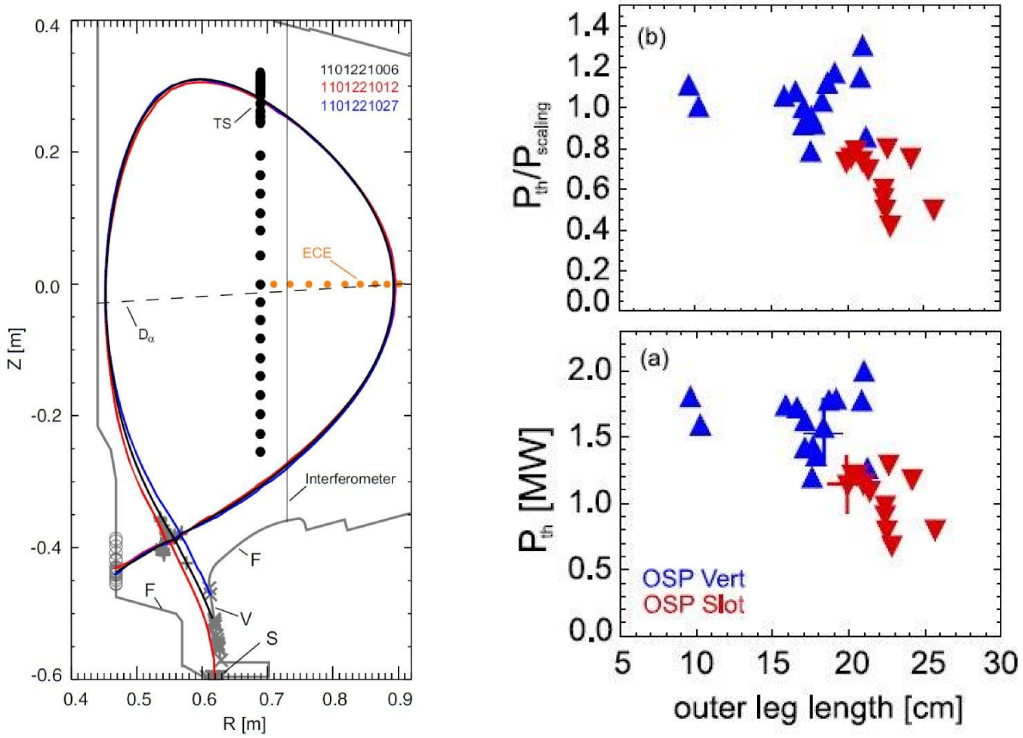

Figure 5.6: Alcator C-mod (a) Poloidal cross-section showing locations of X-point (+), outer ($\times$) and inner (open circles) separatrix strike points investigated. Examples of separatrix contours for vertical-plate (blue) and slot (red) divertor operations are shown. Separatrix contour for a standard C-Mod magnetic geometry is also shown (black). C-Mod facilitates three different divertor configurations: flat-plate, vertical and slot divertor, achieved by placing outer separatrix strike point on the divertor plate(s) labeled 'F', 'V' and 'S', respectively. Figure 1 from [145]. (b) L-H power thresholds, full size and normalized to expression (2.3), as a function of the poloidal distance between X-point and outer strike point L_{out}^{Xpt} (outer leg length, OLL in the paper). $P_{L,LH}$, P_{th} in the paper, is systematically lower when the plasma is operated with a slot divertor (red) compared with a vertical-plate divertor (blue). Figure 2 from [145]

the X-point location was changed while the plasma shape was maintained as fixed as possible. Among a number of potentially relevant shaping parameters, the outer leg length L_{out}^{Xpt} was shown to strongly affect $P_{L,LH}$, see Figure 5.6b. The longer L_{out}^{Xpt} the lower $P_{L,LH}$. The change in L_{out}^{Xpt}, from ~ 10 to ~ 25 cm, was achieved moving the outer strike point from a vertical divertor plate, labelled 'V', to a floor divertor plate, labelled 'S', as shown in Figure 5.6a. This trend contrasts with the observations made in JET, DIII-D and MAST pointing to two different hypothesis: a certain unique character of C-Mod tokamak or the existence of another still unknown parameter responsible for the difference.

NSTX

In NSTX $P_{L,LH}$ was found to be minimum in DN configurations, tending to increase as the plasma was shifted more strongly towards lower- or upper-single null configuration[147]. Scans have been performed using δr_{sep} as controlling parameter. When $|\delta r_{sep}|$ is raised over a poloidal ion gyroradius $P_{L,LH}$ is found to be higher then in balanced DN discharges, i.e. $\delta r_{sep} \sim 0$ [147]. Even if a clear trend has not been found, $P_{L,LH}$ has been reported to depend also on lower triangularity[147].

Summary

A general picture of the previously reported evidences is proposed in Table 5.1. For each device the parameters affecting the H-mode power threshold are highlighted and the proposed explanations are briefly mentioned.

Device	Configuration	Characteristic			
		X-point height	*Strike point position*	*Divertor Leg Length*	*X-points balance or gaps*
JET	SN	Lower $Z_{Xpt} \rightarrow$ lower $P_{L,LH}$. Sensitivity confirmed only with both the strike points on horizontal target. Related to increase of the X-point neutral density			
DIII-D	DN	Lower $Z_{Xpt} \rightarrow$ lower $P_{L,LH}$. SOL neutrals indicated as player			
	CDN	Z_{Xpt} varied changing κ. Lower $Z_{Xpt} \rightarrow$ lower $P_{L,LH}$			$P_{L,LH}$ decreased by a factor two compared to SN if $\lvert\delta r_{sep}\rvert < \rho_i$. Related with SOL flows and edge E_r values
MAST	SN	Lower $Z_{Xpt} \rightarrow$ lower $P_{L,LH}$. Related with edge E_r values		H-L-H pahses induced varying from short to long L_{out}^{Xpt}	
NSTX	DN				$P_{L,LH}$ minimum in CDN. $P_{L,LH}$ increase if $\lvert\delta r_{sep}\rvert$ is raised over ρ_i
C-Mod	LIMITED, SN, DN			X-point topology, gaps and X-points balance influences SOL flows. Favourable SOL flows induce lower $P_{L,LH}$.	
	SN		Longer $L_{out}^{Xpt} \rightarrow$ lower $P_{L,LH}$. Outer strike point changed from vertical to horizontal tile.		

Table 5.1: Summary of the experimental evidences about the X-point geometry influence on H-mode power threshold.

5.2 TCV EXPERIMENTS: EXPERIMENTAL SETUP

From Table 5.1 is evident that the X-point geometry affects the H-mode power threshold in several different ways, also coming to conflicting evidences when different machines are compared. In general, while changing the geometry of the magnetic boundary of the plasma column is not possible to vary a single shaping parameter at a time, so $P_{L,LH}$ dependencies on shaping parameters are usually correlated with each other. Additionally, different physical mechanisms are invoked to explain the same parametric dependence. As a result a neat picture relating the $P_{L,LH}$ to the plasma column geometry is still missing. The TCV shaping capabilities give the chance to extensively investigate many of these effects. The X-point geometry can be changed in several ways: Single and Double Null configurations can be used, the X-point(s) can be moved in both directions in the poloidal plane, the separatrix can be forced to strike the vessel on both vertical and horizontal targets, and so on. However, in order to disentangle, as much as possible, the various effects it was decided to address one problem at a time. The first investigation focused on how the X-point height affects $P_{L,LH}$.

5.2.1 X-point configuration

The standard TCV SN configuration was identified as the most suitable one to investigate Z_{Xpt}. As can been seen from Figure 5.7, this configuration is characterized by a horizontal divertor leg on the high field side and a vertical one striking the vacuum vessel floor tiles. The choice was motivated by the large flexibility of the X-point geometry for a fixed plasma shape. By moving vertically the plasma in the vacuum chamber, the outer divertor leg length can be reduced by more than a factor of 6 without significant variation of the plasma shape. The target shaping parameters chosen for operations were:

$$\begin{array}{ll} \text{elongation} & \kappa \sim 1.7 \\ \text{mean triangularity} & \delta \sim 0.45 \\ \text{lower triangularity} & \delta_l \sim 0.6 \\ \text{upper triangularity} & \delta_u \sim 0.3 \\ \text{HFS wall gap} & \delta^{IN} > 2\,\text{cm} \\ \text{LFS wall gap} & \delta^{OUT} > 2\,\text{cm} \end{array} \tag{5.1}$$

Earlier studies in JET showed the importance of plasma wall separation in influencing bulk and divertor radiation[148]. Moreover, a dependence of $P_{L,LH}$ on δ^{OUT} was highlighted in DIII-D where a larger δ^{OUT} was found to led to a lower $P_{L,LH}$[66]. So particular attention has been posed to minimize such influence, 2 cm was considered as a strict lower limit for the plasma-wall gaps as suggested in [149]. If the LCFS is too close to the material wall the SOL thickness becomes so thin that the plasma behaves like a limited rather than a diverted plasma. A similar behavior was reported in Alcator C-Mod: the H-mode power threshold has

been reported to increase in SN discharges when the gap at the inboard midplane was reduced to less than 2 cm [59]. Moreover Reduced Gap Lower Single Null (RGLSN) discharges showed values of $P_{L,LH}$ intermediate between LSN and limited discharges. Conversely, if the gap was reduced in the X-point surrounding while maintaining the inboard midplane gap greater than 2 cm, no significant change was seen in $P_{L,LH}$[59]. For a discussion of a TCV experimental evidence see Section 5.5.
Four discharges performed at different X-point heights, respecting the requirements made in (5.1), are depicted in Figure 5.7 together with the shaping parameters characterizing each configuration. The plasma magnetic equilibria are reconstructed by the LIUQE code[31] using TCV magnetic measurements, simultaneously to the Thomson Scattering measurements. As can be seen from the table, no significant variations appear in any of the shaping parameters for this four discharges. The plasma shapes are extremely similar while the X-point height is decreased from $\sim$ 57 cm down to $\sim$ 7 cm. In Figure 5.7b the magnetic surfaces of the two discharges with the highest and the lowest X-point are shifted to facilitate the shape

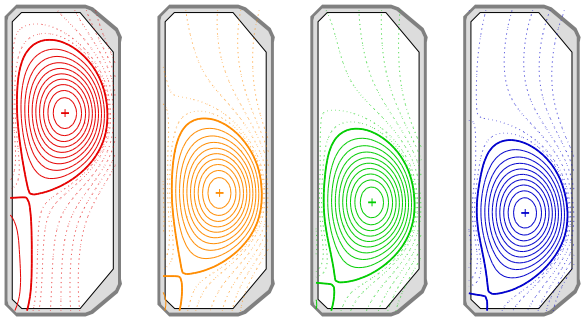

SHOT	42554	42771	45297	45298
κ	1.71	1.73	1.69	1.69
δ	0.449	0.465	0.452	0.438
δ_l	0.621	0.645	0.623	0.611
δ_u	0.278	0.285	0.277	0.265
δ^{IN} [cm]	2.38	3.316	2.853	2.769
δ^{OUT} [cm]	2.98	2.22	2.27	2.45
q_{95}	3.00	3.01	2.86	2.85
S [m^2]	10.79	10.98	10.89	10.80
R_{XPT} [cm]	8.19	8.43	8.40	8.54
Z_{XPT} [cm]	56.86	16.91	12.71	7.19

(a)

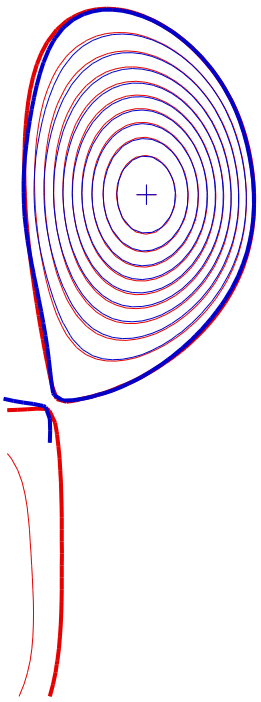

(b)

Figure 5.7: (a) Four plasma discharges at different X-point heights. The shaping parameters are reported in the table. Magnetic reconstructions and shaping parameters refers to the last LIUQE equilibrium prior to the L-H transition. (b) Comparison between two equilibria vertically shifted to match magnetic axis position. The color code is maintained between (a) and (b).

comparison. The quality of the match is evident.

5.2.2 Target plasma

The target plasma parameters were:

$$\begin{array}{ll} \text{plasma current} & I_p \sim 260\,\text{kA} \\ \text{edge safety factor} & q_{95} \sim 3 \\ \text{plasma surface} & S \sim 11\,\text{m}^2 \end{array} \tag{5.2}$$

at a fixed magnetic field $B_T \sim 1.4$ T with the ion ∇B-drift in the favorable direction, i.e. towards the X-point. This set was a trade off between different needs. The plasma shape and $q_{95} \sim 3$ were desirable in order to facilitate the comparison with the other devices. The value of the plasma current was chosen to avoid Ohmic H-mode, which can be triggered at values of plasma current as low as 350 kA in TCV[150]. During the experiments described in this chapter, the L-H transition was triggered via off-axis electron cyclotron resonance heating (ECRH) using two ECH-X2 launchers. In TCV operated with $B_T \sim 1.4$ T, this heating method induces a limit in density: ECH-X2 has a cut-off density at $\approx 4.2{\cdot}10^{19}$ m^{-3}. To ensure a high absorption rate the line average density must be kept lower than $\sim 4.8 \cdot 10^{19}$ m^{-3} [69]. At this line average density the absorption does not occur in the plasma core, instead the ECH power is deposited near the plasma edge. This has been chosen as operating scenario, i.e. heating with the ECH-X2 system aiming at depositing the ECRH power approximately at $\rho \sim 0.8$. This limit in density could have been exceeded exploiting the ECH-X3 system, which allows the access to plasmas at density greatly exceeding the X2 cut-off. However, in [69] a density scan of the H-mode power threshold is reported as measured in TCV. Purely Ohmic L-H transition was obtained for densities larger than $\sim 4{\cdot}10^{19}$ m^{-3}, and $P_{L,LH}$ was found to increase increasing the density. Conversely, in ECH-X2 heated discharges $P_{L,LH}$ was found to decrease as the density was increased up to $\sim 3.5{\cdot}10^{19}$ m^{-3}. A minimum $P_{L,LH}$ can thus be located in the range $3.5 \div 4{\cdot}10^{19}$ m^{-3}. Therefore, the X2 cut-off limit is high enough to allow the measurement of $P_{L,LH}$ in the most favorable density range and allows to investigate both the $P_{L,LH}$ behavior around its density 'turning point' and in the linear increase regime above the 'turning point'. Moreover, the X2 system ensures an excellent deposition localization and more reliable absorption conditions compared to the X3 system.

5.2.3 Experimental procedure

The experimental procedure foresaw to measure the H-mode power threshold by triggering the L-H transition with a ramp of ECRH power during the plasma current flat-top phase. Kinetic and current profiles adjust to ECRH conditions in approximately 50 ms from the ECRH system turn on. The ramp of ECRH power should therefore be slow enough to allow the L-H transition to occur after this time lag has elapsed. Moreover, to a slower ECRH power

ramp corresponds a more accurate determination of the ECRH input power. This need for accuracy in the determination of $P_{L,LH}$ forced to measure it only once a shot and to repeat the measurement on a shot-to-shot basis varying one parameter at a time. Taking advantage of the steerable mirrors of the ECRH launcher system, the ECH power has been deposited at the same plasma radius ($\rho \sim 0.6 \div 0.8$) for all the different positions of the plasma inside the vessel. This procedure ensured that the current profile to be perturbed in the same way.
In order to access the H-mode in every target plasma two gyrotrons were used. Their nominal maximum output power of 465 kW was considered enough to trigger an L-H transition in every foreseen scenario. In order to obtain a unique and continuous power ramp, the two gyrotrons were not simply operated one after the other. In fact, each ECH-system has a minimum delivered power of about 200 kW, if operated with the nominal parameters. If the two systems were operated one after the other at the turn on of the second one a large step in the total input power would had been observed, this in turn could have triggered the L-H transition preventing an accurate estimate of $P_{L,LH}$. Figure 5.8 depicts the experimental realization of the designed discharge scheme. In the first 400 ms the divertor is formed and the plasma shape is established, then the plasma current is raised to the target value in

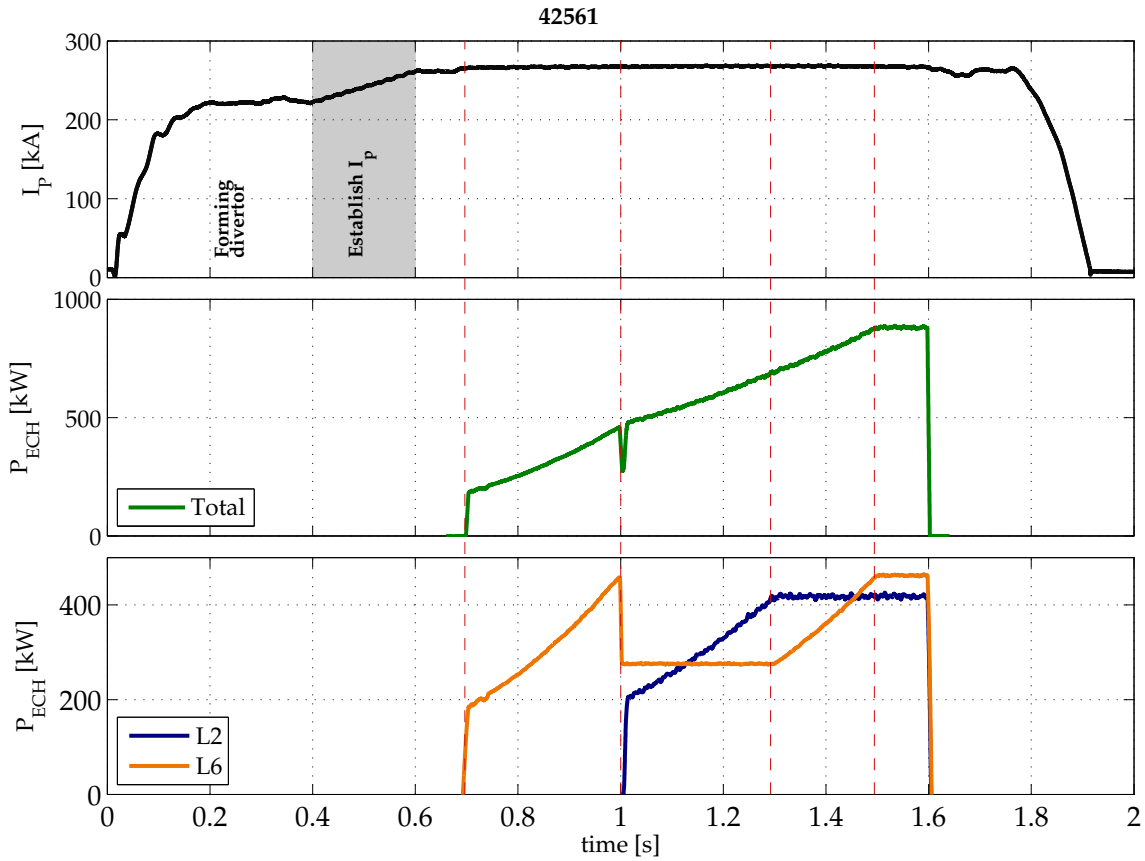

Figure 5.8: Discharge setup (Experimental realization). From top to bottom: plasma current, total ECRH input power, individual ECH-X2 system delivered power.

approximately 200 ms. The first ECH-X2 launcher (L6) turns on at $t \sim 700$ ms, ~ 100 ms after the current reached the target value. Then its power is raised to ~ 450 kW in approximately 300 ms. At $t \sim 1$ s the second ECH-X2 system (L2) is turned on while the power of first one is reduced to ~ 250 kW, so as to obtain ~ 450 kW in total. Afterwards the second is ramped to its maximum power and, finally, the first system is ramped again. In this way a continuous ramp of the total ECRH power from ~ 200 kW to ~ 900 kW, with a 1 MW/s slope, can be obtained. The experimental realization is highly reliable: the ramp is well controlled and almost continuous, as shown in the central panel of Figure 5.8.
An example of the experimental procedure, i.e. a typical performed discharge, is given in Figure 5.9a. The time evolution of plasma current, electron density, total ERCH input power, D_α radiation and soft X-ray emission in the divertor region for the interesting part of the discharge are depicted. The L-H transition is clearly recognizable in D_α signal as a sudden intensity drop. The raise in density and soft X-rays emission are other characteristic signatures of the transition to the H-mode. In Figure 5.9b the radial electron density and temperature profiles 2 ms before the L-H transition are shown together with the radial power density profile of the ECH-X2 input power. The latter represents also the radial profile of the ECRH power first pass absorption fraction. The ECRH absorbed power ($\sim 90\%$ first pass absorption) is deposited almost entirely in the region $0.7 < \rho < 0.8$, as a proof of the excellent deposition localization of the X2-system. The total first pass absorption fraction, i.e. the integral of the absorption profile, is approximately 90%. Finally, in Figure 5.9c the geometry of the X2 rays is plotted as obtained by the TORAY[151] ray-tracing code 2 ms before the L-H transition (the same instant of Figure 5.9b).

5.2.4 Power threshold estimate

The power flux across the LCFS consists of three terms, recalling equation (2.2),

$$P_L \;=\; P_{ohm} + P_{aux} - dW/dt \tag{5.3}$$

where, in the case under analysis, P_{aux} is the ECRH power absorbed by the plasma, namely

$$P_{aux} \;=\; P_{ECH} \cdot P^{\%}_{ABS}$$

where P_{ECH} is the total input power delivered by the gyrotrons while $P^{\%}_{ABS}$ is the first pass percentage absorption evaluated using the ray-tracing code TORAY[151]. The time of the L-H trasition, t_{LH}, can be indified with the time when the D_α emission drastically drops and the density starts to raise. In order to identify the parameters that are required for a transition from L- to H-mode, $P_{L,LH}$, they should be evaluated at a time as close as possible to t_{LH}. In order to accomplish such a goal, (5.3) was evaluated through a linear extrapolation at t_{LH}. To be more precise: the time evolution of each quantity appearing in equation (5.3) was linearly fitted during the 100 ms prior to t_{LH}, then the value at t_{LH} has been extrapolated using the

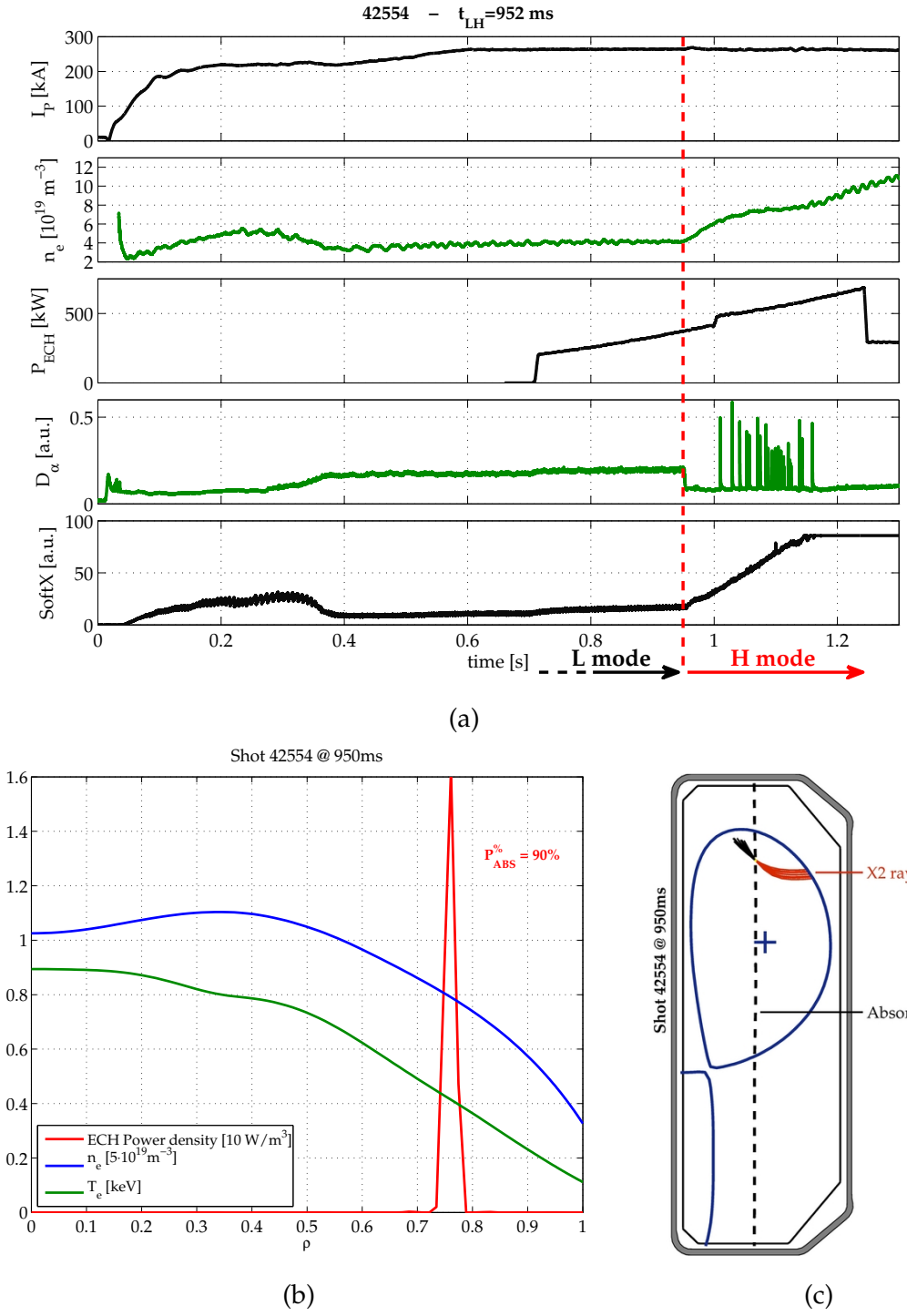

Figure 5.9: (a) A typical discharge. Time traces of plasma current, electron density, total ERCH input power, vertical D_α and soft X-ray emission in the divertor region are reported. The L-H transition in marked by the red dashed line. (b) Electron density and temperature profiles 2 ms before the L-H transition. The profile of ECH-X2 normalized power absorption is reported. (c) ECH-X2 rays path 2 ms before the L-H transition as obtained from the ray-tracing code TORAY.

fit[a]. The TCV Thomson Scattering diagnostic is equipped with three Laser. Each Laser can be operated at 20 Hz, which leads to a 60 Hz continuous acquisition. The linear fit on the time evolution of the quantities involved in equation (5.3) was performed considering about 6 measurement points. The extrapolation was performed paying attention to avoid time measurements too close to the transition (not closer than 2 ms), in this way the extrapolated quantities represent L-mode characteristics leading to the L- to H-mode transition.
Given the aim of the work, the accuracy in determining $P_{L,LH}$ is extremely important, large errors can hinder the possibility to assess differences in $P_{L,LH}$, frustrating the analysis. In order to evaluate the possible sources of uncertainty and eventually their magnitude, some investigations were performed. The uncertainties on P_{ohm} and dW/dt are due either to measurements fluctuations and to the extrapolation method. An overall contribution can be estimated considering the standard deviation evaluated over a time lag in which the plasma is in rather constant conditions, i.e. fixed shape, current flat-top, no ECRH heating. This is found to be approximately the 5-10% for P_{ohm} and 25% for dW/dt. The larger value for dW/dt is due to the time derivative which is numerically computed. The largest contribution to the uncertainty affecting P_{aux} is due to the first pass absorption of the ECRH power, $P^{\%}_{ABS}$. The latter is obtained through the ray-tracing code TORAY, and was found to be extremely sensitive to details of the density profile. An example of such sentivity is reported in Figure 5.10. The TORAY code was used to simulate the ECRH absorption starting from the density and temperature profiles of a real discharge. Then, the density profile given as input to TORAY has been slightly varied so to evaluate the change in the simulated absorption rate. The real density profile (green one) has been augmented and diminished by 2% (blue and red). The radial profile of the ECRH power density changes accordingly. As a result to a total 4% variation of the line average density the total ECRH power absorption varies approximately by a factor 2. It has to be noted that this is a peculiar case where the line averaged density is at the limit of the operational range for ECH-X2 system. In fact, the cut-off layer sits in the plasma outer region, approximately at $\rho \sim 0.7$. As $\langle n_e \rangle_l$ is reduced the sensitivity of $P^{\%}_{ABS}$ reduces. An average estimate for such an uncertainty was evaluated to be of the order of 5 to 10%. The artificial 2% variation of the density profiles lies within the uncertainty due to the interferometer measurements and to the fittig algorithm used to fit the density profile. Considering that the dW/dt contribution to $P_{L,LH}$ is usually a few percent while ohmic and auxiliary contributions are of the same order of magnitude, a relative uncertainty of $\sim$15% can be taken as an estimate for $P_{L,LH}$ uncertainty.

[a]*TORAY needs density and temperature profiles, together with the magnetic equilibria reconstruction, to evaluate the ECRH power absorption. So $P^{\%}_{ABS}$ value is available simultaneously to Thomson Scattering measurements.*

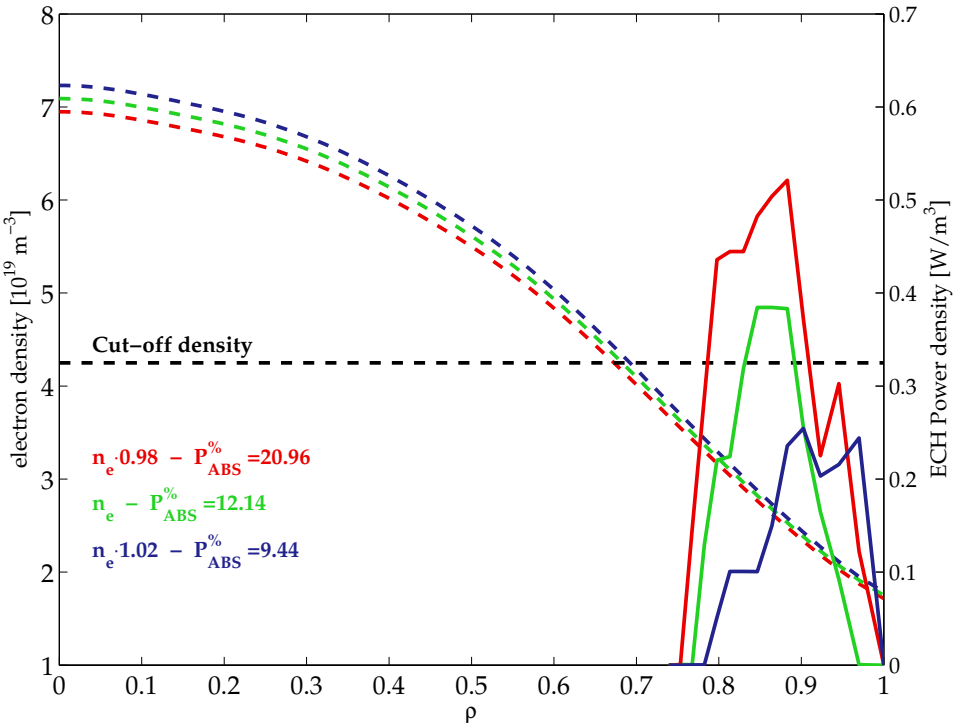

Figure 5.10: Sensitivity verification of $P^{\%}_{ABS}$ estimate. Density profiles with associated ECRH power density, i.e. ECRH power radial absorption. The red profile was obtained scaling the green one by a factor 0.98, the blue one was obtained scaling the green one by a factor 1.02. The line average density value scales accordingly, respectively: 4.9, 5, $5.1 \cdot 10^{19}$ m^{-3}. The total absorption fraction for the three cases are depicted.

5.3 THRESHOLD POWER VERSUS DENSITY

The H-mode power threshold shows a non-monotonic dependence on plasma density. Many different devices have confirmed this evidence, but the 'turning point' varies from one machine to another. The location of the $P_{L,LH}$ minimum is relatively spread in the density domain: from $\langle n_e \rangle_l^{min} \sim 1.5{\cdot}10^{19}\text{m}^{-3}$ found in JT-60U to $\sim 5{\cdot}10^{19}\text{m}^{-3}$ found in Asdex Upgrade, and it is even higher in Alcator C-mod tokamak where $\langle n_e \rangle_l^{min}$ reaches $\sim 1{\cdot}10^{20}\text{m}^{-3}$. In TCV earlier studies located such a minimum approximately at $3.5{\cdot}10^{19}\text{m}^{-3}$ [69]. This minimum was also found to vary in each individual device depending on the discharge conditions. The general power-law scaling for $P_{L,LH}$ takes into account the density dependence only above this minimum, recall expression (2.3). So comparison between P_{thresh} and experimental evaluation of $P_{L,LH}$ are meaningful only for density values greater then $\langle n_e \rangle_l^{min}$. In order to obtain $P_{L,LH}$ values comparable with P_{thresh} a density scan to verify the location of $\langle n_e \rangle_l^{min}$ was performed.

Eight reference shots were performed at different line average densities, $\langle n_e \rangle_l$, in standard SN configuration with the X-point $\sim$ 57 cm above the bottom of the vessel. In Table 5.11a the

	mean	rms	% rms
I_p [kA]	267.8	1.9	0.72
q_{95}	3.00	0.05	1.60
S [m^2]	10.85	0.04	0.34
κ	1.708	0.008	0.49
δ	0.443	0.007	1.57
δ_l	0.614	0.006	1.04
δ_u	0.271	0.013	4.85
δ^{IN} [cm]	2.17	0.16	7.33
δ^{OUT} [cm]	2.88	0.10	3.55
Z_{Xpt} [cm]	57.32	0.29	0.50
R_{Xpt} [cm]	8.44	0.16	1.94

(a)

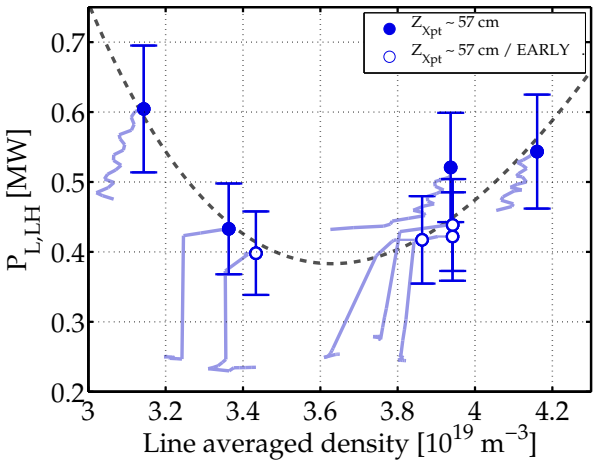

(b)

Figure 5.11: Density scan at $Z_{Xpt} \sim 57$ cm. (a) Mean value, standard deviation and percentage standard deviation for the principal plasma parameters. (b) H-mode power threshold versus line averaged density. Open symbols mark L-H transitions that occur within 50 ms from the ECH turn on. Light blue paths represent the trajectories in the $(\langle n_e \rangle_l, P_L)$ plane, i.e. the time evolution prior to the L-H transition of each discharge. A representative trend is fitted.

mean values and standard deviations for the principal plasma parameters are given. The main outcome of these discharges is depicted in Figure 5.11b: the estimates for $P_{L,LH}$ are reported against line averaged density. Increasing the density, $P_{L,LH}$ decreases until $\langle n_e \rangle_l \sim \langle n_e \rangle_l^{min} \equiv 3.6{\cdot}10^{19}\text{m}^{-3}$, while above $\langle n_e \rangle_l^{min}$ the power threshold increases. In Figure 5.11b open symbols mark shots where the transition to H-mode occurs within the first 50 ms from the ECRH system turn on. Thus, the L-H transition probably occurs before the kinetic and current profiles have been able to adjust to ECRH conditions. Recalling that the gyrotrons deliver approximately 200 kW as minimum power, $P_{L,LH}$ can be overestimated in such cases. This symbol convention will be maintained throughout the entire discussion. In Figure 5.11b the discharge evolution 200 ms prior to the transition is also reported as light blue tracks. As one can expect from the experimental procedure, each shot follows an almost vertical trajectory and undergoes the transition once crossed the threshold. In all of the discharges the density is slightly increasing before the L-H transition and the snake-like path of some trajectories is due to saw-teeth oscillations.

5.4 Threshold power versus X-point height

Considering the 8 discharges obtained at $Z_{Xpt} \sim 57$ cm, a total of 21 discharges were performed at 4 different X-point height: 57, 17, 12 and 7 cm. To allow a meaningful comparison with P_{thresh} all the discharges, after the first 8, were performed at density greater than $\langle n_e \rangle_l^{min}$. The density turning point was assumed to remain fixed while varying the plasma position. This

assumption is the simplest possible and presently there is no experimental evidences pointing towards a variation of $\langle n_e \rangle_l^{min}$ due to a change in the X-point geometry. As shown in 5.2.1, while moving the plasma towards the bottom of the vessel particular attention was paid to keep the inner and outer gaps greater than 2 cm without changing the plasma shape. All the other plasma parameters were kept as fixed as possible, apart from density and plasma current. The change in plasma current was forced to allow an accurate estimate of $P_{L,LH}$. In fact, at low X-point positions, the minimum power delivered by the ECRH system was enough to trigger the L-H transition immediately after the ECRH turn on. To avoid early L-H transitions one could raise the density in order to raise the power needed to enter the H-mode. On the other hand, one can reduce the ohmic contribution to total power loss via a reduction of the plasma current. The density range was limited by the ECH-X2 absorption range, so the plasma current was reduced. With $Z_{Xpt} \sim 12$ cm the $P_{L,LH}$ was so low that the current had to be decreased down to 180 kA in order to obtain a reliable estimate of the threshold power. The complete dataset is depicted in Figure 5.12 and the main plasma parameters are summarized in Table 5.2.

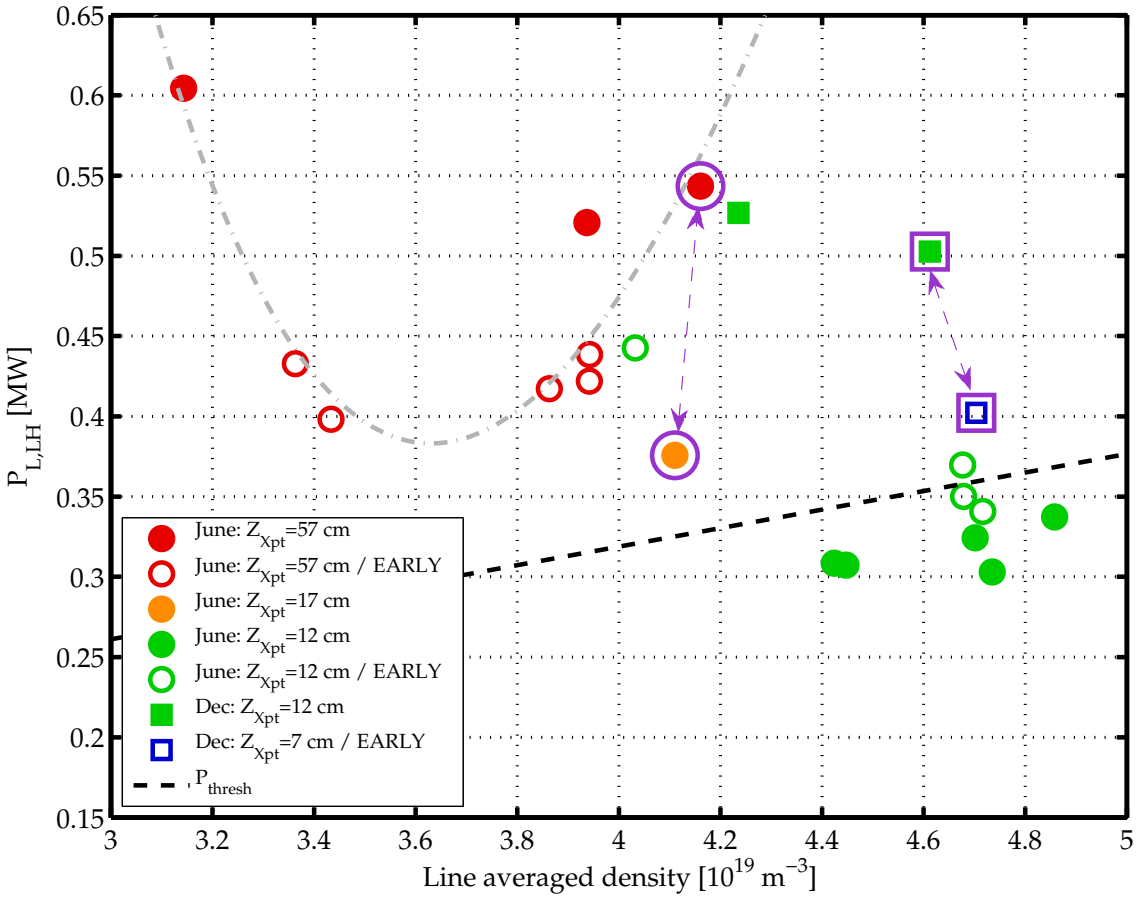

Figure 5.12: The complete dataset. P_{thresh} from [54] is sketched for comparison. The dashed gray curve represent $P_{L,LH}$ as fitted in Figure 5.11b.

	SHOT			I_P [kA]	n_e [10^{19}m^{-3}]	q_{95}	S [m^2]	κ	δ	δ_l	δ_u	δ^{IN} [cm]	δ^{OUT} [cm]	Z_{Xpt} [cm]	R_{Xpt} [cm]
✔	42554	●	June	264.2	4.16	3	10.79	1.71	0.449	0.621	0.277	2.381	2.975	56.86	8.19
✔	42559	●	June	269	3.94	3.01	10.86	1.709	0.448	0.623	0.274	2.092	2.902	57.28	8.36
✘	42560	●	June	269.27	3.14	3.04	10.91	1.718	0.44	0.609	0.271	2.034	2.901	57.08	8.3
✔	42766	○	June	268.38	3.94	2.94	10.8	1.697	0.436	0.609	0.262	2.193	2.872	57.65	8.61
✔	42767	○	June	268.56	3.94	2.95	10.83	1.698	0.439	0.612	0.266	2.078	2.828	57.39	8.48
✔	42768	○	June	268.78	3.86	2.95	10.84	1.7	0.442	0.619	0.266	2.07	2.843	57.36	8.41
✘	42769	○	June	268.25	3.43	2.97	10.86	1.72	0.43	0.61	0.25	2.219	3.012	57.04	8.29
✘	43086	○	June	269	3.36	3.01	10.88	1.713	0.447	0.619	0.274	2.456	2.665	57.71	8.64
✔	42771	●	June	261.73	4.11	3.01	10.98	1.73	0.465	0.645	0.285	3.316	2.223	16.91	8.43
✔	43225	○	June	260.81	4.03	3.03	10.83	1.705	0.454	0.626	0.282	2.392	2.922	12.23	7.52
✘	43226	○	June	260.17	4.68	3.05	10.8	1.708	0.455	0.631	0.28	2.499	2.996	12.17	7.49
✘	43228	○	June	245.41	4.68	3.24	10.87	1.711	0.459	0.628	0.29	2.461	2.836	12.21	7.5
✘	43229	○	June	230.36	4.72	3.48	10.95	1.717	0.464	0.627	0.301	2.465	2.675	12.2	7.48
✔	43230	●	June	215.88	4.86	3.81	11.06	1.739	0.473	0.631	0.315	2.568	2.621	12.04	7.36
✔	43231	●	June	201.09	4.7	4.14	11.15	1.745	0.48	0.634	0.325	2.612	2.434	11.91	7.21
✔	43530	●	June	201.31	4.42	4.07	11.15	1.733	0.476	0.627	0.324	2.468	2.278	11.9	7.32
✔	43531	●	June	200.58	4.73	4.12	11.16	1.741	0.48	0.628	0.333	2.516	2.36	12.02	7.33
✔	43532	●	June	180.07	4.45	4.81	11.32	1.775	0.49	0.636	0.344	2.763	2.269	11.76	7.21
✔	45296	■	Dec	272.91	4.24	2.85	10.91	1.682	0.452	0.624	0.28	2.934	2.012	12.72	8.41
✔	45297	■	Dec	272.77	4.61	2.86	10.89	1.691	0.45	0.623	0.277	2.853	2.268	12.71	8.4
✔	45298	□	Dec	267.07	4.7	2.85	10.8	1.694	0.438	0.611	0.265	2.768	2.447	7.19	8.54

Table 5.2: Complete database. Main plasma parameters are reported. Symbols refer to Figure 5.12. *June* and *Dec* mark rispectively if the shot has been performed between April and June 2011 or in December 2011. Light blue shading marks those shots obtained with plasma current values different from the target $I_p \sim 260$ kA. Symbols in the first column mark whether or not the shot is taken into accunt for Figure 5.15 and subsequent.

The different shots plotted in Figure 5.12 have been grouped considering: X-point height (marked with different colors), $P_{L,LH}$ determination accuracy (empty or full symbols) and experimental campaign (circles or squares). Every symbol is shown aside the relative shot in Table 5.2. The complete dataset contains a large variety of conditions, thus a clear and complete picture is hard to get at a first glance. In order to get clear indications about the influence of the X-point height on $P_{L,LH}$, is convenient to focus the attention on two pairs of shots: those marked in purple and linked by arrows in Figure 5.12. These shots have been selected because of their similarity: within each pair, the two shots are almost equal in terms of density, plasma current and plasma shape. Moreover they are performed in the same campaign so the difference in the estimated power threshold can be attributed to a reduced number of quantities, including the X-point height variation. For the two pairs of discharges, a detailed comparison of the different contributions to the power loss is reported in Figure 5.13. The difference in $P_{L,LH}$ is completely due to a variation in the ECRH contribution, while the Ohmic contribution remains almost unchanged. Even if the dW/dt contribution varies by approximately an order of magnitude, its contribution is so small that can be neglected. The influence of the X-point height is evident. A reduction in Z_{Xpt} turns in a reduction of $P_{L,LH}$ and the power threshold variation is larger when the X-point is closer to the bottom of the vessel. The first pair of shots, those performed in June 2011, shows a decrease of $P_{L,LH}$ approximately by 30% moving the X-point 40 cm down from the highest position, namely Z_{Xpt} is decreased from 57 to 17 cm. In the second case, where the plasma is close to bottom of the vessel, a downward shift of 5.5 cm turns in a 20% decrease of $P_{L,LH}$.
The whole dataset, reported in Figure 5.12, needs a carefull discussion because of its heterogeneous composition. Even if an average decrease in power threshold at lower plasma position can be argued, a large scatter affects the measurements. Let us consider one possible mean at a time. Recalling 5.3, many of the $P_{L,LH}$ evaluation can be overestimated because of the early L-H transition. In particular, three out of the five shots obtained at $\langle n_e \rangle_l \sim 4.7 \cdot 10^{19}\text{m}^{-3}$ are certainly overestimated. In fact, shot 43231 was obtained as a repetition of 43226, 43228 and 43229 decreasing the current value from shot to shot. These tree $P_{L,LH}$ evaluations can, thus, be regarded as upper limit to $P_{L,LH}$ at $\langle n_e \rangle_l \sim 4.7 \cdot 10^{19}$ m^{-3} with $Z_{Xpt} \sim 12$ cm. The change in current does not only imply a decrease in the Ohmic input power, but also carries a variation of more than 50% in q_{95} value, see Table 5.2. However strong changes of $P_{L,LH}$ with edge safety factor was reported only for $q_{95} < 2.5$ [63], not a single discharge reached this limit. In addition, different I_p values and different ECRH input power can result in a decoupling of ion and electron heat flux. This, in turn, can influence the H-mode transition at low density, as speculated in [152].
Even comparing shots at the same current, density and X-point height different values of $P_{L,LH}$ were measured. In fact shots performed before June 2011 show noticeable lower $P_{L,LH}$ compared to shots performed in December 2011, see Figure 5.13. Between the two campaigns the discharges seem to be characterized by different wall conditions. In Figure 5.14a Z_{eff} is reported versus line average density for the entire database. Taking into account only

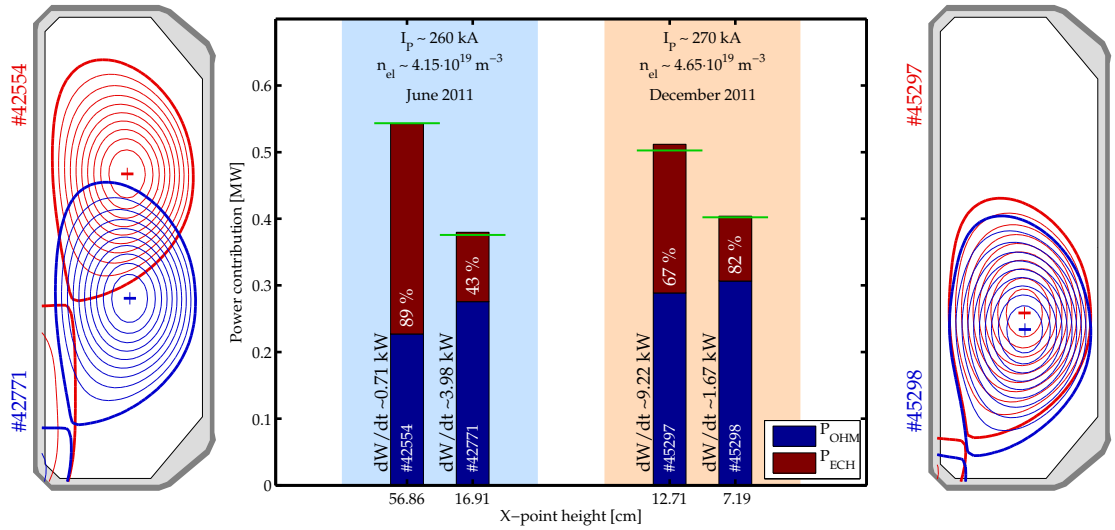

Figure 5.13: Detailed comparison between pairs of shots with similar plasma parameters (x axis is not in scale to facilitate the pair comparison). Contribution to the power loss is depicted. Red bar: ohmic contribution, blue bar: ECRH contribution, internal energy variation given aside each bar. Green lines indicate the measured value of the power loss at the transition, $P_{L,LH}$. The white percentage on ECRH contribution is the calculated first pass absorption. The pairs correspond to the points linked by purple arrows in Figure 5.12. Aside of the bar plot the comparison between the plasma shape within each pair is depicted.

discharges performed in June, i.e. only circles in Figure 5.14a, Z_{eff} is found to decrease as $\langle n_e \rangle_l$ increases as mentioned in [153][a]. Comparing shots at the same density performed in different campaigns, Z_{eff} is approximately 25% higher for shots performed in December. A Z_{eff} denpendence on plasma position inside the chamber was already escluded in [149]. In [155] $P_{L,LH}$ is reported to grow as $(Z_{eff}/2)^{0.7}$, so an increase by 25% in Z_{eff} turns in a 25% increase of $P_{L,LH}$. This correction is not enough to explain the large discrepancy but, at least, brings the estimate closer to each other. Investigating further into wall conditions, no marked differences in the D_α emission from the divertor region are observed between the two campaigns. So, wall conditions seem to play a role in determining the H-mode power threshold, but further investigations are requested to assess how important is its contribution. To clarify the situation a subset of discharges has been selected. Discharges performed at densities lower than $3.6 \cdot 10^{19}\mathrm{m}^{-3}$, and certainly overestimated $P_{L,LH}$ values can be neglected[b]. The density dependence can be reduced dividing $P_{L,LH}$ by the power-law scaling (2.3), moreover the wall influence can be partially reduced dividing it further by $(Z_{eff}/2)^{0.7}$. Such a normalization leads to Figure 5.15a and Figure 5.15b. An average decrease in power threshold at lower plasma position is recognizable, even if a large scatter still affect the database. Such a decrease together with the pair comparisons reported in Figure 5.13, are

[a] *For more general example see [154] or [155].*
[b] *In Table 5.2 the shots retained to draw the scaling are marked by a green tick.*

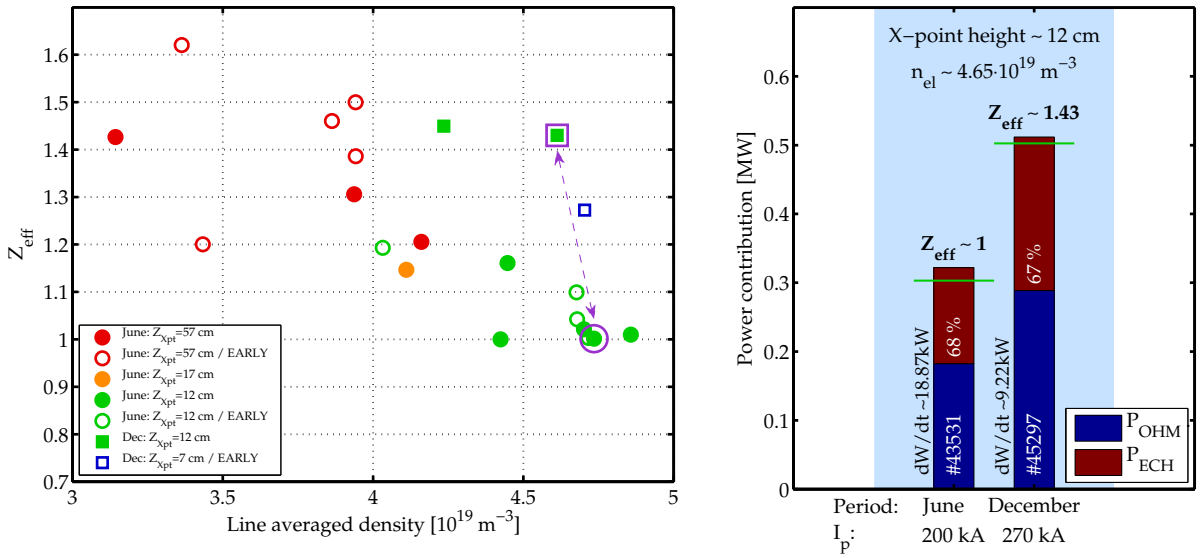

(a) (b)

Figure 5.14: (a) Z_{eff} versus $\langle n_e \rangle_l$ for the entire dataset. (b) Detailed comparison between two shots with similar plasma parameters but performed in two different campaigns. Contribution to the power loss is reported. Red bar: ohmic contribution, blue bar: ECRH contribution, internal energy variation reported aside each bar. Green lines indicate the measured value of the power loss at the transition, $P_{L,LH}$. The white percentage on ECRH contribution is the calculated first path absorption. The pair correspond to the points linked by the purple arrow in (a).

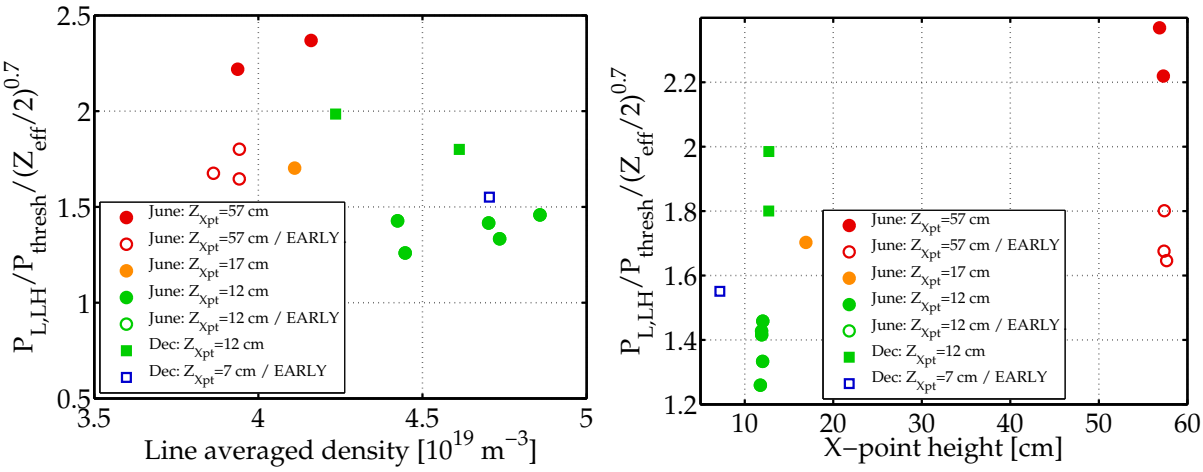

(a) (b)

Figure 5.15: Power threshold normalized to (2.3) and corrected for Z_{eff} dependence, for a selected subset. The retained discharges are those marked by the green tick in Table 5.2. (a) Density dependence. (b) X-point height dependence.

enough to confirm the X-point height influence on $P_{L,LH}$ described in [138], also for the TCV tokamak.
Even if the X-point position has been proved to influence the H-mode power threshold, it is worth to remind that the X-point height does not have any physical meaning. A change in Z_{Xpt}, must therefore trigger a change in one or several physical parameters along with the change in the power threshold. In literature, neutral density near the X-point and SOL flows have been suggested as one of such parameters. During the TCV campaigns no SOL flows data has been collected, while the D_α emission was investigated as a footstep of the neutrals density. In JET, divertor D_α was shown to increase by a factor of two lowering the X-point onto the divertor[138]. This increase was interpreted by the authors as an increase of the neutral density in the vicinity of the X-point. In contrast a drop by a factor 2 in the D_α from the outer strike point has been reported in DIII-D and motivated the authors to point at the SOL neutrals as a responsible for the simultaneous drop of the H-mode power threshold. In TCV 7 photodiodes are dedicated to collected the D_α radiation emitted from the inner wall, in addition a further photodiode collects D_α radiation vertically from the floor of the vessel. A comparison between two shots performed with different X-point height is depicted in Figure 5.16. Looking at the two top panels, is possible to see that the inner strikepoint in shot 45297 (red one) remains almost fixed above the center of the collection area of photodiode #8. In contrast, in shot 45298 (green one) the inner strike point is decreased until the L-H transition, and at $t \sim 0.5$ s crosses the center of the collection area of photodiode #8. Looking at the D_α traces within 0.5 s and 0.7 s, the lower Z_{Xpt} shot shows a lower intensity for the three photodiodes nearest to the inner strike point, namely 8, 9 and 10; whereas for $t < 0.5$ s they shows similar behaviors. This drop can not be seen in the signals from all of the other photodiodes. This situation resambles the finding of DIII-D, even if the drop is not that marked. Unfortunately, at the moment, we are not able to distinguish whether the emission collected from photodiode #8 pertains to the divertor private region rather than to SOL outside the inner strike point[a]. This situation holds similarly for the vertical D_α. So rigorous comparison can be performed with neither DIII-D nor with JET evidences. In principle this would be possible comparing shots at $Z_{Xpt} \sim 57$ cm and $Z_{Xpt} \sim 17$ cm, but unfortunately in those cases only one of the photodiodes was working. Deeper investigations are left for future experimental campaigns.

[a] *Such a confusion is due to the relative position of the strike point compared to the collection area of the photodiodes which deals with the peculiar open divertor configuration of TCV.*

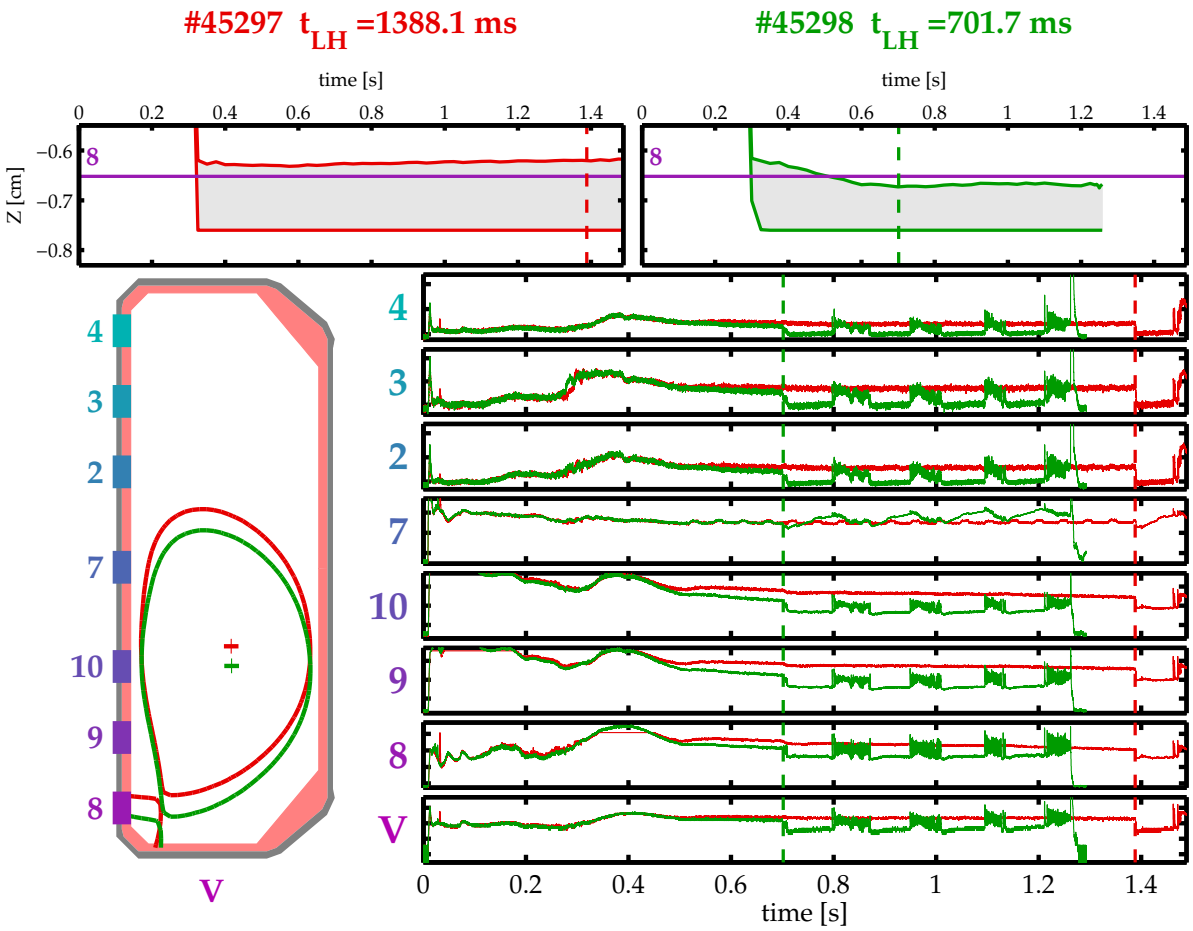

Figure 5.16: Comparison between D_α radiation of two shots at different Z_{Xpt}. On the left the plasma shapes are depicted inside the TCV vessel. On the inner wall, the collection areas of the different photodiodes collecting D_α radiation are sketched. The magnetic reconstructions are performed within 2 ms before the L-H transition. The two top panels represent the time evolution of the inner and outer strike points vertical position. The shaded area marks the divertor private region. The center of the collection areas are depicted as straight lines. The eight central panels report the comparison of the calibrated D_α emission as collected by the different photodiodes. The y scale is not maintained between the panels and is arbitrarily normalized. The L-H transition is marked everywhere with vertical lines.

5.5 GAP INFLUENCE ON H-MODE POWER THRESHOLD

As a side result, during the Z_{Xpt} investigation the influence of plasma-wall gaps on $P_{L,LH}$ was furher confirmed. In order to evaluate such influence, a simple test was performed. A discharge with an accurate estimate of $P_{L,LH}$ which was performed fulfilling all the requests made in (5.1) was chosen. The same discharge was repeated reducing the gaps below 2 cm before the L-H transition occurrence. The shot chosen was 43532 and in its repetition, namely 43538, both the gaps were decreased from 2 cm down to 1 cm during the ECRH ramp. To lower the plasma wall distance κ was decreased from 1.7 to 1.6 and δ was slightly decreased in order to maintain the same plasma surface. These changes turned in a raise of the X-point approximately by two centimeters, passing from 12 to 14 cm. In shot 43532 the H-mode was accessed at $P_L \sim 0.31$ MW while in shot 43538, with full single ECRH-launcher power, $P_L \sim 0.53$ MW was not enough to access the H-mode. The comparison between the two shots is reported in Figure 5.17. The discrepancy in the power loss is too large to be completely ascribed to the different X-point height. Considering the change evaluated in Figure 5.13, a 2 cm increase of Z_{Xpt} would let to a 40 kW difference in the power threshold, well below the 220 kW found by reducing the gaps. The change in P_L can be ascribed to a reduced number of parameters, the more probable of which the reduction of the plasma-wall gaps. In fact, if the LCFS is too close to the material wall the SOL thickness becomes so thin that plasma behave as limited rather than diverted. No experimental confirmation of such explanation can be presently given. Even if earlier studies [148] have shown the importance of plasma wall separation in influencing bulk and divertor radiation: no outstanding difference has been noticed in the D_α radiation from either the inner wall or the vessel bottom.

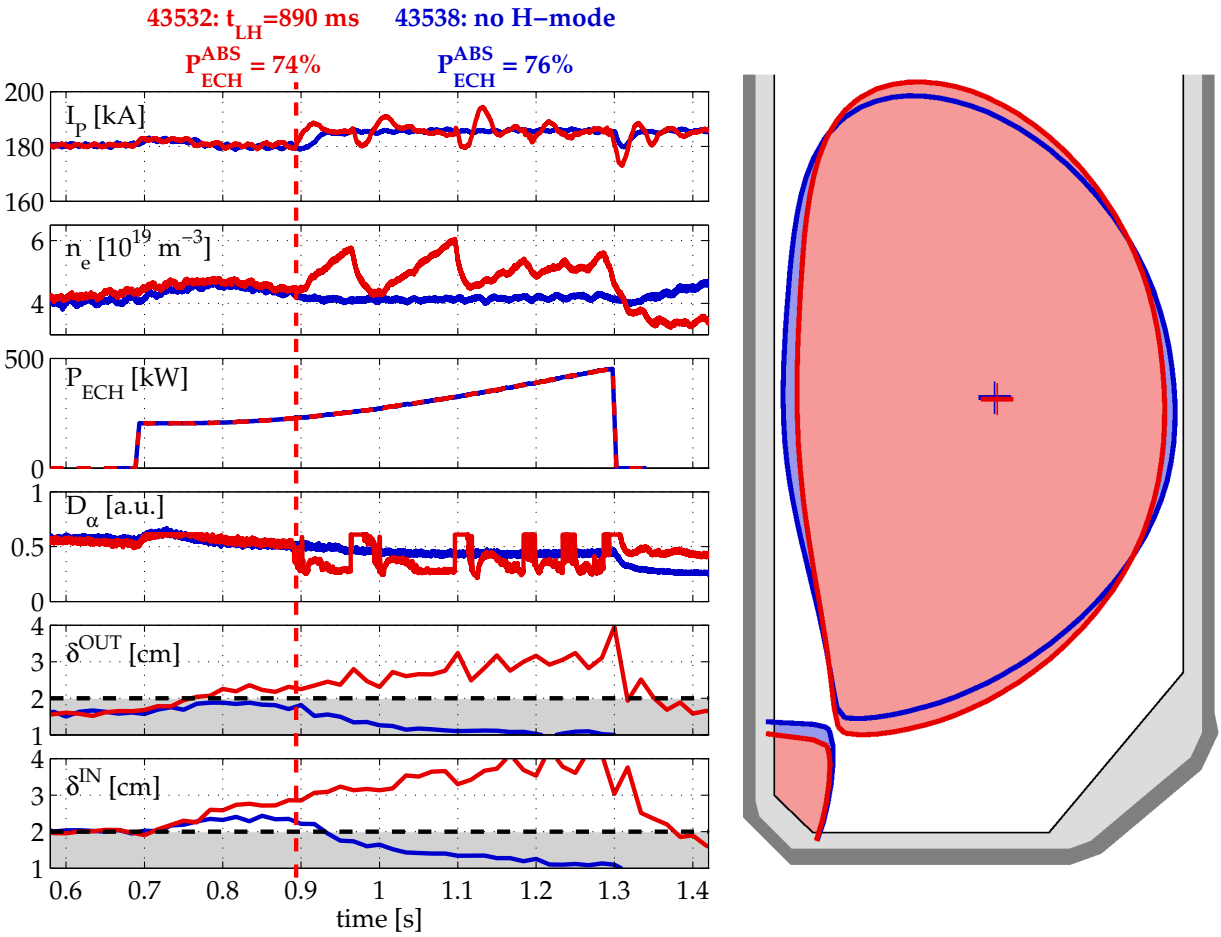

(a) (b)

Figure 5.17: Influence of gaps on H-mode power threshold. Comparison between two discharges approximately equal apart from inner and outer gaps value. (a) Time evolution of the two discharges. From top to bottom: plasma current, density, ECRH power, vertical D_α emission from divertor region, outer and inner gap. Shot 42352 (red one) undergoes the L-H transition at ∼890 ms. (b) Comparison between the two equilibria. The reconstruction are considered at the end of the ECRH ramp for shot 43538 (blue one) and ∼1 ms before the L-H transition for shot 43532 (red one).

5.6 SUMMARY AND REMARKS

During 2011 a series of experiments were performed on TCV to investigate the influence of the X-point geometry on the H-mode power threshold, $P_{L,LH}$. All plasmas were configured with the ion ∇B-drift towards the X-point of a Single Null configuration. The H-mode power threshold, has been measured in a shot-to-shot scan for different plasma vertical positions. In every shot, the L-H transition was triggered during the plasma current flat-top phase with a slow ramp of ECRH heating performed by two ECH-X2 launchers. The H-mode power threshold was shown to be influenced by electron density, X-point height and plasma-wall gaps.

A density scan carried out with the X-point $\sim$ 57 cm above the bottom of the vessel have shown that at low densities a minimum for $P_{L,LH}$ exists, as already reported by many machines. The minimum power threshold is approximately located at $\langle n_e \rangle_l \sim 3.6{\cdot}10^{19}\mathrm{m}^{-3}$, in agreement with earlier TCV studies[69].

The favorable $P_{L,LH}$ decrease with decreasing X-point height, Z_{Xpt}, reported in [138] was confirmed: a reduction in Z_{Xpt} turns in a reduction of $P_{L,LH}$ and the power threshold variation is larger when the X-point is closer to the bottom of the vessel. Moving the plasma 40 cm down from the highest position the H-mode power threshold decreases approximately by 30%. Furthermore, if the plasma is closer to bottom of the vessel, a downward shift of 5.5 cm turns in a 20% decrease of $P_{L,LH}$.

During the Z_{Xpt} investigation the influence of plasma-wall gaps on $P_{L,LH}$ reported in [147] was tested. A discharge, where H-mode was accessed keeping the plasma-wall gaps larger than 2 cm, was repeated reducing the gaps below 2 cm before the L-H transition occurrence. In the first shot the H-mode was accessed at $P_L \sim 0.31$ MW while in the second one $P_L \sim 0.53$ MW was not enough to access it. Such evidence points towards a required minimum SOL thickness to have a plasma behaving as diverted rather than limited despite the X-point configuration.

6

CONCLUSION AND PERSPECTIVES

Ci sono soltanto due possibili conclusioni: se il risultato conferma le ipotesi, allora hai appena fatto una misura; se il risultato è contrario alle ipotesi, allora hai fatto una scoperta.
There are two possible outcomes: if the result confirms the hypothesis, then you've made a measurement. If the result is contrary to the hypothesis, then you've made a discovery.
Enrico Fermi

One of the major concerns in magnetic confinement fusion research is the quest for the best plasma performance which is intimately linked to two main issues: plasma confinement and boundary conditions. In tokamaks, the diverted configuration, conceived for a controlled plasma-wall interaction, led to the discovery of the H-mode, the projected baseline operational scenario for ITER. In RFPs, the spontaneous growth of a dominant MHD mode led to a reduced chaos in the plasma core and to a favorable helical edge topology with a reduced plasma-wall interaction. My three years research activity have been focused on this topic: the accessibility conditions and the characterization of improved confinement regimes in tokamak and RFPs. In this chapter the entire work is summarized and brought to conclusions. The characterization of the RFX-mod temperature profile led to an overall picture of RFX-mod thermal properties relating plasma performance, wall conditions and external means of control. Such a picture can be useful to evaluate the actual machine reference point and to produce possible criteria to evaluate eventual future upgrades. The H-mode accessibility studies performed at TCV led to first confirmations of the beneficial reduction of the X-point height. The study is commented and future developments are proposed.

The search for the best plasma performance is one of the main guideline for each configuration in magnetic fusion devices. This mission assumes different meanings in Tokamaks and RFPs. For tokamaks, the reference point posed by the ITER project imposes the development and improvement of the H-mode baseline scenario as a primary need. One of the main concerns is the input power requirements for accessing H-mode, at the ITER target density, during the first ITER phase of operation. In this respect, a large worldwide effort to characterize the H-mode accessibility is ongoing. On the other hand, for RFPs, the quest for better plasma performance is related to the evaluation whether the RFP configuration will be a possible alternative path towards a fusion reactor. These two open questions have provided the background to my three years activity. In this chapter, the outcome of this activity is summarized and the work presented in the three previous chapters has been brought to conclusions. For both the machines, the characterization of RFX-mod temperature profiles and the H-mode accessibility studies at TCV, an overall picture is proposed together with future perspectives and possible developments.

6.1 RFX-MOD: TEMPERATURE PROFILE CHARACTERIZATION

Temperature is one of the key parameters that qualify fusion plasma performance. As far as only central temperature is considered, in RFX-mod plasmas, temperature is mainly determined by three parameters: plasma current, density and amplitude of secondary modes[107]. This picture becomes more assorted when the entire temperature profile is taken into account. In order to unravel the knot, a characterization method for the electron temperature profile was specifically conceived and a wide-ranging characterization was performed. A particular attention has been posed to investigate the region $0.6 \lesssim |r/a| \lesssim 0.9$, where the large fraction of the temperature drop between the plasma core and the plasma edge occurs.
In RFX-mod, three distinctive shapes of temperature profile mark the achievement of three different magnetic states. The baseline Multiple Helicity state, characterized by a flat temperature profile (black in Figure 6.1), is enhanced by the growth of a dominant MHD perturbation healing the magnetic chaos which governs the plasma volume. The reduced chaos leads to the appearance of a narrow high temperature structure in the plasma core (DAx state) which eventually widens covering approximately the 40% of the plasma volume and triggering the formation of an Internal Transport Barrier (SHAx state), red profile in Figure 6.1. This collection of temperature profile shapes is enlarged by the occasional appearance of extremely high gradients developing at $r/a \sim 0.8$ dubbed External Thermal Barriers (green in Figure 6.1). In order to characterize the temperature drop across the external plasma region, a specific method has been proposed: a fit using the *Fermi fuction* leads to a paradigm similar to the one used in tokamaks for the pedestal region:

$$T_e^{knee} \sim T_e^{foot} + \langle \nabla T_e \rangle \cdot \Delta \qquad . \tag{6.1}$$

In (6.1) T_e^{knee} represents the temperature at the top of the temperature drop, T_e^{foot} the temperature at its bottom, $\langle \nabla T_e \rangle$ the average temperature gradient occurring across the region interested by the temperature drop which spatially extends for Δ. The same model was also used for the eITB region, with T_e^{knee} and T_e^{foot} respectively replaced by T_e^{top} and T_e^{bott}.
Considering previous studies on central temperature[107] and eITBs[113] and evaluating the available evidences on edge temperature[86, 158] a multi-parameter model has been proposed to fit the temperatures above mentioned. Plasma current I_p, line average density $\langle n_e \rangle_l$, reversal parameter F and normalized secondary modes amplitude $\tilde{b}_\varphi^{sec}$ have been considered as significant macroscopic parameters. Moreover, the spatial extent of the temperature drop, Δ, have been added to obtain:

$$T_e \left(I_p, \langle n_e \rangle, |F|, \tilde{b}_\varphi^{sec}, \Delta \right) = \alpha \, {I_p}^{\gamma_{I_p}} \, \langle n_e \rangle_l^{\gamma_{n_e}} \, |F|^{\gamma_F} \, (\tilde{b}_\varphi^{sec})^{\gamma_{sec}} \, \Delta^{\gamma_\Delta} \quad . \tag{6.2}$$

In the case of eETBs, the limited set of data did not allow to perform such a statistical procedure so a direct evaluation of the influence of each parameter has been done. Such a procedure led to an overall picture about the temperature profile modifications and their causes which is reported in the next section and sketched in Figure 6.1.

6.1.1 Main results

In order to understand how the temperature profile behaves is useful to consider a simplified model. The plasma column can be divided in 4 regions, referring to Figure 6.1:

core region exhibits a flat temperature and extends from the plasma core towards $r/a \sim 0.5$ in MH-like profiles. It can be characterized by the presence of a thermal structure related to the chaos reduction due to the onset of the QSH state. In SHAX-like profiles it is bounded by the external transport barrier.

middle region usually flat, in MH-like profiles it can be considered as an extension of the core region towards $r/a \sim 0.7$. In SHAx-like profiles it sits outside the region interested by the internal transport barrier.

external region it is characterized by a large fraction of the temperature drop between the core and the edge. It extends within the region $0.6 \lesssim |r/a| \lesssim 0.9$ and does not have a fixed width. It can be characterized by the presence of extremely high gradients (eETBs).

edge region The very few centimeters directly in contact with the material wall. This region remained out from the investigation of this work. The temperature across this region, as measured by the THB diagnostic and the Langmuir probes, has been used as a boundary condition to evaluate the temperature drop occurring in the external region.

The table in Figure 6.1 gives a brief overview of the various dependence characterizing the temperature across the three regions.
The leading knob to vary the electron temperature is the plasma current, a quasi-linear relation between I_p and T_e holds throughout the entire profile independently from the

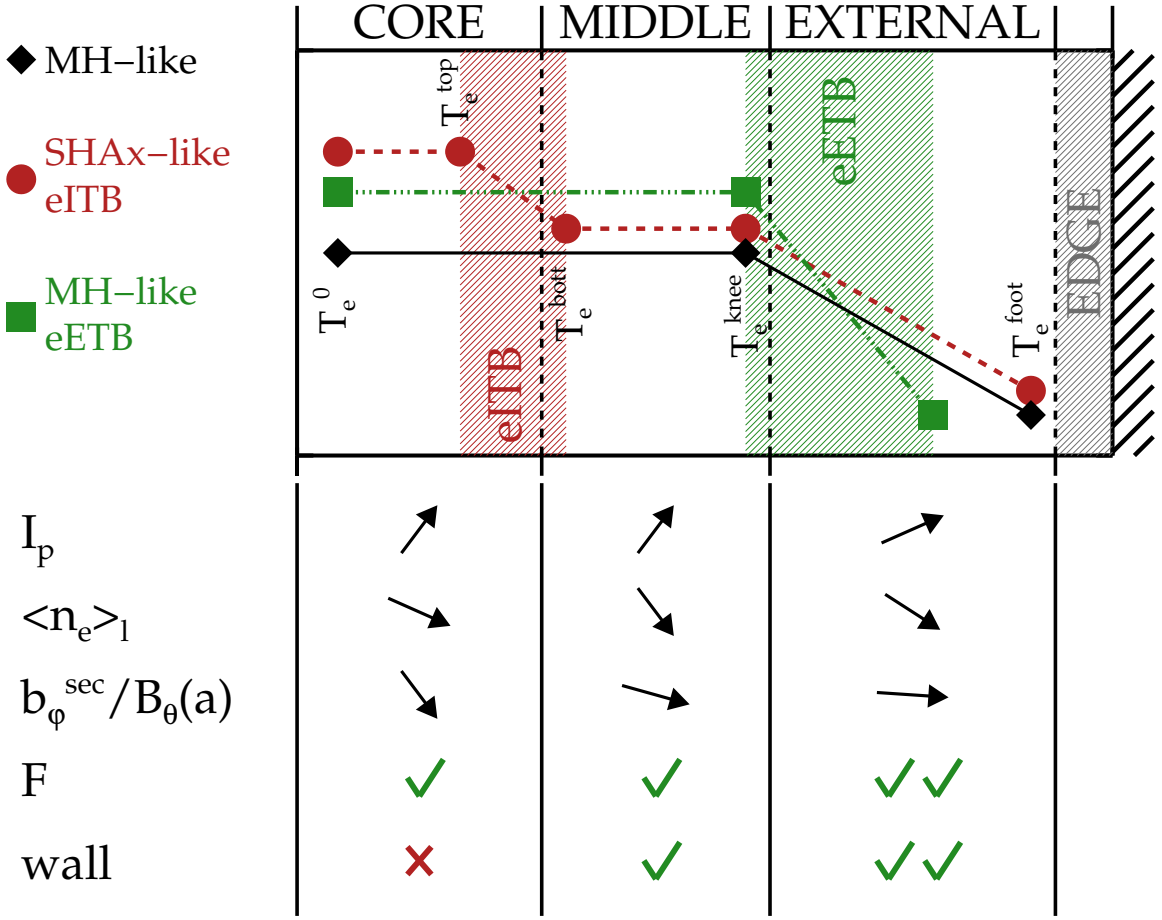

Figure 6.1: Cartoon of three different distinctive temperature radial profiles: MH-state (black), SHAx-like profile with eITB appearance (red) and MH-like profile with eETB appearance (green). Neither the x-axis nor the y-axis are in scale. The region interested by the occurrence of the barriers are shaded. The plasma column has been divided in four regions and the dependence of the temperature profile in each region is depicted in the table below the figure. The arrows represent the behavior of the temperature in the relative region responding to an increase of the parameter depicted in the first column. The angle of the arrow indicates qualitatively how strong is the link between the two: horizontal means almost null link, vertical stands for linear relation. The last rows qualitatively indicate whether the temperature in a particular region depends or not on the parameter on the left: red cross marks no dependence, one green tick weak dependence, two green ticks significant dependence.

magnetic state. RFX-mod is heated by Ohmic means only, so an increase in the plasma current turns in a larger power input. The strong link between T_e and plasma current is not easily disentangled by others secondary dependencies. The temperature profile response to an increase of the plasma current is not homogeneous. The temperature in the core and middle regions is more sensitive to current changes than the temperature in the external one.
Increasing the current, the plasma spends a larger fraction of the total discharge duration in QSH magnetic state, thus with a lower magnetic chaos. The main transport mechanism, the parallel transport in a stochastic magnetic field, is reduced in the core region with a consequent temperature increase and eventually leading to the formation of the eITBs. The external region is less interested by chaos reduction thus a weaker dependence is found. Such a mechanism is directly reported in Figure 6.1 as a dependence on the normalized amplitude of the secondary modes. As a proof, γ_{sec} in (6.2) grows from ~ -0.3 towards zero moving from the central region towards the plasma edge. So an increase in plasma current generally conveys a reduction of the magnetic chaos which can led to a temperature profile peaked in the core.
On the other hand, considering the external region, changes in I_p trigger variations in the magnitude of T_e while they do not affect the profile shape which remains self-similar. Such self-similarity states that to an increase in I_p corresponds no significant changes in the transport properties of the external region: a higher input power turns in a higher temperature at the knee of the temperature decrease and consequently in a steeper external gradient.

Beside plasma current and secondary modes amplitude, the other macroscopic parameter influencing the temperature is density. As for plasma current, the dependence is not homogeneous throughout the entire plasma radius. The anti-correlation between density and temperature is fairly strong in the middle and edge regions, it becomes weaker in core one. For a given pressure, an increase in density leads to a general decrease in temperature and also to a modification of the neutrals penetration depth and, in turn, the electron density and neutral density profiles in the external and edge regions vary.
In RFX-mod the plasma density is generally established by the high-recycling carbon wall, the neutrals are highly localized outside $r/a \sim 0.8$ and so they form a large toroidally and poloidally distributed, radially localized source of cold electrons and ions. The neutrals penetration depth is reduced as the density gradient increases, which in RFX-mod generally increases as the Greenwald density fraction, n/n_G, does. Indeed as n/n_G increases the density profile tends to peak at the plasma edge becoming hollow[120], the density gradient increases and neutrals penetration depth in turn reduces. The only way to limit this unfavorable loop consists in reducing the wall recycling, in other words an efficient wall conditioning is needed. A well conditioned wall results in less peaked density profile at the plasma edge and turns in a steeper temperature decrease across the external region. A large amount of ionization processes occurs in the region outside $r/a = 0.8$, as a matter of fact the location of the foot of the external temperature drop is found to move towards the wall as n/n_G incerases. As a

result the region interested by the external temperature drop broadens and both T_e^{foot} and T_e^{knee} decreases as n/n_G is raised. As a consequence, density variations lead to modifications of the temperature profile across the external region: as the density increases the temperature drop tends to broaden and flatten.

The last macroscopic parameters taken into account in the model (6.2), is the reversal parameter F. A general beneficial effect on temperature is seen when operating at shallow F, i.e. $F \gtrsim -0.1$. This effect can be generally related to a plasma edge which becomes colder and more resistive as the reversal surface is brought farther from the wall. Beside this general feature, shallow F discharges can be related to a significant change of the edge topology. As F is increased towards zero the reversal surface, thus the $m = 0$ islands chain, approaches the wall. If the $m = 1/n = -7$ MHD mode amplitude is large enough to hinder the large $m = 0/n = 1$ deformation related to the wall locking of the MHD modes, the $m = 0$ islands chain is spatially regular. Provided this regularity, pushing the reversal surface towards the wall the $m = 0$ islands can intercept it and the LFCS, generally laying between the islands chain and the wall, changes location passing inward with respect to the island chain. If the wall is well conditioned and such topology arises, a diverted-like configuration is formed: the $m = 0$ islands touch the wall creating an effective-SOL with almost flat temperature up to the LCFS with a steep increase inside it. Such a topological change reflects in a generally lower temperature at the LCFS and a higher temperature at the knee. If the reversal surface further approaches the wall, provided the topology is maintained, the improvement is so large to give rise to extremely high gradients dubbed electron External Thermal Barriers (eETBs). The eETBs are found to be stronger as the volume enclosed between the LCFS and the wall becomes smaller.

The above mentioned evidences are related to the three main knobs available in RFX-mod to modify the thermal properties of the plasma: plasma current, density and equilibrium control via the F parameter. While the plasma current is mainly related to the input power and substantially affects the plasma core, density and F deal with wall conditions being thus related to the behavior of the more external region of the plasma column. A higher plasma current results in a higher average temperature and eventually leads to the formation of internal transport barrier, provided the magnetic chaos is sufficiently reduced (the normalized secondary modes amplitude is low enough). Such a reduction is related to the growth of a dominant MHD mode over a sea of secondary MHD modes and is effective only in the plasma core leaving almost unvaried the region outside $r/a \sim 0.5$.
Conversely, to enhance the plasma behavior in the outer region of the plasma column one has to focus on ameliorating the plasma-wall interaction looking for the best edge topology (shallow F with a regular $m = 0$ islands chain intercepting the wall), trying to minimize the wall recycling and conceiving a way to remove the high concentration of neutrals present near the material surface. Optimizing simultaneously the two radial regions, it should be possible

to obtain an internal transport barrier (reduced magnetic chaos) occurring on a high T_e^{bott} caused by the presence of a high external temperature gradient (milder PWI).

Beside this operational scheme, some other mechanisms affecting the temperature profile can not presently be controlled. In RFX-mod the large fraction of the plasma volume is dominated by parallel transport in a stochastic magnetic field, so an estimate of the electron thermal conductivity due to magnetic stochasticity was given in [156] as

$$\chi_{st}(r) = D_M(r) v_{th}(r)$$

where v_{th} is the electron thermal velocity and D_M is the magnetic diffusivity of test particles in a stochastic magnetic field. Considering the field lines as randomly moving inside the plasma volume, this diffusivity can be estimated as the ratio between the average radial square displacement of field lines $\langle \Delta r^2 \rangle$ after a length L:

$$D_M(r) = \frac{\langle \Delta r^2 \rangle}{2\Delta L} \propto \sum_{m,n} \frac{|b^{m,n}(r)|^2}{B(a)^2} \quad .$$

In the previous $b^{m,n}(r)$ is the amplitude of the magnetic field fluctuations. The former provides a possible explanation for the low influence of a secondary mode reduction in the middle and external region of the temperature profile. As a matter of fact, in the region $r/a > 0.7$ generally all the MHD modes $m = 1/|n| > 15$ resonate, while only the normalized amplitude of MHD modes $m = 1/|n| < 24$ is measured and thus shown to decrease with plasma current. So the transport characterizing the region outside the eITB, when formed, and generally outside $r/a > 0.7$, probably remains highly stochastic increasing the current. This speculation may explain the self-similarity of the temperature profile in the external region while the current is varied.

6.1.2 Future perspectives and developments

The wide-ranging analysis performed will be extended and refined so to consider presently ongoing experiments: lithium wall conditioning, plasma fuelling by pellet injection and non-zero boundary conditions (BCs) discharges. The Fermi fit characterization procedure provided a reliable method to characterize the temperature profile in the external region of the plasma column. It would be interesting to couple the results obtained with this method to a modelling of the RFX-mod plasma edge, for example using a transport code capable to model both the physics of electron and ions and the influence of neutrals.

The method to characterize the temperature profile proposed in this work turned out to be reliable and well suited to match both the internal transport barrier and the external temperature decrease. Nevertheless, the edge boundary conditions statistically imposed and the flat character of the Fermi function outside the temperature drop allows only a qualitative

match of the temperature profile across the edge region. Exploiting the newly working edge Thomson scattering system, the lack of measurements in the region $0.8 < r/a < 0.9$ can be ridden out and a new function can be used to match the entire region going from $r/a \sim 0.7$ up to the wall. So it will be useful to merge together the data from main TS, edge TS, THB and Langmuir probes to build up a consistent temperature profile. These diagnostic are located at different toroidal and poloidal positions so their mapping can not be simply performed. In fact, the edge magnetic topology strongly modifies the edge plasma kinetic structure, as reported in [92, 93, 158]. So, to map the measurements of the four diagnostics together a common frame of reference is needed. This can be built considering the radial shift δ_r of magnetic surfaces due to the coupling of the $m = 1/n - 7$ mode with the $m = 0$ islands chain. The new frame of reference can be built as follow

$$x \;=\; x(r,\theta,\phi) \;\equiv\; r - \delta_r(\theta,\phi) \qquad .$$

Exploiting this new coordinate the four diagnostics can be mapped together leading the possibility of a more detailed mapping. Using the modified $tanh$ function commonly used in tokamak community, a new mapping function can be used:

$$F(x) = \underbrace{\frac{h}{2}\tanh\left(\frac{x-x_0}{d}+1\right)}_{\text{temperature drop}} + \underbrace{k(x-x_0-d)\mathrm{H}\left(x-x_0-d\right)}_{\text{core raise}} + \underbrace{m(x-x_0+d)\mathrm{H}\left(x-x_0+d\right)}_{\text{edge decrease}} + b$$

where $H(\cdots)$ marks the Heavyside function. The former is composed by three terms which allow to map the main temperature decrease and leave the possibility to map an eventual temperature raise towards the plasma core and a decreasing temperature towards the wall. The former leaves unvaried the intuitive appeal of the Fermi fit parameters, in fact x_0 depict the postion of the maximum gradient (i.e. the average postion of the temperature decrease), h is twice the temperature drop while d is a half of its spatial extent.

6.2 TCV: H-MODE ACCESSIBILITY

In many tokamak devices the relative location of the X-point in the poloidal plane and its geometry is reported to affect the H-mode power threshold. Exploiting the flexible shaping capabilities of the standard Single Null configuration, dedicated investigations have been performed in TCV. The H-mode power threshold, $P_{L,LH}$, has been measured in a shot-to-shot scan for different plasma vertical positions. In every shot, the L-H transition was triggered during the plasma current flat-top phase with a slow ramp of ECRH heating performed by two ECH-X2 launchers.

6.2.1 Main results

Approximately 20 discharges have been performed with $B_T \sim 1.4$ T moving rigidly the plasma inside the vessel. The H-mode power threshold was shown to vary with electron density, X-point height and plasma-wall gaps.
A density scan carried out with the X-point ∼57 cm above the bottom of the vessel has shown that at low densities a minimum for $P_{L,LH}$ exists, as already reported by many machines. The minimum power threshold has been approximately located at $\langle n_e \rangle_l \sim 3.6{\cdot}10^{19}$ m^{-3}.
The favorable $P_{L,LH}$ decrease with decreasing X-point height, Z_{Xpt}, reported in [138] was confirmed: a reduction in Z_{Xpt} turns in a reduction of $P_{L,LH}$ and the power threshold variation is larger when the X-point is closer to the bottom of the vessel. Moving the plasma 40 cm down from the highest position the H-mode power threshold decreases approximately by 30%. Furthermore, if the plasma is closer to bottom of the vessel, a downward shift of 5.5 cm turns in a 20% decrease of $P_{L,LH}$.
During the Z_{Xpt} investigation the influence of plasma-wall gaps on $P_{L,LH}$ reported in [147] was tested. A discharge, where H-mode was accessed keeping the plasma-wall gaps larger than 2 cm, was repeated reducing the gaps below 2 cm before the L-H transition occurrence. In the first shot the H-mode was accessed at $P_L \sim 0.31$ MW while in the second one $P_L \sim 0.53$ MW was not enough to access it. Such evidence points towards a required minimum SOL thickness to have a plasma behaving as diverted rather than limited despite the X-point configuration.

6.2.2 Future perspectives and possible developments

The entire analysis suffered from a certain degree of variability: different wall conditions and impurity concentration due to the time elapsed between different experimental sessions, the forced reduction of plasma current target value are some examples. Given the large number of known $P_{L,LH}$ dependencies is extremely important to limit such variability in order to disentangle them. Maintaining the same operational method, further investigations will be useful to ground the obtained evidences. A more accurate density scan at low X-point height will allow to assess if the X-point decrease beneficial effect is homogeneous throughout the

entire explorable density range. To verify whether the $P_{L,LH}$ decrease linearly with Z_{Xpt} a coarse scan at intermediate X-point positions, X-point ∼30 cm above vessel bottom, should be performed. Indications about an influence of the wall conditions on the H-mode power threshold were obtained, further investigations in these respects are desirable.
The discussed discharges have been performed with the largest possible plasma surface which, in turn, hindered the possibility to move the plasma on the horizontal axis. A reduction of the plasma radial dimension will allow such a movement, in this way further interesting analysis will become possible. As a matter of fact, measurements of the H-mode power threshold performed while moving the X-point in the radial direction, will allow to face two different topics. On the one hand the radial X-point position influence on $P_{L,LH}$ reported in NSTX[147] can be investigated. On the other hand, one can clarify the large increase in $P_{L,LH}$ due to reduced plasma-wall gaps. To complete the picture, it will be interesting to investigate whether moving the outer strike point onto the vertical target will affect the H-mode power threshold.

REFERENCES

[1] edited by M. Kikuchi, K. Lackner, M. Tran, *Fusion Physics* (International Atomic Energy Agency (IAEA), Vienna, 2012). http://www.pub.iaea.org/MTCD/Publications/PDF/Pub1562_web.pdf.

[2] Internation Thermonuclear Experimental Reactor (ITER). http://www.iter.org.

[3] European fusion network information. http://www.fusion-eur.org.

[4] J. P. Fridberg, *Plasma Physics and fusion energy* (Cambridge Univerity Press, Cambridge, 2007).

[5] J. P. Fridberg, *Ideal Magnetohydrodynamics* (Plenum Press, New York, 1987).

[6] H. P. Furth, J. Killeen, M. N. Rosenbluth, *Finite-Resistivity Instabilities of a Sheet Pinch*, *Physics of Fluids* **6**, 459 (1963).

[7] A. H. Boozer, *What is a stellarator?*, *Physics of Plasmas* **5**, 1647 (1998).

[8] J. Wesson, *Tokamaks* (Oxford University Press, Oxford, 2004).

[9] S. Ortolani, D. D. Schnack, *The Magnetohydrodynamics of Plasma Relaxation* (World Scientific, 1993).

[10] J. P. Fridberg, *MHD Instabilities* (MIT Press, Cambridge, 1978).

[11] J. Nührenberg, W. Lotz, P. Merkel, C. Nührenberg, U. Schwenn, E. M. Strumberger, *et al.*, *Overview of Wendelstein 7-X theory*, *Proc. 6th Int. Conf. on Plasma Physics and Controlled Nuclear Fusion* (Tokio, Japan, 1994), p. 71.

[12] G. Grieger, C. D. Beidler, H. Maaßberg, E. Harmeyer, F. Herrnegger, J. Junker, *et al.*, *Physics and engineering studies for Wendelstein 7-X*, *Plasma Physics and Controlled Fusion Research (Proc. 13th Int. Conf., Washington, DC, 1990) vol.3* (1991), p. 525.

[13] L. Artsimovich, *Tokamak devices*, *Nuclear Fusion* **12**, 215 (1972).

[14] J. B. Taylor, *Relaxation of Toroidal Plasma and Generation of Reverse Magnetic Fields*, *Phys. Rev. Lett.* **33**, 1139 (1974).

[15] W. Baker, S. D. Bello, D. Marcuzzi, P. Sonato, P. Zaccaria, *Design of a new toroidal shell and support structure for RFX*, *Fusion Engineering and Design* **63-64**, 461 (2002).

[16] P. Sonato, *et al.*, *Machine modification for active MHD control in RFX*, *Fusion Engineering and Design* **66-68**, 161 (2003). 22nd Symposium on Fusion Technology.

[17] G. Rostagni, *RFX: an expected step in RFP research*, *Fusion Engineering and Design* **25**, 301 (1995).

[18] L. Fellin, P. Kusstatscher, G. Rostagni, *Overall plant design, layout and commissioning*, *Fusion Engineering and Design* **25**, 315 (1995).

[19] A. Alfier, R. Pasqualotto, *New Thomson scattering diagnostic on RFX-mod*, *Review of Scientific Instruments* **78**, 013505 (2007).

[20] A. Alfier, A. Fassina, F. Auriemma, G. Spizzo, R. Pasqualotto, *Electron pressure measurements in the outer region of RFX-mod with the upgraded edge Thomson scattering diagnostic*, *Plasma Physics and Controlled Fusion* **52**, 035004 (2010).

[21] P. Innocente, S. Martini, *A two color multichord infrared interferometer for RFX*, *Review of Scientific Instruments* **63**, 4996 (1992).

[22] P. Innocente, S. Martini, A. Canton, L. Tasinato, *Upgrade of the RFX CO_2 interferometer using in-vessel optics for extended edge resolution*, *Review of Scientific Instruments* **68**, 694 (1997).

[23] M. Agostini, P. Scarin, R. Cavazzana, A. Fassina, A. Alfier, V. Cervaro, *Optical measurements for turbulence characterization in RFX-mod edge*, *Review of Scientific Instruments* **81**, 10D715 (2010).

[24] R. Cavazzana, *et al.*, *Optical and electrical diagnostics for the investigation of edge turbulence in fusion plasmas*, *Review of Scientific Instruments* **75**, 4152 (2004).

[25] G. Serianni, W. Baker, S. D. Bello, *High-spatial resolution edge electrostatic probe system for RFX*, *Review of Scientific Instruments* **74**, 1558 (2003).

[26] H. Tsui, R. Bengtson, G. Li, H. Lin, M. Meier, C. Ritz, A. Wootton, *A new scheme for Langmuir probe measurement of transport and electron temperature fluctuations*, *Review of Scientific Instruments* **63**, 4608 (1992).

[27] M. Spolaore, N. Vianello, M. Agostini, R. Cavazzana, E. Martines, G. Serianni, P. Scarin, E. Spada, M. Zuin, V. Antoni, *Magnetic and electrostatic structures measured in the edge region of the RFX-mod experiment*, *Journal of Nuclear Materials* **390-391**, 448 (2009). Proceedings of the 18th International Conference on Plasma-Surface Interactions in Controlled Fusion Device.

[28] F. Hofmann, *et al.*, *Creation and control of variably shaped plasmas in TCV*, *Plasma Physics and Controlled Fusion* **36**, B277 (1994).

[29] T. Goodman, S. Alberti, M. Henderson, *et al.*, *Design and installation of the electron cyclotron wave system for the TCV tokamak*, *Proc. 19th Symposium on Fusion Technology September 1996* (Lisbon, Portugal, 1996), pp. 565–568.

[30] S. Coda, *et al.*, *High-power ECH and fully non-inductive operation with ECCD in the TCV tokamak*, *Plasma Physics and Controlled Fusion* **42**, B311 (2000).

[31] F. Hofmann, G. Tonetti, *Tokamak equilibrium reconstruction using Faraday rotation measurements*, *Nuclear Fusion* **28**, 1871 (1988).

[32] S. Barry, *The extension of the FIR interferometer of TCV to a polarimeter and measurements of the Faraday rotation caused by the poloidal magnetic field*, Ph.D. thesis, École Polytechnique Fédérale de Lausanne (1999). Published as Lausanne Report LRP 638/99.

[33] L. Curchod, *High Density Plasma Heating in the Tokamak á Configuration Variable*, Ph.D. thesis, École Polytechnique Fédérale de Lausanne (2011). `http://library.epfl.ch/theses/?nr=5012`.

[34] R. Behn, S. Franke, Z. Pietrzyk, *et al.*, *The Thomson scattering diagnostic on TCV*, *7th International Symposium on Laser-Aided Plasma Diagnostics* (Fukuoka, Japan, December, 1995), pp. 565–568.

[35] S. Franke, *Application of Thomson scattering at 1.06 mm as a diagnostic for spatial profile measurements of electron temperature and density on the TCV tokamak*, Ph.D. thesis, École Polytechnique Fédérale de Lausanne (1997). `http://library.epfl.ch/theses/?nr=1654`.

[36] A. Pitzschke, *Pedestal Characteristics and MHD Stability of H-Mode Plasmas in TCV*, Ph.D. thesis, École Polytechnique Fédérale de Lausanne (2011). `http://library.epfl.ch/theses/?nr=4917`.

[37] ITER Physics Basis Editors, ITER Physics Expert Group Chairs and Co-Chairs, ITER Joint Central Team and Physics Integration Unit, *Chapter 1: Overview and summary*, *Nuclear Fusion* **39**, 2137 (1999).

[38] S. Itoh, K. Itoh, A. Fukuyama, *Physics of edge plasmas in enhanced confinement modes*, *Journal of Nuclear Materials* **220-222**, 117 (1995).

[39] J. Winter, *Wall conditioning in fusion devices and its influence on plasma performance*, *Plasma Physics and Controlled Fusion* **38**, 1503 (1996).

[40] W. Fundamenski, *Power Exhaust in Fusion Plasmas* (Cambridge Univerity Press, Cambridge, 2009).

[41] P. C. Stangeby, *The Plasma boundary of magnetic fusion devices* (Institute of physics publishing, Bristol and Philadelphia, 2000).

[42] European Fusion Development Agreement (EFDA). http://www.efda.org.

[43] M. Keilhacker, A. Team, *The ASDEX divertor tokamak*, *Nuclear Fusion* **25**, 1045 (1985).

[44] F. Wagner, *et al.*, *Development of an Edge Transport Barrier at the H-Mode Transition of ASDEX*, *Phys. Rev. Lett.* **53**, 1453 (1984).

[45] C. Gormezano, *et al.*, *Chapter 6: Steady state operation*, *Nuclear Fusion* **47**, S285 (2007).

[46] E. A. Lazarus, *et al.*, *Higher Fusion Power Gain with Current and Pressure Profile Control in Strongly Shaped DIII-D Tokamak Plasmas*, *Phys. Rev. Lett.* **77**, 2714 (1996).

[47] H. Zohm, *Edge localized modes (ELMs)*, *Plasma Physics and Controlled Fusion* **38**, 105 (1996).

[48] F. Wagner, *A quarter-century of H-mode studies*, *Plasma Physics and Controlled Fusion* **49**, B1 (2007).

[49] ITER Physics Expert Group on Confinement and Transport and ITER Physics Expert Group on Confinement Modelling and Database and ITER Physics Basis Editors, *Chapter 2: Plasma confinement and transport*, *Nuclear Fusion* **39**, 2175 (1999).

[50] K. H. Burrell, *et al.*, *Physics of the L-mode to H-mode transition in tokamaks*, *Plasma Physics and Controlled Fusion* **34**, 1859 (1992).

[51] J. W. Connor, H. R. Wilson, *A review of theories of the L-H transition*, *Plasma Physics and Controlled Fusion* **42**, R1 (2000).

[52] E. Doyle (Chair Transport Physics), *et al.*, *Chapter 2: Plasma confinement and transport*, *Nuclear Fusion* **47**, S18 (2007).

[53] W. Fundamenski, F. Militello, D. Moulton, D. McDonald, *A new model of the L-H transition in tokamaks*, *Nuclear Fusion* **52**, 062003 (2012).

[54] Y. R. Martin, T. Takizuka, the ITPA CDBM H-mode Threshold Database Working Group, *Power requirement for accessing the H-mode in ITER*, *Journal of Physics: Conference Series* **123**, 012033 (2008).

[55] T. Fukuda, T. Takizuka, K. Tsuchiya, Y. Kamada, N. Asakura, *Reduction of L-H transition threshold power under the W-shaped pumped divertor geometry in JT-60U*, *Plasma Physics and Controlled Fusion* **42**, A289 (2000).

[56] Y. Andrew, *et al.*, *H-mode access in the low density regime on JET*, *Plasma Physics and Controlled Fusion* **48**, 479 (2006).

[57] F. Ryter, *et al.*, *H-mode threshold and confinement in helium and deuterium in ASDEX Upgrade*, *Nuclear Fusion* **49**, 062003 (2009).

[58] Y. Ma, J. Hughes, A. Hubbard, B. LaBombard, R. Churchill, T. Golfinopolous, N. Tsujii, E. Marmar, *Scaling of H-mode threshold power and LâĂŞH edge conditions with favourable ion grad-B drift in Alcator C-Mod tokamak*, *Nuclear Fusion* **52**, 023010 (2012).

[59] B. LaBombard, *et al.*, *Transport-driven scrape-off layer flows and the X-point dependence of the L-H power threshold in Alcator C-Mod*, *Physics of Plasmas* **12**, 056111 (2005).

[60] J. Snipes, *et al.*, *H mode power threshold database for ITER*, *Nuclear Fusion* **36**, 1217 (1996).

[61] E. Righi, *et al.*, *Isotope scaling of the HÂămode power threshold on JET*, *Nuclear Fusion* **39**, 309 (1999).

[62] P. Gohil, T. Jernigan, T. Osborne, J. Scoville, E. Strait, *The torque dependence of the H-mode power threshold in hydrogen, deuterium and helium plasmas in DIII-D*, *Nuclear Fusion* **50**, 064011 (2010).

[63] ITPA H-mode Power Threshold Database Working Group presented by T Takizuka, *Roles of aspect ratio, absolute B and effective Z of the H-mode power threshold in tokamaks of the ITPA database*, *Plasma Physics and Controlled Fusion* **46**, A227 (2004).

[64] S. Toda, S.-I. Itoh, M. Yagi, Y. Miura, *A theoretical model of H-mode transition triggered by condensed neutrals near X-point*, *Plasma Physics and Controlled Fusion* **39**, 301 (1997).

[65] T. Fukuda, *'Hidden' variables affecting the L-H transition*, *Plasma Physics and Controlled Fusion* **40**, 543 (1998).

[66] F. Ryter, the H-mode Threshold Database Group, *Progress of the international H-mode power threshold database activity*, *Plasma Physics and Controlled Fusion* **44**, A415 (2002).

[67] H. Weisen, *et al.*, *Overview of TCV results*, *Nuclear Fusion* **41**, 1459 (2001).

[68] Y. R. Martin, *et al.*, *Accessibility and properties of ELMy H-mode and ITB plasmas in TCV*, *Plasma Physics and Controlled Fusion* **45**, A351 (2003).

[69] Y. R. Pitts, *et al.*, *1999 Proc. 26th EPS Conf. on Conrtolled Fusion and Plasma Phys.* (Maastricht, Netherlands, 1999). `http://epsppd.epfl.ch/Maas/pdf/p3033.pdf`.

[70] H. Ji, A. Almagri, S. Prager, J. Sarff, *Time resolved observation of discrete and continuous magnetohydrodynamic dynamo in the reversed-field pinch edge*, *Phys. Rev. Lett.* **73**, 668.

[71] H. Ji, S. Prager, *The alpha dynamo effects in laboratory plasmas*, *Magnetohydrodynamics* **18**, 191 (2002).

[72] F. D'Angelo, R. Paccagnella, *The stochastic diffusion process in reversed-field pinch*, *Physics of Plasmas* **3**, 2353 (1996).

[73] S. Cappello, R. Paccagnella, *Nonlinear plasma evolution and sustainment in the reversed field pinch*, *Physics of Fluids B: Plasma Physics* **4**, 611 (1992).

[74] J. Finn, R. Nebel, C. Bathke, *Single and multiple helicity Ohmic states in reversed-field pinches*, *Physics of Fluids B: Plasma Physics* **4**, 1262 (1992).

[75] P. Martin, *et al.*, *Overview of quasi-single helicity experiments in reversed field pinches*, *Nuclear Fusion* **43**, 1855 (2003).

[76] D. F. Escande, *et al.*, *Quasi-Single-Helicity Reversed-Field-Pinch Plasmas*, *Phys. Rev. Lett.* **85**, 1662 (2000).

[77] P. Martin, *Magnetic and thermal relaxation in the reversed field pinch*, *Plasma Physics and Controlled Fusion* **41**, A247 (1999).

[78] S. Cappello, D. F. Escande, *Bifurcation in Viscoresistive MHD: The Hartmann Number and the Reversed Field Pinch*, *Phys. Rev. Lett.* **85**, 3838 (2000).

[79] R. Lorenzini, *et al.*, *Improvement of the magnetic configuration in the reversed field pinch through successive bifurcations*, *Physics of Plasmas* **16**, 056109 (2009).

[80] R. Lorenzini, *et al.*, *Self-organized helical equilibria as a new paradigm for ohmically heated fusion plasmas*, *Nature Physiscs* **5**, 570 (2009).

[81] M. Valisa, *et al.*, *High current regimes in RFX-mod*, *Plasma Physics and Controlled Fusion* **50**, 124031 (2008).

[82] R. Lorenzini, D. Terranova, A. Alfier, P. Innocente, E. Martines, R. Pasqualotto, P. Zanca, *Single-Helical-Axis States in Reversed-Field-Pinch Plasmas*, *Phys. Rev. Lett.* **101**, 025005 (2008).

[83] E. Martines, R. Lorenzini, B. Momo, S. Munaretto, P. Innocente, M. Spolaore, *The plasma boundary in single helical axis RFP plasmas*, *Nuclear Fusion* **50**, 035014.

[84] A. Canton, S. D. Bello, R. Cavazzana, P. Innocente, *Density control in RFX-mod Reversed Field Pinch device*, *2008 Proc. 35th EPS Conf. on Control. Fusion and Plasma Phys.* (Heraclion, Greece, 2008). `http://epsppd.epfl.ch/Hersonissos/pdf/D1_002.pdf`.

[85] G. Spizzo, S. Cappello, A. Cravotta, D. F. Escande, I. Predebon, L. Marrelli, P. Martin, R. B. White, *Transport Barrier inside the Reversal Surface in the Chaotic Regime of the Reversed-Field Pinch*, *Phys. Rev. Lett.* **96**, 025001 (2006).

[86] N. Vianello, *et al.*, *Transport mechanisms in the outer region of RFX-mod*, *Nuclear Fusion* **49**, 045008 (2009).

[87] P. Zanca, *et al.*, *Analysis of phase locking of tearing modes in reversed field pinch plasmas*, *Physics of Plasmas* **8**, 516 (2001).

[88] P. Innocente, A. Alfier, L. Carraro, R. Lorenzini, R. Pasqualotto, D. Terranova, the RFX Team, *Transport and confinement studies in the RFX-mod reversed-field pinch experiment*, *Nuclear Fusion* **47**, 1092 (2007).

[89] P. Zanca, L. Marrelli, G. Manduchi, G. Marchiori, *Beyond the intelligent shell concept: the clean-mode-control*, *Nuclear Fusion* **47**, 1425 (2007).

[90] R. B. White, M. S. Chance, *Hamiltonian guiding center drift orbit calculation for plasmas of arbitrary cross section*, *Physics of Fluids* **27**, 2455 (1984).

[91] G. Spizzo, *et al.*, *Investigation on the relation between edge radial electric field asymmetries in RFX-mod and density limit*, *Plasma Physics and Controlled Fusion* **52**, 095011 (2010).

[92] P. Scarin, *et al.*, *Topology and transport in the edge region of RFX-mod helical regimes*, *Nuclear Fusion* **51**, 073002 (2011).

[93] N. Vianello, *et al.*, *3D effects on RFX-mod helical boundary region*, *24th Fusion Energy Conference* (San Diego, USA, 2012). Paper EX/P8-02 and submitted to Nuclear Fusion.

[94] M. Puiatti, *et al.*, *Wall conditioning and density control in the Reversed Field Pinch RFX-mod*, *24th Fusion Energy Conference* (San Diego, USA, 2012). Paper EX/P5-01 and submitted to Nuclear Fusion.

[95] M. Puiatti, *et al.*, *High density physics in reversed field pinches: comparison with tokamaks and stellarators*, *Nuclear Fusion* **49**, 045012 (2009).

[96] D. Terranova, F. Auriemma, A. Canton, L. Carraro, R. Lorenzini, P. Innocente, *Experimental particle transport studies by pellet injection in helical equilibria*, *Nuclear Fusion* **50**, 035006 (2010).

[97] S. Barison, A. Canton, S. D. Bello, S. Fiameni, P. Innocente, A. Alfier, S. Munaretto, F. Rossetto, *Analysis of the interaction between plasmas and the graphite first wall in RFX-mod*, *Journal of Nuclear Materials* **415**, S274.

[98] A. Canton, M. Agostini, L. Carraro, R. Cavazzana, S. D. Bello, L. Grando, P. Scarin, M. Spolaore, B. Zaniol, M. Zuin, *Studies of spatial uniformity of glow discharge cleaning plasmas on the RFX-mod device*, *20th International Conference on Plasma Surface Interaction* (Aachen, Germany, 2012). Paper P3-73 and submitted to Journal of Nuclear Materials.

[99] S. Munaretto, *et al.*, *RFX-mod wall conditioning by lithium pellet injection*, *Nuclear Fusion* **52**, 023012 (2012).

[100] L. Carraro, *et al.*, *High current plasmas in RFX-mod Reversed Field Pinch*, *24th Fusion Energy Conference* (San Diego, USA, 2012). Paper EX/P3-04 and submitted to Nuclear Fusion.

[101] M. E. Puiatti, *et al.*, *High density limit in reversed field pinches*, *Physics of Plasmas* **16**, 012505 (2009).

[102] R. Lorenzini, F. Auriemma, P. Innocente, E. Martines, S. Martini, D. Terranova, *Confinement loss during dynamo relaxation event in RFX-mod*, *Plasma Physics and Controlled Fusion* **50**, 035004 (2008).

[103] R. B. Howell, J. C. Ingraham, G. A. Wurden, P. G. Weber, C. J. Buchenauer, *Asymmetric magnetic flux generation, m=1 activity, and edge phenomena on a reversed-field pinch*, *Physics of Fluids* **30**, 1828 (1987).

[104] K. Hattori, Y. Hirano, T. Shimada, Y. Yagi, Y. Maejima, I. Hirota, K. Ogawa, *Behavior of magnetic field fluctuations during dynamo activity and its effect on energy confinement in a reversed-field pinch*, *Physics of Fluids B: Plasma Physics* **3**, 3111 (1991).

[105] K. Kusano, T. Tamano, T. Sato, *MHD simulation of the toroidal phase locking mechanism in a reversed field pinch plasma*, *Nuclear Fusion* **31**, 1923 (1991).

[106] A. Fassina, *Thermal and transport characterization of RFP plasmas from electron temperature data*, Ph.D. thesis, Universitá degli studi di Padova (2010). `http://paduaresearch.cab.unipd.it/2938/1/tesi.pdf`.

[107] P. Innocente, A. Alfier, A. Canton, R. Pasqualotto, *Plasma performance and scaling laws in the RFX-mod reversed-field pinch experiment*, *Nuclear Fusion* **49**, 115022 (2009).

[108] R. J. Groebner, T. H. Osborne, *Scaling studies of the high mode pedestal*, *Physics of Plasmas* **5**, 1800 (1998).

[109] M. Greenwald, *Density limits in toroidal plasmas*, *Plasma Physics and Controlled Fusion* **44**, R27 (2002).

[110] P. R. Bevington, D. R. Robinson, *Data reduction and error analysis for the physical sciences* (McGraw-Hill, Inc., 1992).

[111] M. Loreti, *Teoria degli Errori e Fondamenti di Statistica* (Edizione privata, 2008). `http://wwwcdf.pd.infn.it/labo/INDEX.html`.

[112] A. Alfier, R. Pasqualotto, G. Spizzo, A. Canton, A. Fassina, L. Frassinetti, *Electron temperature profiles in RFX-mod*, *Plasma Physics and Controlled Fusion* **50**, 035013 (2008).

[113] R. Lorenzini, *et al.*, *On the energy transport in internal transport barriers of RFP plasmas*, *Nuclear Fusion* **52**, 062004 (2012).

[114] G. Pereverzev, P. Yushmanov, *ASTRA - An Automatic System for Transport Analysis in a Tokamak*, *IPP Report No 5/98*, Max-Planck Institut für Plasmaphysik (2002). `http://edoc.mpg.de/282186`.

[115] P. Martin, *et al.*, *A new paradigm for RFP magnetic self-organization: results and challenges*, *Plasma Physics and Controlled Fusion* **49**, A177 (2007).

[116] A. Ruzzon, A. Fassina, P. Franz, M. Gobbin, L. Marelli, *Temperature profile dynamics in QSH regimes with multichords Soft X-Rays diagnostic in RFX-mod*, *2012 Proc. 39th EPS Conf. & 16th Int. Congress on Plasma Phys.* (Stockholm, Sweden, 2012). `http://ocs.ciemat.es/EPSICPP2012PAP/pdf/P2.023.pdf`.

[117] P. Franz, L. Marrelli, A. Murari, G. Spizzo, P. Martin, *Soft X-ray tomographic imaging in the RFX reversed field pinch*, *Nuclear Fusion* **41**, 695 (2001).

[118] U. Stroth, G. Kühner, H. Maassberg, H. Ringler, *Dimensionally similar discharges in the W7-AS stellarator*, *Phys. Rev. Lett.* **70**, 936 (1993).

[119] P. J. Rousseuw, A. M. Leroy, *Robust Regression and Outlier Detection* (John Wiley & Sons, 1987).

[120] D. Gregoratto, L. Garzotti, P. Innocente, S. Martini, A. Canton, *Behaviour of electron density profiles and particle transport analysis in the RFX reversed field pinch*, *Nuclear Fusion* **38**, 1199 (1998).

[121] G. D. Masi, R. Cavazzana, A. Fassina, E. Martines, B. Momo, M. Moresco, *Edge density characterization in the RFX-mod experiment using the ultrafast reflectometry technique*, *Nuclear Fusion* **51**, 053016 (2011).

[122] R. Lorenzini, F. Auriemma, A. Canton, L. Carraro, *Particle transport in reversed field pinch helium plasmas*, *Physics of Plasmas* **13**, 112510 (2006).

[123] M. Agostini, P. Scarin, R. Cavazzana, F. Sattin, G. Serianni, M. Spolaore, N. Vianello, *Edge turbulence characterization in RFX-mod with optical diagnostics*, *Plasma Physics and Controlled Fusion* **51**, 105003 (2009).

[124] M. Moresco, R. Dubhghaill, E. Spada, *Application of microwave reflectometry for plasma density diagnostics in a reversed-field pinch machine*, *International Journal of Infrared and Millimeter Waves* **13**, 609 (1992).

[125] P. W. Terry, *Suppression of turbulence and transport by sheared flow*, *Rev. Mod. Phys.* **72**, 109 (2000).

[126] B. Zaniol, L. Carraro, E. Gazza, I. Predebon, M. Puiatti, P. Scarin, G. Spizzo, M. Valisa, *Impurity flow studies in RFX-mo operation with reduced MHD mode activity*, *2007 Proc. 34th EPS Conf. on Control. Fusion and Plasma Phys.* (Warsaw, Poland, 2007). `http://epsppd.epfl.ch/Warsaw/pdf/P1_082.pdf`.

[127] P. Scarin, M. Agostini, R. Cavazzana, F. Sattin, G. Serianni, N. Vianello, *Edge turbulence in RFX-mod virtual-shell discharges*, *Journal of Nuclear Materials* **363-365**, 669 (2007).

[128] T. Bolzonella, N. Pomaro, G. Serianni, D. Marcuzzi, *New wide bandwidth in-vessel magnetic measurement system for RFX*, *Review of Scientific Instruments* **74**, 1554 (2003).

[129] S. Martini, *et al.*, *Active MHD control at high currents in RFX-mod*, *Nuclear Fusion* **47**, 783 (2007).

[130] R. Lorenzini, D. Terranova, F. Auriemma, R. Cavazzana, P. Innocente, S. Martini, G. Serianni, M. Zuin, *Toroidally asymmetric particle transport caused by phase-locking of MHD modes in RFX-mod*, *Nuclear Fusion* **47**, 1468 (2007).

[131] B. Momo, *Studio della struttura magnetica della regione esterna nell'esperimento RFX-mod*, Master thesis, Universitá degli studi di Padova (2008).

[132] B. Momo, E. Martines, D. F. Escande, M. Gobbin, *Magnetic coordinate systems for helical SHAx states in reverse field pinch plasmas*, *Plasma Physics and Controlled Fusion* **53**, 125004 (2011).

[133] M. Gobbin, *et al.*, *Heat transport in helical RFX-mod plasmas by electron temperature dynamics from soft-X-ray diagnostics*, *2012 Proc. 39th EPS Conf. & 16th Int. Congress on Plasma Phys.* (Stockholm, Sweden, 2012). `http://ocs.ciemat.es/epsicpp2012pap/pdf/P4.094.pdf`.

[134] P. Martin, *et al.*, *Overview of RFX-mod results*, *Nuclear Fusion* **49**, 104019 (2009).

[135] E. Martines, *et al.*, *Equilibrium reconstruction for single helical axis reversed field pinch plasmas*, *Plasma Physics and Controlled Fusion* **53**, 035015 (2011).

[136] K. F. Schoenberg, J. R. W. Moses, R. L. Hagenson, *Plasma resistivity in the presence of a reversed-field pinch dynamo*, *Physics of Fluids* **27**, 1671 (1984).

[137] B. Momo, *et al.*, *Magnetic topology and role of the m=0 islands in the plasma-wall interaction in RFX-mod*, *2012 Proc. 39th EPS Conf. & 16th Int. Congress on Plasma Phys.* (Stockholm, Sweden, 2012). `http://ocs.ciemat.es/EPSICPP2012ABS/pdf/P4.061.pdf`.

[138] Y. Andrew, *et al.*, *JET divertor geometry and plasma shape effects on the L-H transition threshold*, *Plasma Physics and Controlled Fusion* **46**, A87 (2004).

[139] ITPA Confinement and H-mode Threshold Database Working Group presented by J A Snipes, *Multi-Machine Global Confinement and H-mode Threshold Analysis*, *2002 Proc. 19th IAEA Fusion Energy Conf.* (Lyon, France, 2002). `http://www-pub.iaea.org/MTCD/publications/PDF/csp_019c/pdf/ctp_04.pdf`.

[140] P. Gohil, T. Evans, M. Fenstermacher, J. Ferron, T. Osborne, J. Park, O. Schmitz, J. Scoville, E. Unterberg, *L-H transition studies on DIII-D to determine H-mode access for operational scenarios in ITER*, *Nuclear Fusion* **51**, 103020 (2011).

[141] H. Meyer, *et al.*, *Improved H-mode access in connected DND in MAST*, *Plasma Physics and Controlled Fusion* **47**, 843 (2005).

[142] H. Meyer, *et al.*, *Active control of the H-mode transition on MAST*, *Plasma Physics and Controlled Fusion* **50**, 015005 (2008).

[143] H. Meyer, *et al.*, *L-H transition and pedestal studies on MAST*, *Nuclear Fusion* **51**, 113011 (2011).

[144] H. Meyer, *et al.*, *H-mode physics of near double null plasmas in MAST and its applications to other tokamaks*, *Nuclear Fusion* **46**, 64 (2006).

[145] Y. Ma, J. W. Hughes, A. E. Hubbard, B. LaBombard, J. Terry, *H-mode power threshold reduction in a slot-divertor configuration on the Alcator C-Mod tokamak*, *Plasma Physics and Controlled Fusion* **54**, 082002 (2012).

[146] J. A. Snipes, the International H-mode Threshold Database Working Group, *Latest results on the H-mode threshold using the international H-mode threshold database*, *Plasma Physics and Controlled Fusion* **42**, A299 (2000).

[147] R. Maingi, *et al.*, *Overview of L-H power threshold studies in NSTX*, *Nuclear Fusion* **50**, 064010 (2010).

[148] A. Loarte, *et al.*, *Plasma detachment in JET Mark I divertor experiments*, *Nuclear Fusion* **38**, 331 (1998).

[149] R. P. B. Duval, J. Moret, M. Fenstermacher, A. Loarte, W. Meyer, J. Mlynar, A. Refke, J. Rommers, *Divertor Detachment in TCV Ohmic Plasmas*, *1999 Proc. 26th EPS Conf. on Conrtolled Fusion and Plasma Phys.* (Maastricht, Netherlands, 1999). `http://epsppd.epfl.ch/Maas/web/pdf/p3035.pdf`.

[150] Y. R. Martin, the TCV team, *H-mode threshold power in TCV Ohmic plasmas*, *Plasma Physics and Controlled Fusion* **44**, A143 (2002).

[151] K. Matsuda, *Ray tracing study of the electron cyclotron current drive in DIII-D using 60 GHz*, *IEEE Transactions on Plasma Science* **17**, 6 (1989).

[152] P. Sauter, *et al.*, *L- to H-mode transitions at low density in ASDEX Upgrade*, *Nuclear Fusion* **52**, 012001 (2012).

[153] B. Duval, A. Bortolon, A. Karpushov, R. Pitts, A. Pochelon, A. Scarabosio, *Bulk plasma rotation in the TCV tokamak in the absence of external momentum input*, *Plasma Physics and Controlled Fusion* **49**, B195 (2007).

[154] X. Garbet, *et al.*, *Turbulence and energy confinement in TORE SUPRA Ohmic discharges*, *Nuclear Fusion* **32**, 2147 (1992).

[155] ITPA H-mode Power Threshold Database Working Group presented by T Takizuka, *Roles of aspect ratio, absolute B and effective Z of the H-mode power threshold in tokamaks of the ITPA database*, *Plasma Physics and Controlled Fusion* **46**, A227 (2004).

[156] A. Rechester, M. Rosenbluth, *Electron heat transport in a tokamak with destroyed magnetic surfaces*, *Physics Review Letters* **40**, 38 (1978).

[157] P. Martin, J. Adamek, P. Agostinetti, M. Agostini, A. Alfier, C. Angioni, V. Antoni, L. Apolloni, F. Auriemma, O. Barana, S. Barison, M. Baruzzo, P. Bettini, M. Boldrin, T. Bolzonella, D. Bonfiglio, F. Bonomo, A. Boozer, M. Brombin, J. Brotankova, A. Buffa, A. Canton, S. Cappello, L. Carraro, R. Cavazzana, M. Cavinato, L. Chacon, G. Chitarin, W. Cooper, S. D. Bello, M. D. Palma, R. Delogu, A. D. Lorenzi, G. D. Masi, J. Dong, M. Drevlak, D. Escande, F. Fantini, A. Fassina, F. Fellin, A. Ferro, S. Fiameni, A. Fiorentin, P. Franz, E. Gaio, X. Garbet, E. Gazza, L. Giudicotti, F. Gnesotto, M. Gobbin, L. Grando, S. Guo, Y. Hirano, S. Hirshman, S. Ide, V. Igochine, Y. In, P. Innocente, S. Kiyama, S. Liu, Y. Liu, D. L. Bruna, R. Lorenzini, A. Luchetta, G. Manduchi, D. Mansfield, G. Marchiori, D. Marcuzzi, L. Marrelli, S. Martini, G. Matsunaga, E. Martines, G. Mazzitelli, K. McCollam, S. Menmuir, F. Milani, B. Momo, M. Moresco, S. Munaretto, L. Novello, M. Okabayashi, S. Ortolani, R. Paccagnella, R. Pasqualotto, M. Pavei, G. Perverezev, S. Peruzzo, R. Piovan, P. Piovesan, L. Piron, A. Pizzimenti, N. Pomaro, N. Pomphrey, I. Predebon, M. Puiatti, V. Rigato, A. Rizzolo, G. Rostagni, G. Rubinacci, A. Ruzzon, H. Sakakita, R. Sanchez, J. Sarff, F. Sattin, A. Scaggion, P. Scarin, W. Schneider, G. Serianni, P. Sonato, E. Spada, A. Soppelsa, S. Spagnolo, M. Spolaore, D. Spong, G. Spizzo, M. Takechi, C. Taliercio, D. Terranova, V. Toigo, M. Valisa, M. Veranda, N. Vianello, F. Villone, Z. Wang, R. White, D. Yadikin, P. Zaccaria, A. Zamengo, P. Zanca, B. Zaniol, L. Zanotto, E. Zilli, G. Zollino, M. Zuin, *Overview of the RFX fusion science program*, *Nuclear Fusion* **51**, 094023 (2011).

[158] M. Agostini, A. Scaggion, P. Scarin, G. Spizzo, N. Vianello, *Interplay between edge magnetic topology, pressure profile and blobs in the edge of RFX-mod*, *Plasma Physics and Controlled Fusion* **54**, 065003 (2012).

[159] M. Puiatti, M. Valisa, M. Agostini, F. Auriemma, F. Bonomo, L. Carraro, A. Fassina, M. Gobbin, R. Lorenzini, B. Momo, A. Scaggion, B. Zaniol, A. Alfier, L. Apolloni, M. Baruzzo, T. Bolzonella, D. Bonfiglio, A. Canton, S. Cappello, R. Cavazzana, S. D. Bello, G. D. Masi, D. Escande, P. Franz, E. Gazza, S. Guo, P. Innocente, G. Marchiori, L. Marrelli, P. Martin, E. Martines, S. Martini, S. Menmuir, L. Novello, R. Paccagnella, P. Piovesan, L. Piron, I. Predebon, A. Ruzzon, F. Sattin, P. Scarin, A. Soppelsa, G. Spizzo, S. Spagnolo, M. Spolaore, D. Terranova, M. Veranda, N. Vianello, P. Zanca, L. Zanotto, M. Zuin, *Internal*

and external electron transport barriers in the RFX-mod reversed field pinch, *Nuclear Fusion* **51**, 073038 (2011).

[160] A. Scaggion, M. Agostini, L. Carraro, A. Fassina, R. Lorenzini, B. Momo, S. Munaretto, M. Puiatti, G. Spizzo, M. Valisa, N. Vianello, *Characterization of external electron temperature profiles in the RFX-mod Reversed Field Pinch*, *2011 Proc. 38th EPS Conf. on Control. Fusion and Plasma Phys.* (Strasbourg, France, 2011). http://ocs.ciemat.es/EPS2011PAP/pdf/P5.059.pdf.

[161] A. Scaggion, Y. Martin, H. Reimerdes, the TCV team, *H-mode access with different X-point height in TCV*, *2012 Proc. 39th EPS Conf. & 16th Int. Congress on Plasma Phys.* (Stockholm, Sweden, 2012). http://ocs.ciemat.es/epsicpp2012pap/pdf/P2.093.pdf.

[162] M. Agostini, L. Carraro, R. Cavazzana, G. D. Masi, A. Scaggion, P. Scarin, G. Spizzo, M. Spolaore, N. Vianello, B. Zaniol, *Interaction between turbulence and electron profiles in the RFX-mod helical plasma edge*, *2012 Proc. 39th EPS Conf. & 16th Int. Congress on Plasma Phys.* (Stockholm, Sweden, 2012). http://ocs.ciemat.es/epsicpp2012pap/pdf/P1.037.pdf.

Il vero viaggio non consiste nel cercare nuove terre,
ma nell'avere nuovi occhi.

Marcel Proust

Alla fine di ogni buon viaggio è necessario, e dico proprio necessario, congratularsi con i compagni d'avventura, ringaraziare gli ospiti volontari o meno, ricordare gli amici ed i lieti incontri, salutare i passanti ed i curiosi, riconoscere gli oppositori ... e abbracciare chi ci ha aspettato all'arrivo.

Non posso non cominciare brindando alla salute di Marco ed Emanuele fondatori, ideatori e sostenitori del primo ed unico dottorato enogastronomico in scienza ed ingegneria della fusione. Ramiro, il Tacao Grande, Versailles, lo scopone scientifico di João, i taxi a 5 posti, la torta bavarese a quadratoni ... quante belle cose ... peccato che Emanuele si sia perso qualcosa!

Un sentito ringraziamento all'uomo vestito di viola che mi ha fatto da fratello maggiore e mi ha sempre spronato: grazie Matteo!

Un cinque alto per tutto il popolo giovane (e anche un po' meno giovane) del consorzio: per chi ha introdotto l'usanza del frisbee, per chi con grande dolcezza si fa pigliare ogni giorno per i fondelli, per chi rompe ogni santo giorno perchè ha fame, per chi si vanta di saper giocare a calcio, per chi c'era a Skrötøsborg ...

Un abbraccio a tutti coloro che hanno sopportato la mia insolenza, la mia passione per la fisica, le mie letture impegnate e i miei sproloqui.

Grazie mamma. Grazie papá. Grazie Giulia.

Gennaio 2013

E alla fine un po' di ilaritá!

"Lutto nel mondo della scienza: Giacobbo sta una bellezza."

"Stephen Hawking compie 70 anni. O 100mila chilometri."

"Gelmini le spara grosse sul tunnel dei neutrini.
E ancora non avete sentito Giovanardi sui busoni di Higgs..."

`www.spinoza.it`